Technical Transactions

Czasopismo Techniczne

Contents

ENVIRONMENTAL ENGINERING

MECHANICS

PHYSICS

Teresa Bardzińska-Bonenberg (teresa@message.pl)

Department of Architecture and Design, Poznan University of Art

1960's polish modernistic industrial buildings today

Polskie modernistyczne obiekty przemysłowe z lat 1960–1970 dzisiaj

Abstract

The 1960s in Poland was a period when formal boundaries of the Stalinist period were being shaken off. The economy, with its reliance on heavy industry, was in dire need of new production facilities, the shape of which was dictated by the available technology. The mounting restrictions imposed by the centrally controlled state and changing investment priorities did not affect production undertakings inasmuch as other construction industry disciplines. At that time, equipment and industrial unit designs were not subject to categorisation yet, and furthermore enjoyed privileged status when it came to acquiring building materials. Such a situation gave designers a free run at shaping their creations to accommodate technological requirements and in accordance with the modernistic line. Numerous outstanding examples of industrial architecture were created, constituting an important element of the Polish post-war architecture. Unfortunately, only a few survive to this day.

Keywords: industry, technology, architecture, construction

Streszczenie

W Polsce lata 60. XX w. były okresem odchodzenia od ograniczeń formalnych okresu stalinowskiego. Gospodarka, której podstawą był przemysł ciężki, wymagała nowych zakładów produkcyjnych, a ich kształt dyktowała technologia. Narastające ograniczenia narzucane przez centralnie sterowane państwo oraz zmienne priorytety inwestycyjne dotyczyły w mniejszym stopniu przedsięwzięć produkcyjnych niż innych dziedzin budownictwa. Projekty hal i urządzeń nie podlegały jeszcze typizacji, a ponadto miały uprzywilejowany status w pozyskiwaniu materiałów budowlanych. W tej sytuacji projektanci mogli kształtować je zgodnie z wymaganiami technologii i w konwencji estetyki modernistycznej. Powstała grupa wybitnych, niestety w większości nieistniejących już dzieł architektury przemysłowej, stanowiących ważny element w historii polskiej powojennej architektury.

Słowa kluczowe: przemysł, technologia. architektura, konstrukcja

1. Growth of industry and growth of the country

Post –war industrial buildings erected under the Polish People's Republic (PRL) for various reasons constituted an exceptional group of investments. Industrialisation of Poland became the primary direction for developing the economy, which was also to be the driving force behind the country's growth. This favoured industrial and accompanying investments. In imposing functional solutions, production plant technologies determined the structure, which was decisive when it came to the formal aspect of solutions. The financing of these investments involved central and ministry specific grants in "exchangeable currencies" (i.e. West European), which made it possible to purchase Western materials and technological solutions. These were decisive when it came to the appearance of production halls and auxiliary buildings. The above factors meant that work in state industrial design offices was often better paid on account of the official "per volume" conversion tables and workers could afford more freedom, contact with Western technologies and materials, while also being provided with an opportunity to travel.

Kombinat Metalurgiczny Nowa Huta [Nowa Huta Steelworks] is a flagship example of the early "People's Republic" achievements. It is clear that only the representative buildings were in line with the "national" architecture of the Stalinist period. A city for 100 thousand inhabitants – Nowa Huta – was constructed together with the steelworks. The urban project took into account the terrain structure, but did not create a clear communication link with Kraków. However, the layout conveyed clear references to the Polish pre-war modernism. The buildings were erected in accordance with the social realism architecture principles of the 1950s.

2. Industrial architecture in Poland – more freedom of form and less technical restrictions

The 1960s were a period during which, after October '56, architects were able to return to modernism, which was the dominant European aesthetic formula. That return was difficult, as from year to year residential norms were becoming stricter and mass building systems were gradually stripped down. House factories were a visible sign thereof, whose products severely limited the potential impact of engineers and designers [7].

"Prestigious", high rank and influential buildings were also part of the privileged group. These included large-scale entertainment venues, train and bus stations, large sports facilities, some public use buildings, exhibition pavilions. A small sector of the private investors remained, providing church buildings and some private houses, which also afforded a larger degree of freedom.

During the period in question, rivalry between the two European political systems was predominantly taking place on the heavy industry stage, and that is why in Poland construction of industrial facilities of this type received support at every level. The prefabrication of repeatable elements, preferred and enforced in other sectors of the construction industry,

was fully justified when it came to large production halls. It facilitated the creation of an open space to accommodate changing technological processes and was also economically sound.

The above conditions, faced by Polish architects in the 1960s, meant that many new industrial plants, similar to those built all over Europe, sprung up. Undisputed achievements of this trend in Poland, arising from engineering and formal freedom, were publicised only to a small extent. Similar to other areas of life, censorship kept a close watch over the secrets of heavy, and sometimes not so heavy industry. As a result, only small photographs, outlines and fragmentary publications found their way to professional press. This meant also that not all works were in the public knowledge. Even a thorough review of the professional press from the period does not present the entire picture.

This paper outlines the history and subsequent fate of a number of selected, formerly flagship heavy and light industry plants, mentioned in professional press:

- ▸ a complex of cooling ventilators at Skawina Power Station (1960–1961),
- ▸ „Runotex" in Kalisz (1962),
- ▸ Furniture Factories [*Fabryka Mebli*] in Wyszyków (1962),
- ▸ Elana in Toruń (1963),
- ▸ Lime Production Plant [*Zakłady Przemysłu Wapienniczego*] in Bukowa (1964), today's Lhoist, Bukowa Cement Plant,
- ▸ Tank Furnace Hall at the Sandomierz Glassworks (1965), today's Piklington Sandomierz,
- ▸ Ski Factory in Szaflary near Zakopane (1966).

3. Modernism – theoretical assumptions and industrial logic

Modernistic architecture referred to geometric divisions, rhythms, sequences, dominant colours. It drew inspiration from arts that developed its non-objective, abstract line. In the first decades of the 20th century, theoreticians and young architects also assumed a similar, ascetic framework for creating functions, structures and building spatial forms. The "box" [10, p. 91] architecture popularised by Bauhaus, accepted and employed by the Polish pre-war architectural avant-garde, was abruptly interrupted by WW2 and the Stalin era. European modernism was changing during that time. In architecture of the 1940s and 1950s, purism introduced a new, soft line and sleek shapes, expressionism, although out of the limelight, still persevered, from time to time making an appearance on the European stage. Op-art, which began in the USA, appeared in European art in the 1950s. It made use of optical illusions. in the form of "eye catching" black and white, sometimes colour compositions. Repeatability of elements in large-scale units, light façade areas and dark windows, linear perspective and scale provided similar experiences. That is probably why the buildings themselves, as well as the methods used to draw them, bear resemblance to op-art aesthetics [6, p. 12].

Technical equipment, such as pipelines, fans or filters, constituted attractive counterpoints in the geometric environmental compositions. Curved installations set against rectangular halls appeared in general plans next to tanks; they were dominant in façades and hand drawn

perspectives. The layout of buildings and systems was imposed by technological processes, and as such, the spatial freedom of composure relied heavily on media distribution and communication – which was determined by the general blueprints for the facilities. In its level of abstraction, the convention for presenting architectural designs was similar to abstract art pieces. One of the reasons for this was the fact that at working meetings of all levels, both the designers as well as the investors, were professionals who paid attention to the essence of the matter at hand. The graphical presentation and how the project was drawn were down to the architect [5, p. 13]. Here, it would be difficult not to mention the impact of the then architecture guru, Le Corbusier, and his famous and specific method of drawing.

The search for industrial plant aesthetic expression was conducted under the influence of European solutions glimpsed in rarely obtainable professional publications. A small group of Polish architects and designers was able to verify their experiences abroad, during business trips. Despite that, in the 1960s, works were created in Poland, which were subsequently cited in foreign literature. This stands testament to the quality of Polish industrial architecture on a European scale. Teams of architects, engineers, technicians and artists employed at large, often specialist design firms were engaged in solving problems associated with designing industrial plants. In comparison with functional solutions, up-to-date forms and structural concepts, workmanship, building materials and available details and finishes were of a poor quality.
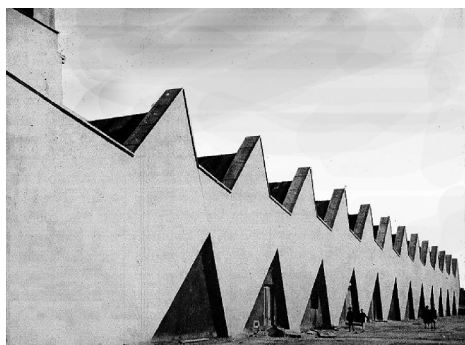
Fig. 1 a, b. "Runotex" weaving mill building in Kalisz in early sixties [12, s. 24] and now

The "Runotex" weaving mill building in Kalisz from 1962 is one of the more interesting, discussed in Polish as well as foreign publications and textbooks [8, p. 237], [2, p. 413], [11, p. 73], [9, p. 31], [8, p. 299]. It was designed by architects Stanisław Sikorski and Jerzy Główczewski as well as engineers Wacław Zalewski, Zenon Zieliński and Jan Kocy [12, p. 24]. The distinctive feature at "Runotex" is a flat, "saw tooth" elongated modular façade of the weaving mill. This is a result of the adopted roof structure for covering the 30-m span of the hall. It is made up of concave trough-like forms, interspersed with bands of windows. The white façade plaster is in stark contrast to the triangular, dark, recessed wall surfaces of the ground floor. Such a composition was a formal solution, only partially stemming from the structural system: the aim was to create a powerful, recognisable spatial form. It was soon

to be the inspiration for the logo displayed on products manufactured at the factory, now changed despite the fact that the unit still stands today.

The Furniture Factory building in Wyszków near Warsaw is one of the most interesting light industry buildings erected in the 1960s (1962) [2, p. 413], [12, p. 23], [8, p. 236], [9]. At the foundation of the structural solution lay the freedom to arrange changing production lines and an entirely flexible interior space. That is why the staff facilities were located on the mezzanine inside the hall, leaving an unobstructed ground floor space. The designers used a repeatable shell elements in the shape of a wide "V", 1.5 m long and 6 m wide, with the lower rib prepared for pre-stressing. The elements aligned next to each other and pre-stressed made up groove girders supported at their ends by reinforced concrete pillars. These were used to cover two production halls, 30 m and 15 m wide.
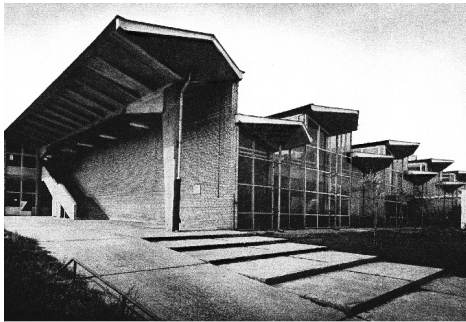
Fig. 2a, b. Wyszków, main production hall of the Furniture Factory in 1965, [13, p. 86] and now, author's own photograph

The effective shape of the spatial form was achieved by alternating the heights of subsequent roof "girder" sections. This also made it possible to achieve uniform lighting of the interior through bands of windows. Extreme segments of each girder were extended creating characteristic, triangular canopies, sheltering and casting shadows on the flat, glass façade. It opened a view of a greenery contained within the plant. At the ends of the halls, the "girders" were left open, providing a roofed staircase to the mezzanine and ground level entry to the hall. Bicycle stands are also located therein. The technical difficulties encountered during construction were described in the documents: the rubber window gaskets "... within a short time were cracked and not tight..." [2, p. 415] and "the contractor had innumerable problems with the glass adhesion technology at the construction site" [2, p. 415]. As it can be seen these were pioneering struggles, aiming to create architecture far and above the mundane technical reality of PRL. The furniture factory in Wyszków was designed by architects Andrzej Dzierżawski, Zbigniew Pawelski and Maciej Siennicki as well as engineers Wacław Zalewski and Aleksander Włodarz [12, p. 23]

The Skawina Power Plant was built between 1957 and 1961 and at that time, it was the largest enterprise of this type in Poland. The most interesting technical and formal solutions within this facility included the complex of cooling ventilators. Constructed in

1960–1961, according to a design by architect Władysław Zembaty and engineer Zygfryd Napieraj [12, p. 22], it was a technological novelty. It replaced traditional cooling towers and its structure was simpler and could be constructed in less time. The ventilators were arranged into a single battery and the exhaust tubulars from each one pointed upwards, crowning a concrete cuboid standing on thin pillars "cut off" from its wall. The whole form is reminiscent of abstract modernistic compositions. Vertical grey stripes were painted on the steel ventilator "chimneys", which together with the rhythm of their outside metal sheeting resulted in a Mondrian monochrome composition [1, p. 241]. The flat, reinforced concrete "cube" housing the technological levels is 15 cm thick and it is in stark contract with the rich structure and colour of the "tubulars".
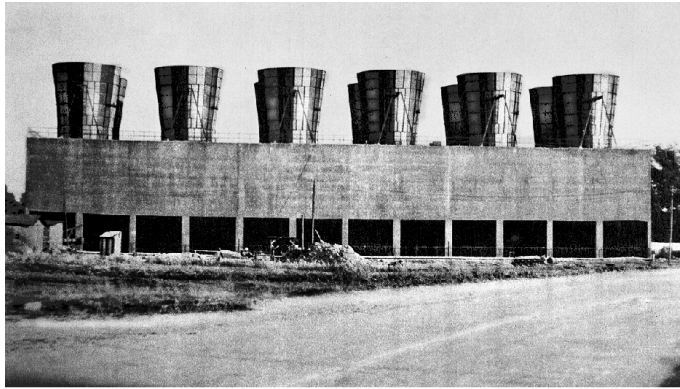
Fig. 3a. Skawina, power plant, ventilators complex [1, p. 241]
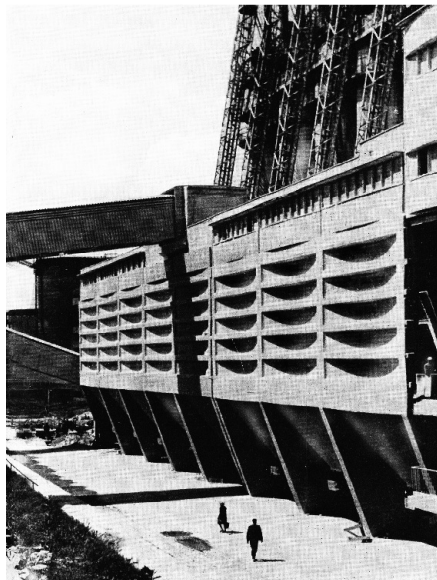
Fig. 3b. Bukowa, Lime Production Plant, rock and aggregate containers [3, p. 16]

An equally interesting optical effect resulted from the stone and coke containers structure at the Bukowa Lime Production Plant (1964), located in Świętokrzyskie Province. This work was coined by architects Alina Dębska and Aleksander Dębski as well as engineer Stanisław Srokowski. The containers supplied adjacent lime furnaces. Traditionally, siloses were installed at such locations. A repeatable structural module of the containers yielded tangible economic benefits, and the structural requirements dictated their interesting visual form. A monolithic reinforced concrete skeleton, which holds the container shells, forms bold triangular supports, separating particular chutes. [3, p. 16]. Concrete shells supported by horizontal ribs allow free movement of the contents.

Elana, the synthetic and mixed fabrics plant was built in Toruń in 1963. At that time, its buildings were fitted with an annealed glass façade on an aluminium framework – a novelty in Poland. This modular façade, already well established in the West, made its home in the Polish industrial construction industry for good when, at the beginning of the 1960s, national production of this universal system commenced. A vast glass front wall provided the light for Elana's main production hall. The same system, appropriately scaled, was used for the office building and smaller units. The design of the plant was prepared by architects Stanisław Turczynowicz, Zbigniew Bobrowski, Henryk Marconi, Barbara Rogińska, Jerzy Romański, Leszek Szycht and a team of engineers. [13, p. 77], [4, p. 231]

The largest group of industrial buildings erected during that period were production halls of various types. The main problem associated with roof coverings spanning more than 24 meters was solved using pre-stressed or cable tensioned reinforced concrete girders arranged on different levels. A variety of shell shaped net-concrete covers were laid on these, facilitating uniform distribution of light to the entire units. The buildings were as a rule based on a rectangular plan, featuring reinforced concrete or brick walls between reinforced concrete pillars. Diversified forms of roofs enriched simple, cubic volumes of industrial halls and were signalized by copings and saw-rhythms of the outer walls. The frame based structure and flat walls facilitated unobstructed installation of side windows, conveyor belts, ventilators, entrances and gates in accordance with the technological requirements.

The 1965 Sandomierz Glassworks structure was an exception. The Tank Furnace Hall was a hyperbolic shell closed at both ends by glass walls. It was designed by architect Zdzisław Bajtyngier and engineer Zbigniew Piwowarczyk [9]. Similar curved sculpture forms were rarely seen in industrial architecture – here, the massive cooling towers, dominating industrial landscapes, were an exception. It is difficult not to associate the Tank Furnace Hall shape with the 1952 *Laboratorio Rayos Cósmicos* in Mexico by Félix Candela.

The smallish ski-manufacturing hall in Szaflary near Zakopane designed by Stanisław Karpiel and built in 1966 was another atypical solution. Despite its reinforced concrete structure, the spatial form reflects the Podhale region construction character: a steep roof, low set windows in characteristic triangular "lunettes", use of stone on façades. At first sight, it blends in with the surrounding greenery and seems nothing like an industrial facility. It may be considered a precursor example of Polish vernacular architecture.

There was one further group of industrial plants, the documentation of which was not published due to a confidentiality clause. These were buildings associated with the arms
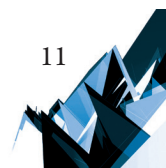
industry or, to a large extent, working for the needs of the country defence. Mikrohuta, built in the mid-1960s near Katowice, was one such example. The buildings of this complex, the main hall including, feature cuboidal forms, as dictated by technological requirements. Roof skylights, extractors, ventilators pipes and scattered windows enrich the volume. The façades and roofs were covered by imported Thyssen corrugated steel sheets, a novelty at the time. Mikrohuta units represented a new trend: steel framework structure was covered by corrugated plate sandwich type walls. Today, this is a standard solution.
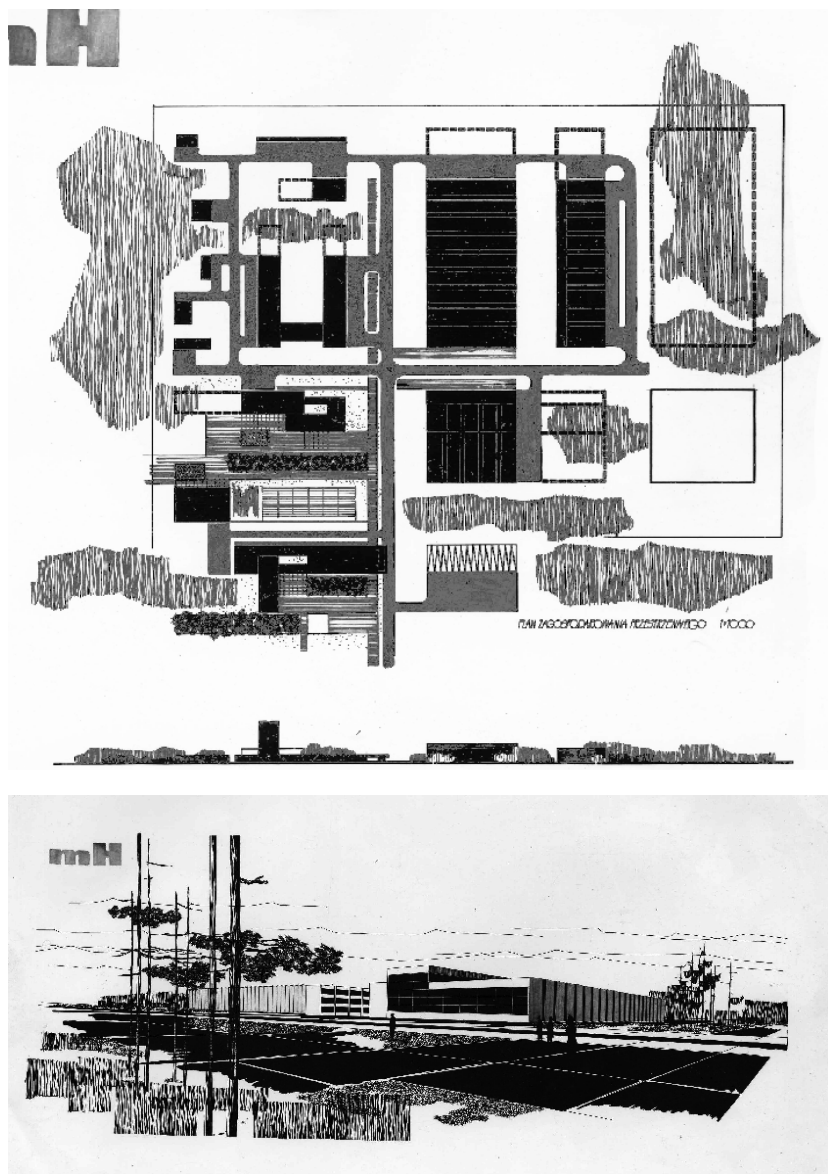
Fig. 4a, b. Dąbrowa Górnicza, Mikrohuta, initial general layout and main plant (arch. Z. Stanik), author's archive

4. The fate of 1960s industrial architecture

Few industrial buildings dating back to the first half of the 20th century managed to find new, better roles in the new, better reality. At the turn of the century, Bytom's Orzeł Biały mine lamp room was converted onto the architect's own apartment. However, this is an isolated event.

It is often difficult to find out what is happening with former industrial units and factories. The new owners: Lhoist in Bukowa, Piklington in Sandomierz and others are not forthcoming with information and restrict access to their properties.

Some of the buildings described herein survive to this day:

- ▸ "Runotex" in Kalisz (1962): the industrial unit is still standing and production still takes place there, the building is in a deplorable state despite the fact that the private enterprise is doing well;
- ▸ There is not much left of the Furniture Factory in Wyszków. The plot is criss-crossed with fences and divided between eighteen owners. The hall structure still stands, the glass units have been bricked up, some are still visible in bands of trough roof coverings. The yard between the industrial units has been built up as well as the North manoeuvring yard. The East side of the plot has been The East side of the plot has been sliced away. It included: the office building, workshop, flammable materials storage, fire water reservoir;
- ▸ The ski-manufacturing unit Szaflary near Zakopane: the structure is still intact, the premises are also used by multiple owners, the spatial form is slightly changed on the outside and the interior is partitioned;
- ▸ Magnificent halls of Warsaw Pump Factory and Cracow Steel Constructions Plant are still in use as before;
- ▸ The ventilator complex at Skawina Power Plant: not there anymore, new installation is working on this place;
- ▸ Lime Production Plant in Bukowa (today's Lhoist, Bukowa Cement Plant): the rock and coke containers are most probably gone. Information is not available, but observation (Google) shows that the buildings are no longer there;
- ▸ Elana in Toruń ceased to exist in 2008, production buildings are dilapidated, office buildings split into small units and rented out;
- ▸ Tank Furnace Hall at the Sandomierz Glassworks (today's Piklington Sandomierz): not there anymore;
- ▸ In the last years, Mikrohuta was also abandoned, its main hall dilapidating.

The technological and technical maturity for all units discussed herein is long gone. They were often in the way of the new private owners' or Western companies' and corporations' development plans. Modernizations and upgrades of technological buildings are not practiced in industrial reality. New owners often refuse to refer to the past days of the plant they own. The history starts for them with the day it was taken over or bought – in Poland, usually at the end of the 20th century.

There are however people who take care of the past, and in their blogs they publish old photographs referring to the past events and people who were working in the plants long ago.

It would be a loss for Polish culture if, after the disappearance of buildings, which used to be a significant part of Polish post-war achievements, the buildings as well as the names of their designers and constructors were to be forgotten.

References

[1] Architektura 7/63.

[2] Architektura 11/63.

[3] Architektura 1/69.

[4] Arct Z., *Projektowanie architektoniczne zakładów przemysłowych*, Arkady, Warszawa 1974.

[5] Bardzińska-Bonenberg T., *Zapis graficzny projektu architektonicznego, krótka historia zmian*, [in:] *Definiowanie przestrzeni architektonicznej*, M. Misiągiewicz, D. Kozłowski (eds.), No. 441, Vol. 1, Wydawnictwo Politechniki Krakowskiej, Kraków 2013.

[6] Bardzińska-Bonenberg T., Barbara Świt-Jankowska, *Changing techniques of architectural design presentation*, ACEE Journal, 3/2015, The Silesian University of Technology.

[7] Basista A., *Betonowe dziedzictwo. Architektura w Polsce czasów komunizmu*, Wydawnictwo Naukowe PWN, Warszawa–Kraków 2001.

[8] Bąbiński Cz., *Projektowanie zakładów przemysłowych*, Wydawnictwa Naukowo-Techniczne, Warszawa 1961.

[9] *Budownictwo i architektura w Polsce 1945–1966*, J. Zachwatowicz (ed.), Interpress, Warszawa 1968.

[10] Czarnecki W., *To był też mój Poznań*, Wydawnictwo Poznańskie, Poznań 1987.

[11] Henn J., *Industriebau. Internationale Beispiele*, Callwey, Munchen 1962.

[12] Lisowski B., *Modern Architecture in Poland*, Interpress Publishers, Warszawa 1968.

[13] Szafer P.T., *New architecture Poland, diariusz lat 1966–1970*, Arkady, Warszawa 1972.

[14] Szafer P.T., *Polska architektura współczesna*, Wydawnictwo Interpress, Warszawa 1977.

Wiesława Gadomska (wiga@uwm.edu.pl)

Department of Landscape Architecture, University of Warmia and Mazury in Olsztyn

Governors island: a new park in new york

Governors island: nowy park nowego jorku

Abstract

The paper presents the process of transformation of a specific part of New York, i.e. Governors Island, located south of Manhattan, into yet another large municipal park. The specific natural and cultural conditions of the area, which is separate from the intense city network, have influenced the manner of developing the new park space. The basic design issues included: reference to the clear historical context resulting from the heritage of the defence fort, which functioned here for centuries, taking into account difficult eco-physiographic conditions resulting from the island's location in an area exposed to dangerous weather anomalies; and the use of the significant landscape potential of the island, offering excellent conditions for the visual perception of the characteristic city skyline and its surroundings. The project, implemented in stages, forms an example of the broader, interesting issue of urban space *recycling* [1] and the incorporation of new functions into an outdated spatial context.

Keywords: island park, urban space recycling, landscape context

Streszczenie

Artykuł prezentuje proces transformacji specyficznego fragmentu Nowego Jorku – położonej na południe od Manhattanu wyspy Governors Island – w kolejny, duży park miejski. Specyficzne uwarunkowania naturalne i kulturowe odizolowanego od intensywnej tkanki miejskiej terenu bezpośrednio wpłynęły na sposób kształtowania nowej przestrzeni parkowej. Podstawowymi zagadnieniami projektowymi były: odniesienie się do czytelnego kontekstu historycznego wynikającego z dziedzictwa funkcjonującego przez wieki fortu obronnego, uwzględnienie trudnych warunków ekofizjograficznych wynikających z położenia wyspy w obszarze narażonym na groźne anomalia pogodowe oraz wykorzystanie dużego potencjału krajobrazowego wyspy, stwarzającego warunki doskonałej percepcji widokowej charakterystycznej sylwety miasta i jego otoczenia. Realizowany etapami projekt stanowi przykład szerszej, interesującej problematyki swoistego recyklingu przestrzeni miejskiej [1] i wpisywania nowych funkcji w zdezaktualizowany kontekst przestrzenny.

Słowa kluczowe: park na wyspie, recykling przestrzeni miejskiej, kontekst krajobrazowy

1. Introduction

A radical change in the status of Governors Island from an enclosed military zone into an open public space has had its precedence in the history of the city. One of them was the transformation of Ellis Island[1], an island that initially performed a military function and later an administrative one, related to the immigration procedures in the USA. Ellis Island was transformed into an attractive public space managed by the Museum of Immigration, together with a unique garden of remembrance [3]. In the case of Governors Island, the attractive historical and recreational complex, constructed in stages and made available to the public successively, constitutes another step towards developing municipal green areas in the special conditions of the "Culture of Congestion" [4] of the New York metropolis. The rapidly growing popularity of the park, which is being built in stages, is confirmed by the increasing numbers of visitors[2], and validates the justifiability of the strategy of providing the city with special "green infrastructure" [6] and offering it a growing role in the functioning of the modern metropolis[3]. The characteristics of park visits are also symptomatic: the area is used mainly by New Yorkers[4] during weekends – the new venue has not just become a new seasonal tourist attraction; it is mainly used by city inhabitants.

When observing the process of establishing yet another large municipal park, it is worth appreciating the scale of the phenomenon of setting up new green areas in New York, in particular in the context of the relatively high "green" index in the city [9]. In parallel to the establishment of the park on Governors Island (the surface area of the park is approx. 35 hectares), the construction of *Brooklyn Bridge Park* (surface area of the park: 34 hectares) is also being completed; what is more, in the last decade, the following parks were established and implemented in stages in the city: *Hudson River Park* in Manhattan (surface area of the park: 220 hectares, approx. 9 km of developed coastline) [10] and *Hunter Point Park* in Queens. The new park investments, significant in the scale of the city and conducted on a spectacular scale with respect to design and implementation, should be treated as a phenomenon characteristic for the city, and worthy of academic interest[5].

---

[1] The island lies at a distance of just 2 km from Manhattan, and its surface area is 11 hectares; it is managed by the National Park Service; apart from its rich history, its ownership structure is also complex – a significant part of it belongs to the State of New Jersey [2].

[2] After the military function had expired, the island was opened to the public in 2005; at that time it was visited by approx. 8,000 people. Opening the park to the public in May 2014 caused an influx of 450,000 visitors in 2015 [5].

[3] The complex issue of establishing new green areas in the metropolis in the multi-directional approach of sustainable development is presented in the article [7].

[4] It is estimated that 85% of visitors to the island are inhabitants of New York [8].

[5] Since 2003, the author has been observing the changes and development of park areas in New York.

2. Governors island: an island within the city

Governors Island is located at a distance of just one kilometre from the southern bank of Manhattan, and, together with many other islands of the extensive archipelago, makes up the administrative area of New York[6]. The current surface area of the island is almost 70 hectares, which, in comparison to nearby Manhattan, constitutes only 1% of its surface; in reference to the entire surface area within the borders of New York, it is just a thousandth part. As part of the administrative division into five major city boroughs[7], Governors Island belongs to Manhattan. In spite of its small size, the island had strategic significance in the city's development, resulting from its special location in the topographic configuration.

3. Natural conditions

The coastline of the island is surrounded by the waters of New York Bay – an extensive natural harbour, in the east designated by the coastline of New York, and in the west by the bank of New Jersey[8]. The northern coast of the island is washed by the East River and the Hudson River, and in the south the waters of New York Bay mix with Lower Bay and the waters of the Atlantic Ocean.

Today's shape of the island and its size are the result of engineering interference in the landscape, which took place in 1912. The original, natural island[9], with a surface area of just 30 hectares, was extended by compressing almost 4 million m^3 of soil, derived from the first line of the New York underground, which was under construction. The significant scale of the interference resulted in the extension of Governors Island by over 40 hectares, supplementing its area in the south-west[10]. The artificially shaped, flat area of the island was surrounded by a low, regular coastline.

The location of Governors Island in a special point of convergence of two river valleys and the ocean's waters exposes the area of the island to the impact of strong (including hurricane) winds, which, in synergy with low and flat hypsometric characteristics, causes a high risk of damage and periodic flooding of its area by the waters of the bay[11].

---

[6] The area of New York, apart from solid land, is made up of islands: Manhattan, Staten Island, the western part of Long Island, and several other smaller islands [11].

[7] The City of New York is divided into five main boroughs; apart from Manhattan, these are: Brooklyn, Queens, Bronx and Staten Island [12].

[8] Harbours in Newark, Elizabeth, Jersey City and Hoboken form a part of New York Harbour [13].

[9] On the basis of a map from 1776 [14].

[10] It is worth noting that the applied method of creating new land surface was used a number of times in subsequent years, *inter alia*, when support for large park projects was built – e.g. Battery Park City [15].

[11] New York is located within an area at risk of hurricane winds and the repercussions related to it, consisting, *inter alia*, in the flooding of low coastal areas; cataclysms recorded since the 17th century have hit the coasts of New York over 80 times; the last one, Hurricane Sandy in 2012, caused catastrophic destruction, flooding the area of lower Manhattan; the threat is recurring and intensifying [16].

4. Cultural determinants, history

Throughout the centuries, in the pre-colonial period, the island could have been used as a place for finding food and resources guaranteeing a material base for the existence of the local native people. The original name in the local language (*Paggank*) denoted the place as the "island of nuts", whereas its coastal water provided an abundance of fish and crustaceans. The place, together with the entire archipelago of islands surrounding it, was discovered by Hudson's expedition in September 1609. European settlers started settling on the island in 1624. The Dutch West India Company made the first investment: a lumber mill providing timber for further extension of the settlement was built. Today's name of the island, deriving from the period of British colonisation, indicated its privileged status as the place of residence of the important person of royal governor. Later use of the island, which dominated its character for almost 200 years, was determined by its location, ideal for developing military functions and defence infrastructure. The island became a strategically located element of the New York Bay defence system. In 1800, New York State assigned the island to the federal government. In subsequent years, important military facilities were located within its borders, along with the base of American military administration structures. During WWI, the island functioned as logistic back-up facilities related to the formation of troops sent to Europe. During WWII, it was an administrative centre and a recruitment facility. In 1966, military use of the island expired, along with the decision of the U.S. Department of Defense on the reduction of military installations. However, the special location of the place continued to be used – this time as the base of the United States Coast Guard. After 30 years of operation, in 1996, the base was closed down. The almost 200-year period of military and similar use of the island has exerted a clear impact on the character and the form of its management, and has created specific cultural heritage considered valuable and worthy of protection. In 1985, over 50% of the island's surface area was included under the status of a National Historic Landmark. The area of protection encompassed the northern section of Governors Island, with fortifications, administrative buildings, barracks and residential facilities. Its unique facilities included: the extensive and impressive Fort Jay, with its bastion structure, and Castle Williams, a circular artillery fortification located on the north-western cape of the island. Furthermore, an extensive complex of administrative buildings with a courtyard-type layout and supplementary development, encompassing residential buildings, a public school and places of religious worship also contribute to the characteristic arrangement of the area. Intense management of the island was also continued in the post-military period, when the place was used as the coast guard location. The new function stimulated the enclosed space; approx. 3,500 people lived on the island permanently, and over 1,500 arrived there on an every-day basis to work. The investments performed in this period were located in the southern section of the island, and encompassed complexes of residential development along with infrastructure necessary for autonomous functioning. The decision on the expiry of the hitherto function of the island was made in 1995, and was dictated by a change in the

direction of operation of the Department of State Defense and the general necessity of reducing the costs of numerous federal agencies. The distribution of the administrative division, back-up facilities and equipment was completed in August 1996[12].

5. Modern times

A large attractive area located close to Manhattan posed an open question about the future use of the island. The initial plan assumed the possibility of establishing a public park, but at the same time, it allowed for a significant share of commercial investments. In 1996, the Van Alen Institute announced an open idea competition under the name "Public Property" [17], the objective of which was to examine the island's potential in its broad urban, cultural and eco-physiographic context. Proposals submitted by over 200 participants from 14 countries showed the great receptivity of the place and flexibility in shaping its future functions. The most important advantage of the competition was the initiation of a broad social discussion focused on open public access to the island and providing it with the character of an active place with respect to recreation, culture, art and innovation. At the same time, the ownership status of the island was undergoing significant changes: in 2001, its northern part, with a surface area of almost 9 hectares encompassing the two most important historical facilities (Fort Jay and Castle Williams), received the status of the Governors Island National Monument, and was transferred under the federal administration of the National Park Service. The remaining area was given to the State of New York, under the conditions of using the island for public benefit, and a ban on locating any permanent residential functions within its area.

The basic form of managing the island's surface was determined via a closed design competition announced in 2006 by the Trust for Governors Island. Five teams[13] of recognized international renown were invited to present their concepts, which were shown to the public in the middle of 2007. In December 2007, the winner of the competition was announced: international design company West 8 Urban Design & Landscape Architecture, which has operated since 1987[14].

---

[12] On the basis of chronology resulting from the exhibition presented on the Island, illustrating its history. The author became acquainted with it in September 2015.

[13] The list of finalists was made up of: Field Operation/Wilkinson Eyre Architects New York, USA/London, United Kingdom; Hargreaves Associates/Michael Maltzan Architecture, Inc. New York, USA/Los Angeles, USA; Ramus Ella Architects (REX)/Michel Desvigne Paysagistes (MPD) New York, USA/Paris, France; West 8 urban design landscape architecture b.v./Rogers Marvel Architects/Diller Scofidio + Renfro Rotterdam, The Netherlands/New York, USA;WRT LLC/Weiss/Manfredi/Urban Strategies. Inc. Philadelphia, USA/ New York, US /Toronto, Canada [5].

[14] West 8 is an international design office active in the area of interference of spatial planning and landscape architecture; apart from its registered office in the Netherlands, it has a branch in Belgium and, after winning the competition, also a branch in New York. Among many projects implemented in Europe it is worth paying attention to the participation of West 8 in the "City of Tomorrow" exhibition, which took place in 2001 in Malmö, with a strong emphasis on the issue of ecology and sustainable development, along with local landscape identity [18].

Opening of the island's surface for public use was preceded by numerous actions aimed at changing the image of Governors Island and promoting it as a new and attractive venue on the city map. Among numerous promotional and artistic events, the one whose scale went beyond the borders of the city was a temporary installation called The New York Waterfalls, presented in 2008 by the Public Art Fund in cooperation with the City of New York. One out of the four places of the display of forty-metre monumental waterfalls presented in the city landscape was Governors Island [19].

In May 2012, construction of the park based on the design concept selected in 2007 and the master plan prepared on its basis was commenced. Two years later, in May 2014, after completion of the first stage of the investment, the new recreational space of New York was opened for the public; completion of the second stage took place in June 2016.

6. Governors island – *master plan*

The plan, prepared in 2010, encompassed over 35 hectares out of the 70 hectares of the surface of Governors Island. The northern, historical part of the island received the status of public space, and the adaptation of functions of the historical development for the new needs was permitted. A surface area of over 16 hectares was assigned for the park, located in the central and the southern part of the island. One of the basic determinants of the plan was ensuring the continuity of the promenade, encompassing the island's circumference, with a length of 3.5 km. The remaining area, including the belt of land along the eastern and western coast, was assigned for the zone of development with absolute exclusion of residential function, yet allowing for hotel, conference and educational functions (Fig. 1).

1. Governors Island National Monument
2. Historic Discrict
3. Liggett Terrace
4. Hammock Grove
5. Play Lawn
6. The Hills
7. The Great Promenade
8. Development Zone
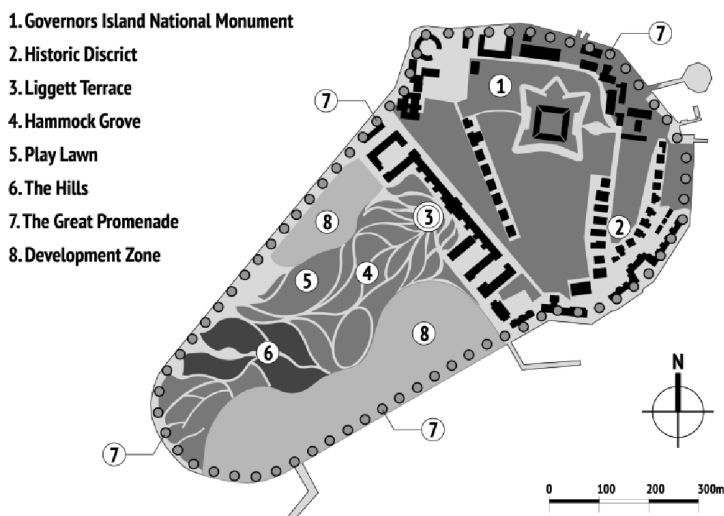
Fig. 1. Historical and modern forms of management – main functionalzones
(author's own study on the basis of information materials)

7. Park: main assumptions

Transformation of a military island, closed off to the public for several decades, into a public recreational space could have been evaluated as risky on account of numerous premises. In spite of successful examples of recycling New York's urban space and establishing parks in untypical locations, whose original functions have expired[15], the case of Governors Island was marked with clear, specific limitations. The physical barrier of the waters of New York Bay and the absence of any tradition of the place related to public access, leisure and recreation of the transformed space could have been obstacles that were difficult to overcome. The design of the new park space had to assume an interdisciplinary adaptation of natural and cultural determinants of the island for the needs of space that was unique in the scale of the city, offering individual, broader and a more extensive utility programme than the remaining New York parks. The main assumptions included:

- ► creating an easily accessible, attractive public space, maintaining a balance between the cultural and the natural potential of the place[16];
- ► protecting the park area from adverse and dangerous atmospheric phenomena: strong winds, high waves of the waters of the bay surrounding the island, and periodic flooding of its area;
- ► maximum extension and use of the landscape assets of the island as a unique element of an active exhibition related to the multidirectional reception of the city skyline[17];
- ► introduction of individual solutions stimulating interaction with the park area and the surrounding landscape[18];
- ► staging of the investment, making the completed fragments of the park available to users within a relatively short time and to a relatively extensive degree[19].

---

[15] A spectacular example of this phenomenon is *High Line* Park, where an overhead railway line was used as a ase for creating a unique linear park [20, 21].

[16] The idea of preserving the historical and cultural heritage as the basis for constructing new park areas underlies multiple modern projects in New York; apart from the above-mentioned example of *The High Line,* it is worth mentioning *Gantry Plaza State Park* [22], where artefacts of the former reloading station from a railway line to the ferry line between New Jersey and Long Island are displayed, and *Concrete Plant Park* [23], adapting the area of the former concrete plant, along with its original technical infrastructure.

[17] The problem of displaying the unique Manhattan skyline from the perspective of such a unique place as a park was signalled as early as at the beginning of the 1970s by Robert Smithson [24] in his project *Study For Floating Island To Travel Around Manhattan* (implemented in 2005 in cooperation with, *inter alia*, the Whitney Museum of American Art); the valuable landscape relation which transformed a municipal park into a vantage point, directed towards the characteristic silhouette of Manhattan, has been used a number of times in modern park projects – apart from the already mentioned ones, such as *Gantry Plaza* or *Brooklyn Bridge Park,* it is also worth mentioning *Roosevelt Four Freedoms Park* (design: Louis Kahn 1972, opened in 2012) on Roosevelt Island, where the southern edge of the island was used as a unique vantage point, and, at the same time, a compositional and dramatic culmination for the commemorative space.

[18] Modern New York parks show clear formal differentiation resulting from the context of the place and rich design invention, manifested, *inter alia*, in composition, individual architectural details, selection of plants, etc. Diverse parks that make up Battery Park City, include: *Rockefeller Park, Teardrop Park, Iris Hunger Memorial, North Cove, Rector Park.*

[19] Investment staging did well with respect to a number of parks created in modern times; the process is visible using the example of linear *Hudson River Park*, which was initiated in 1997 and which is being opened to users

8. Design solutions

Fulfilment of the adopted assumptions required the application of a number of individual design solutions, clear both on the macro-scale of the created space, as well as the scale of details dedicated to it:

▸ in spite of the initial proposal of connecting the area of the island via a gondola lift with the area of Manhattan and Brooklyn[20], mass transport between the island and the city relies on two ferry lines offering, initially seasonally, and nowadays year-round regular passenger cruises at affordable prices;

▸ the spatial composition of the new mode of managing Governors Island relies on a clear junction close to the geometric centre of the island (Fig. 1); a zone where the extensive historical architectural interior merges with the modern park design was planned in its vicinity (Liggett Terrace): an unhampered layout of the park with soft, undulating lines of pedestrian and bicycle alleys created an interesting contrast for the geometrically set out, post-military development of the island. The arrangement of the park made use of the natural isolation of the place and its separation from the dense urban space of New York – numerous recreational annexes were introduced, allowing for individual views of the surroundings and the landscape (Fig. 2);

▸ protection of the park from the effects of flooding of the island by the waters of New York Bay was solved by changing the original lie of the land: as a result of macro-levelling activities, the altitude coordinates of the central part of the park were increased, and clear drops were made towards the coastline (Fig. 3). In the southern part of the park, a series of controlled flood areas were made, supplemented with vegetation increasing their natural retention; protection from strong winds is provided by four artificially shaped hills located in the windward area of the island – a range of hills with extensive bases and heights ranging from 7 to almost 21 metres creates, at the same time, a natural breakwater shielding the area of the park and the interior of the island [26];

▸ the area of the island offers excellent conditions for multidirectional perception of the surrounding landscape – the promenade leading along the coastline is an efficient element of active landscape display ensuring reception of the dynamically changing landscape of New York Bay (an area of very intense navigation traffic) and the characteristic urban silhouette of Manhattan, New Jersey, Staten Island and Brooklyn within the full 360º (Fig. 4). The highest among the four planned hills will be a special vantage point – its height of 21 metres will ensure a unique, far-reaching view allowing

---

successively, building the capital of trust and social approval necessary, apart from material funds, to continue the project.

[20] In 2005, Santiago Calatrava, at the request of the deputy mayor of New York, agreed to prepare a concept for connecting Governors Island with Manhattan and Brooklyn via a gondola lift, ensuring efficient communication between the Island and the city; a visually light structure resting on three structural pylons was going to, by assumption, introduce interesting and terse spatial forms into the landscape of the waters of New York Bay – the bold proposal was not implemented on account of the estimated high cost of the project [25].

for comprehensive reception of the characteristic city topography, along with its five main boroughs[21];

▸ individual architectural details that highlight the cosy, human scale of the island and a wide array of functional forms were provided with great significance in the attractive management of the place. The applied solutions are conducive to interaction with the surrounding space and landscape – apart from classic stationary benches used in the historical part of the island, the park has also been provided with several types of portable furniture, and individual users can decide about its configuration and arrangement. The presence of places allowing for rest in a reclining position is a unique solution in the public space of New York[22]. An area provided with freely available hammocks turned out to be an attraction of the park [26] (Fig. 2). Special attention should also be paid to a playground with unique spatial forms (Fig. 5), encouraging not only the youngest park users to take part in physical activity. The open playground convention[23], quite rare in New York, made use of the central, well-monitored area of the island;

Fig. 2. Hammock Grove: a boutique park interior with a view at the southern Manhattan skyline
(source: photo by author)

---

[21] In the scale of the city this is the only publicly available vantage point with a view of the five main districts of the city.

[22] Even though the *Rules & Regulations of the New York City Department of Parks & Recreation; § 1-04 Prohibited Uses* do not clearly ban the use of benches in a reclining position, the majority of park benches have a structure preventing such use; the issue refers to the difficult and widespread problem of homeless people in the public space.

[23] Adults are not allowed to stay within the area of most playgrounds in New York, unless they accompany children younger than 12 years of age (*Rules & Regulations of the New York City Department of Parks & Recreation; § 1-04 Prohibited* Uses).

▸ implementation of the park project was planned in two stages: the first one, encompassing 12 hectares of the central area of the island, along with the zone of direct penetration with the historical development, was completed in May 2015; completion of the second stage, encompassing the southern edge of the island, is scheduled for June 2016. Making Governors Island widely available before the completion of the entire investment allowed the inhabitants of New York to have direct experience of the process of the creation of municipal space with respect to the basic earthwork, arrangement work, and providing the area of the island with greenery.

Fig. 3. The area of the park was shaped to provide protection from flooding and strong winds
(source: photo by author)

Fig. 4. Promenade along the island provides views of the city skyline and the surrounding areas
(source: photo by author)

Fig. 5. Spatial forms encouraging physical activity: an out-of-scale coat hanger as a piece of gym equipment (source: photo by author)

9. Recapitulation

The development of green areas conducted in the special conditions of New York's "Culture of Congestion" requires searching for new and untypical locations. Implying original formal and functional solutions that are implemented in the park on Governors Island is yet another example of this phenomenon.

The dominant function within the surface area of the island comprises public areas and a park. The zone of commercial development constitutes less than 20% of its surface, with a complete ban on locating residential development – this index determines clear preferences in shaping public city areas and is worth emphasising in the context of very strong investment pressure characterising New York.

The park created on Governors Island, in a manner characteristic for numerous modern park investments established in New York, makes references to urban space; apart from its basic function within the scope of shaping green and recreational areas, it creates a high standard for public city areas, protects and displays its cultural heritage, and contributes to forming the structure of interesting landscape relations within its area.

References

[1] Greenstein R., Sungu-Eryilmaz Y. (ed.), *Recycling the City. The Use and Reuse of Urban Land*, Lincoln Institute of Land Policy, Cambridge Massachusetts, 2004.
[2] Sirefman S., *New York. A guide to recent architecture,* Ellipsis, London 2001, 1.2.
[3] Kosiński W., *Ogród pamięci imigrantów pod Statuą Wolności – uwarunkowania, konteksty, realizacja,* Czasopismo Techniczne, 2-A/2012, Vol. 7, 183–201.

[4] Koolhaas R., *Deliryczny Nowy Jork*, Karakter, Kraków 2013, 10.

[5] https://govisland.com/ (access: 10.06.2016).

[6] Kosiński W., *Sześciesiąt parków Manhattanu – kanwa jakości życia,* Czasopismo Techniczne, 7-A/2012, 163–251.

[7] Jost D., *Gotham goes green*, Landscape Architecture, 7, 2010, 54–59.

[8] http://www.landezine.com/index.php/2015/01/governors-island-ph-1-by-west8 (access: 20.06.2016).

[9] Zachariasz A., *Zieleń jako współczesny czynnik miastotwórczy ze szczególnym uwzględnieniem rolo parków publicznych*, Monografia 336, Politechnika Krakowska, Kraków 2006.

[10] Gadomska W., *Hudson River Park – współczesny park nad rzeką*, [In:] *Język architektury krajobrazu*, Wydawnictwo „Wieś Jutra", Warszawa 2010, 116–121.

[11] *Wielka Encyklopedia PWN*, Wydawnictwo Naukowe PWN, Vol. 19, Warszawa 2003, 204.

[12] Leech M., *Nowy Jork Przewodnik*, Könemann, Köln 2000, 5.

[13] *Wielka Encyklopedia PWN*, Wydawnictwo Naukowe PWN, Vol. 18, Warszawa 2003, 491.

[14] Bloomberg M.R., *Before the Grid*, [In:] *The Greatest Grid. The Master Plan of Manhattan 1811–2011*, Ballon H. (ed.), Museum of the City of New York and Columbia University Press, 2012, 18.

[15] *Remaking the Urban Waterfront*, collective work, Urban Land Institute, Washington 2004, 90–95.

[16] http://www1.nyc.gov/site/em/ready/coastal-storms-hurricanes (access: 15.06.2016).

[17] https://www.vanalen.org/.../public-property-an-ideas-competition (access: 20.06.2016).

[18] Betsky A., *Landscrapers: Building with the Land,* Thames & Hudson, London 2002, 46–47.

[19] *Studio Olafur Eliasson. An Encyclopedia*, Taschen 2008, 360.

[20] Gadomska W., Gadomski W., *Park High Line – przestrzeń publiczna jako rezultat rewitalizacji postindustrialnego dziedzictwa zachodniego Manhattanu*, Przestrzeń i Forma, 21, 2014, 273–284.

[21] Gadomska W., *Humanizacja postindustrialnej przestrzeni miejskiej – przykład nowojorskiego parku High Line jako udanej rewitalizacji dawnej linii kolejowej*, Humanistyka i Przyrodoznawstwo, No. 20, Olsztyn 2014, 535–545.

[22] Lynn R., Morrone F., *New York City. Urban Landscapes,* W.W. Norton & Company, New York–London 2013, 119–122.

[23] Mclntyre L., *The Bronx is Blooming. Concrete Plant Park greens the Bronx River waterfront, Mafia blocks and all,* Landscape Architecture Magazine, 11, 2010, 66–77.

[24] Nicolin P., Repishti F., *Dictionary of Today's Landscape Designers*, Skira, Milano 2003, 309.

[25] Jodidio P., *Calatrava Complete Works 1979–2007*, Taschen, Köln 2007, 501–509.

[26] Lerner J., *Treasure Island,* Landscape Architecture Magazine, 6, 2015, 102–123.

Krzysztof Neupauer (kneupauer@chemia.pk.edu.pl)
Krzysztof Kupiec

Faculty of Chemical Engineering and Technology, Cracow University of Technology

Heat transfer during storage of hot liquid in the tank

Przenoszenie ciepła podczas magazynowania gorącej cieczy w zbiorniku

Abstract

In the article, a mathematical model of heat transfer in a storage tank for hot water with a non-uniform initial temperature is presented. The influence of the initial temperature distribution of the liquid in the tank and the influence of thermal resistance of the tank's walls, bottom and cover on temperature profiles of the liquid in the tank and changes of these profiles in time were analysed. A good conformity of the results obtained based on the process model with the results of measurements of water temperatures carried out under laboratory conditions was obtained.

Keywords: thermal stratification, thermal energy storage, renewable energy sources

Streszczenie

W artykule przedstawiono model matematyczny przenoszenia ciepła w zbiorniku magazynującym gorącą ciecz o niejednorodnej temperaturze początkowej. Przeanalizowano wpływ początkowego rozkładu temperatury cieczy w zbiorniku oraz wpływ oporu cieplnego ścian, dna oraz pokrywy zbiornika na profile temperatur cieczy w zbiorniku, a także czasowe zmiany tych profili. Uzyskano dobrą zgodność wyników otrzymanych na podstawie modelu procesu z wynikami pomiarów temperatur wody przeprowadzonych w warunkach laboratoryjnych.

Słowa kluczowe: stratyfikacja termiczna, magazynowanie ciepła, odnawialne źródła energii

Nomenclature

a	–	thermal diffusivity,
A	–	heat transfer area,
B	–	dimensionless constant defined by (17),
Bi	–	Biot number,
c	–	heat capacity,
D	–	tank diameter,
h	–	convective heat transfer coefficient,
k	–	thermal conductivity,
q_v	–	volumetric internal heat source capacity,
$\dot{Q}$	–	rate of heat transfer,
R	–	heat resistance,
U	–	overall heat transfer coefficient between the liquid and the environment,
s	–	height of the tank,
t	–	time,
T	–	temperature,
T_a	–	ambient temperature,
T_m	–	average temperature,
x	–	position coordinate,
V	–	volume,
Δs	–	thermocline thickness
ρ	–	liquid density,
ϑ	–	dimensionless temperature,
τ	–	dimensionless time,
η	–	dimensionless position coordinate,
$\Delta\eta$	–	dimensionless thermocline thickness,
0 *(index)*	–	bottom of the tank,
1 *(index)*	–	top of the tank.

1. Introduction

The tasks of heating equipment consists in generating heat streams for specific energetic needs of persons or technological processes. The amounts of heat generated and received are generally different in heating systems. These differences are particularly important in solar installations serving the purpose of acquiring heat from the solar radiation energy, where both daily and yearly cycles occur. In order to ensure effective operation of such installations, in which periodical production excesses or deficiencies occur, tanks with exchangers for heat storage, so-called storage containers, are used. The heat transfer to a storage container may occur in a spiral-tube exchanger (pipe coil), an external exchanger (plate heat exchanger, JAD type) or a combined storage container [2]. At the heat take-off side in the exchanger, most often water is used as a widely available medium with

a high thermal capacity. Usually, it is hot service water or a thermal buffer, simultaneously serving the purpose of a fluid coupling. Heat take-off by the storage container may take place using the whole volume of the water stored, or by layers. In a tank loaded by layers, the upper layers are heated at first, not the whole volume of the water present in the storage container. It provides the following advantages: an increase in thermal output of the heating system (better performance of the heat source, e.g. solar collectors) and availability of water with a higher temperature with the same total amount of heat stored in the storage container [1].

The phenomenon of temperature stratification has been a subject of numerous experimental papers. Current review of issues connected with temperature stratification in storage containers filled with water is presented in paper [8]. Various types of storage containers for temperature stratification and the research method is described in [3].

In paper [9], the results of a test of a closed tank completely filled with water, with temperature stratification, are reported. Water has played the role of a heat accumulator and there have been no water inflow to or water outflow from the tank. The heat has been delivered to the tank and collected from it via two spatial spiral pipe coils. Profiles of water temperatures storing the heat have been determined. Also, the influence of various configurations, heights and locations of the pipe coils on the water temperature in the tank and at the heat collection side has been taken into account.

In this paper, a mathematical model of heat transfer in a storage tank for hot water with a non-uniform initial temperature is presented. The model takes into account the temperature equalisation of the liquid in the tank and heat losses to the environment through the walls, bottom and cover of the tank. The goal of the paper is to verify the model experimentally and study the effects of various model parameters on the temperature profiles of the liquid in the tank, and their changes in time.

2. Thermocline

A thermocline, as a geographic term, is the middle water layer in lakes of the temperate zone, with temperature decreases rapidly with an increase in depth. A thermocline in tanks storing warm water is defined analogously.

The thermocline precludes convection mixing of the water layers, enabling maximum utilisation of the storage container volume [5].
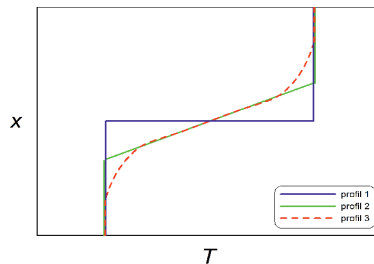
Fig. 1. Temperature profiles of the liquid in the tank with thermal stratification: 1 – profile without an intermediate zone, 2 – profile with a linear intermediate zone, 3 – realistic profile

Fig. 1 shows various temperature profiles of the water in the tank with thermal stratification. Profile 1, without an intermediate zone, does not occur in practice and is of theoretical significance only. Profile 2, with a linear intermediate zone, is closer to reality and easy to describe mathematically. The actual temperature profile in the tank with thermal stratification is curvilinear (profile 3).

3. Model of the process

A mathematical model of the heat transfer process in the tank with thermal stratification is based on the following assumptions:
- ▸ The tank has a cylindrical shape with a vertical axis,
- ▸ Temperature of the liquid in the tank changes only in the axial direction,
- ▸ Thermal properties of the liquid are constant in time and location-independent,
- ▸ Equalisation of temperature of the liquid may be described using the equation of heat conduction,
- ▸ The initial temperature distribution of the liquid in the tank corresponds to profile 1 or 2, shown in Fig. 1.
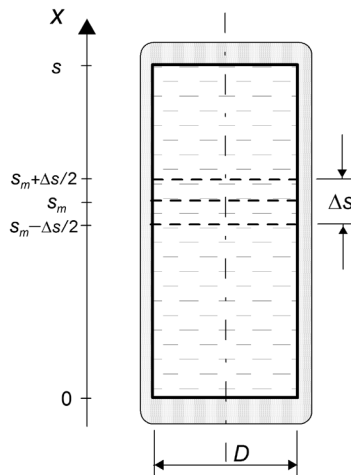
Fig. 2. A tank with thermal stratification

Fig. 2 presents a diagram of the discussed tank having a height s and a diameter D. For the initial temperature distribution without an intermediate zone (profile 1), the tank is filled with colder liquid having a temperature T_0 up to the height s_m; and there is warmer liquid above this height, having a temperature T_1.

For the initial temperature distribution with a linear intermediate zone (profile 2), the tank is filled with a colder liquid up to the height $s_m - \Delta s/2$, and there is warmer liquid above the height $s_m + \Delta s/2$. In the intermediate zone with a thickness Δs, the temperature of the liquid changes linearly from T_0 to T_1.

The heat equation has the following form:

$$\frac{\partial T}{\partial t} = a\frac{\partial^2 T}{\partial x^2} + \frac{q_v}{\rho c} \tag{1}$$

Thermal diffusivity of the liquid is defined by the following dependence:

$$a = \frac{k}{\rho c} \tag{2}$$

Heat transfer through the sidewall is described by the equation of heat transmission:

$$d\dot{Q} = U(T - T_a)dA \tag{3}$$

Because of the assumed lack of changes in the liquid temperature in the radial direction, the rate of heat transfer per unit volume in the source term of equation (1) amounts to:

$$q_v = -\frac{d\dot{Q}}{dV} = \frac{dA}{dV}U(T_a - T) \tag{4}$$

Geometry of the cylindrical tank leads to a conclusion that:

$$\frac{dA}{dV} = \frac{4}{D} \tag{5}$$

so:

$$q_v = \frac{4U}{D}(T_a - T) \tag{6}$$

The initial condition with a lack of an intermediate zone (profile 1) in the tank has the following form:

$$t = 0 \qquad T = \begin{cases} T_0 & \text{for } 0 < x \le s_m \\ T_1 & \text{for } s_m < x \le s \end{cases} \tag{7}$$

When the temperature in the intermediate zone is a linear function of location (profile 2), the initial condition is as follows:

$$t = 0 \qquad T = \begin{cases} T_0 & \text{for } 0 < x \le s_m - \dfrac{\Delta s}{2} \\ T_0 + \left(x - s_m + \dfrac{\Delta s}{2}\right)\cdot\dfrac{T_1 - T_0}{\Delta s} & \text{for } s_m - \dfrac{\Delta s}{2} < x \le s_m + \dfrac{\Delta s}{2} \\ T_1 & \text{for } s_m + \dfrac{\Delta s}{2} < x \le s \end{cases} \tag{8}$$

31

In both cases, the average liquid temperature in the beginning of the process amounts to:

$$T_m = \frac{s_m}{s} T_0 + \left(1 - \frac{s_m}{s}\right) T_1 \tag{9}$$

The boundary condition for the tank's bottom has the following form:

$$x = 0 \qquad k \frac{\partial T}{\partial x} = \frac{T - T_a}{R_0} \tag{10}$$

An analogous condition was assumed for the tank's cover:

$$x = s \qquad -k \frac{\partial T}{\partial x} = \frac{T - T_a}{R_1} \tag{11}$$

External thermal resistances R_0 and R_1 result from summation of external convective heat transfer resistance $(1/h)$ and conduction through insulation layers (s_i/k_i), respectively:

$$R_0 = \frac{1}{h_0} + \frac{s_{i0}}{k_{i0}} \qquad\qquad R_1 = \frac{1}{h_1} + \frac{s_{i1}}{k_{i1}} \tag{12a and b}$$

In the proposed model, heat transfer through the side walls is described by the source term of the heat equation (1), while transfer through the tank's bottom and cover – by the boundary conditions (10) and (11) [4].

The model equations were transformed into dimensionless forms. Dimensionless temperature:

$$\vartheta = \frac{T - T_a}{T_m - T_a} \tag{13}$$

dimensionless time

$$\tau = \frac{at}{s^2} \tag{14}$$

and dimensionless location coordinate were introduced:

$$\eta = \frac{x}{s} \tag{15}$$

The dimensionless heat conduction equation has the following form:

$$\frac{\partial \vartheta}{\partial \tau} = \frac{\partial^2 \vartheta}{\partial \eta^2} - B\vartheta \tag{16}$$

while the constant B amounts to:

$$B = \frac{4Us^2}{Dk} \tag{17}$$

The initial condition for the profile without an intermediate zone has the following form:

$$\tau = 0 \qquad \vartheta = \begin{cases} \vartheta_0 & \text{for } 0 < \eta \leq \eta_m \\ \vartheta_1 & \text{for } \eta_m < \eta \leq 1 \end{cases} \tag{18}$$

and the initial condition for the linear temperature profile in the intermediate zone is as follows:

$$\tau = 0 \qquad \vartheta = \begin{cases} \vartheta_0 & \text{for } 0 < \eta \leq \eta_m - \dfrac{\Delta\eta}{2} \\ \vartheta_0 + \left(\eta - \eta_m + \dfrac{\Delta\eta}{2}\right) \cdot \dfrac{\vartheta_1 - \vartheta_0}{\Delta\eta} & \text{for } \eta_m - \dfrac{\Delta\eta}{2} < \eta \leq \eta_m + \dfrac{\Delta\eta}{2} \\ \vartheta_1 & \text{for } \eta_m + \dfrac{\Delta\eta}{2} < \eta \leq 1 \end{cases} \tag{19}$$

while the constants amount to:

$$\eta_m = \frac{s_m}{s}; \quad \Delta\eta = \frac{\Delta s}{s}; \quad \vartheta_0 = \frac{T_0 - T_a}{T_m - T_a}; \quad \vartheta_1 = \frac{T_1 - T_a}{T_m - T_a} \tag{20 a, b, c, d}$$

The boundary conditions have the following form:

$$\eta = 0 \qquad \frac{\partial \vartheta}{\partial \eta} - Bi_0 \vartheta = 0 \tag{21}$$

$$\eta = 1 \qquad \frac{\partial \vartheta}{\partial \eta} + Bi_1 \vartheta = 0 \tag{22}$$

Biot numbers for the bottom and the cover are defined as follows, respectively:

$$Bi_0 = \frac{s}{R_0 k} \qquad Bi_1 = \frac{s}{R_1 k} \tag{23a and b}$$

Equations of the model were solved numerically using the CrankNicolsonmixed procedure [6].

4. Calculation results

In order to determine the influence of the individual process parameters on the courses of temperature in the tank filled with liquid (water) with a non-uniform initial temperature, parametric analysis of the process was carried out. Temperature profiles for various values of the considered process parameters were determined. In the analysis, dimensional quantities were used, so the graph of the temperature profiles in the tank pertains to the following coordinate system: dimensionless location variable vs. dimensionless temperature. The following parameters were chosen: Biot numbers Bi_0 and Bi_1, dimensionless thickness of the intermediate layer (thermocline) in the initial condition $\Delta\eta$ and parameter B in equation (16). In all calculations,

$\vartheta_0 = 0.2$ and $\vartheta_1 = 2$ were assumed. For a defined tank height s and thermal conductivity of the liquid k, the value of Biot number is inversely proportional to the external thermal resistance, which in turn depends on the thermal resistance of the external convective heat transfer and the insulation thermal resistance. The higher the thermal resistances, the lower the value of Biot number; with a perfect insulation of the tank's bottom or cover, the respective Biot numbers are equal to zero. It was assumed in the calculations that the Biot numbers for the bottom Bi_0 and the cover Bi_1 are equal. In this calculation series, the other parameters were assumed constant: $B = 300$, $\Delta\eta = 0.2$. The latter value means that the intermediate temperature zone in the beginning of the process constitutes 20% of the tank's height.
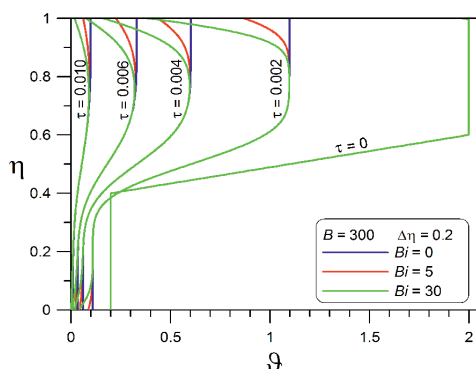
Fig. 3. Dimensionless temperature profiles in the tank for various process durations and various values of Biot number

Results of the calculations are shown in Fig. 3. With time, the profiles shift towards lower temperatures, and the changes in the upper portion of the tank are faster because of a higher driving force of convective heat transfer. Moreover, the upper portion of the tank transmits a part of heat to the lower portion because of temperature equalisation inside the tank. Cooling of the tank content in the lower portion indicates that more heat is transmitted to the walls than transferred from the upper portion in the result of temperature equalisation. At the infinite duration of the process, the system reaches a dimensionless temperature of $\vartheta = 0$, corresponding to equalisation of the liquid temperature and that of the environment. Profiles corresponding to various values of Biot number are designated with various colours. As one can see, various values of Bi give various profiles, but only near the tank ends, particularly the upper end. Heat transfer at the tank ends does not affect the temperature profiles in the central portion of the tank. For perfectly insulated bottom or/and the cover, the temperature profiles are vertical. The worse the thermal insulation, the more deformed the profiles at the ends of the tank. The profile deformation strongly depends on the process duration and the heat transfer location; the biggest deformations occurs for short durations and pertain to the cover. In both cases, it results from a high temperature of the liquid, causing a high driving force of heat transfer.

Fig. 4 shows the influence of the thickness of the intermediate layer in the beginning of the process. The calculations concern constant values of $Bi = 5$ (for the bottom and the cover)

and $B = 300$. The value of dimensionless thickness $\Delta\eta = 0$ means a lack of an intermediate zone (profile 1 in Fig. 1). Such a case is hard to realise in practice; it corresponds to an abrupt border between the layers of the liquid having different temperatures. A larger initial thickness of the intermediate zone results in the liquid temperature more equalised for a significant duration of the process than for smaller $\Delta\eta$ values. However, for long durations of the process, the temperatures in the tank become increasingly more equalised, and the influence of the initial condition becomes increasingly less important.
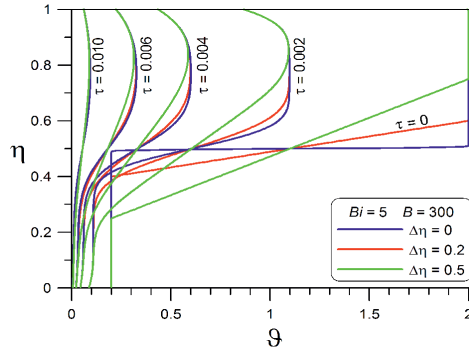
Fig. 4. Dimensionless temperature profiles in the tank for various process durations and various values of $\Delta\eta$

The influence of the parameter B on the dimensionless temperature profiles in the tank is shown in Fig. 5. For defined dimensions of the tank and a defined type of the liquid in the tank, the parameter B is proportional to the overall heat-transfer coefficient through the walls of the tank U. Most often, the strongest influence on the values of U is exerted by the thickness of the thermal insulation of the tank; thus the thicker the insulation layer, the lower the value of B. For a lower B value, the tank cools itself slower. The calculations were carried out for constant values of the other parameters: $Bi = 5$ and $\Delta\eta = 0.2$.
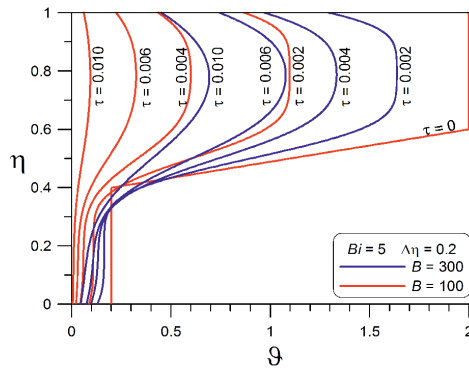
Fig. 5. Dimensionless temperature profiles in the tank for various process durations and various values of parameter B

35

5. Experimental setup

The experimental studies were carried out in a vertical tube with an inner diameter 44 mm and length 1.8 m, wherein sensors for temperature measurements spaced at 0.1 m were located. The glass tube had an insulation layer. Temporal courses of the water temperature were measured at different heights. The measurement results were recorded automatically. The measurements were performed using two layers of water at different temperatures. At the beginning of the experimental studies, a glass tube was filled with cold water and then through pipe 1 hot water was entered in a controlled amount in order to achieve the position of the two water layers boundary at the desired level. During the supply of hot water to the measuring tube, the cold water from the bottom part of the glass tube was discharged to the outside through pipe 2 and its volume, equal to the volume of the hot water at the inlet, was measured. Measurement details and the installation diagram are presented in paper [4].

6. Comparison of the calculation results with the experimental results

The results of one of the measurement series are shown in Fig. 6 and 7 in the form of symbols. For comparison, a course resulting from the solution of the equations of the presented mathematical model. Physical properties of water at average temperature were assumed: $c = 4190\,\text{J}/(\text{kg·K})$; $\rho = 1000\,\text{kg/m}^3$, $k = 0.6\,\text{W}/(\text{m·K})$; initial temperatures of both layers of water amounted to: $T_0 = 23°C$, $T_1 = 48°C$; ambient temperature $T_a = 22°C$; tube dimensions $s = 1.8\,\text{m}$, $D = 0.04\,\text{m}$. Moreover, as the initial amounts of colder and warmer water were equal, $s_m = 0.9\,\text{m}$ was assumed. Based on these data, the average water temperature in the beginning of the process was calculated: $T_m = 35.5°C$. Parameters associated with thermal resistances were estimated as: $R_0 = R_1 = 1\,\text{m}^2\text{K/W}$; $U = 0.6\,\text{W}/(\text{m}^2\text{K})$. The thickness of the intermediate zone was considered a set parameter; $\Delta s = 0.35\,\text{m}$ was assumed. The following values of the dimensionless parameters were determined: $\vartheta_0 = 0.074$, $\vartheta_1 = 1.93$, $\eta_m = 0.5$; $\Delta\eta = 0.194$; $B = 324$; $Bi_0 = Bi_1 = 3$.
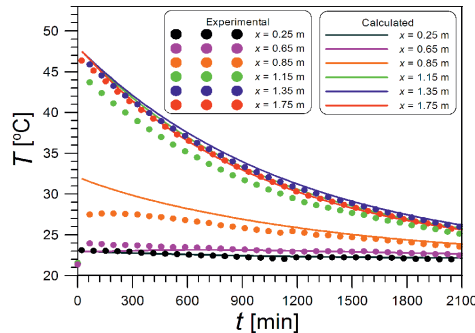
Fig. 6. History of water temperatures at various tube levels – comparison of the results of measurements with the results of model calculations
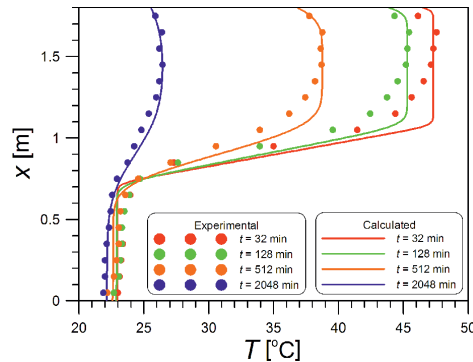
Fig. 7. Profile of water temperatures in the tube for various process durations – comparison of the results of measurements with the results of model calculations

Figure 6 pertains to the course of the water temperature in time at various heights in the tank, presented in a dimension coordinate system. The experimental and calculated courses are quite consistent with one another, apart from the central zone of the tank, where the calculated values are higher than the experimental values.

The temperature profiles are shown in Fig. 7. Also in this case, discrepancies between the experimental and calculated values occur in the central zone. Near the ends of the tank, and in the range of long durations of the process, the accordance between the results is very good.

7. Conclusions

- ▸ The thermocline layer is very important for maintaining thermal stratification of the liquid stored in the tank. The thermocline precludes a convective heat transfer between the layers of the liquid having different temperatures.
- ▸ Heat transfer in the tank with thermal stratification may be described by the heat equation with the heat source term. Thereby, heat transport inside the tank, heat transmission through the side walls (via the source term) and convective heat transfer to the bottom and the cover of the tank are taken under consideration.
- ▸ The numerical calculations confirmed the influence of the thickness of the intermediate zone (thermocline) on temperature distributions in a tank cooling down. However, this influence decays in time.
- ▸ A good accordance between the calculated and the experimental results confirms the correctness of the proposed model. Slight discrepancies were found only in the initial stage of cooling down of the tank and only in its central portion.

References

[1] Cruickshank C.A., Harrison S.J., *Heat loss characteristics for a typical solar domestic hot water storage*, Energy and Buildings, 42, 2010, 1703–1710.

[2] Duffie J.A., Beckman W.A., *Solar engineering of thermal processes*, Wiley, New York 2006.

[3] Han Y.M., Wang R.Z., Dai Y.J., *Thermal stratification within the water tank*, Renewable and Sustainable Energy Reviews 13, 2009, 1014–1026.

[4] Kupiec K., Neupauer K., Larwa B., *Thermal destratification in an insulated vessel filled with water*, Heat and Mass Transfer 52, 2016, 163–167.

[5] Lew J.V., Li P., Chan C., Karaki W., Stephens J., *Analysis of heat storage and delivery of a thermocline tank having solid filler material*, J. Sol. Energy Eng., 133, 2011, 021003.

[6] Marciniak A., Gregulec D., Kaczmarek J., *Basic Numerical Procedures In Turbo Pascal in Your PC*, NAKOM, Poznań 1992.

[7] Neupauer K., Komorowicz T., Kupiec K., *Cooling of hot water with non-uniform initial temperature*, Czasopismo Techniczne, 1-Ch/2016, 101–110.

[8] Njoku H.O., Ekechukwu O.V., Onyegegbu S.O. (2014) Analysis of stratified thermal storage systems: an overview. Heat Mass Transfer 50:1017–1030.

[9] Rahman A., Smith A.D., Fumo N., *Performance modeling and parametric study of a stratified water thermal storage tank*, Applied Thermal Engineering 100, 2016, 668–679.

Wacław Andrusikiewicz (andrus@agh.edu.pl)

Departpent of Underground Mining, Faculty of Mining and Geoengineering, AGH University of Science and Technology

Effect of salt mining on land surface

Wpływ górnictwa solnego na powierzchnię terenu

Abstract

The author discusses the issues associated with the changes of land surface shaping, caused by underground mining of salt. The characteristic of salt mining is essentially different from that of mining of other types of minerals, which is associated with salt's physical properties of salt rock mass. Consequently, the effects of underground salt mining that appear on land surface, although well known from other types of mining, are essentially different in dynamics and development in time. Most certainly, mining effects also depend on salt mining methods. Our analysis allows us to conclude that land surface deformations do not have to cause menace provided that proper technical and technological procedures are observed. The mistakes made in the salt mining art and practice may not be generally corrected and often end in mining catastrophes.

Keywords: salt mining, operating effects, mining land category

Streszczenie

W artykule omówiono zagadnienia związane ze zmianą ukształtowania powierzchni terenu, jakie wywołuje podziemna eksploatacja soli kamiennej. Specyfika górnictwa solnego w istotny sposób odbiega od górnictwa innych surowców mineralnych, co wynika z cech fizycznych górotworu solnego. W związku z tym efekty górnictwa solnego ujawniające się na powierzchni terenu, mimo iż są znane z górnictwa innych surowców mineralnych, istotnie różnią się dynamiką i przebiegiem w czasie. Niewątpliwie na skutki tego oddziaływania ma także wpływ sposób pozyskiwania soli. Prześledzenie przykładów pozwala na stwierdzenie, że przy zachowaniu właściwego reżimu techniczno-technologicznego powstające deformacje wcale nie muszą być problemem. Błędy popełnione w sztuce wydobywania soli są na ogół nie do naprawienia i najczęściej kończą się katastrofą górniczą.

Słowa kluczowe: górnictwo solne, wpływy eksploatacyjne, kategoria terenu górniczego

1. Introduction

Each form of mining is associated with the occurrence of negative effects in the natural environment. The types of such effects are characteristic for particular mining methods, and the effects are different in the cases of open-pit or underground operations, or solution mining which is also a form of underground mining. Salt mining is rather based on underground extraction, although particular methods are quite diverse.

Polish salt mining is proud of its nearly eight centuries of history. Salt was or has been extracted in four regions in Poland:

- ▸ southern (Wieliczka–Bochnia Foothills);
- ▸ central (Kłodawa and Inowrocław in the Kujawy region);
- ▸ western (near Polkowice);
- ▸ northern (the Bay of Puck area).

A number of salt extraction methods was developed during centuries. We can distinguish three basic groups of such methods:

- ▸ traditional underground mining, initially with the use of primitive tools and presently with the application of blasting and cutting machines;
- ▸ leaching (dissolving salt with fresh water) conducted in underground workings;
- ▸ leaching through boreholes drilled either underground or from land surface.

Each of those methods leads to the occurrence of workings of specific dimensions and shapes. However, the operation of gravitation forces causes that caverns are subjected to convergence. Without going into the details of the process, we can say that the appearance of the convergence effects on land surface is a question of time. Such effects are demonstrated by the change of shape and of hydrogeological relationships etc. Consequently, the natural environment can be affected (e.g. in visible replacement of vegetation species) and land use may also dramatically change, owing to mining menace [7, 11].

2. Mining menace: land surface shape effects

Generally speaking, mining menace refers to the damage caused by mining operations associated with the extraction of minerals. The range of damage is often fairly extensive, from rock mass and land surface deformations to disturbance or destruction of surface structures. This paper will discuss only the issues relating to land surface deformations caused by underground salt mining.

Land surface deformations triggered by mining operations, especially those with the use of underground mining methods, can be divided into two groups:

- ▸ the first one is identified owing to the type of mutual relationships of extraction and its influence exerted on rock mass and land surface (being direct, indirect, or secondary influence);
- ▸ the second one refers to the types of consequential deformations (continuous or discontinuous).

Direct effects include, as we can guess, the relocation of rock mass towards the excavation voids. The movement generates further rock mass deformations around workings (mainly in their roof and wall areas, less often in their floor areas), which are later reflected on land surface. Indirect effects result from direct extraction influences: they can appear outside the area affected by direct mining effects. The disturbance of hydrogeological relationships can be an example of that process. Secondary effects concern the consequences of continuous mining in the rock mass that has been affected by previous extraction, as well as land deformations appearing on the areas of old and retired mines [3].

Continuous land deformation consists in the process that does not cause visible disturbance of soil or rock compactness. Most often, that type of deformation is demonstrated by the appearance of sinkholes, but also sporadically by land elevation. Discontinuous deformations are of surface type (craters, depressions, or sinkholes) or linear type (fractures, cracking, or landslides).

The types of deformations depend on a number of factors. The most important of them include the following:

▸ the geological form of the deposit being extracted (e.g. layered sediments or salt domes);
▸ geological structure (in particular, roof rock mass) and tectonics;
▸ depth of mining;
▸ total height of workings (in a given cross-section);
▸ mining field dimensions;
▸ methods of workings' liquidation.

In the case of salt mining, we deal with both continuous and discontinuous deformations. Although continuous ones do not pose considerable threat, the discontinuous ones usually lead to mining catastrophes. Such phenomena are not rare since the salt rock mass is exposed to destructive influence of water which penetrates underground workings, owing either to the mistakes made in mining practice or the selection of inadequate extraction technology, and can flood a mine in a short time. 36 salt or potassium mines were flooded in Germany in 1851–1951, within several or about a dozen of years after their implementation, and 61 others were stopped, owing to a considerable water hazard. Besides, those mines were flooded soon after they had ceased to operate [14]. Serious problems with salt mine operation were also suffered in Poland, causing liquidation under emergency procedures (the "Kronprinz" Salt Mine in Inowrocław (1911) and those in Wapno (1977) and Łężkowice (1987)). When possible threat was predicted, a planned liquidation procedure was applied only to the "Solno" Salt Mine in Inowrocław (1997). The Bochnia and Wieliczka Salt Mines have also been subjected to planned partial liquidation, with the priority to protect the most valuable landmark workings.

3. Categories of mining areas

Owing to the types of discontinuous deformations (rock mass cracking, land subsidence etc.), the areas affected by such deformations are basically disqualified as potentially useful for development purposes. Reclamation of such lands is a long-term and expensive process, without

any guarantee as to durable and complete elimination of hazards. Consequently, such post-mining lands can be used only in the way that would not pose any threat to human life or health.

Underground mining is dealing with mostly continuous types of direct mining effects on a daily basis. Those include land subsidence caused by sagging of the layers close to land surface. In mining practice, land subsidence maps are applied. They are produced on the basis of either actual surveys, or predictions applying the Budryk-Knothe theory (which is currently most frequently used in world mining). However, such tools are only auxiliary because land subsidence may not be decisive for certain forms of development. It is the indicators characterizing the sinkhole geometry that are of key importance [15]:

- ► maximum land slope: T_{max}, mm/m;
- ► minimum land curvature radius (convex or concave): R_{min}, km;
- ► extreme horizontal land deformation: ε_{extr}, mm/m.

Fig. 1 shows a graphic interpretation of particular surface deformation indicators.
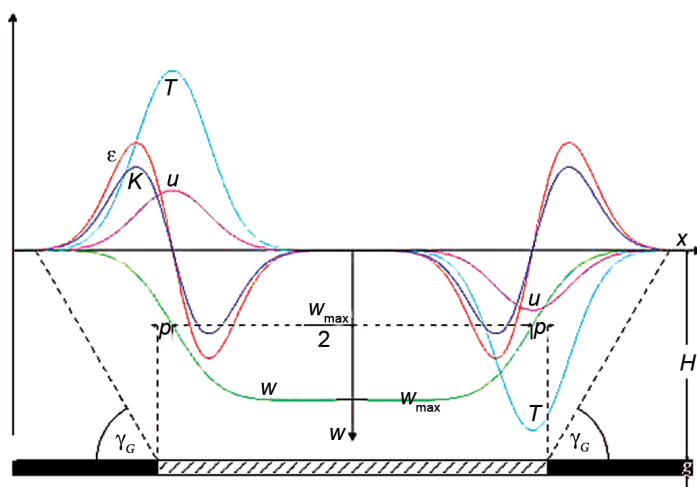
Fig. 1. Surface deformation indicators: their distribution over a mining field: w – subsidence, T – slope, u – horizontal displacement, ε – horizontal deformation, K – curvatures, p – mining field boundary, γ_G – angle of main influences, H – mining depth, g – layer thickness

Categories of mining areas are distinguished depending on specific indicator values, see Table 1.

Land is qualified under a specific category in respect of particular indicator values, with the most beneficial indicator assigning an area to the highest category. Nevertheless, other types of categories are also applied to mining land categories, assuming the qualification criteria separately for each indicator, e.g.: I (T), II (R), and I (ε).

As our structural development experience suggests, a mining area qualified to the Categories of 0 and I is refers to the land which is fully useful for development purposes. However, a number of restrictions apply to the areas belonging to Categories II and III, in reference to both existing and newly designed structures. The lands qualified to higher categories are not basically suitable for any development purposes.

Table 1. Mining area categories

Mining land category	Land deformation indicator values		
	slope T [mm/m]	curvature radius R [km]	land deformation ε [mm/m]
0	$T < 0.5$	$|R| > 40$	$|\varepsilon| < 0.3$
I	$0.5 < T < 2.5$	$40 > |R| > 20$	$0.3 < |\varepsilon| < 1.5$
II	$2.5 < T < 5.0$	$20 > |R| > 12$	$1.5 < |\varepsilon| < 3.0$
III	$5.0 < T < 10.0$	$12 > |R| > 6$	$3.0 < |\varepsilon| < 6.0$
IV	$10.0 < T < 15.0$	$6 > |R| > 4$	$6.0 < |\varepsilon| < 9.0$
V	$T > 15.0$	$|R| < 4$	$|\varepsilon| > 9.0$

4. Salt mining methods

Generally, salt mining methods belong to two types: dry and wet processes [6].

The dry method consists in salt rock cutting by blasting or mining tools and machines. Several extraction systems have been designed under that method (e.g. longwall caving, or chamber mining). Currently, the proper dry room-and-pillar method, with blasting, is applied in the "Kłodawa" Salt Mine. The other salt mine using the dry method in Poland, although with the operation of cutting combines, is the "Polkowice–Sieroszowice" Mining Company. In that case, the room-and-pillar system is practiced. Looking back at past operations, dry methods were also applied in the Wieliczka, Bochnia, and Wapno Salt Mines, with such systems as longwall caving, with conveyor belt transportation (Bochnia), or chamber cutting (Bochnia, Wieliczka, and Wapno). In addition, dry method works were conducted in Inowrocław to make preparations to proper wet extraction processes.

The wet (or leaching) methods are based on dissolving salt deposits with fresh water. Brine obtained by the process is subjected to evaporation to regain salt. Wet methods are applied in three options. The first one, which is currently used in Poland, consists in sprinkling the salt deposit in the virgin salt rock with a nozzle system. That process allows to form workings with specific dimensions and shapes by proper nozzle operation. In that case, the workings system is apparently similar to that obtained by dry methods. The second option, which is also currently applied, relies on dissolving salt rock in the so-called leaching plants, or chambers where salt is dissolved in stagnant water. After specific density has been reached, brine is pumped out and the chamber filled with fresh water. Both options were applied in the Wieliczka, Bochnia, and Inowrocław Salt Mines. The third option, called solution mining, starts with drilling boreholes from either land surface or underground workings towards salt deposits, followed by mounting pipes in the boreholes. Pipelines are designed to inject fresh water under pressure and collect brine, with various salt saturation. Fully saturated brine is transported for further processing, while unsaturated brine is subjected to a process designed for obtaining full saturation. Salt leaching through underground boreholes was applied in the Bochnia and Inowrocław Salt Mines, while the system of leaching

from land surface was used in Barycz and Łężkowice (retired salt mines), and presently the process is continued in cavern leaching in Mogilno, Góra, and Kossakowo.

As this short review indicates, quite diverse methods are used in salt extraction. Those processes depend on physical properties of salt rocks which are quite different than those of other types of rocks.

5. Peculiarities of salt rock mass affected by mining and the mining effects on land surface

Each method of mineral extraction, in particular those concentrated underground, interferes with the original rock mass equilibrium. Violation of equilibrium causes generation of a secondary state of equilibrium and that leads to the changes in the state of stress and deformation on workings' boundaries [8]. Consequently, the rock mass displays a tendency to relocate towards the workings (free space underground). That movement can be limited by the application of mining support systems. Such phenomena are generally observed in coal, copper, and other types of mines. Those phenomena are associated with the term of workings' stability understood as a capability to maintain shape and location. Loss of stability is visible in the occurrence of rock falls, mainly from the workings' roofs, or wall convergence.

Those processes also occur in the salt rock mass that is subjected to the same forces. Nevertheless, that type of rock mass is characterized by certain properties that are essentially different than those of other types of rocks: salt rock mass displays rheological features, or elastic-viscous-plastic ones. Without going to details, we will mention the practical consequences of salt rock mass dissimilarity. Salt rock mass, or rather the workings within, is characterized by long-term stability and they often do not require any classical support systems. The salt chambers of the landmark salt mines (e.g. in Bochnia or Wieliczka) are good examples of that, similarly to younger workings in currently operated salt mines (e.g. in Kłodawa). We should mention here that those workings are very large in size which is not the case of mining other kinds of minerals. Salt mining is rather free of workings' roof rock collapses, except for some local slides in the form of salt blocks separated from roofs or walls. However, convergence is quite well visible in workings. In the initial phase of workings' existence, the convergence process is the quickest and it slows down with time. Despite such processes, we can recognize that workings are fairly stable and the convergence process will inevitably lead to complete closure of workings. However, after hundreds of years.

In the situation of the absence of roof rock collapses, no sudden rock mass destruction processes occur around workings. A fairly slow convergence process affects the surrounding rock mass, but the workings' boundary relocation process does not cause any dramatic cracking around the workings either. The extraction rate is also important in the process of rock mass relocation around the workings. In the case of other minerals (e.g. coal or ores), the extraction methods allow to obtain operating front progress, counted in dozens of metres a month, however, the progress of the chamber or room-and-pillar systems amounts to a dozen or several dozens of metres a year. Salt extraction from a standard chamber of $15 \times 15 \times 100$ m takes about a dozen

of months, which is a fairly long period for the attainment of the secondary state of equilibrium. In the case of the mining system with pillars between chambers, we observe the phenomena of creep and relaxation. Those phenomena result in fairly small rock mass relocations around the workings, which are visible in equally insignificant land surface subsidence. Since the vertical relocations of land surface are small, other forms of land surface deformation are insignificant as well. Thus land can be made available for structural development.

Such a course of processes is observed in the salt mines that are free of the phenomena causing sudden loss of stability, owing to the layout of the mine's workings. Nevertheless, a number of failures occurred in the salt mines in recent years, ending with the liquidation of salt mines under emergency procedures. Practically, such liquidations were mainly caused by the encroachment of fresh water or low-density brine into workings, which affected the salt rocks by dissolving them. The process of uncontrolled leaching of protective rock formations (pillars between chambers or shelves between corridors and chambers) propagates quite dramatically, causing quick rock salt destruction, followed by the rock mass collapse around the mining area. Land surface is affected by the appearance of discontinuous deformations which often bring about catastrophic consequences.

6. Experiences in the area of land surface protection, using the examples of Polish salt mines

Polish salt mining companies conducted or have been conducting mining operations within two types of salt deposits: salt seams (Bochnia, Wieliczka, Łężkowice, Barycz, Polkowice and Kossakowo) and salt domes (Inowrocław, Wapno, Kłodawa, Mogilno and Góra,). In addition, we can distinguish boulder salt rocks in which the oldest Wieliczka chambers were cut out. Dry and wet methods were applied in both seam and salt-dome deposits. That also concerned classical underground salt mines and extraction by solution mining. Consequently, we can say that the experiences of Polish salt mining are quite rich. Below, we will discuss particular underground salt mines, followed by solution mining operations, as they were established in the chronological order.

6.1. "Bochnia" Salt Mine

Brine was collected for obtaining salt by evaporation on the present lands of Bochnia even 3,500 years BC. However, only in the middle of the 13th century, the first underground workings were dug out. Salt mining continued until 1990 there, and the Salt Mine has been converted into a museum and spa facility. It is estimated that the total volume of the Bochnia workings amounts to ca. 4.3 million cubic metres [9]. The conclusion of extraction did not stop certain mining operations which mainly consist in the protection of the most valuable industrial landmarks and the liquidation of the lowest levels. During the centuries, collapses occurred in the mine and they caused local discontinuities on land surface.

In 1952, observation of land surface effects started, with regular expansion of the measurement benchmark network. However, only the measurements taken since 1972 are valid for drawing conclusions. Fig. 2 presents land surface subsidence in 1997–2015.
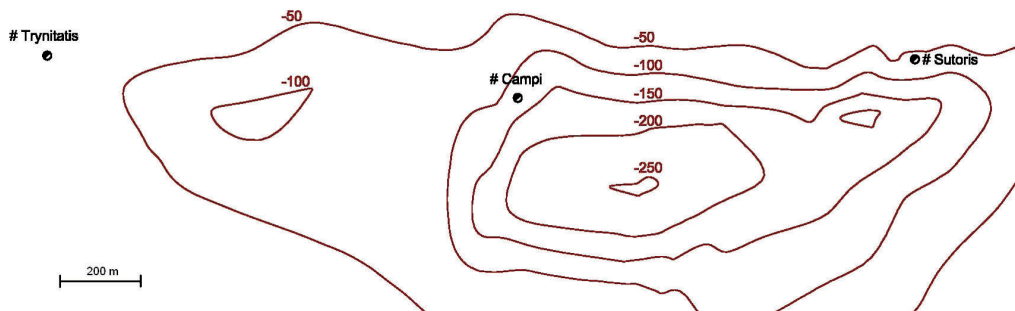
Fig. 2. Land surface subsidence in Bochnia in 1997–2015, based on observations

We can infer from Fig. 2 that the maximum subsidence reached about 250 mm in the past 18 years, and the sinkhole centre is located on the southern side of the mine's workings. Fig. 3 presents the projected land surface category, in respect of structural engineering needs.
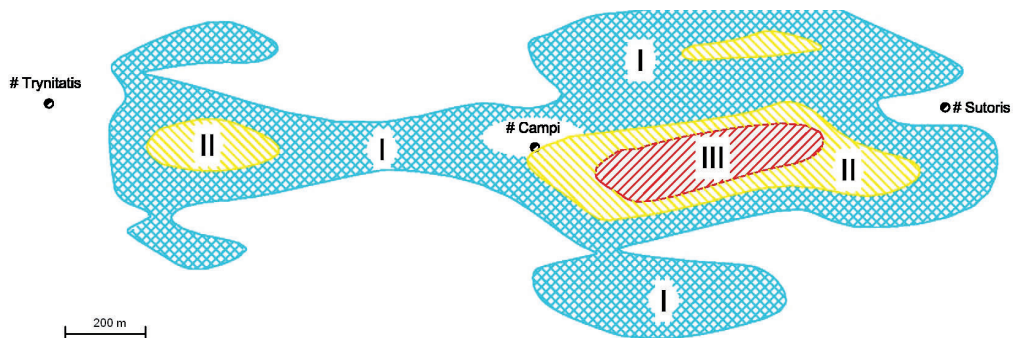
Fig. 3. The projected land surface category of land use for development purposes

Upon comparison of both figures, we can conclude that the northern section of subsidence affects the projected land surface category of land use for development purposes. Presently, it is difficult to estimate in what timeframe particular categories will be obtained. The forecast states that the least beneficial situation should affect the urbanized municipal areas, dominated by dispersed development.

6.2. "Wieliczka" Salt Mine

The "Wieliczka" Salt Mine is almost contemporary of the Bochnia one. However, both salt mines are quite different at least in their geological structures. The "Bochnia" Salt Mine was based on seam salt deposits, while the earliest mining activities started on a boulder salt deposit in the "Wieliczka" Salt Mine. Other types of salt formations were discovered later underneath,

and deep mining operations started after the boulder had been extracted. Finally, ca. 7.5 million cubic metres of voids have been produced [9]. A considerable proportion of workings is not available any more, owing to rock mass degradation (convergence, collapses etc.).

Presently, mining activities are continued on the liquidation of post-mining voids that could affect the landmark sections of the salt mine. Liquidation by filling proceeds vertically, down to the lowest levels, and horizontally, from the peripheral sections to the centre of the salt mine. In the past, catastrophic occurrences were recorded owing to fairly shallow workings. Those events could have stopped further mining operations, as they were demonstrated by discontinuous deformations on land surface. The last dangerous collapse happened nearly twenty-five years ago when water flooded the Mina cross-corridor, resulting in fairly serious damage of surface structures.

Land surface observations started in Wieliczka in 1926. 1,500 measurement benchmarks have been set until present day. However, only the measurements that have been recorded since the 1960's represent documentary value. The previous ones were not accurate enough since some benchmarks had been destroyed. Fig. 4 shows a fragment of the mining area map, with the subsidence isolines of 1970–2015, while Fig. 5 presents the projection of the category of land usability for development purposes.
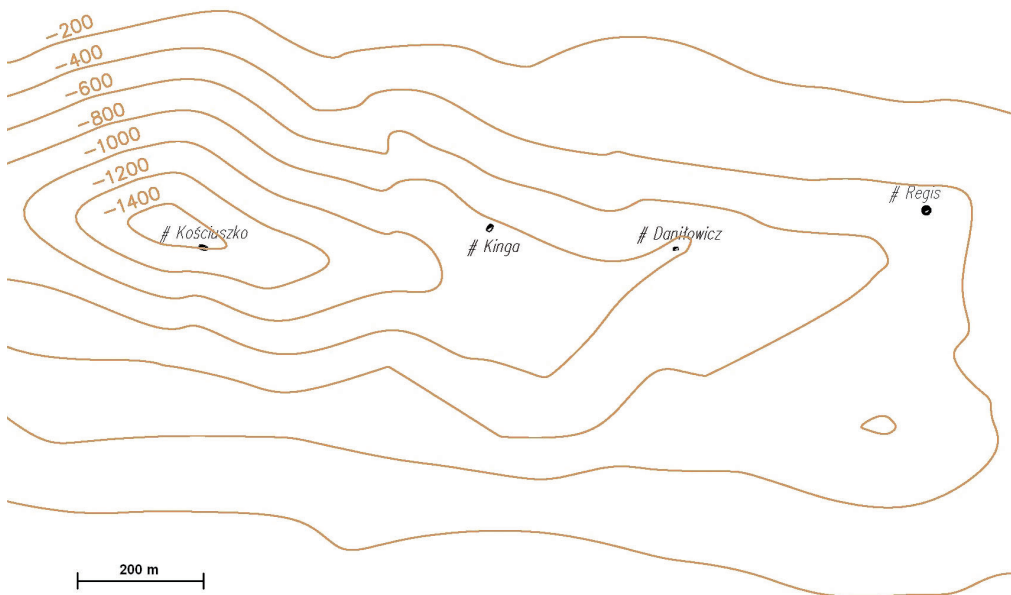
Fig. 4. Fragment of the mining area map, with the subsidence isolines of 1970–2015

The analysis of both figures leads to the conclusion that the majority of sinkholes that reached even 1,500 mm during the monitoring period, is correlated with the projected category of land usability for development purposes. Presently, the area for which Category II is projected is characterized by scarce and dispersed development.

Fig. 5. Projected category of land usability for development purpose

6.3. "Kronprinz" and "Solno" Salt Mines in Inowrocław

The discovery of salt dome structures in the Kujawy region in the 19th century resulted in the opening of the first underground salt mine in the area in 1871. Salt was extracted there by the wet method. In 1907, water inflow forced the miners to close down the plant. Deformations in the form of cylindrical sinkholes, with lateral surface area of several hundred square metres each, appeared on land surface. The northern transept of the Annunciation Church collapsed in 1909 (Fig. 6) and a sinkhole, with the surface area of ca. 1,400 m^2 appeared, which quickly ruined several residential buildings (Fig. 7).

However, brine extraction continued from the flooded workings and even a solution mining process was implemented there. Brine pumping had to be stopped in 1933 in view of the appearance of new and extensive damages on land surface. Unfortunately, no surveying measurements were conducted on land surface and only photographs show the consequences of salt mining.

The conception of starting a new mine was developed after the "Kronprinz" Salt Mine had been abandoned. It was implemented in 1923 under the name of "Solno". Wet process was applied there in 1932, and about 15.4 million cubic metres of voids were leached until 1986 [10]. The decision of the mine liquidation by flooding, with brine and post-leaching waste filling, was made in reference to the events relating to the salt mine in Wapno (see below). The liquidation process was conducted in 1986–1992. It is hard to say even today whether that decision was right or wrong.

Fig. 8 (left hand side) shows the surface subsidence isolines of Inowrocław in 1952–1992. The "Solno" Salt Mine was responsible for that mining effect, although some rather limited influence of the "Kronprinz" Salt Mine cannot be excluded either. Maximum land subsidence reached ca. 300 mm in that period. The subsidence isolines of 1992–1995 after flooding (right hand side of the same figure) look quite interesting. The sinkhole reached 6 mm at the lowest point, although elevations of about 5 mm also appeared there, probably as a result of the changes in hydrological relationships underground and close to the surface.
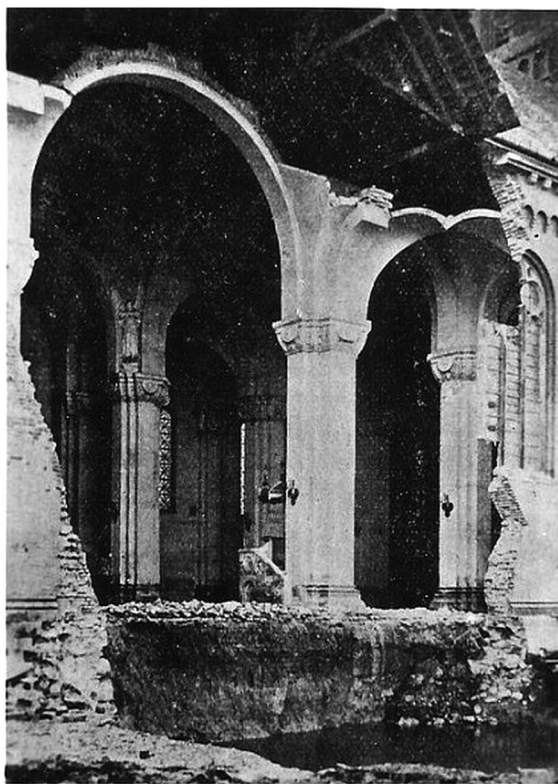
Fig. 6. Annunciation Church with a destroyed transept [17]

Fig. 7. Fragment of the sinkhole [17]
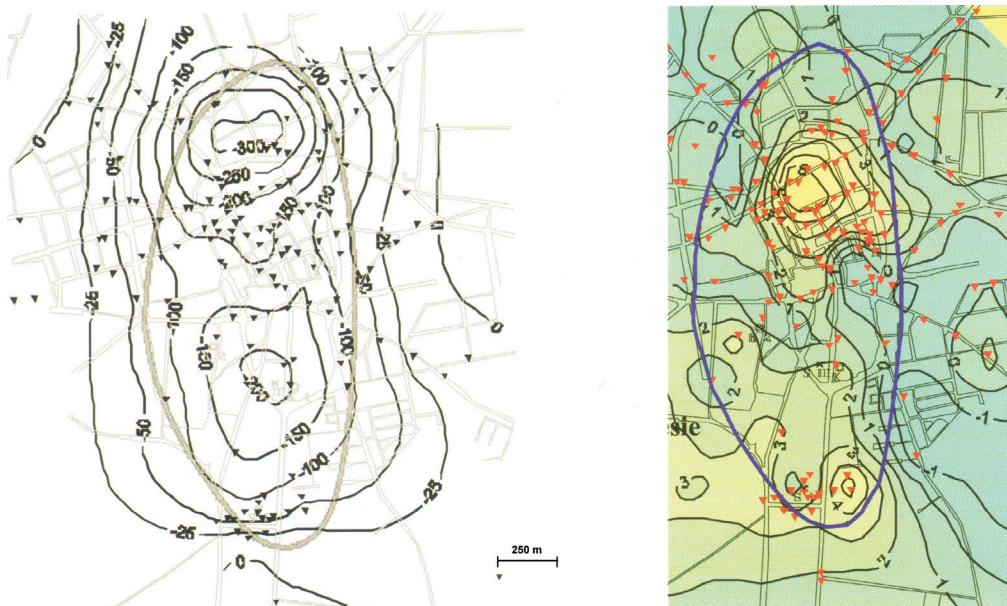
Fig. 8. The subsidence isolines of 1952–1992 (left) and 1992–1995 (right) [10]

The sinkhole and elevation areas developed there, right in the centre of Inowrocław, the town with typical urban structures. However, no significant mining menace was recorded there. Local deformations within the town caused delineation of a zone in which new capital projects are subjected to special design and construction procedures, similar to those that apply to the areas affected by mining menace.

6.4. Salt Mine in Wapno

The origin of that salt mine goes back to 1829. Initially, it was an open-pit gypsum mine, but the mining operations went underground later. Only after nearly 80 years, salt deposits were discovered below the gypsum layer, and the salt mine was constructed in 1911. It is obvious that the gypsum cap over a salt dome had been mined for several dozens of years! Such an operation would be recognized today as an elementary salt mining practice error.

The salt mine continued its proper chamber mining process at 8 of 13 designed levels, from Level III to Level X. The occurrence of sinkhole was identified on land surface. It reached its maximum value of about 600 mm after 40 years of mining (Fig. 9).

The decision of expanding mining to the new Level III was adopted in the 1970's and that decision caused significant consequences. A number of mistakes were made when salt mining was started through a considerably degraded gypsum cap. A sudden water inflow started into the workings at Level III in 1977. The intensity of encroachment was so strong that the whole salt mine was flooded within several weeks. It was estimated that about 30,000 m³ of water flew into the mine at the rate of 2,000 m³/min., within the first 15 minutes. The protective

rock mass was quickly leached causing multiple discontinuous deformations on land surface, in the form of huge sinkholes and cracking. About 50 buildings were damaged (Fig. 10) including a multi-family residential house, and about 1,400 residents had to be evacuated.

The case of the salt mine in Wapno was the largest mining catastrophe in the history of Polish salt mining.
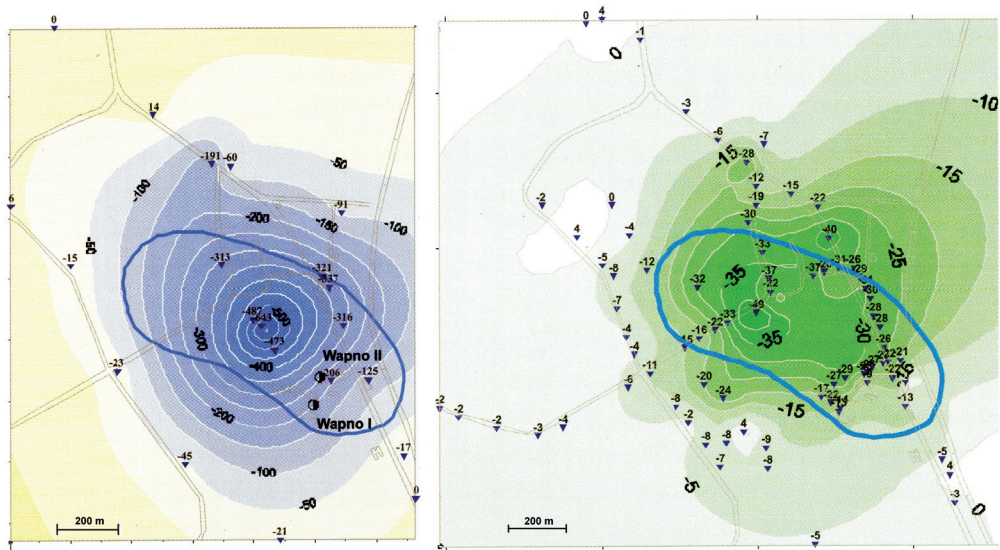
Fig. 9. The subsidence isolines of 1952–1992 (left) and 1992–1995 (right) [10]

Fig. 10. Consequences of the catastrophe in the salt mine in Wapno [16]

The recent phenomena associated with land subsidence were recorded on the area in 2007 and 2010. Sudden linear, discontinuous deformations appeared there in the form of cracks. Unfortunately, there are justified fears that Mother Nature will show its power again in the future. Land reclamation issues have not been resolved until today. The local government intends to change the zoning plan and redesignate lands for other socially useful purposes [12].

6.5. "Kłodawa" Salt Mine

The "Kłodawa" Salt Mine is unique in Poland since it is based on salt domes and applies the dry mining method. It was implemented in 1951, and the first salt production was obtained in 1954. The salt mine has been conducting salt extraction for more than 60 years. About 18 million cubic metres of voids were dug out during that period.

The salt mine has been operating a surface monitoring system since its beginning [1]. The first surveying network was implemented in 1952, with about 70 benchmarks distributed on the area of ca. 6 km². The network was expanded in 2011 and reached 280 benchmarks on the area of ca. 44 km². The measurements revealed the development of a large area land subsidence, with two centres corresponding to Mining Fields 1 and 2. The largest sinkhole developed over Mining Field 2 in 1978–2011, owing to its size, and it reached ca. 180 mm. The other centre of Mining Field 1, with the depth of ca. 80 mm, is shown in Fig. 11. The sinkhole dimensions are probably associated with the vertical and horizontal sizes of the respective mining fields.

Fig. 11. Vertical relocations of land surface measured in 1978–2011 [5]

As to land management of the area subjected to the largest subsidence, zoning plans cover the centre of Kłodawa, located above Mining Field 2. However, the areas over Mining Field 1 are used for farming purposes. Presently, the salt mine holds a mining concession until 2019, but the management has applied for a prolongation until 2052. The plans indicate that mining will be continued within the currently exploited fields but at lower levels than the existing ones. It is also assumed that magnesium-potassium salt will be extracted in Mining Field 7, which was only partly extracted by excavation of two small chambers.

Presently, the areas affected by mining consequences are generally classified under Category 0 and locally under Category I. The mining land category ranges, as predicted for 2052, are shown in Fig. 12.

If salt extraction is continued until 2052, we can expect that the area belonging to Category I will be extended, with the appearance of areas covered by Category II, in the period of several dozens of years after 2052. However, considering the time of such development, the issue is not considered to be problematic now.

Fig. 12. Projected mining land category ranges in 2052 [5]

6.6. "Polkowice-Sieroszowice" Mining Company

The salt mine has been extracting salt in the "Bądzów" field for more than 20 years. A layered salt deposit is located above the copper ore deposits. We can say that salt extraction is a side production, in parallel to copper mining. Salt is cut mechanically by the room-and-pillar method. Three mining levels have been designed, with the plan to continue mining during 50–60 years, with the output of 1 million tons a year. However, the copper ore deposits should be exhausted earlier (in about 20–30 years) and it would be hardly possible to maintain the plant facilities afterwards only for the needs of salt mining.

Possible salt mining effects are currently difficult to estimate because, despite its large capacity, the salt mine's output is limited to saleable quantities. The demand for salt depends

mainly on weather conditions during the winter period. In addition, the mining effects have to be considered in the context of copper ore mining.

As specific analyses have demonstrated, the most pessimistic scenario, assuming complete extraction of only the "Bądzów" field deposit and filling of voids in 90%, the largest subsidence can reach a stable state at about 2.5 m (in about 150 years!). Almost the whole "Bądzów" field area will be covered then by Category I, with a small section qualified under Category II in the northern part of the field. However, if copper mining effects are also taken into consideration, land subsidence will reach nearly 4 m, with a considerable field area to be qualified under Category II and a small section qualified under Category III in the northern part of the field [4]. The applicable future period scenario is so distant that the projected mining effects can be essentially limited because the scope of mining operations remains unknown.

6.7. „Barycz" Hole Salt Mine

The salt mine was operated in 1924–1998, using the solution mining method in a seam deposit. During that period, 980 operating and 44 exploratory boreholes were drilled. In total, ca. 10.5 million tons of salt was produced in the form of brine on 4 mining fields (Pagory, Centralne, Słoneczne, and Soboniowice). The boreholes were drilled from land surface, and an underground leaching process was applied, without cavern roof protection. That method contributed to the development of many large caverns out of control. The mining effects have the form of discontinuous deformations: multiple landslides and sinkholes [2]. The damages affected green areas, not developed land. Fig. 13 shows the distribution of sinkholes and land subsidence isolines, based on the observations conducted in 1926–1976.
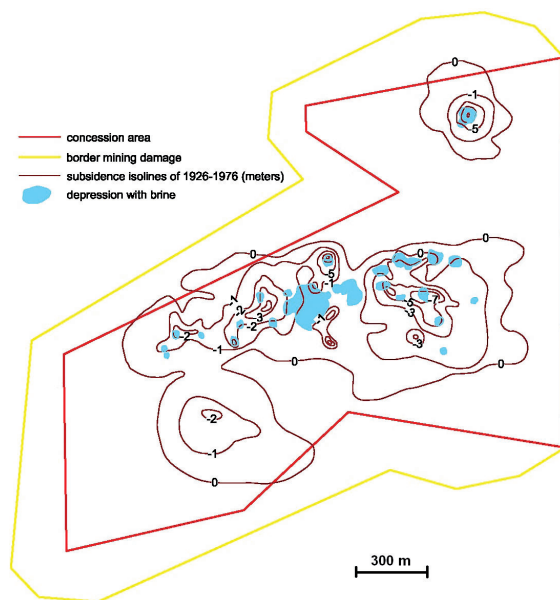
Fig. 13. The subsidence isolines of 1926–1976 and depressions with brine

Fig. 14. Municipal landfill construction on the Central Field (from archive Salt Mine "Wieliczka")

Fig. 15. Municipal landfill during operation (from archive Salt Mine "Wieliczka")

Partial chamber filling activities were conducted under a land reclamation project, which was a complex task, owing to the existence of uncontrolled connections between the chambers. In addition, surface reclamation works were completed. A municipal landfill was constructed in part of the Central Field that was subjected to the largest degradation. Fig. 14 presents the landfill development stages and Fig. 15 shows the condition during the landfill operation.

6.8. "Łężkowice" Hole Salt Mine

The "Łężkowice" Hole Salt Mine, using the solution mining method, was operated shortly in 1968–1988. Its liquidation took another twenty years and mainly concerned the liquidation of mining effects.

Brine was obtained by salt rock leaching, with two boreholes drilled from land surface for that purpose. Mining layout was designed with sets of caverns. Each set was composed of three caverns, 25 m in diameter each, distributed in a triangle 35 m apart. Consequently, the protective pillars were 10 m wide.

Mining was conducted without cavern roof protection and at small depth of 120–400 m below the ground level. Land subsidence appeared fairly soon, together with multiple sinkholes. Those resulted from specific geological structure of both deposit and overburden, causing a number of problems associated with the leaching structure of the designed caverns, as well as the mining method which was subjected to adjustments to current geological difficulties. Consequently, hydraulic connections were developing between the caverns, with the occurrence of unplanned caverns, rock mass cracking etc. After the rock mass collapse, the nearby Raba River was filled with brine containing about 1 million tons of salt, equivalent to about 15% of the total output of that salt mine [13].

After mining operations had been stopped, protective and reclamation works were implemented. The degraded land surface was fenced off and miners started to fill underground caves. Presently the land has been reclaimed and designed for farming purposes (Fig. 16).

Fig. 16. Fragment rehabilitated mining area (photo by K. Poborska-Młynarska)

However, the projections indicate that a whole selection of mining land categories will appear there in the future, from Category 0 to Category V (Fig. 17).
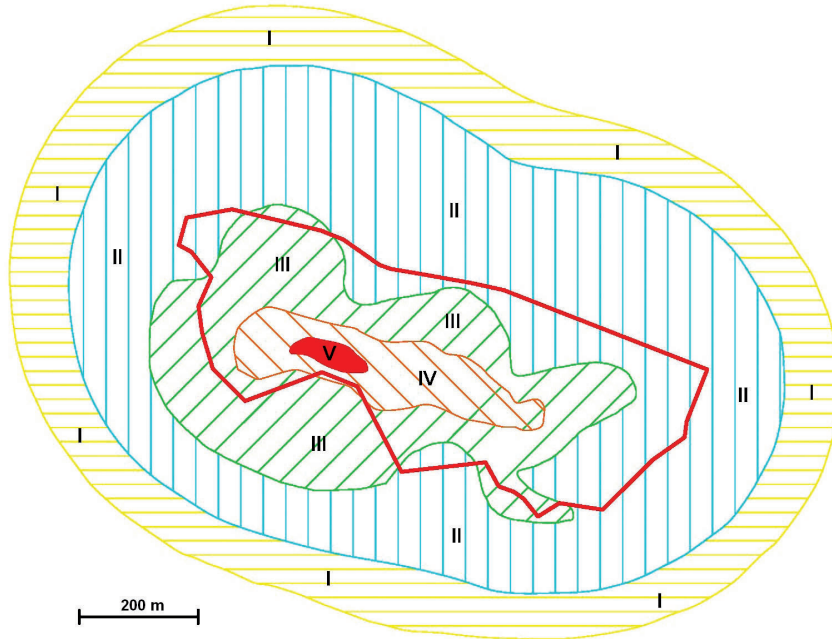
Fig. 17. Projected mining land category ranges in 2052

6.9. "Solino" Salt Mine in Inowrocław

The company has been operating two solution mining facilities in Góra (since 1968) and Mogilno (since 1987). The mines apply wet processes to extract brine from the salt domes in which caverns of ca. 50 m diameter and the depth of even more than 1,000 m are leached.

Upon our analysis of cavern stability, we concluded that the situation was exceptionally good as to geomechanical aspects. Firstly, caverns have always been filled with more or less saturated brine, which obviously influences wall stability. Secondly, the mining process applied there provides for cavern roof protection, with the use of solar oil. Its relatively thin layer effectively protects the cavern ceiling against uncontrolled leaching. The only hazard can be related to uncontrolled hydraulic connections between neighbouring caverns. To prevent that occurrence, protective pillars 100 m thick have been maintained.

After salt extraction, the caverns were turned into underground storage facilities for natural gas and liquid fuels. Consequently, the stored media constantly supports the cavern walls inside. Still, the caverns are subjected to the convergence process reflected in the occurrence of sinkholes on land surface. When analyzing the sinkholes one can conclude that subsidence is insignificant: up to several dozens of centimetres. That would not cause menace since the salt mine is situated on farmlands, with scarce farms, and thus the land has been qualified under Category 0.

7. Conclusions

This paper provides a review of all the salt mines which were or have been operated recently in Poland. Our first conclusion concerns mining catastrophes which are caused by:

► encroachment of underground water into workings;
► extraction of brine from flooded salt mines;
► loss of control over the solution mining process.

Each mining catastrophe is reflected on land surface, with more or less dramatic effects. The stories of sudden inflow of water into the Mina cross-corridor (1992) or upward propagating collapse of the Schmidt chamber (1960) in Wieliczka ended with a relative success. More tragic were the consequences of the salt mine flooding in Wapno (1977), contributing to the destruction of a town district, with the consequences showing and hurting still today. Similar phenomena were recorded in Inowrocław (1906–1911), although on a small scale. Also, the solution mining facilities in Barycz and Łężkowice caused extensive land surface devastation. Luckily, the mine locations were outside developed areas, although land reclamation took a lot of time and involved high expenditures. Those areas are still disqualified for development, despite recovery and reclamation operations.

Still, as our experience indicates, a salt mine does not have to be perceived as a source of land devastation, causing loss of valuable land features. Long-term mining activities, sometimes conducted even for centuries, lead to the occurrence of sinkholes where subsidence can be measured not only in centimetres, but also in metres. Nevertheless, we should consider the fact that the processes in question are distributed over long periods, which considerably reduces the scale and size of the properties that decide about the usability of land affected by mining for development purposes. Good examples of that are available in Bochnia, Wieliczka, and Kłodawa.

It seems that the background described here calls for a discussion among the geological, mining, and building circles whether the categorization of mining lands applied to coal and ore mine areas is equally adequate for salt mine areas. A similar issue can be raised in respect of land deformation projections which apply to very long periods. Practically, verification of such predictions will be possible a dozen or dozens of years into the future. Undoubtedly, it is necessary to conduct land surface monitoring activities on salt mining areas and, as far as possible, observations of the relocation of working's profiles. Such activities will contribute to the increase of our knowledge on salt rock mass and its movements in reaction to mining operations.

References

[1] Bieniasz J., Marcola-Sadowska J., Kurdek D., *System kontroli deformacji poeksploatacyjnych górotworu nad polami eksploatacyjnymi w KS „Kłodawa"*, XXI Międzynarodowe Sympozjum Solne „Quo Vadis Sal", 5–8 October, Zawoja 2016.

[2] d'Obyrn K., *Analiza wpływu otworowej eksploatacji pokładowego złoża soli Barycz na środowisko naturalne*, Seria Rozprawy Monogrfie nr 284, Wydawnictwa AGH, Kraków 2013.

[3] Głowacki T., Milczarek W., *Powierzchniowe deformacje wtórne dawnych terenów górniczych*, "Mining Science", Vol. 20, 2013, 39–55.

[4] Hejmanowski R., Kwinta A., Malinowska A., *Opracowanie prognozy wpływów eksploatacji soli złoża Bądzów na powierzchnię terenu*, 4GIS Ryszard Hejmanowski, Kraków 2015.

[5] Hejmanowski R., Malinowska A., Marcola-Sadowska J., Kurdek D., *Prognoza ciągłych deformacji powierzchni terenu dla złóż soli na przykładzie Kopalni Soli „Kłodawa" S.A.*, XXI Międzynarodowe Sympozjum Solne „Quo Vadis Sal", 5–8 October, Zawoja 2016.

[6] Hwałek S., *Górnictwo soli kamiennych i potasowych*, Śląsk, Katowice 1977.

[7] Kaszowska O., *Wpływ podziemnej eksploatacji górniczej na powierzchnię terenu*, „Problemy Ekologii", Vol. 11, No. 1, 2007, 52–57.

[8] Kłeczek Z., *Geomechanika górnicza*, Śląskie Wydawnictwo Techniczne, Katowice 1994.

[9] Kortas G. (ed.), *Ruch górotworu i powierzchni w otoczeniu zabytkowych kopalń soli*, Instytut Gospodarki Surowcami Mineralnymi i Energią PAN, Kraków 2004.

[10] Kortas G. (ed.), *Ruch górotworu w rejonie wysadów solnych*, Instytut Gospodarki Surowcami Mineralnymi i Energią PAN, Kraków 2008.

[11] Kwiatek J. (ed.), *Ochrona obiektów budowlanych na terenach górniczych*, Główny Instytut Górnictwa, Katowice 1997.

[12] Langer P., *Rekultywacja i zagospodarowanie poeksploatacyjne terenów salinarnych,* „Czasopismo Techniczne", 7-A/2007, 309–315.

[13] Poborska-Młynarska K., *Techniki eksploatacji ługowniczej w złożu solnym Łężkowic – z historii produkcji solanki na Podkarpaciu*, „Geologia", Vol. 35, No. 3, 2009, 393–405.

[14] Spackeler G., *Lehrbuch des Kali- und Steinsalzbergbaues*, Verlag von Wilhelm Knapp, Halle (Saale) 1957.

[15] *Wymagania techniczne dla obiektów budowlanych wznoszonych na terenach górniczych*, Instrukcja No. 364, Instytut Techniki Budowlanej, Warszawa 2007.

[16] www.google.pl (access: 20.10.2016)

[17] www.inowroclawfakty.pl (access: 20.10.2016).

Robert Bucoń (r.bucon@pollub.pl)
Michał Tomczak

Department of Construction Project Engineering, Faculty of Civil Engineering and Architecture, Lublin University of Technology

Nalysis of green solutions for new residential projects

Analiza rozwiązań ekologicznych dla nowych inwestycji mieszkaniowych

Abstract

Improvement of the ecological aspect in residential buildings is connected with the need for high investment expenses, which meets with little interest from investors, who are mainly interested in decreasing investment building costs rather than maintenance costs or environmental protection. To change this attitude, it is necessary to evaluate the validity of applications in terms of pro-ecological solutions, technologies and materials used. This is the basis for developing a mathematical decision support model when choosing ecological solutions. Application is demonstrated on the example of the selection of ecological solutions for a residential building.

Keywords: decision making, ecological criteria, ecological evaluation of a building, decision optimization

Streszczenie

Poprawa ekologiczności budynków mieszkalnych wiąże się z koniecznością poniesienia wysokich nakładów inwestycyjnych, co spotyka się z niewielkim zainteresowaniem ze strony inwestorów, których interesuje przede wszystkim obniżenie kosztów inwestycyjnych budowy, a nie kosztów eksploatacyjnych i ochrona środowiska. Aby zmienić to nastawienie, konieczna jest ocena zasadności stosowania proekologicznych rozwiązań projektowych, technologicznych i materiałowych. Problem stanowił podstawę do opracowania matematycznego modelu wspomagania decyzji przy doborze rozwiązań ekologicznych. Jego zastosowanie pokazano na przykładzie jednorodzinnego budynku mieszkalnego.

Słowa kluczowe: podejmowanie decyzji, kryteria ekologiczne, ocena ekologiczna budynku, optymalizacja wyboru

1. Introduction

Housing development based on outdated project solutions, energy-inefficient materials and fossil fuels largely contributes to a detrimental effect on the natural environment. It is responsible for high energy and water consumption as well as the changes in the quality of air and atmosphere [1, 2]. The reduction in the amount of natural resources consumed by the construction industry is a key factor for the environment. In order to limit its negative influence, it is necessary to simultaneously apply modern technology, materials, designs, and introduce changes in the behaviour and consumption models of building users. This means that apart from the introduction of innovative technologies and solutions to the market, it is necessary to take actions facilitating the awareness of their use and try to broaden the knowledge of investors and users as to the available possibilities of shaping the influence of buildings on the environment, both during actual use and at the investment planning stage.

Ecological housing combines the issues of the rational design, efficient execution, economical structure exploitation, ecology, and optimum conditions of use [7]. To fulfil these conditions it is necessary to use modern material and execution technologies, renewable energy sources (solar panels, geothermal, wind energy, heat pumps), and a responsible composition of the architecture into the surrounding environment etc. In order to achieve these goals, it is necessary to reach proper cooperation among designers, investors, the construction industry, and the contractors. This cooperation covers the following aspects: construction resource design and management, material selection, practical properties of the building, as well as the contribution to urban and economic growth [9].

New apartments offered on the market only meet ecological requirements to a small extent. This is the result of a number of factors, such as social, economic, cultural, and behavioural, which influence investors' decisions in various degrees. Nevertheless, it is currently visible that environment-related issues tend to be increasingly noticed by investors, as they determine how attractive an apartment or a house is on the market. More attention is currently paid to the application of design, material and technological solutions.

This interest has become the subject of scientific research, in which authors present the profitability of applying solutions improving the sustainability of buildings. Unfortunately, while assessing the solutions for the construction industry the dominant factor determining their choice is energy saving in the building without taking into consideration other important factors that determine the building's sustainability [8]. It can be assumed that this attitude will be changed together with the increase of ecological awareness of future accommodation customers whose requirements will become higher with time and they will concern more advanced solutions leading to the improvement in the sustainability of buildings. Currently, many of the pro-ecological solutions offered on the market, particularly related to the renewable energy sources based systems, are reluctantly used in the contemporary housing industry. The cause may be found in the fact that improving the sustainability of a building is connected with higher investment costs, which undoubtedly limits the implementation of pro-ecological solutions in the housing industry.

It is a difficult task to convince an investor to apply ecological solutions, since, apart from the environment-related arguments, it also requires a demonstration of other benefits such as economic and social. There is a need, therefore, to develop tools which would serve for the evaluation and comparison of materials, technologies and processes in respect of a balanced development involving environmental, economic and social benefits [6, 7, 9]. The challenge that the authors undertook was to create a decision support model with the consideration of ecologically efficient solutions. The model demonstrated in the paper constitutes a multi-stage approach, which includes both the selection of the evaluation criteria and ecological solutions as well as an evaluation of given ecological solutions in order to point out those which lead to the biggest benefits complying with the construction cost minimization.

2. Sustainable development in construction

The concept of balanced development in housing is connected with creating and responsible management of the urban area based on the rule of effective and ecological use of natural resources. It takes into consideration environmental factors, the quality of life, cultural issues, social justice, and economic limitations [9]. It is necessary to underline the fact that such an approach may differ depending on the type of a building undertaking (housing, office, industrial and infrastructural structures etc.).

Activities undertaken for the purpose of balanced housing objectives can be divided into pro-ecological (environmental), economic, and social [1, 7]. The pro-ecological (environmental) actions are intended to minimize the negative influence on the natural environment, mostly through efficient use of natural resources, recycling, waste production limiting and the use of renewable energy sources. The economic actions are related to lowering the economic costs (reduction of material and energy consumption) throughout all the lifespan stages of a building. The social actions are to improve the quality of life mostly through improving the interior environment quality, the transportation solutions and through appropriate localization of a building.

The way to accomplish the objectives of balanced housing is based on the proper application of scientifically prepared methods which allow an evaluation to be made and the material, technology, structural solutions, construction process, variants and strategies in respect to meeting the requirements of the balanced development in the best possible way to be selected. In practice, it relies on a multi-criteria decision support system during the design, realization, exploitation and demolition stages.

3. Housing investment preparation

The most important stage of the investment process is the preparation stage, during which the decisions affecting the whole lifespan of a building are made. The decisions made at this stage have to result from the analyses of many criteria, the building's influence on people

and the environment during the states of construction, exploitation and demolition. What is crucial during the preparation stage is the selection of the concept and the methods used to accomplish the task. This requires strict cooperation among all of the participants involved in the design process. The primary concept and project assumptions may determine the success of all the following stages of the construction process, the funding model for the structure as well as the possibility to reuse the resources and demolish the building in a way that enables further recycling of materials.

The preparation of the project documentation should comply with the multi-criteria optimization of the decision making with the consideration of the needs of investors (investment cost minimization), users (exploitation cost minimization) and the environment (detrimental effect minimization). The factors that must be considered in the design of an ecological building are as follows [3, 7]:

- ▸ Energy saving,
- ▸ The use of renewable energy sources,
- ▸ The possibility of material recycling,
- ▸ The improvement of the quality of the interior environment (acoustics, ventilation, heating),
- ▸ Saving natural resources (terrain, water, air),
- ▸ Building localization and geographical orientation,
- ▸ Lifespan prolongation of a building,
- ▸ Improvement in transportation solutions.

In order to adopt specific project solutions (architectural, installation) it is necessary to meet a number of requirements related to urban planning, utility supply methods, guarantees of construction and fire safety, providing essential health and hygiene conditions, environment and landscape preservation as well as protection against noise and tremors.

4. The description of the proposed method

The proposed decision-making support method for the preparation of an ecological design for a housing project is supposed to help make the optimal choice of solutions improving the sustainability of a building. It involves four stages, which require doing proper calculations (the solution evaluation and selection optimization) as well as choosing ecological solutions for a building and the evaluation criteria for them. Individual stages of the prepared model are shown in Figure 1.

The evaluation of a building's sustainability is a significant element during the stage of building concept development. In order for the building to meet the ecological requirements, it is necessary to select and properly define its evaluation criteria K_j. When selecting them, we must take into consideration the economic, environmental and social aspects as well as clearly define the effects of its influence on the environment and the tenants. The stage of selecting the ecological solutions for the analysis will reflect the subjective and individual approach of a person who prepares it. The selection of a proper ecological solution set R

$= (r_1, r_2, ..., r_n)$ requires appropriate market research in terms of the solutions improving the sustainability of buildings on offer. When choosing the ecological solutions, it is, first of all, important to consider the technical possibilities of applying them in a building (the shape of a building, its location, surroundings, etc.). The prepared set of i th solutions should make it possible to improve the sustainability of a building in respect of the assumed evaluation criteria.

SELECTION OF THE CRITERIA FOR THE BUILDING ECOLOGY EVALUATION
SELECTION OF THE SOLUTIONS FOR THE BUILDING ECOLOGY IMPROVEMENT
COMAPARATIVE ANALYSIS OF THE PROPOSED SOLUTIONS IN RESPECT OF THE ADOPTED CRITERIA
SELECTION OPTIMIZATION FOR THE SOLUTIONS IMPROVING BUILDING ECOLOGY IN RESPECT OF FINANCIAL LIMITATIONS
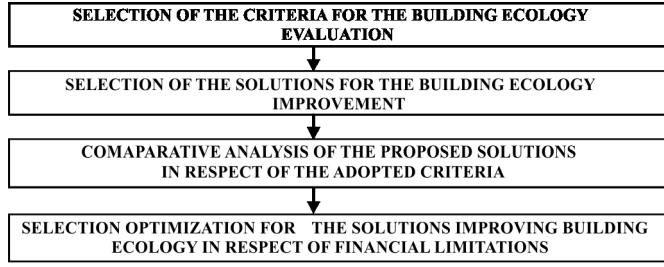
Fig. 1. The stages of the proposed method

The proposed ecological solutions for building need an evaluation concerning the adopted criteria. For that purpose the fuzzy AHP method was adopted [4, 5], which makes it possible to aggregate the opinions of a number of experts. Each of them makes $m = n(n-1)/2$ pairwise criteria comparisons using the following grading scale: 1, 3, 5, 7, 9 possibly extended with intermediary marks. As a result of the pairwise criteria comparisons a matrix set $A_k = \{a_{ijk}\}$, $i = 1, 2, ..., n-1$, $j = 2, 3, ..., n$, $j > i$, $k = 1, 2, ..., K$ is obtained, where a_{ijk} denotes a preference of the criterion mark i over j, reflected in the adopted fuzzy grading scale and expressed by an expert k. The aggregated evaluation marks are obtained from the following equations [5]:

$$l_{ij} = \min(a_{ijk}), \quad m_{ij} = \left(\prod_{k=1}^{K} {}_{ijk} \right), \quad u_{ij} = \min(a_{ijk}) \qquad (1) (2) (3)$$

For the aggregated expert evaluations, the characteristic points of triangular membership functions $\tilde{a}_{ij} = (l_{ij}, m_{ij}, u_{ij})$ are calculated using equation [5]:

$$\tilde{r}_{ij} = \left(\prod_{j=1}^{n} \tilde{a}_{ij} \right)^{1/n} \text{ where: } \quad \tilde{o}_{ij} = \tilde{r}_{ij} / \sum_{i=1}^{n} \tilde{r}_{ij} \quad i = 1, 2, ..., n \quad j = 1, 2, ..., m \quad (L_{ij}, M_{ij}, U_{ij}) \qquad (4) (5)$$

The fuzzy set obtained through the aggregation of the partial marks requires defuzzification in order to obtain crisp mark values for the individual solutions. The defuzzification procedure is carried out using the BNP method (Best Nonfuzzy Performance) [4]:

$$o_{ij} = \frac{L_{ij} + M_{ij} + U_{ij}}{3} \tag{6}$$

The solution marks obtained for the individual criteria are the basis for the next calculations with the use of the optimization method prepared. Its purpose is to identify the most efficient ecological solutions for the adopted improvement assumptions of the criteria evaluation marks concerning the sustainability of the building. This means that the most economical solution option which meets the assumptions s_{jz} for the criterion j is sought. The evaluation of every sustainability criterion of a building is carried out on the basis of equation (9), while the selection of the ecological solution option is made on the basis of the target (7) as a result of the optimization procedure. The mathematical description of the optimization method is presented in the following way:

$$\min z : z = K \tag{7}$$

$$K = K_b + K_r \tag{8}$$

$$s_j = \sum_{i=1}^{n} \sum_{h=1}^{t} o_{ij} \cdot x_h \quad i = 1, 2, ..., n, \quad h = 1, 2, ..., t \tag{9}$$

$$s_j \geq s_{jz} \quad \forall \quad j = 1, 2, ..., m \tag{10}$$

where:

  K – the cost of the prepared building concept $[\text{PLN/m}^2]$,
  K_r – the ecological solutions cost $[\text{PLN/m}^2]$,
  K_b – the base building cost $[\text{PLN/m}^2]$,
  o_{ij} – the evaluation of the i th ecological solution for the j th criterion,
  s_j – the evaluation of the j th criterion,
  s_{jz} – the projected evaluation of the j th criterion,
  x_h – the binary variable.

5. A calculation example

The application of the decision support system in terms of ecological solutions selection is presented using the example of a single-family detached house, whose usable floor area is 250 m². It was assumed that the base cost of the building was $K_b = 3500 \, [\text{PLN/m}^2]$. This reflects the average price of one square metre of usable floor area for a detached house in the Lubelskie Voivodeship. For the purpose of the analysis, six criteria were adopted for the evaluation of the building's sustainability. The criteria, along with the description of their influence effects are presented in the Table 1. These criteria do not include all possible activities related to the improvement of the ecological effectiveness of the building, but only constitute a portion of those whose application requires increasing certain investment costs when compared to a building constructed only for the purpose of meeting the modern legal and norm related requirements.

Table 1. The evaluation criteria for the building sustainability and their influence effects

j	Criterion K_j	The evaluation of the ecological effects
1	Energy saving	the improvement of the building partition isolation limiting the heat loss in the building
2	The use of renewable energy sources	the use of heating, ventilation, air conditioning and electrical systems powered by renewable energy sources
3	Interior environment quality	the improvement of the practical apartment convenience in terms of acoustics, ventilation, heating, lighting
4	Material recycling	the possibility of use and reuse of processed materials or their adaptation for other purposes
5	Environment pollution	the limitation of pollution sources such as waste, exhaust fumes which are disposed in the exterior environment
6	Reasonable use of natural resources	The use of natural resources which do not require a high level of processing (low accumulated energy consumption)

Table 2 presents the ecological solutions proposed for further analysis. The set below consists of nine solutions, whose application enables the improvement of the building sustainability in terms of the criteria k.

Table 2. Proposed changes for the improvement of the building sustainability

i	Ecological solution r_i with description	
1	Ground heat exchanger for the central heating system	Pipe heat exchanger in a broken version with length of 50 m with inlet sampling point
2	Mechanical ventilation with recuperation	Mechanical supply and exhaust ventilation ($V = 350$ m³) with cross flow heat exchanger
3	Solar system for domestic hot water (DHW)	System built out of two flat solar collectors with 300 litres DHW storage container
4	Photovoltaic installation	system built out of 12 photovoltaic panels with power of 3.06 KW –without batteries
5	Household sewage treatment system	Biological sewage treatment system 2.5 m³ with infiltration area
6	Energy-efficient lighting system	Energy-efficient light source (LED technology) with automated control
7	Passive exterior carpentry	Energy-efficient carpentry $U_w = 0.6$ W/m²·K
8	Passive exterior building partition	External double layer partition in system $U = 0.11$ W/m²·K
9	Passive bedplate	Bedplate in lost shuttering system $U = 0.09$ W/m²·K
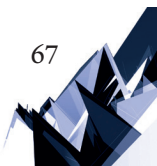
In order to establish the significance of the proposed solutions, 10 experts were asked for their opinions. Each of them made an evaluation through pairwise comparisons of the significance of the i th solutions for every j th criteria. Then, on the basis of (1)–(3) relations, the aggregation of the marks was performed. On the basis of the aggregated opinions $\tilde{a}_{ij}$ with the use of the equations (5) the values of the fuzzy evaluation vector $\tilde{o}_{ij} = \left(L_{ij}, M_{ij}, U_{ij}\right)$ of the i th solutions were calculated for the j th criteria. As a result of the conducted calculations modified by the AHP method the crisp values of the marks of the i th solutions in regard to the j th ecological criteria were obtained. The cost of the proposed solutions was obtained through the requests for quotation. The values were shown in Table 3.

Table 3. The evaluation of the ecological solutions oij and the solution cost K_r

r_i	The evaluation of the ecological solutions for j th sustainability criterion						K_r [PLN/m²]
	1	2	3	4	5	6	
1	0.103	0.156	0.043	0.244	0.084	0.336	64
2	0.128	0.085	0.178	0.043	0.09	0.036	48
3	0.086	0.153	0.054	0.047	0.073	0.039	12*
4	0.086	0.159	0.054	0.053	0.072	0.041	32*
5	0.046	0.266	0.042	0.132	0.204	0.172	52
6	0.085	0.079	0.109	0.046	0.058	0.051	28
7	0.146	0.036	0.158	0.095	0.129	0.084	140
8	0.189	0.033	0.19	0.161	0.187	0.127	72
9	0.13	0.033	0.171	0.179	0.103	0.114	144

* The price includes financial support

The final calculation stage for the proposed model was to identify the optimal set of ecological solutions. For the calculations, the assumptions s_{jz} which are related to the improvement of the building sustainability in terms of the j th criteria were adopted. As a result of these optimization calculations, the most satisfactory solutions for the improvement of the building sustainability were identified. The results are shown in Table 4.

Table 4. Selected ecological solutions ri for the adopted assumptions s_{jz}

The assumed mark s_{jz}/received mark s_j for the j th criterion						Selected ecological solutions r_i	Solution variant cost K_r [PLN/m²]
1	2	3	4	5	6		
0.3/0.402	0.3/0.473	0.3/0.384	0.3/0.380	0.3/0.305	0.3/0.462	1, 2, 3, 6	152
0.5/0.592	0.5/0.586	0.5/0.519	0.5/0.548	0.5/0.506	0.5/0.579	1, 2, 3, 4, 8	228
0.7/0.783	0.7/0.808	0.7/0.774	0.7/0.768	0.7/0.825	0.7/0.845	1, 2, 3, 5, 6, 7, 8	416

6. Conclusion

The analysis of the ecological solutions dedicated to a single-family detached house presented in the paper involves merely a narrow range of the applicable solutions offered by manufacturers. Improvements in housing sustainability require taking a number of actions leading to measurable effects in the environmental, economic and social aspects. It is possible to achieve them mostly thanks to the application of modern solutions for the improvement of building sustainability. This is connected, however, with the need to increase the investment costs in comparison to the conventional building solutions, which effectively limits their use.

The perception of building sustainability in terms of higher investment costs without noticing the effects which it is possible to achieve requires certain changes in approach from the investor. The decision support system concerning the selection of sustainability improvement solutions may serve as an example. It constitutes an innovative tool which may be helpful at the stage of the building concept formulation. It takes into account the construction cost limitations searching for the cheapest solutions leading to the desired improvement in the building sustainability. The mathematical methods used for the calculation of the individual model tasks facilitate its application in the practice.

References

[1] Akadiri P.O., Chinyio E.A., Olomolaiye P.O., *Design of a sustainable building: A conceptual framework for implementing sustainability in the building sector*, Buildings, Vol. 2(2), 2012, 126–152.

[2] Anderson J.E., Wulfhorst G., Lang W., *Energy analysis of the built environment – A review and outlook*, Renewable and Sustainable Energy Reviews, vol. 44, 2015, 149–158.

[3] Broniewicz M., *Modernizacja istniejących obiektów budowlanych zgodnie z zasadami zrównoważonego rozwoju*, Ekonomia i Środowisko, Vol. 3(46), 2013, 126–135.

[4] Chang T.H., Wang T.C., *Using the fuzzy multi-criteria decision making approach for measuring the possibility of successful knowledge management*, Information Sciences, vol. 179(4), 2009, 355–370.

[5] Chang, C.W., Wu, C.R., Lin, H.L., *Applying fuzzy hierarchy multiple attributes to construct an expert decision making process*, Expert Systems with Applications, Vol. 36(4), 2009, 7363–7368.

[6] Jalaei F., Jrade A., Nassiri M., *Integrating Decision Support System (DSS) and Building Information Modeling (BIM) to Optimize the Selection of Sustainable Building Components*, ITcon, vol. 20, 399–420.

[7] Maltese S., Daniotti B., Re Cecconi F., *Sustainability multi-criteria analysis method – real estate assessment tool for sustainable refurbishment*, Proceedings of Conference Central Europe towards Sustainable Building CESB, 26–28 June, Prague 2013, 1–10.

[8] Sadowska B., *Model operacyjny projektowania energooszczędnych budynków mieszkalnych w zabudowie jednorodzinnej*, rozprawa doktorska, Białystok 2011.

[9] Sinha A., Gupta R., Kutnar A., *Sustainable Development and Green Buildings*, Drvna Industrija, Vol. 64 (1), 2013, 45–53.

Małgorzata Gołaszewska

Department of Building Materials and Processes Engineering, Faculty of Civil Engineering, Silesian University of Technology

Marek Salamak (marek.salamak@polsl.pl)

Department of Mechanics and Bridges, Faculty of Civil Engineering, Silesian University of Technology

Challenges in takeoffs and cost estimating in the bim technology, based on the example of a road bridge model

Wyzwania w przedmiarowaniu i kosztorysowaniu w technologii bim na przykładzie modelu wiaduktu drogowego

Abstract

Technical and economic analysis of a construction project carried out using BIM can improve the process of cost-estimating at all stages of design and construction works. More and more designers choose to use BIM within a range of cost estimates; however, in contrast to design software, cost-analysing BIM software is less widespread and used. The following paper presents problems and issues that could be encountered while performing cost estimates and quantity takeoffs applying BIM tools on the example of a model of a road bridge.

Keywords: BIM, cost-estimating, cost-analysing

Streszczenie

Analiza techniczno-ekonomiczna przedsięwzięcia budowlanego wykonywana przy wykorzystaniu technologii BIM może usprawnić proces wyceny na wszystkich etapach projektowania oraz wykonawstwa. Coraz więcej projektantów decyduje się na używanie BIM w zakresie obejmującym także oszacowania kosztowe; w przeciwieństwie jednak do programów do projektowania oprogramowanie do analizy kosztowej jest mniej rozpowszechnione i używane. W artykule przedstawiono na przykładzie wykonanego modelu wiaduktu drogowego problemy i przeszkody, na jakie natrafić może wykonujący kosztorysy i przedmiary stosujący narzędzia BIM.

Słowa kluczowe: BIM, kosztorysowanie, analiza kosztowa

1. Introduction

Technical and economic analysis of a building is one of the key elements of a project, often determinative regarding the decision to start or plan the construction phase. A well-prepared cost estimate leads to better planning of the construction process and the use of financing, while an incorrect or careless cost estimate can lead to problems and delays during the construction process, or even stop it outright.

Until recently, the software available changed little in the process of making the cost estimates. Cost-estimating programs contain many facilities and shortcuts for this process; however, they still remain specialised and well prepared spreadsheet programs. They have limited compatibility with takeoff programs and require manual input of all information.

A qualitative change in the way software affects the takeoff and cost estimates can be introduced by BIM (Building Information Modeling). It is a fast-developing technology of design, which changes the way a design process is perceived. A construction project is no longer perceived as a set of drawings, but as a dataset, which changes the way a building is designed, but also the process of takeoff and cost estimating [3].

This paper is an attempt to check the options and new possibilities opened by BIM in the field of quantity takeoff and cost estimating, with special attention paid to the software popular in Poland. A design project of a road bridge was conducted entirely in the BIM environment in a team, to simulate the conditions of a design company and observe how BIM affects the design process. The process of takeoff and cost estimating was a notable part of the project, and is described in the following paper.

2. Building Information Modelling in takeoff and cost-estimation

According to the definition in British standard BS 8536-1:2015 [1], BIM is a "digital representation of physical and functional characteristics of a facility. A BIM is a shared knowledge resource for information about a facility forming a reliable basis for decisions during its life-cycle; defined as existing from earliest conception to demolition". This means that BIM creates an interactive data set for a building or object and its physical and functional characteristics at every stage of its life-cycle, instead of creating a set of drawings. It allows for more informed decision-making due to a more holistic approach to information concerning the object [8].

During the programming and conceptual design, BIM tools allow for better communication with the investor and better representation of their expectations, as well as creating a template for further work on the project. Detailed project and documentation are based on the conceptual design to a higher degree than in the case of traditional designing methods – conceptual design gets overwritten with details, rather than being a different drawing which shows the general structure of a designed object. The process of designing is also divided into phases, in which the project undergoes subsequent detail enhancements of all project elements (construction, installations) until reaching a set detailing level for the phase [10]. In traditional design work, the drawings are made already with the final detailing level [5].

2.1. Takeoff in BIM

Takeoff itself can be defined as the process of calculating the amount, type and installation method of all elements in the object, made before the construction process [9].

In the traditional way of designing, it is a time-consuming and labour-intensive process, susceptible to human error. While takeoff programs were available before the BIM technology, they only offer a less time-consuming way to count the amount of material, and still require mainly manual input [9].

The BIM technology introduces many improvements, both in the process of takeoff itself, but also in sharing information about the elements and their installation in the construction. Elements can contain additional information about each element, in addition to which they can be divided in the way they will be installed. The information can be processed automatically to create a takeoff table. The design software in BIM technology (i.e. Revit) usually has integrated options for the takeoff for modelled elements; however, the scope of possibilities and displayed information is different for each design program.

There are also additional BIM programs for takeoff (i.e. Vico Takeoff Manager), as well as BIM cost-estimating programs (i.e. Zuzia BIM) with those functions, usually with more possibilities for modifying and collecting data. It must be noted that programs have a different ways of displaying and reading data from the BIM models, which can lead to programs displaying data differently or not displaying it at all.

The automation speeds up the process of making the takeoff and leads to fewer mistakes and omissions caused by oversights in the human factor. However, using BIM tools creates new problems, such as the fact that the data pertaining to the takeoff must be input during the design stage. It requires close cooperation between the designers and the takeoff makers at every stage of the design work. Olatunji et al. [7] also point out that the automatically compiled takeoffs do not show the actual amount of materials used, but the amounts of materials included in the 3D model. It also does not show materials that are not included in the model. This can lead to the omission of some materials and labour.

To sum up, the BIM tools introduce automation of the takeoff making process, speeding it up and lowering the risk of miscalculations and omissions caused by human error. It can also include additional information vital for the takeoffs and cost-estimates, such as the assembly order. The effective use of BIM tools requires a model of the set detailing degree, with information and descriptions included in a way compatible with the takeoff.

2.2. Cost-estimation in BIM

The process of cost-estimating is tightly tied to the takeoff – a well-prepared takeoff can make cost-estimating less labour-intensive, faster and less prone to omissions due to human error. A well-prepared takeoff is vital for the cost estimate, as without a properly detailed record of the elements that need to be priced, the cost assessment will be incomplete.

In traditional design work, accurate cost-estimating is only possible after completion of the documentation, when the exact amounts of materials and labour are available. Before

that moment, at the concept stage and during the designing process, the cost is estimated on the basis of previous experience with similar buildings, or set rates for a square metre of similar or the same construction type. The rates are calculated for standard constructions, and while there is a way to modify the rates to suit a particular construction, it is hard to obtain satisfactory accuracy. This is particularly pronounced in the case of atypical construction builds with new technologies.

Using BIM gives new opportunities to make cost estimates more accurate and detailed. In the conceptual stage, the model is more detailed than in the case of a traditional designing process, as it is a base for future changes [2]. That allows making a more detailed and more accurate estimate of the cost on this stage. Moreover, the automation of the takeoff process enables a faster analysis of the costs and variants of the construction.

Similarly to the takeoff, the main advantage of BIM-aided cost-estimates is the automation. Instead of having to manually input all the information, BIM tools create a spreadsheet structured correspondingly to the construction elements, with automatic or semi-automatic takeoff included. Also, the basic problem with using BIM tools for cost estimates is the fact that the automation is only possible if the model is created according to the standards set by the cost-estimator and corresponding to the programs used to estimate costs. Without this, the automation might give incorrect values, or be impossible to obtain.

Even when the cost estimate is calculated on the basis of a well-prepared model, it requires a lot of work from the cost estimator. The automation concerns the materials and their amount that are modelled in the design – it does not include additional materials and labour. In Poland, these elements are usually taken from National Contractor's Estimator (KNR).

Design programs such as Autodesk Revit or Tekla Structures have tools for basic cost-estimation on the basis of the automatic takeoff; however, the tools do not allow for any additional positions. More complex cost estimates can be carried out in add-ons for the design programs, or in BIM cost estimating software such as CostX BIM. In Poland, the most widely known cost estimating program is BIMestimate.

To sum up, cost estimating in BIM is strictly connected to takeoff and shares mostly the same advantages and disadvantages. It introduces higher process automation, but only in the case of a well-prepared BIM model, and this process is not fully automated.

3. Practical use of BIM

To conduct an analysis of how BIM tools affect the takeoff and cost estimating processes, the authors created a model of a road bridge with accompanying takeoff and cost estimate. The work was conducted by a team of 6 people, to approximate the groupwork usually conducted in the BIM designing process.

3.1. Model of a road bridge

The model of a road bridge was made on the basis of existing 2D documentation of a road bridge marked WD-179, which leads the national road no. 62 over the highway A1 in direction Toruń-Styków. The road class is G, meaning it is a main road. The documentation was made available by its authors [5].

The bridge is a post-tensioned concrete construction. It is a continuous, two-span slab and beam construction. The support is realised with two abutments on both ends of the slab and a reinforced concrete pillar in the midspan. All supports are founded on reinforced concrete high-diameter drilled piling. The superstructure is made of two main girders of changing width – over the main support, they widen to a max width of 1.50 m. The diaphragms in the structure have changing height – 1.40 m over the pillar and 0.70 m over the abutments.

3.2. Work organization

The project was done by a work group consisting of 6 people, with the intention of simulating work in a design studio [8]. The organisation chart for the work group is presented in Fig. 1.
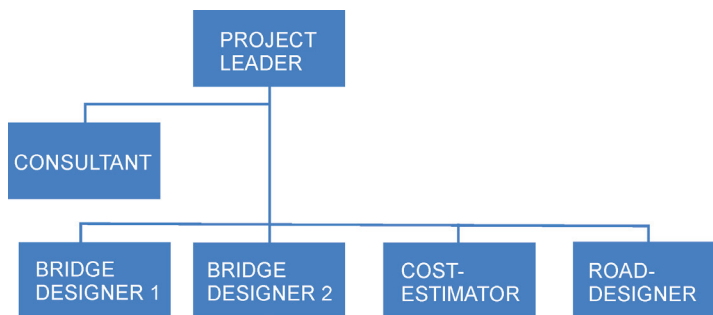
Fig. 1. Organization chart of the created BIM workgroup

The project leader prepared the work environment, set tasks, controlled the ongoing work and analysed the results of the work. The consultant was not directly involved in the project but assisted in case of issues with the BIM tools and their compatibility. Two bridge designers made the 3D model, the road designer was responsible for the project of the road leading to the bridge. The cost estimator prepared the takeoff and cost estimates for the object. Neither the designers nor cost estimator had previous solid experience with BIM technology and the BIM aspects of the software used. Cooperation within the work group was mainly conducted remotely. A meeting was held once a week, during which problems and issues were discussed and plans were made for future tasks. The model and file exchange was conducted using a server, namely Google Drive.

The bridge was modelled in the programs Autodesk Revit 2015 and 2016. For the road designing program AutoCAD, Civil 3D was used. Data from the model was then exported to the cost-estimating software, Zuzia BIM, which required an additional program, BIM Vision, which is a free IFC model viewer.

4. Issues of BIM-aided takeoff and cost-estimating

During the process of making the model and cost estimates, the team encountered many issues, which may be considered characteristic in working with BIM technology.

4.1. Choice of software

The first issue that became prominent during the project was choosing the right software. There are numerous programs for modelling in BIM, all of which offer slightly different functionality. The choice was made mostly on the basis of the availability of a student's version of the programs and previous experience of the workgroup with those programs or programs similar to those. The information given by the software developers was usually precise in describing the functionality and many of the programs considered had a demo or student's version available. There were also presentations and videos available showing the functions of the software.

In the case of takeoff and cost estimating software, the information obtained from the websites of the programs was scarce, and usually did not present the full abilities of the program, instead concentrating on listing the advantages of using BIM tools. There were also very few videos available to see the functions of the software. This affects the choice of suitable cost-estimating software for designers and design studios, as it does not allow for more informed decision making.

4.2. Team communication

The most basic problem which was present during the whole process of making the model and cost estimates was communication between the members of the workgroup.

Good communication was needed at every stage of the project, due to the specifics of working in the BIM environment. Each and every modelled element had to be coordinated between the members of the team, as its description of properties could potentially tie into the possibility of automation of data transfer between the programs. In the case of any issues with automation or information transfer the work had to be paused, and a proper modelling method had to be found.

The problem of constant communication between designers was present in part due to the fact that the workgroup had very little experience with BIM tools; however, even after acquiring better knowledge of the software, it was still necessary to keep each other informed about any changes and issues, or the compatibility of the created model with other BIM tools. In a traditional design process communication is also crucial; however, each designer works on their own copy and it is the end-result from each of them that matters, not the way an object or element is drawn or described. Therefore, it can be concluded that communication is one of the key issues while conducting a project in the BIM environment.

4.3. Element description

In the case of using BIM tools to make an automated or semi-automated takeoff and cost-estimate, it is necessary to describe the model elements in a way which will allow other BIM tools to correctly interpret the information. The absence of a description or different way of including the information can lead to mistakes or inaccuracies in the takeoffs and cost-estimates.

Including descriptions during the process of modelling is a rather simple action when it comes to elements prepared in the base design software. However, it was noticed that the options are quite limited in the case of elements downloaded or copied from other programs, for example, AutoCAD. During the course of the project, several elements were made in different programs, usually due to the fact that either pre-existing elements were found or the complicated geometry of an element was easier to model with different software. After uploading the elements into the program, there were extremely limited description options, not even a type of material could be assigned to the element. This hindered the automated takeoff process, as the elements did not appear in the takeoff lists compiled by Revit.

The issue was not solved, as the elements were just remodelled in Revit. It was an inconvenience especially in the case of experienced designers who are starting work with BIM tools – the library of non-BIM elements they might have accumulated is not fit to be used. In the case of small-scale buildings, such elements can be quickly found in an automated takeoff or cost-estimate; however, in the case of bigger or more complicated elements, it can be easily overlooked, leading to mistakes.

4.4. Simplifications in the model

During making the model, many simplifications were made. Elements such as railings were only symbolically drawn in, without keeping their geometry. In the case of traditional projects, it is of practically no importance, as those elements are usually described in the written description. It poses a problem, however, for the automatic takeoff and cost-estimation in BIM. Any simplification leads directly to inaccuracies in the takeoff, as the volume, length or amount of elements does not correspond to the real amount. The amounts can be taken from the description or comments in the model, but this stands in opposition to the automation of the process. It can also cause some elements not to be counted in at all if the simplification means they are not to be modelled at all.

The simplifications in the model play an important role in the designing and model-making – it saves time and labour while keeping the functionality and aesthetics of the model. Fewer elements keep the software from overloading and keep the working in the program smoother. Therefore, there is no reason not to use simplifications in the model.

In the project, the issue of simplifications was solved by continuous contact between the designers and the cost estimator, where it was determined which elements should and could be simplified. It was necessary to set a set of rules concerning the simplification of elements and units, as well as make comments about the missing layers or materials.

5. Conclusions

The aim of the paper was to explore the possibilities for using BIM technology in takeoff and cost-estimation. For that purpose, a literature review of the information about cost-estimating and takeoff in BIM has been done, as well as a team project showcasing the main issues cost-estimators and designers can encounter, especially if they do not have experience with BIM tools.

The most important aspect that has been observed is the change of the labour schedule for the cost estimator. Traditionally, after preparing an initial, conceptual cost-estimate, the cost-estimator starts work practically after the documentation is finished. After getting the finished project, making the cost estimate is labour-intensive work, mostly due to the takeoff. In the case of BIM technology, the cost estimator should be present during each phase of design to determine the way objects and elements are meant to be described and modelled if any automation of the process of cost-estimating is required. They should also give input on possible simplification of the elements in the model. However, during the cost estimating phase, the labour input from the cost estimator should be lower, as the takeoff and parts of cost estimate can be done automatically and semi-automatically.

On the basis of the literature and experience, it can also be concluded that the effective use of BIM is dependent on the communication within the workgroup. Regular communication amongst the designers and cost-estimators allows a working model to be created which can be used for further processing in different BIM tools. The need for constant communication imposes a better information flow. Future research should investigate the influence of BIM tools on the exact project duration, as well as, in the wider perspective, test how it translates to changes in the construction work itself.

To conclude, BIM technology introduces many simplifications in the work of the cost estimator, both in the case of takeoff and the cost estimate itself. It changes the way a project is managed, as it requires constant contact between the workgroup members. BIM technology is a step in the direction of better cost-management and more productive cost-estimating.

References

[1] Abanda F.H., Vidalakis C., Oti A.H., Tah J.H.M., *A critical analysis of Building Information Modelling systems used in construction projects*, "Advances in Engineering Software", Vol. 12, 2015, 183–201.

[2] Hergunsel M.F., *Benefits of building information modeling for construction managers and BIM based scheduling*, Doctorate, Worcester Polytechnic Institute, 2011.

[3] Iskdag, U., Underwood J., Aouad G., Trodd N., *Investigating the Role of Building Information Models as a Part of an Integrated Data Layer: A Fire Response Management Case*, "Architectural Engineering and Design Management", Vol. 12, 2006, 124–142.

[4] Jasiński M., Płaszczyk T., Salamak M., *Modelowanie geometrii wybranych elementów konstrukcji podpór obiektów mostowych w technologii BIM*, „Mosty", Vol. 5, 2016, 22–27.

[5] Kogut P., Tomana A., *Aplikacje 4D i 5D w środowisku BIM*, CMM-2013 – Computer Methods in Mechanics , 27–31 August, Poznań 2013, Poland.

[6] Kossakowski P., *Modelowanie Informacji o Budynku (BIM) – obowiązkowy standard przyszłości?*, „Przegląd Budowlany", Vol. 4, 2014, 48–50.

[7] Kulasekara G., Jayasena H.S., Ramadewa K.A.T.O., *Comperative Efectiveness of Quantity Surveying in a Building Information Modelling Implementation*, The Second Wolrd Construction Symposium 2013: Socio-Economic Sustainability In Construction 14–15 June, Colombo 2013, Sri Lanka.

[8] Płaszczyk T., Jasiński M., Salamak M., *Współpraca w infrastrukturalnym zespole projektowym korzystającym z technologii BIM*, „Mosty", Vol. 5, 2016, 16–20.

[9] Shen Z., Issa R.R.A., *Quantitative evaluation of the BIM-assisted construction detailed cost estimates*, "Journal of Information Technology in Construction" (ITcon), Vol. 15, 2010, 234–257.

[10] Tomana A., *BIM. Innowacyjna technologia w budownictwie*, Kraków 2015.

Bożena Hoła

Mariusz Szóstak (mariusz.szostak@pwr.edu.pl)

Department of Construction Methods and Managements, Faculty of Civil Engineering,
Wroclaw University of Science and Technology

A mathematical model of accident event development in the construction industry

Matematyczny model rozwoju sytuacji wypadkowej w budownictwie

Abstract

Accidents at work constitute a heavy psychological and economic burden for companies and societies. The vast majority of cases can be prevented by appropriate and effective preventive measures. Knowledge about the course of events, their causes and consequences is required in order to carry out such actions. The knowledge gained can provide a basis for drawing conclusions of a preventive nature. The article presents a mathematical model, which was used in the study of the phenomenon of accidents in the construction industry, and provides the test results that were obtained using 350 sample cases.

Keywords: construction industry, accident at work, cause-and-effect model

Streszczenie

Wypadki przy pracy stanowią bardzo duże obciążenie psychiczne i ekonomiczne dla przedsiębiorstw i społeczeństw. Zdecydowanej większości wypadków można zapobiec poprzez odpowiednie i skuteczne działania prewencyjne. Aby takie działania prowadzić, należy mieć wiedzę o przebiegu wypadków, ich przyczynach i skutkach. Uzyskana wiedza może stanowić podstawę do formułowania wniosków o charakterze prewencyjnym. W artykule przedstawiono: matematyczny model zastosowany w badaniu zjawiska wypadkowości w budownictwie oraz zamieszczono wyniki badań uzyskane na próbie 350 wypadków.

Słowa kluczowe: budownictwo, wypadek przy pracy, model przyczynowo-skutkowy

1. Introduction

The construction sector is one of the most dangerous industries in the world. This is evidenced by the reports of organizations and agencies that deal with issues of safety, including, among others: the National Safety Council – NSC, the Bureau of Labour Statistics – BLS, the National Institute of Occupational Safety and Health – OSHA, the Commission of European Communities – CEC, the Health and Safety Executive – HSE and the Polish Central Statistical Office – GUS.

During the recent 20th World Congress on Health and Safety at Work, which was held in 2014 in Frankfurt, the International Labour Organization (ILO) stated that about 350,000 workers die each year as a result of accidents at work. At least 60.000 fatal accidents at work occur every year on construction sites all over the world. This means that on average, one employee dies every 10 minutes when at work [1]. In 2015 there were 5.776 accidents at work on Polish construction sites, of which 69 resulted in the death of an employee [2].

Accidents at work are the subject of studies and analysis by many researchers [3–6]. The aim of this study is to detect specific regularities that characterize the phenomenon of accidents, which may indicate the directions of preventive measures.

The aim of the research conducted by Drozd [3] was to show the importance of the characteristics of a construction site and also the behaviour of employees when defining the circumstances of an accident at work. Study [4] presents the results of research on the phenomenon of accidents that occurred in 2014 in 28 European Union countries. The results obtained indicate that the construction industry, among all sections of the national economy, is in third place in terms of the total number of accidents at work. Spain is the European country with the highest accident rate [7].

Up to 34.6% of the total number of accidents at work in the construction industry in Spain are serious accidents and 33.9% are fatal accidents [8, 9]. In turn, fatal accidents are most often caused by falling from a height (33.8%) and being hit by a moving vehicle (15.9%). Studies on the identification of events, which are inconsistent with the appropriate conduct of the work process and usually cause a fatal accident, indicated that the most common event that leads to an accident is a fall from a height. 30% of people were injured as a result of falling from scaffolding and 12.1% as a result of falling from a roof structure during roofing work [10].

The results obtained by the authors of study [11] confirm that accidents occur most frequently as a result of a fall from a height or a fall at the same level (43.9%). The most common injuries are fractures of limbs (35.3%) and the most vulnerable part of the body that gets injured is the head (16.3%). According to research [12], a fall most often occurs during the installation of steel structures (33.22%), the concreting of ceilings (6.67%) and the plastering or painting of exterior walls (10.00%). Understanding the mechanisms of the occurrence of accidents at work is the first step in the process of preventing accidents and improving safety in the workplace.

Each accident at work occurs according to a specific scenario. The aim of the research presented in this article is to define possible accident scenarios in the construction industry on the basis of analysis of an appropriately numerous set of accidents. Moreover, the authors also aim to develop a model that illustrates the phenomenon of accidents in the construction industry.

2. Description of the problem

Accidents at work occur in different places and at different time periods. These events, organized in accordance with the passage of time t_z, create an infinite sequence of accidents, which can be analysed as a discrete accident process:

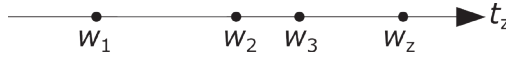$$W = \{w_z; z = 1, ..., n_w\} \tag{1}$$

Fig. 1. Discrete accident process (own work)

Every accident event $\{w_z; z = 1, ..., n_w\}$ in the W process runs according to a specific scenario. An accident process model, which was proposed by the European Statistical Office (EUROSTAT), was modified for the purpose of this research and used to describe the scenario of a single accident at work. The authors' own model of an accident, in the form of a cause-and-effect chain that consists of 11 events (nodes) connected with relations, was developed using definitions, concepts and codes from the EUROSTAT model [13]. The previous event in this sequence is the cause of the following event, while the following event is a result of the previous event. The general model of a single accident is shown in Figure 2.
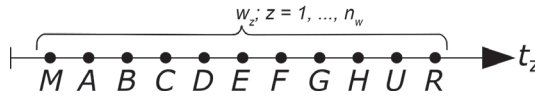
Fig. 2. The cause-and-effect chain of the course of a single accident (own work)

The following events (nodes) are separated in the model:

M – the event that initiates a single accident process,
A – the working environment,
B – the working process,
C – the specific physical activity performed by the persons injured at the time of the accident
D – the material agent of the specific physical activity performed by the persons injured at the time of the accident,
E – the event that is a deviation from the normal state,
F – the material agent of the event that is a deviation from the normal state,
G – the event that causes an injury,
H – the material agent that is the source of an injury associated with the event that causes the injury,
U – the type of injury,
R – the type of accident.

In order to consider all the circumstances of the course and consequences of an accident, two types of events were proposed in the model:

▸ a real event, which according to the theory of systems causes a change in the state of a system – a construction site (E i G),

▸ an apparent event, which describes the circumstances in which an accident occurred and also its consequences (A, B, C, D, F, H, U, R).

Each individual accident is initiated by an apparent event (M).

3. Description of events in the model

Each node in the model that is shown in Figure 2 can have many different meanings, depending on the type of construction site, location, type of work and equipment used. The individual specific cases are identified by the index included in the letter designation of the node. This index is a numerical code taken from the methodology of the accident course analysis proposed by EUROSTAT. The following nodes indicate:

▸ $A = \{a_i; i = 0.21, 0.22, ..., 0.26, 0.29\}$ – that the place of an accident at work is a construction site and can be, among others: a building being constructed – a_{021}; a building being demolished, repaired or maintained – a_{022} or an opencast quarry, opencast mine, excavation or trench – a_{023}. Moreover, the place of the construction can be located: underground – a_{024}; on/over water – a_{025} or other types of working environments not listed in this group – a_{029}.

▸ $B = \{b_j; j = 21, 22, ..., 25, 29\}$ – the process of work that is carried out by the injured person at the time of accident initiation. The following processes, which are characteristic for the construction industry, were distinguished: excavation – b_{21}; a new construction – building – b_{22}; a new construction – civil engineering, infrastructures, roads, bridges, dams, ports – b_{23}; remodelling, repairs, extensions, building maintenance – all types of constructions – b_{24} or demolition – all types of constructions; other types of working processes not listed in this group – b_{29}.

▸ $C = \{c_k; k = 1, 2, ..., 9\}$ – the specific physical activity performed by the persons injured at the time of the accident, namely: operating a machine – c_1; working with hand-held tools – c_2; driving/being on board a means of transport or handling equipment – c_3; handling of objects – c_4; carrying things by hand – c_5; movement – c_6; presence – c_7 or other specific physical activities not listed in this group – c_9.

▸ $D = \{d_l; l = 00, 01, ..., 20, 99\}$ – the material agent of the specific physical activity performed by the persons injured at the time of the accident. The following material factors can be distinguished for the construction industry: buildings, structures, surfaces – at ground level – d_{01}; buildings, structures, surfaces – above ground level – d_{02}; buildings, structures, surfaces – below ground level – d_{03}; hand tools, not powered – d_{06}; hand-held or hand-guided tools, mechanical – d_{07}; land vehicles – d_{12}; materials, objects, products, machine or vehicle components, debris, dust– d_{14}; bulk waste – d_{19}; physical phenomena and natural elements – d_{20}; other material agents not listed in this group – d_{99} or no material agent – d_{00}.

- $E = \{e_o; o = 0, 1, ..., 9\}$ – the event that is a deviation from the normal state, therefore, an event incompatible with the appropriate conduct of the work process that initiates the occurrence of a dangerous accident. Such an event can be, among others: deviation due to electrical problems, explosions, fire – e_1; breakage, bursting, splitting, slipping, falling, collapsing of a material agent – e_3; loss of control of a machine, means of transport or handling equipment, hand-held tools or objects – e_4; slipping, stumbling and falling, the fall of a person – e_5; other deviations not listed in this group – e_9 or no information – e_0.
- $F = \{f_p; p = 00, 01, ..., 20, 99\}$ – the material agent of the event that is a deviation from the normal state. The classification of material factors overlaps with the list of the factors distinguished in node D.
- $G = \{g_q; q = 0, 1, ..., 9\}$ – the dangerous event that is a consequence of a deviation and causes an injury. The following events were qualified as hazardous: contact with electrical voltage, extreme temperature, hazardous substances – g_1; being drowned, buried or enveloped – g_2; horizontal or vertical impact with or against stationary objects – g_3; being struck by an object in motion, collision – g_4; contact with a sharp, pointed, rough or coarse material agent – g_5; being trapped, crushed – g_6; other event causing an injury not listed in this group – g_9 or no information – g_0.
- $H = \{h_s; s = 00, 01, ..., 20, 99\}$ – the material agent that is the source of an injury associated with the event that causes the injury. The classification of material factors overlaps with the list of the factors distinguished in node D.
- $U = \{u_v; v = 000, 010, ..., 140, 999\}$ – the type of injury caused by contact with a hazardous material agent. The following injuries were distinguished, among others: bone fractures – u_{020}; dislocations, sprains and strains – u_{030}; traumatic amputations – u_{040}; concussion and internal injuries – u_{050}; drowning and asphyxiation – u_{080}; multiple injuries – u_{120}; injury after falling from a height – u_{130}; injury due to backfilling with soil – u_{140} or death of a victim – u_{150}.
- $R = \{r_x; x = 1, 2, 3\}$ – the type of accident. A result of an accident at work can lead to the death of the victim (fatal accident) – r_1; severe body injuries (severe accident) – r_2 or small body injuries (light accident) – r_3.

4. Mathematical description of the model

Every accident begins with an initiating event and runs through specific indirect events that lead to the occurrence of the final event i.e. the type of accident. Based on the analysis of post-accident protocols, it should be noted that every accident follows a separate accident scenario [14]. Graphical illustration of a large number of different scenarios, in the form of a directed graph, is shown in Figure 3.

The directed graph (Y) is defined as an ordered pair of sets N and T, as follows:

$$Y = \langle N, T \rangle, \tag{2}$$

where:

N – is a random non-empty set of vertices and nodes,

T – is a set of possible ordered pairs of adjacent nodes N, which are called directed edges or arcs.
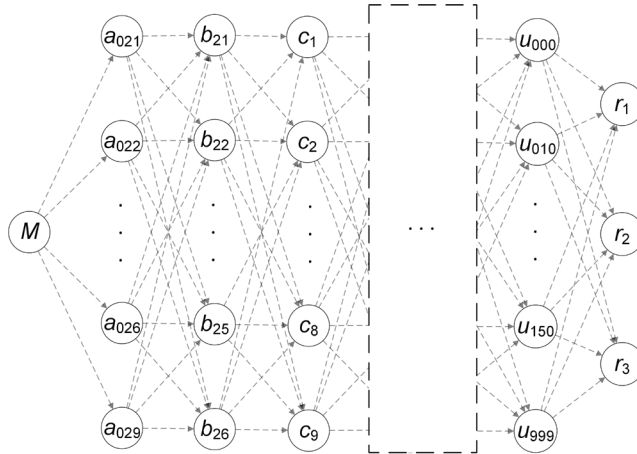

Fig. 3. Model of the development of an accident event in the construction industry (own work)

The N set consists of 11 subsets that include events classified into the specified following groups: $M, A, B, C, D, E, F, G, H, U, R$ each of which contains selected detailed information on the course of an accident:

$$N = M \cup A \cup B \cup C \cup D \cup E \cup F \cup G \cup H \cup U \cup R \tag{3}$$

The T set of the ordered pairs of adjacent N events (nodes) can be written as follows:

$$T = \left\{ (m,a_i)(a_i,b_j),(b_j,c_k),(c_k,d_l),(d_l,\varepsilon_o),(\varepsilon_o,f_p),(f_p,g_q),(g_q,h_s),(h_s,u_\upsilon),(u_\upsilon,r_x) \right\}$$

$$T = \{(M,A),(A,B),(B,C),(C,D),(D,E),(E,F),(F,G),(G,H),(H,U),(U,R)\} \tag{4}$$

For the phenomenon of accidents examined, the sought function is a function describing the course of events in a hypothetical case, for which it is possible to obtain the maximum value of the probability of a particular scenario. The sought objective function can be represented as follows:

$$P(T) = P(M \cap A \cap B \cap C \cap D \cap E \cap F \cap G \cap H \cap U \cap R) \rightarrow \max \tag{5}$$

The probability of the occurrence of scenario $P(T)$ may be presented using the formula of the conditional probability of dependent events [15]:

$$P(T) = P(M \cap A \cap B \cap C \cap D \cap E \cap F \cap G \cap H \cup U \cap R) = \ldots$$
$$= P(R|M \cap A \cap B \cap C \cap D \cap E \cap F \cap G \cap H \cap U) \cdot P(U|M \cap A \cap B \cap C \cap D \cap EF \cap G \cap H) \cdot$$
$$P(H|M \cap A \cap B \cap C \cap D \cap E \cap F \cap G) \cdot P(G|M \cap A \cap B \cap C \cap D \cap E \cap F) \cdot \tag{6}$$
$$P(F|M \cap A \cap B \cap C \cap D \cap E) \cdot P(E|M \cap A \cap B \cap C \cap D) \cdot$$
$$P(D|M \cap A \cap B \cap C) \cdot P(C|M \cap A \cap B) \cdot P(B|M \cap A) \cdot P(A|M)$$

5. Test results obtained on the basis of accident analysis

An accident process that consists of 350 accidents at work, which happened in the Polish construction industry in the years 2008–2014, was simulated. The study involved accidents that happened in 4 Polish provinces: Lower Silesia, Kujawsko-Pomorskie, Lubelskie and Lubuskie. Post-accident protocols, obtained from branches of the State Labour Inspectorate, were the source of information on accidents. The investigated accidents happened during the erection of new buildings and also renovation works.

Table 1 shows part of the matrix of the relations between successive nodes A and B, and C, and Figure 4 presents the course of the most often occurring accident processes. Each scenario shows the specified path in the graph, which begins in node M and ends in node R. Each node is described by: sign, numerical code, number of events. The numbers included on the arches define multiplicity of the transition in the path.

Table 1. Part of the matrix of the relations between nodes

	b_{21}	b_{22}	b_{23}	b_{24}	b_{25}		c_1	c_2	c_3	c_4	c_5	c_6	c_7
a_{021}	17	**148**	37	–	–	b_{21}	–	6	1	1	3	6	1
a_{022}	–	–	–	126	15	b_{22}	3	21	1	43	24	**55**	1
a_{024}	1	–	–	3	–	b_{23}	4	7	–	9	4	11	3
a_{025}	–	–	1	2	–	b_{24}	2	29	4	31	7	54	4
						b_{25}	1	8	–	5	1	–	–

The following conclusions can be drawn on the basis of the results of the simulation of the process that consisted of 350 accidents at work in the construction industry:
- ▸ 202 cases of accidents at work, which were assigned to the construction sector, occurred during the construction of new buildings (a_{021}), while 141 cases occurred during the renovation and demolition of existing building objects (a_{022}),
- ▸ the process that causes the most accidents and is performed during the initiation of an accident is the construction of new buildings (b_{22}); there were 148 such situations identified. 131 accidents happened during the rebuilding, repair, extension and maintenance of building objects (b_{24}), and 38 during the construction of infrastructure facilities (b_{23}),
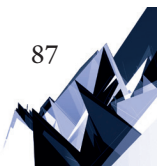
- accidents occurred most commonly during the movement of an employee along a flat area, ascending or descending to another level, entering or leaving other spaces and also during jumping or moving (c_6); there were 126 such reported cases. In 89 cases, the handling of objects (c_4) was the activity that was performed by the victim and in 71 cases the work involved the use of hand tools (c_2),
- the largest group of material factors related to accidents in the construction industry, which was identified in 176 cases, consisted of buildings, structures and their components above ground level (d_{02}), including among other things: roofs of buildings, stationary or mobile scaffolding and also work platforms or ladders; another often identified material factor was heavy transport vehicles (d_{12}), which was seen in 39 cases,
- the most common events that are incompatible with the appropriate course of the work process include slipping, stumbling or the falling of a person (e_5), which was recorded in 149 cases, and also the damage, bursting, breaking off, slipping, falling and collapsing of a material factor (e_3), which occurred in 118 cases,
- the falling of a victim from a height and from buildings or structures located above ground level (f_{02}) occurred in 136 accidents,
- the most common event that caused injury was a collision with an immovable object (g_3); such events were reported in 204 cases, out of which the hitting a horizontal surface located at ground level (h_{01}) occurred in 173 cases,
- 141 analysed cases were followed by the death of a victim (r_1); serious injuries happened in 201 cases (r_2), and light injuries in 8 cases (r_3).
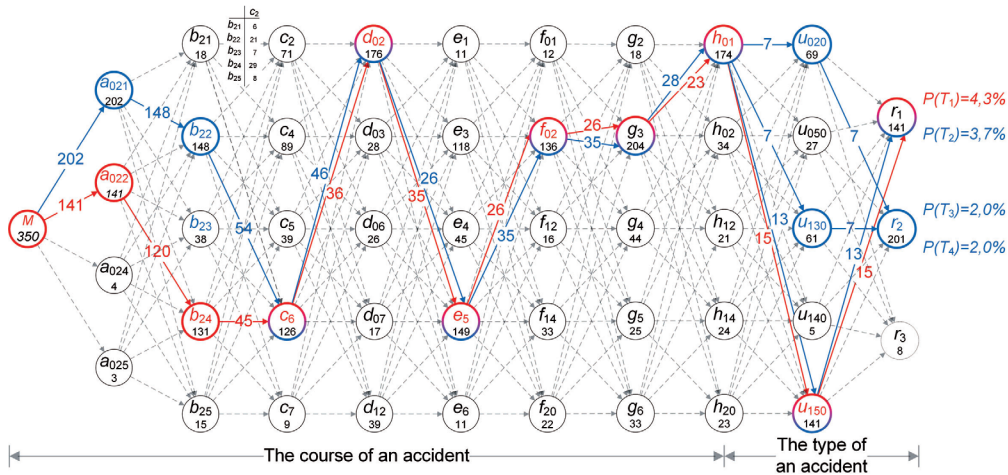
Fig. 4. The course of the most often occurring accident processes (own work)

Figure 4 shows that the following scenario has the highest probability: an accident occurring in buildings that are being dismantled, demolished, or renovated (a_{022}) during their rebuilding, repair, expansion or maintenance (b_{24}) and while there is movement of an employee (c_6) along surfaces that are at a height above ground level (d_2). During this operation a person slips, trips or falls (e_5) on elements of a building or structure that are located on

a lower level, but above ground level (f_{02}). The falling is followed by a vertical collision with a stationary object or by hitting an immovable object (g_3) that is located at ground level (h_{01}). The most common type of injury, which results from these events, was the death of a victim (u_{150}), i.e. a fatal accident (r_1). For the 350 analysed accidents at work, the probability of such a scenario, which is marked in red in Figure 4, is equal to 4.3%. The course of the subsequent scenarios with the highest probability of the occurrence of scenario is marked in blue.

6. Summary

The paper presents a mathematical and graphical model in the form of a directed graph of the development of an accident event in the construction industry. Each path in the graph represents a possible course of a single accident. The course of a single accident consists of a sequence of apparent and real events that identify the circumstances, causes and consequences of the accident. The simulation of a process that consists of 350 accidents was carried out using the computer model constructed. The model makes use of a database containing data of accidents at work in the construction industry.

References

[1] International Labour Organization, *Safety and Health at Work: A Vision for Sustainable Prevention*, XX World Congress on Safety and Health at Work 2014, Global Forum for Prevention, 24–27 August, Frankfurt 2014, Germany.

[2] Główny Urząd Statystyczny, *Wypadki przy pracy w 2015 r. Informacje i Opracowania Statystyczne*, Warszawa 2016.

[3] Drozd W., *Charakterystyka terenu budowy w aspekcie zagrożeń bezpieczeństwa pracy*, Czasopismo Inżynierii Lądowej, „Środowiska i Architektury", Vol. XXXIII, Issue 63 (1/I/16), 2016, 165–172.

[4] Hoła B., Szóstak M., *Analysis of the State of the Accident Rate in the Construction Industry in European Union Countries*, Archives of Civil Engineering, Vol. 1, Issue 4, 2015, 19–34.

[5] Khan F., Rathnayaka S., Ahmed S., *Methods and models in process safety and risk management Past, present and future*, Process Safety and Environmental Protection, Vol. 98, 2015, 116–147.

[6] Wu W. Yang, H. Li Q., Chew D., *An integrated information management model for proactive prevention of struck-by-falling-object accidents on construction sites*, Automation in Construction, Vol. 34, 2013, 67–74.

[7] Camino López M.A., Ritzel D.O., Fontaneda I. Gonzales, Alcantara O.J., *Construction industry accidents in Spain*, Journal of Safety Research, Vol. 39, 2008, 497–507.

[8] Pérez-Alonso J., Callejón-Ferre A.J., Carreño-Ortega A., Sánchez-Hermosilla J., *Approach to the evaluation of the thermal work environment in the greenhouse-construction industry of SE Spain*, Building and Environment, Vol. 46, 2011, 1725–1734.

[9] López Arquillos, Rubio Romero J.C., Gibb A., *Analysis of construction accidents in Spain, 2003–2008*, Journal of Safety Research, Vol. 43, Issue 5–6, 2012, 81–388.

[10] Lin Y.H., Chen C.Y., Wang T.W., *Fatal occupational falls in the Taiwan construction industry*, Journal of the Chinese Institute of Industrial Engineers, Vol. 28, No. 8, 2011, 586–596.

[11] Chi S., Han S., *Analyses of systems theory for construction accident prevention with specific reference to OSHA accident reports*, „International Journal of Project Management", Vol. 31, Issue 7, 2013, 1027–1041.

[12] I. M. Razwanul I., Tarek M., *Safety Practices and Causes of Fatality in Building Construction Projects: A Case Study for Bangladesh*, "Jordan Journal of Civil Engineering", 11(2), 2017.

[13] Eurostat European Commission, *European Statistics on Accident at Work (ESAW). Summary methodology*, Eurostat Methodologies & Working papers, 2013.

[14] Hoła B., Szóstak M., *Analysis of the Development of Accident Situations in the Construction Industry*, Procedia Engineering, Vol. 91, 2014, 429–434.

[15] Hebda A., *Metoda techniczno-ekonomicznej oceny składników oraz uciążliwości ryzyka wystąpienia wypadków przy pracy w kopalniach węgla kamiennego*, Uczelniane Wydawnictwa Naukowo-Dydaktyczne, Kraków 2005.

Krystyna Kuźniar

Institute of Technology, Pedagogical University of Cracow

Tadeusz Tatara (ttatara@pk.edu.pl)

Institute of Structural Mechanics, Cracow University of Technology

ASSESSMENT OF THE INFLUENCE OF EPICENTRAL DISTANCE OF MINING SHOCKS ON THE TRANSITION OF FREE-FIELD VIBRATIONS TO BUILDING FOUNDATIONS

OCENA WPŁYWU ODLEGŁOŚCI EPICENTRALNEJ WSTRZĄSU GÓRNICZEGO NA PRZEKAZYWANIE DRGAŃ Z PODŁOŻA NA BUDYNEK

Abstract

The paper deals with the analysis of measurements of vibrations induced by mining rockbursts in the Legnica–Glogow Copperfield District (LGCD) to estimate the influence of mining tremor epicentral distance on the curve of relationship (*RRS*) between the response spectra from the simultaneously measured ground and building foundations vibrations. Non-dimension acceleration response spectra (β) as well as dimension acceleration response spectra (S_a) from the horizontal vibrations were taken into account. The focus is on apartment buildings – medium-rise and high-rise buildings. Additionally, a comparison of conclusions of research carried out in the case of response spectra with the corresponding earlier results regarding the reduction of maximum values of accelerations of vibrations during the transfer from the ground to building foundations were performed.

Keywords: mining tremors, epicentral distance, response spectra, ground vibrations, foundation vibrations, transmission of vibrations, apartment building

Streszczenie

W pracy dokonano analizy wyników pomiarów drgań górniczych w Legnicko-Głogowskim Okręgu Miedziowym (LGOM) w celu oceny wpływu odległości epicentralnej wstrząsu górniczego na postać krzywej relacji (*RRS*) spektrum odpowiedzi od drgań gruntu i spektrum odpowiedzi od jednocześnie mierzonych drgań fundamentu budynku. Pod uwagę wzięto bezwymiarowe przyśpieszeniowe spektra odpowiedzi (β) i odpowiednie spektra wymiarowe (S_a) policzone na podstawie drgań poziomych. Skupiono się na budynkach mieszkalnych – budynku średniej wysokości i budynku wysokim. Dodatkowo dokonano porównania wniosków z badań przeprowadzonych w przypadku spektrów odpowiedzi, z wcześniejszymi wynikami uzyskanymi w odniesieniu do redukcji maksymalnych wartości przyśpieszeń drgań przy ich przekazywaniu z gruntu na fundamenty budynków.

Słowa kluczowe: wstrząsy górnicze, odległość epicentralna, spektra odpowiedzi, drgania gruntu, drgania fundamentu, przekazywanie drgań, budynek mieszkalny

1. Introduction

Underground mining exploitation can result in randomly occurring mining shocks. This type of free-field vibration is a kinematic forcing for surface structures, and the vibrations are classified as so-called paraseismic vibrations. Mining-related vibrations stand out among the greatest intensity of paraseismic vibrations. It is therefore essential to assess the impact of this type of vibration on buildings.

During the transition of vibrations from the free-field to the building there is the phenomenon so-called dynamic soil-structure interaction. Simultaneously occurring free-field and building foundation vibrations may vary substantially [4, 8, 11, 12, 15]. It should be appreciated that the foundation vibrations allow for more accurate assessment of the harmfulness of vibrations to buildings than free-field vibrations [10]. Therefore it is particularly significant and important in practice to assess the vibrations transition to the foundations of the structure.

A simple and often used method for assessing the transition of free-field vibrations to the building foundation is to compare the maximum values of the vibrations of the building foundation and the ground next to the building recorded at the same time [2, 9, 14]. Analysis of the results of measurements of vibrations caused by mining tremors in respect to the reduction of the maximum value of the horizontal components of acceleration and velocity at their transition from free-field to the foundation of the building leads to the conclusion that the size of this reduction is a function of many variables: the mining shock energy, epicentral distance, the direction of wave propagation, maximum value of ground vibrations, vibration direction (parallel to the longitudinal or transverse axis of the building), and the dominant frequency of vibrations of the ground next to the building [5–7, 9].

In this study we focused on assessing the impact of epicentral distance of mining shocks on a curve of relationship (ratio) of response spectrum from the vibrations of the building foundation and the response spectrum from simultaneously measured free-field vibrations (*RRS – Ratio of Response Spectra*). Dimensionless acceleration response spectra from horizontal vibrations (β) and dimensional spectra (S_a) were taken into account, calculating on the basis of them the respective relationships $RRS(\beta)$ and $RRS(S_a)$. The influence of the type of building on relationships $RRS(\beta)$ and $RRS(S_a)$ was also analysed in the subsequent ranges of epicentral distances.

Additionally, a comparison of the conclusions from studies using response spectra with previous results [9] obtained in relation to the reduction of the maximum values for vibration acceleration at the transition from free-field to the building foundations was performed.

It is worth mentioning that the use of response spectra and their relationships *RRS* for studying the differences in the simultaneously recorded free-field vibrations and building foundation is a more advanced approach in the analysis of the dynamic soil-structure interaction than the use the maximum values of vibrations for this purpose [3, 4, 8, 12, 13].

2. Experimental studies – scope of the analysis

The source of vibration was mining shocks originating from underground exploitation in the Legnica–Głogow Copper District (LGCD). Only records induced by rockbursts with energy higher than 10^6 J and horizontal components of peak ground accelerations larger than 10 cm/s² were analysed. The epicentral distances of the mining shocks considered are in the range $re = 270 - 5839$ m.

The differences between simultaneously occurring free-field vibrations next to the building and its foundation for residential buildings: the medium-rise building S (5-storey) and high-rise building W (12-storey), were analysed. These are prefabricated structures. Building S is constructed using the large-block system and building W is erected as a large panel structure. Both buildings have basements, foundations in the form of continuous footings and they are located close together under one housing estate.

The natural fundamental frequency f_1 experimentally determined in horizontal directions of the building S is equal 2.9–3.3 Hz in a direction parallel to the transverse axis (x) and 2.9–3.1 Hz in a direction parallel to the longitudinal axis (y). On the other hand, in building W the natural fundamental frequency f_1 experimentally determined in horizontal directions is equal 1.44–1.50 Hz in a direction parallel to the axis (x), and 2.06–2.17 Hz in a direction parallel to the longitudinal axis (y) [12].

Acceleration records of free-field vibrations next to the building and on the building foundation were measured simultaneously using the so-called "armed partition" accelerometers for each of the mining shocks considered. Accelerometers on the ground were placed a few metres away from a building.

The focus is on the horizontal components of vibration accelerations, respectively parallel to the transverse axis (x) and longitudinal (y) of each of the buildings.

Both dimensionless spectra β and dimensional spectra S_a were calculated on the basis of assumed free-field and building foundation acceleration vibrations. An averaged fraction of critical damping equalling about 3% was adopted in the calculations according to dynamic experimental investigations presented in [1].

The number of analysed pairs (free-field – building foundation) of acceleration response spectra ($β$ and S_a) in the successive ranges of epicentral distances are listed in Table 1.

Table 1. Summary of the number of analysed pairs (free-field – building foundation) of response spectra ($β$ and S_a) in the successive ranges of epicentral distances

re [m]	Building S		Building W	
	β	S_a	β	S_a
to 500	2	2	3	3
501–800	26	29	11	12
801–1100	22	28	44	51
1101–1700	25	27	17	23
1701–2500	34	44	24	41
over 2501	44	60	25	47
whole range	153	190	124	177
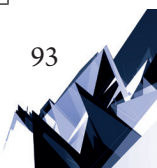
3. The influence of epicentral distances of mining tremors on the transition of free-field vibrations to the building foundations

Dimensionless acceleration response spectra (β) from horizontal vibrations and the corresponding dimensional spectra (S_a) calculated using simultaneously recorded free-filed vibrations next to the building and the building foundation were used to try to assess the impact of epicental distances of mining tremors on the transition of free-field vibrations to the building foundations.

The pairs of response spectra (free-field – building foundation) thus determined were used for calculation using the formula (1) the relationship (ratio) $RRS(\beta)$ for the dimensionless acceleration response spectra (β), and a calculation using the formula (2) the relationship (ratio) $RRS(S_a)$ in the case of dimensional acceleration response spectra (S_a).

$$RRS(\beta) = \frac{\beta_f}{\beta_g} \tag{1}$$

$$RRS(S_a) = \frac{S_{af}}{S_{ag}} \tag{2}$$

where:

$RRS(\beta), RRS(S_a)$	– relationship (ratio) describing the transition of response spectra from the free-field to the building foundation in the case of dimensionless and dimensional acceleration response spectra respectively,
β_f, S_{af}	– respectively dimensionless and dimensional acceleration response spectrum originating from the building foundation vibrations,
β_g, S_{ag}	– respectively dimensionless and dimensional acceleration response spectrum obtained on the basis of free-field vibrations next to the building.

Separately, for building S and W, each of the relationships $RRS(\beta)$ and $RRS(S_a)$ defined for each of the considered mining shocks are placed into one of six groups. The criterion for assigning RRS relation to the group was the epicentral distance of the mining shock. Successive ranges of epicentral distances which correspond to the established relationship groups RRS are given in Table 1.

Averaged relationships were determined in each set of relationships $RRS(\beta)$ and $RRS(S_a)$. They corresponded to the range of epicentral distances. Furthermore, averaged relationships $RRS(\beta)$ and $RRS(S_a)$ were also calculated in the whole range of epicentral distances of the mining shocks, both in the case of building S and building W.

Referring to the building S, Fig. 1 shows relationships $RRS(\beta)$ and $RRS(S_a)$ averaged in intervals of epicentral distances of the mining shocks. Analogous curves designated for the building W are given in Fig. 2.

Additionally, Table 2 shows the values $RRS(\beta)$ and $RRS(S_a)$ averaged within the adopted ranges of epicentral distances corresponding to mean values of the natural fundamental frequency f_1 in the x and y directions of building S and building W.
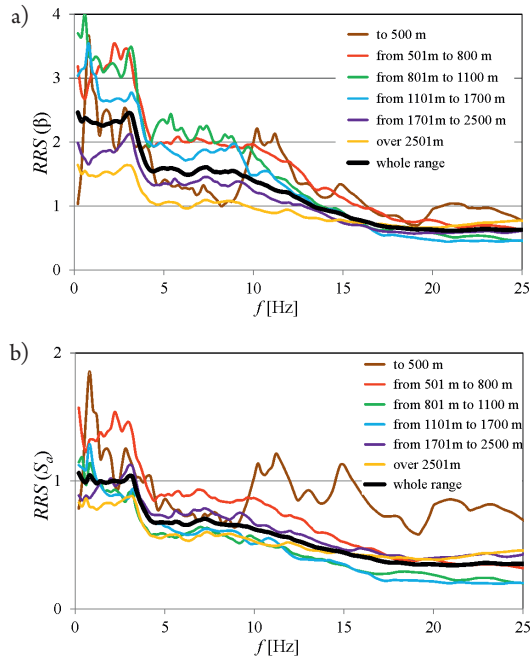
Fig. 1. Relations *RRS* averaged in the ranges of mining tremors epicentral distances – building *S*:
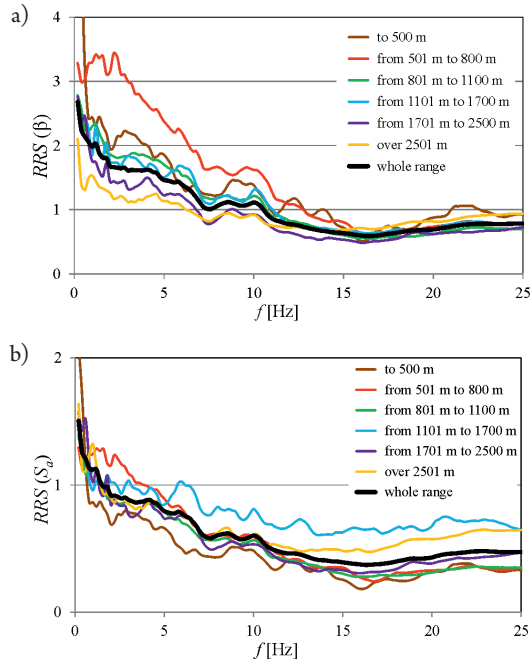a) *RRS*(β); b) *RRS*(*S*$_a$)

Fig. 2. Relations *RRS* averaged in the ranges of mining tremors epicentral distances – building *W*:
a) *RRS*(β); b) *RRS*(*S*$_a$)

In Fig. 1 and Fig. 2 significant differences in the curves $RRS(\beta)$ and $RRS(S_a)$ which were obtained by averaging of the collections referring to individual ranges of epicentral distances, are visible. In addition, the graphs RRS made for the epicentral distance ranges are clearly distinguishable from charts averaged over the range of distances. These applications relate to the transition of vibrations from the free-field to the foundations of the building S and the building W.

Table 2. Values of $RRS(\beta)$ and $RRS(S_a)$ corresponding to the frequencies of natural vibrations f1 of S and W buildings, averaged in the successive ranges of epicentral distances

re [m]	Building S $- f_1 = 3$ Hz		Building W $- f_1 = 1.8$ Hz	
	$RRS(\beta)$	$RRS(S_a)$	$RRS(\beta)$	$RRS(S_a)$
to 500	2.41	1.19	2.18	0.77
501–800	3.45	1.46	3.11	1.17
801–1100	3.41	0.91	1.89	0.90
1101–1700	2.68	0.87	2.05	1.08
1701–2500	2.11	1.12	1.72	1.07
over 2501	1.64	0.88	1.30	0.93
whole range	2.45	1.04	1.80	0.98

In the case of curves $RRS(\beta)$ and $RRS(S_a)$ relating to building S as well as in the case of $RRS(\beta)$ referring to building W, these differences are especially evident at frequencies important from a practical point of view, namely in the relatively low frequency range (to approx. 10 Hz).

Both in the case of building S and building W, in ordinates of relationship RRS referring to the dimensionless acceleration response spectra (β), there are bigger differences in the individual ranges of epicentral distance than in the same relationship RRS based on dimensional acceleration response spectra (S_a).

Substantial differences may occur in the values (ordinates) $RRS(\beta)$ and $RRS(S_a)$ corresponding to the natural fundamental frequencies of the buildings, calculated in the individual ranges of epicentral distances. This is evident in Table 2. For example, both in the case of building S and building W, the value $RRS(\beta)$ in the range of epicentral distances within 501–800 m is approximately twice as high as that calculated for epicentral distances within the range over 2.501 meters. However, the differences in the RRS values corresponding to the natural fundamental frequencies of the buildings from the individual intervals of epicentral distances, in relation to the values RRS averaged over the range of epicentral distances, reach tens of percent (building S: $RRS(\beta)$ – approx. 30%, $RRS(S_a)$ – approx. 40%; building W: $RRS(\beta)$ – approx. 70%, $RRS(S_a)$ – approx. 20%).

In addition, the relationships $RRS(\beta)$ averaged in the dedicated ranges of epicentral distances of mining shocks (the whole range, from 501 m to 800 m, from 801 m to 1100 m, from 1101 m to 1700 m, from 1701 m to 2500 m and over 2501 m) in the case of the medium-rise building S and the high-rise building W, are compared in Fig. 3. The same comparison referring to the relationship $RRS(S_a)$ is made in Fig. 4.

Practically, in most of the individual ranges of epicentral distances a significant dependence of differences in the relationship $RRS(\beta)$ referring to the different building construction of buildings S and W against epicentral distance is not seen. However, in some ranges of the epicentral distances such a relationship can be seen, for example from 801 m to 1100 m and 1101 m to 1700 m.

In general, in the case of curves $RRS(S_a)$ this dependence is much less clear than for the $RRS(\beta)$. The differences are relatively small. An exception here may be ranges from 501 m to 800 m and from 1101 m to 1700 m.

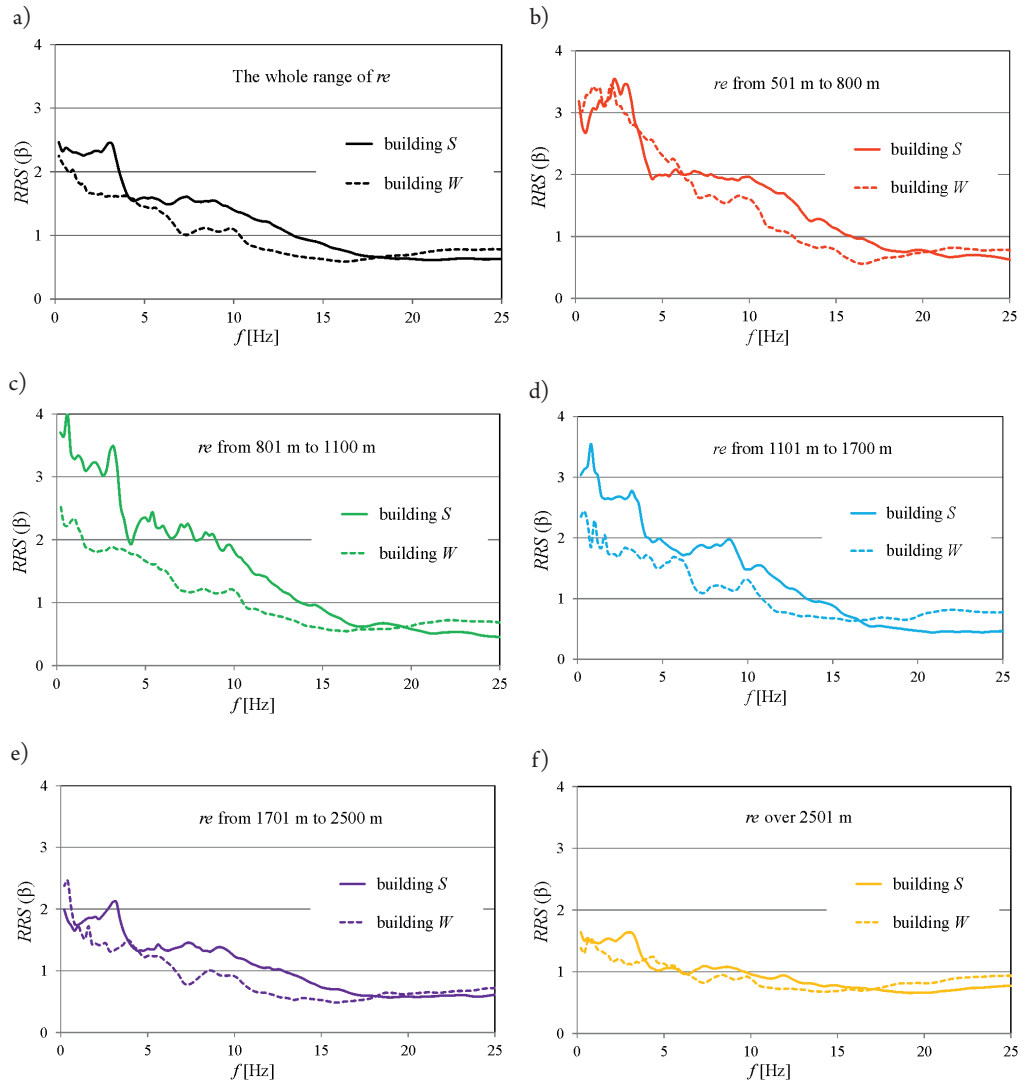Fig. 3. Buildings S and W – relations $RRS(\beta)$ averaged in the ranges of mining tremors epicentral distances: a) the whole range; b) from 501 m to 800 m; c) from 801 m to 1100 m; d) from 1101 m to 1700 m; e) from 1701 m to 2500 m; f) over 2501 m

Fig. 4. Buildings *S* and *W* – relations $RRS(S_a)$ averaged in the ranges of mining tremors epicentral distances: a) the whole range; b) from 501 m to 800 m; c) from 801 m to 1100 m; d) from 1101 m to 1700 m; e) from 1701 m to 2500 m; f) over 2501 m
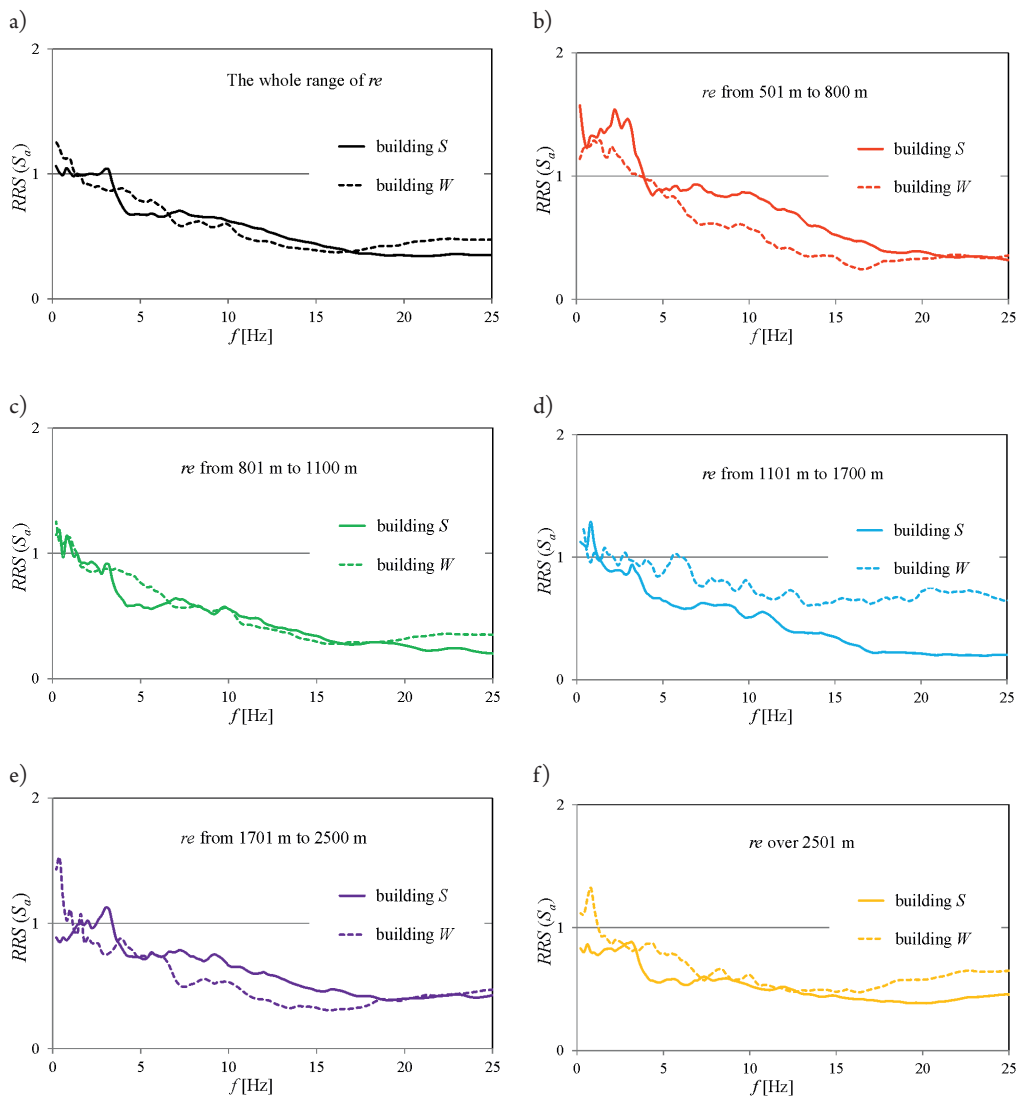
It is interesting to compare the results of the analysis of the influence of the epicentral distance on the relations *RRS* of response spectra from both the measured vibrations of the free-field and the building foundations with similar studies referring the different way of evaluating the transition of vibrations from ground to the building foundation. This way corresponds to reducing the maximum value of vibration acceleration in transition from free-field on the building foundations. This approach was used to elaborate measurements of vibrations in LGCD and presented in paper [9].
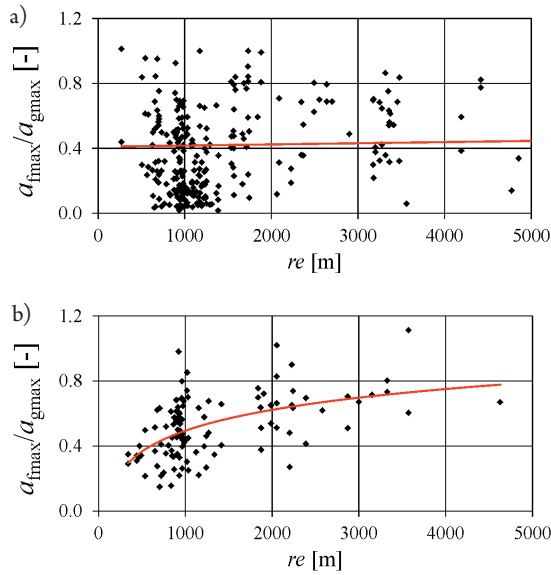
Fig. 5. Ratios a_{fmax}/a_{gmax} versus epicentral distances (re) in the case of buildings: a) S; b) W

Fig. 5 shows the fractions a_{fmax}/a_{gmax} (a_{fmax}, a_{gmax} – maximum value of the foundation and ground vibration acceleration, respectively) versus epicentral distance (re) in the case of medium-rise building S (Fig. 5a) and high-rise building W (Fig. 5b). While it may be found the growth in the values of those fractions with an increase in epicentral distances in the relation to the high-rise building W, in the case of the medium-rise building S the range of fractions a_{fmax}/a_{gmax} in successive ranges of epicentral distances is similar. This is confirmed by the trend lines shown in Fig. 5. Thus, it is different than in the relationship RRS in which this dependence of curves $RRS(\beta)$ and $RRS(Sa)$ on epicentral distances is clearly visible.

4. Conclusions

Analyses show that the epicentral distance of mining shocks can have a significant impact on the transmission of response spectra from the free-field to the foundations of medium-rise and high-rise buildings. This effect is more visible in the case of curves $RRS(\beta)$ determined using dimensionless acceleration response spectra β than in the case of curves $RRS(S_a)$ calculated for corresponding pairs of dimensional spectra Sa. No significant effect of the type of building structure on the differences in the relationship $RRS(\beta)$ and $RRS(S_a)$ in the individual ranges of epicentral distance is observed. Taking into account the epicentral distance of mining shock in assessing the transmission of the free-field vibrations to the building foundations has a much greater impact on the outcome of this assessment in the examination of relationships' appropriate response spectra than the maximum value of vibration acceleration.

References

[1] Ciesielski R., Kuźniar K., Maciag E., Tatara T., *Damping of vibration in precast buildings with bearing concrete walls*, "Archives of Civil Engineering", 41(3)/1995, 329–341.

[2] Ciesielski R., Maciąg E., *Drgania drogowe i ich wpływ na budynki*, Wydawnictwa Komunikacji i Łączności, Warszawa 1990.

[3] FEMA 440, *Improvement of Nonlinear Static Seismic Analysis Procedures,* ATC-55 Project, 2005.

[4] Kim S., Stewart J.P., *Kinematic soil-structure interaction from strong motion recordings*, "Journal Geotechnical and Geoenvironmental Engineering" 129(4)/2003, 323–335.

[5] Kuźniar K., *Sieci neuronowe w analizie drgań budynków wywołanych wstrząsami parasejsmicznymi i sejsmicznymi*, Wydawnictwo Politechniki Krakowskiej, Kraków 2013.

[6] Kuźniar K., Chudyba Ł., *Ocena wpływu wybranych parametrów wstrząsów górniczych i drgań gruntu na przekazywanie drgań z podłoża na budynek*, [In:] *Aktualne problemy wpływów sejsmicznych i parasejsmicznych na budowle*, Vol. II: *Badania wstrząsów górniczych i drgań komunikacyjnych*, ed. K. Stypuła, Monografia 477/2, Wydawnictwo Politechniki Krakowskiej, Kraków 2015, 23–37.

[7] Kuźniar K., Maciąg E., *Wpływ parametrów wstrząsów górniczych na interakcję dynamiczną grunt-budynek,* "Zeszyty Naukowe Politechniki Rzeszowskiej Budownictwo i Inżynieria Środowiska", 243(45)/2007, 113–123.

[8] Kuźniar K., Maciąg E., Tatara T., *Acceleration response spectra from mining tremors*, First European Conference on Earthquake Engineering and Seismology (ECEES), Geneva 2006, Switzerland, Abstract Book, 466–467 (full paper on CD).

[9] Kuźniar K., Tatara T., *Przekazywanie drgań od wstrząsów górniczych z gruntu na fundamenty budynków różnego typu*, "Przegląd Górniczy", 6/2014, 30–34.

[10] Maciąg E., *Ocena szkodliwości wstrząsów górniczych dla budynków na podstawie drgań ich fundamentów czy gruntu?*, "Inżynieria i Budownictwo", 12/ 2005, 670–677.

[11] Maciąg E., *Interakcja układu budynek-podłoże gruntowe w świetle doświadczalnego badania drgań parasejsmicznych,* "Inżynieria Morska i Geotechnika", 4/2006, 240–250.

[12] Maciag E. Kuźniar K., Tatara T., *Response Spectra of the Ground Motion and Building Foundation Vibrations Excited by Rockbursts in the LGC Region*, "Earthquake Spectra", 32(3)/2016, 1769–1791.

[13] NIST GCR 12-917-21, *Soil-Structure Interaction for Building Structures*, prepared by NEHRP Consultants Joint Venture (a partnership of the Applied Technology Council and the Consortium of Universities for Research in Earthquake Engineering), 2012.

[14] Stypuła K., *Drgania mechaniczne wywołane eksploatacją metra płytkiego i ich wpływ na budynki*, "Zeszyty Naukowe Politechniki Krakowskiej", seria Inżynieria Lądowa, 72, Kraków 2001.

[15] Tatara T., *Odporność dynamiczna obiektów budowlanych w warunkach wstrząsów górniczych*, Wydawnictwo Politechniki Krakowskiej, Kraków 2012.

Krystian Czernek

Małgorzata Płaczek (m.placzek@po.opole.pl)
Department of Process Engineering, Faculty of Mechanical Engineering,
Opole University of Technology

Hydrodynamics of two-phase flow in tubular reactor

Hydrodynamika przepływu dwufazowego w reaktorze rurowym

Abstract

In the paper, the possibility of using an optoelectronic system for measuring the parameters relating to the hydrodynamics of liquid film in two-phase flow of highly viscous liquids and gas was evaluated. The methodology of the measurement and experimental results in relation to the annular co-current air–oil falling flow was given.

Keywords: two-phase flow, flow pattern, optoelectronic measurement system

Streszczenie

W pracy dokonano oceny możliwości wykorzystania układu optoelektronicznego do pomiaru wielkości opisujących hydrodynamikę filmu cieczy przy dwufazowym przepływie cieczy bardzo lepkiej i gazu. Podano metodykę prowadzenia pomiarów oraz ich wyniki w odniesieniu do współprądowego opadającego przepływu pierścieniowego powietrze–olej.

Słowa kluczowe: przepływ dwufazowy, struktury przepływu, optoelektroniczny układ pomiarowy

1. Introduction

The reports available on that subject matter contain a few papers related to the dynamics of the annular two-phase flow of gas and liquid with very-high viscosity. Most of the scientific papers cover the flow of low-viscosity-liquids: Andritsos et al. [1], Czernek [2–4], Czernek et al. [5], Du et al. [6], Patnaik et al. [7], Troniewski et al. [8], Witczak et al. [9], with viscosity specifications comparable to that of water. The calculation models, which have been developed so far, and which describe flow conditions in a thin film of a viscous liquid, have been seldom verified for liquids with the coefficient of dynamic viscosity higher than 100 mPa·s. Hence, it may be risky to employ them for high-viscosity liquids and it may yield incorrect findings.

High-viscosity liquids and two-phase flows can be found frequently in the process equipment of the chemical and petrochemical industry, in static falling film evaporators, in thin film evaporators, in fractional distillation columns and in heterogeneous flow reactors. Moreover, the viscosity of a liquid quite often increases when the liquid passes through such pieces of process equipment due to chemical reactions, which take place in two-phase systems.

The basic condition, which is decisive for the proper operation of thin film equipment, is the formation of a thin film of liquid over the whole length of the process equipment. The minimum thickness of that film then has to be maintained during the whole process. The available literature data show that in most cases the thin film of a liquid is formed in thin film equipment by mechanical means or by gravity, which makes it very hard to maintain its thickness uniform when it travels through the equipment and to keep the equipment surface completely wet over its whole length.

The latest design configurations for the distribution of liquid on the tubular surface inside the equipment, which displace the gravitational and mechanical methods, make it possible to provide thin and stable liquid films through controlled hydraulics. Liquid and gaseous feeds are charged to a pipe at the same time, and their velocities are adjusted to give the annular flow. This procedure [2, 7, 8] makes it possible to employ multi-pipe shell-tube equipment for heat and mass transfer processes, and to obtain much higher efficiency figures than the ones available for traditional design equipment.

2. Dynamics of annular two-phase gas-high viscous liquid flow

In order to determine the flow phenomena, which take place in co-current downward annular flow of gas and very-high viscosity liquid, a test stand was built in which the waving performance of such a flow can be evaluated.

The scheme of the experimental stand for the tests on the flow of two-phase mixtures has been presented in Figure 1.

Compressed air was supplied to the stand. It passed through the pressure reducing valve 15, and its velocity was controlled by a battery of air flow meters 1. The pressure reducing valve maintained the stable pressure in the system, hence preventing fluctuations of set-points of rotameters. The air stream was then routed to the feeding system 3, of a central
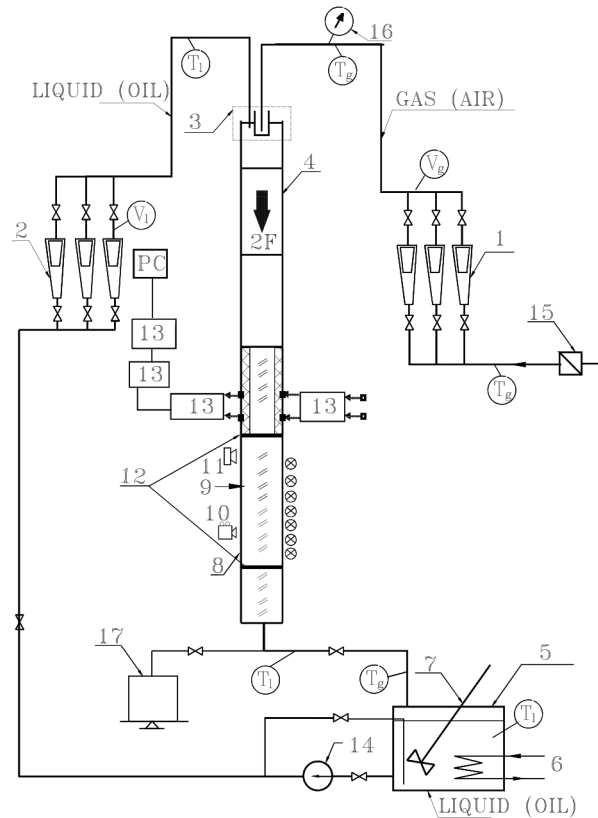
Fig. 1. Scheme of stand: 1 – rotameter of air, 2 – rotameter of oil, 3 – feeding chamber (central jet),
4 – measuring channel, 5 – oil tank, 6 – heater, 7 – mixer, 8 – transparent section of measuring channel,
9 – registration of flow, 10 – registration of video, 11 – photographic registration, 12 – cut of valve,
13 – system of optoelectronic sensor, 14 – pump, 15 – reductive valve, 16 – manometer of air,
17 – laboratory weight, T – measurement of temperature, V – measurement of stream flow

nozzle design. Air temperature was measured upstream of the stand, at the location of T_p, and manometer 16 was used to measure air pressure in the stand. There was oil placed in the vessel 5.

The vessel was equipped with the agitator 7 and 8 kW heaters 6 with a thermostat in order to maintain the required temperature level. The agitator provided uniform distribution of temperature in the oil volume. Oil was pumped to the stand by a gear pump 14, driven by a DC motor. That type of drive made it possible to smoothly adjust the pump's rotational speed, and to preliminarily control the oil flow rate in the stand in this way. The pump forced oil through the battery of oil flow meters 2, where the required flow rate of this component of the mixture was adjusted precisely. From the battery of rotameters, oil was routed to the feeding chamber 3, where the two-phase mixture was prepared, and namely its annular flow was organised. The two-phase mixture then went through the non-transparent part of measuring passage 4; its length was satisfactory in order to obtain and to stabilise the annular flow over the measuring section

of the stand. The optoelectronic sensors 13, connected to a PC equipped with a data storage and processing card, were used to measure the local thickness of liquid films and to determine the character of their waving. From the non-transparent section of the measuring passage, the mixture entered the measuring passage made of plexiglass 8, with ball valves 12 installed at its inlet and outlet to form the so-called trap. The transparent section of the passage was intended for visual observations 9 of the flowing forms, and these could be additionally recorded by means of a digital video camera 10 and photo-camera 11. After leaving the stand, the mixture was transferred to a vessel where it was separated into air (released to atmosphere) and oil. When the valves 12 were closed, oil trapped in the transparent section of the pipe went down and was collected in its bottom part. Oil volume could be measured that way, which made it possible to establish volume fractions for the components in the flowing two-phase mixture. These were then utilised to calculate the average liquid film thickness values.

The measuring system as presented above allowed for conducting the research under adiabatic conditions, i.e. at constant temperature over the length of the measuring passage.

The measuring system was designed and constructed, and working media were selected to enable measurements of a number of quantities, which are specific for the flow of gas-liquid mixtures going co-currently down the vertical pipes. Air and oil were used as working media to test the performance of a two-phase mixture. In order to be able to change the oil viscosity parameter over a wide range, the flow hydrodynamics was tested over the temperature range of 0–50°C, which offered the values of $\eta_l = (0.055-1.517)$ Pa·s for the oil component (Newtonian liquid). In order to give consideration to the effects of air and oil streams on the nature of the liquid films formed, the tests covered a wide scope of superficial velocities of both phases, i.e. $w_{g,0} = (0-29.8)$ m/s for air and $w_{l,0} = (0.0007-0.25)$ m/s for oil. Variability of phase streams was selected to obtain both laminar and turbulent flows of the gas phase at laminar flow of the liquid phase.

In order to find the effects of pipe geometry on the hydrodynamics of the two-phase flow (gas and very-high viscosity liquid), the measuring passages with internal diameters of 12.5, 16, 22 and 54 mm were employed in the tests. The type of flow patterns obtained under adiabatic conditions were determined for all pipe diameters, while for 12.5, 16 and 22 mm pipes – the average values of volume fractions for both phases and liquid film thickness were analysed as well.

In order to be able to evaluate dynamics of the annular, downward flow of the gas-liquid two-phase composition, the optoelectronic measuring system was set up which comprised optical probes and an optical endoscope. The thickness of oil film was measured indirectly by measuring attenuation of the optical signal, with the use of a photo-detector illuminated by diode-based illuminators from the other side.

The local thickness of the liquid film was measured and the nature of its waving was determined with the use of optoelectronic sensors connected to a PC station equipped with the *Tauron* digital measuring system (recording and storage of images) and a card with software.

The wavelength of the light emitted by the illuminators was selected experimentally after the analysis of the absorption spectrum of the oil sample, and it was adjusted at 470 nm (blue colour) since the highest attenuation was observed for oil at just this wavelength. The light
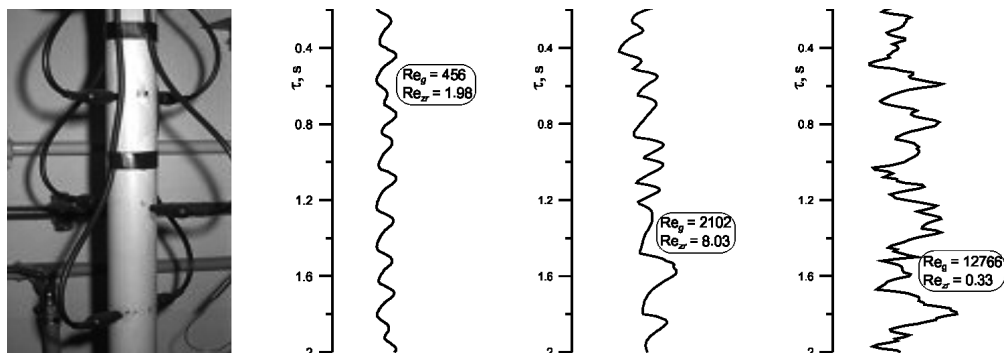
Fig. 2. The optoelectronic system and example results of measurements

signal from the light source and the return signal from photo-detectors were connected to the measurement controller by means of light pipes, 2 pipes for each measuring probe. The optoelectronic system and examples of experimental findings were shown in Figure 2. Spacing for the measuring probes was 100 mm, and the probes were arranged in pairs – perpendicular to each other.

The measurement controller was equipped with amplifiers in order to amplify the signals from photo-detectors. It was controlled by a microprocessor and its software for two-way communication with the PC software for the control of the measurement procedure. The PC software instructed the controller to start collecting signals and it received the in-coming samples at regular (programmed) time intervals, over the sampling time as fixed. The software was able to calculate the period for the appearing oil waves on the basis of the absolute time difference, which was found between crests and troughs of waves, as indicated by the user. The frequency of oil waves could also be determined. Moreover, velocity figures could be calculated for oil waves from the difference in time noted for the same crests or troughs of waves appearing and passing by the successive detectors.

The waving character of the flowing oil films was investigated in two stages. The first stage was based on the use of a high-definition digital video camera, recording in SVHS system, at the transparent section of the measuring passage. That camera recorded the flow structures, which appeared in front of it, and these were then analysed in the Tauron measuring system and with the use of other image analysis software. The character of waving in liquid films was studied this way. The resolution of the shutter of the optical system (1/10000) made it possible to precisely determine the nature of waving, which appeared in the falling films of viscous liquids.

In order to verify the findings obtained this way, the second stage of evaluation procedure followed. Owing to the CCD-video interface of the digital video camera, it was possible to interconnect the camera and the endoscope. Such a complex system was placed inside the measuring passage. The images were digitally recorded and analysed to verify the character of waving in the falling films of oil, and to add new observations to the previously collected sets of data. A source of light with adjustable illumination was supplemented to the endoscope to be able to record images in the non-transparent section of the measuring passage. So,

the obtained images of liquid film flow in cross-section added to previous findings to yield comprehensive observations of degree of waving and type of waving on the inter-phase boundary of gas and very-high viscosity liquid, for various flow parameters.

After the flow parameters became stable in the measuring passage, the structures appearing in the flow of the mixture were observed in the transmitted light; they were recorded by a photo-camera and a digital video camera. The examples were presented in Figures 3 and 4.
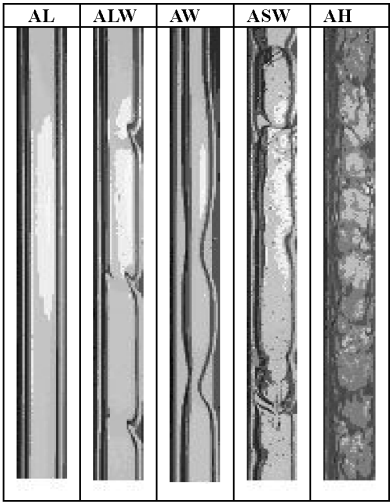
Fig. 3. Flow patterns of cocurrent annular downward two-phase gas-high viscous liquid flow: AL – annular smooth, ALW – annular lightly wave, AW – annular wave, ASW – annular strongly wave, AH – annular hydraulic

ALW
$w_{l,0} = 0.012$ m/s
$w_{g,0} = 1.042$ m/s

AW
$w_{l,0} = 0.03$ m/s
$w_{g,0} = 1.248$ m/s

ASW
$w_{l,0} = 0.05$ m/s
$w_{g,0} = 0.801$ m/s

AH
$w_{l,0} = 0.02$ m/s
$w_{g,0} = 4.387$ m/s

Fig. 4. The influence of flow parameters on wave forming of oil film

Moreover, the condition of the interfacial surface was recorded, i.e. images coming from the optical endoscope were utilised for that purpose. The experimental findings were utilised to classify the observed forms of the flow, and they also made a basis for the formulation of certain correlations, which characterise the dynamics of the annular two-phase flow of gas and liquid wi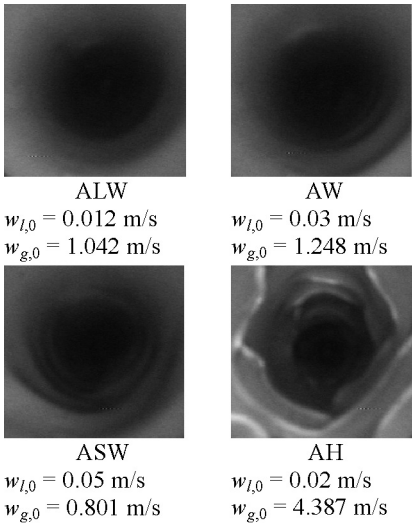th very-high viscosity. The optoelectronic system, capable of measuring the local liquid film thickness, its velocity, as well as amplitude and period of the appearing waves, was employed to evaluate the forms of flow as observed earlier, and to find the limits of their occurrence.

As results from Figure 3, the character of flowing liquid films can be strongly diversified. At low velocities of the liquid phase, the liquid film was most often smooth over a relatively wide scope of velocities of the gas phase. The size and nature of the created waves, with various amplitudes and frequencies, was dependent mainly on the flow rate and viscosity of the liquid, and on the flow rate of the gas phase.

The extensive study revealed the presence of sinusoidal waves, rolling waves and irregular capillary waves, for which the wavelengths were conditioned by the changes in the flow rate of the gas phase. Both long waves, with wavelength of $(0.1-0.5)$ m, and very short waves, with wavelengths of $(0.001-0.01)$ m, were observed. In case of strongly waving flows and the annular hydraulic flow, the surfaces of liquid films were irregular in most cases, with complex waving, which resulted from superposition of waves with different characters.

In order to determine the influence of flow rates of individual phases on the values of quantities characterising the dynamics of the annular two-phase flow of gas and very-high viscosity liquid, at various Reynolds numbers for liquid and for gas, the collected experimental data were subjected to detailed analysis. When distribution of data points in Figures 5 and 6 is considered, it becomes clearly evident that the increasing value of equivalent Reynolds number Re_z (see eq. 7) at constant value of Re_g results both in a higher occurrence of waves and in a higher speed at which they travel.
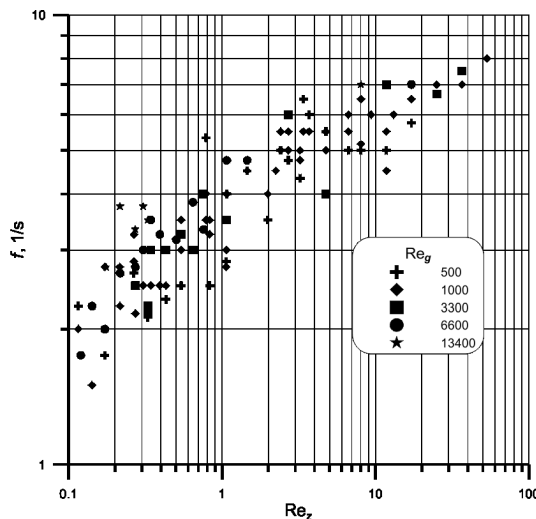

Fig. 5. Wave frequency in upon gas – high-viscous liquid annular flow
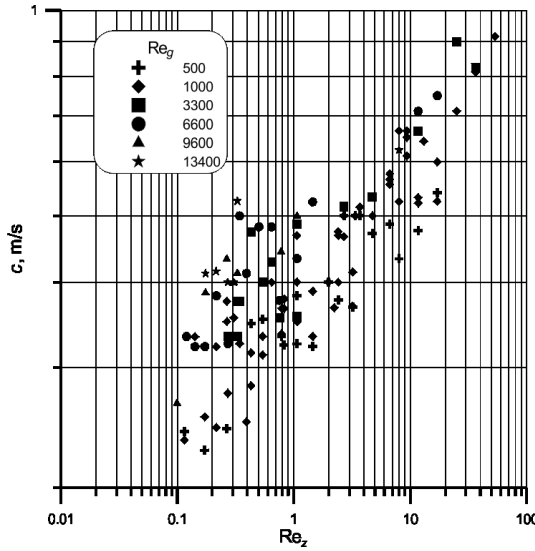
Fig. 6. Speed wave motion in gas – high viscous liquid annular flow

It was found at the same time (Fig. 7) that the speed at which the waves travel, when related to the average velocity of the liquid film $(c/w_{1,0})$, strongly declines for increasing values of the Reynolds number Re_z. The reason is undoubtedly higher surface turbulence on the liquid layer, and hence poorer conditions for a regular formation of waves.
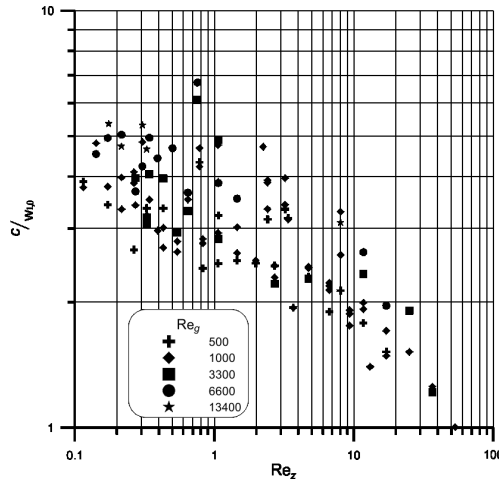
Fig. 7. Relative speed wave motion in gas – high-viscous liquid annular flow

The declining equivalent wavelength values λ for increasing values of Re_z, at various figures for Re_g, was shown in Fig. 8. No unequivocal effect was yet found in this case from the flow rate of gas on the value of wavelength. One can notice, however, that the increasing value of Re_z results in a tiny increase of wavelength, while the increasing value of the Reynolds number for gas is responsible for a reduction in the wavelength.
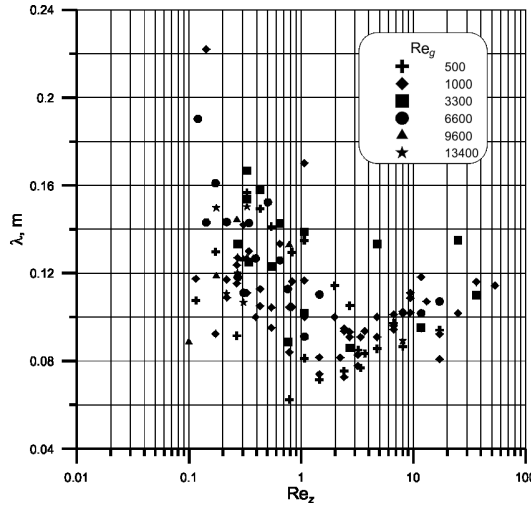
Fig. 8. Length of waves in gas – high-viscous liquid annular flow

It was observed when analysing the effects of Re_z and Re_g numbers on the values of amplitudes of waves that the increase in Re_z at constant Re_g yielded higher amplitudes. The increasing gas velocity represented by Re_g, at constant Re_z, also had a similar effect.

The research and analyses made the grounds for developing correlations applicable when calculating individual quantities, and namely:

▸ frequency of waves, f:

$$\frac{f\vartheta_z}{w_{l,0}} = 0.9177 \left(\frac{\varepsilon}{1-\varepsilon} \right)^{0.344} \text{Re}_g^{-0.272} \text{Re}_z^{-0.429} \tag{1}$$

▸ speed at which waves travel, c:

$$\frac{c}{w_{l,0}} = 141.1 \left(\frac{\varepsilon}{1-\varepsilon} \right)^{0.848} \text{Re}_g^{-0.725} \text{Re}_z^{0.112} \tag{2}$$

▸ wave lengths, λ:

$$\frac{\lambda}{\vartheta_z} = 65.23 W e_z^{0.373} \left(\frac{\text{Re}_z}{1+\text{Re}_g} \right)^{0.029} \tag{3}$$

▸ wave amplitudes, a:

$$\frac{a}{\vartheta_z} = 0.0222 \left(\frac{\varepsilon}{1-\varepsilon} \right)^{0.476} \text{Re}_g^{-0.109} \text{Re}_z^{0.744} \tag{4}$$

where:

$$\varepsilon = \frac{w_{g,0}}{w_{g,0} + w_{l,0}} \tag{5}$$

$$\mathrm{Re}_g = \frac{w_{g,0} d \rho_g}{\eta_g} \tag{6}$$

$$\mathrm{Re}_z = \frac{4\Gamma}{\eta_l} \tag{7}$$

$$\Gamma = \frac{\dot{m}_l}{\pi d} \tag{8}$$

$$We_z = \frac{\sigma_l}{\breve{g}\rho_l \vartheta_z^2} \tag{9}$$

$$\vartheta_z = \left(\frac{\eta_l^2}{\breve{g}\rho_l^2} \right)^{1/3} \tag{10}$$

The developed relations offer high accuracy (accuracy calculations above 80%) and they can be useful when designing and analysing the operation of those pieces of process equipment in which a film of liquid is formed hydraulically.

Having in mind that the interfacial surface area makes an important and decisive parameter for the conditions of heat exchange and mass transfer, an attempt was made to find that value. For that purpose, numerical calculations were employed to find the value for the contact surface for gas and liquid, F_{2F}, on the basis of the profiles of changes in liquid film thickness versus time, which had been obtained earlier. To be able to refer the value of F_{2F} to the total internal surface area of the empty pipe F_p, it was assumed that:

$$F_p = \pi d \Delta L_{cal} \tag{11}$$

where:

$$\Delta L_{cal} = w \cdot \Delta \tau \tag{12}$$

The calculated length ΔL_{cal} in this case stands for the distance to be covered by the liquid film travelling at the velocity of was found for the average film thickness of s, as calculated from the relation:

$$\frac{s}{s_0} = \frac{1}{1 + 5.68 \cdot 10^{-3} \, \mathrm{Re}_z^{0.132} \, \mathrm{Re}_g^{0.471}} \tag{13}$$

where:

$$\frac{s_0}{\vartheta_z} = 0.8252\,\mathrm{Re}_z^{0.516} \quad \text{for Re}_z < 2 \tag{14}$$

where:

$$\frac{s_0}{\vartheta_z} = 0.9335\,\mathrm{Re}_z^{0.334} \quad \text{for Re}_z \geq 2 \tag{15}$$

Fig. 9, on the other hand, presents the effect of gas velocity on the reduction of the thickness of liquid film in two-phase flow, in relation to its thickness observed for neat downward flow by gravity.
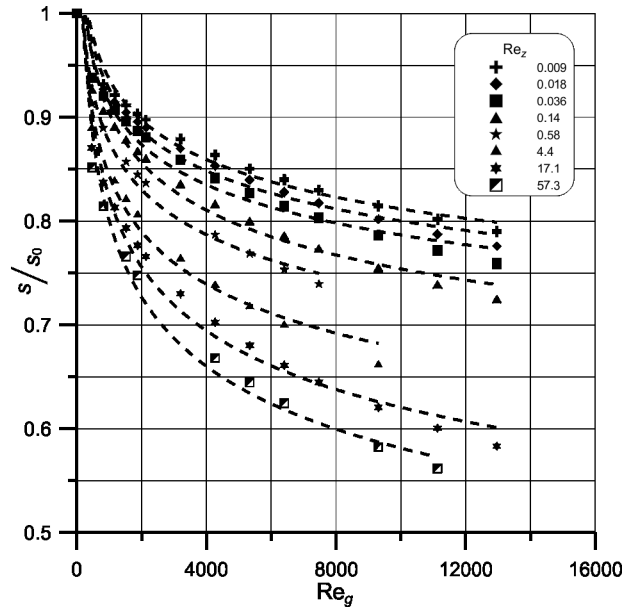
Fig. 9. The influence of gas stream on liquid thin layer in downward two-phase air-oil flow

The calculation findings were illustrated in Figures 10 and 11.

As can be seen from the arrangement of lines, even a small stream of gas causes a considerable reduction in liquid film thickness.

The arrangement of data points in Fig. 10 proves that, for constant value of Re_g, any increase in the Reynolds number for liquid (Re_z) results in a substantial reduction of the effective surface area. This is caused both by the increased liquid film thickness and by the changes in its waving character.

The effect of Re_g is hard to determine unequivocally in the presented co-ordinate system. On the other hand, that effect becomes clear in the system as presented in Fig. 11, where the borderline between the laminar flow and the turbulent flow of the gas phase is sharply outlined.
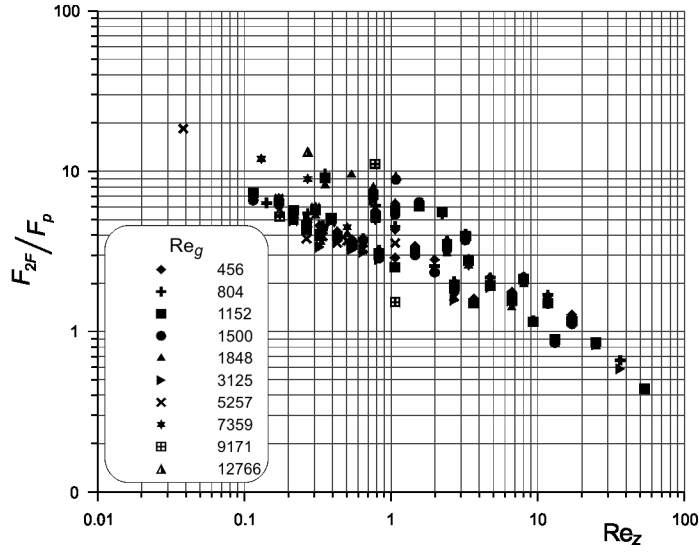
Fig. 10. Influence of flow parameters on the relative value of the interface surface for $\mathrm{Re}_g = \mathrm{const}$

Fig. 11. Influence of flow parameters on the relative value of the interface surface for $\mathrm{Re}_z = \mathrm{const}$

The detailed analysis has shown that this borderline can be determined as a function of the relation of the gas velocity to the liquid velocity, i.e.:

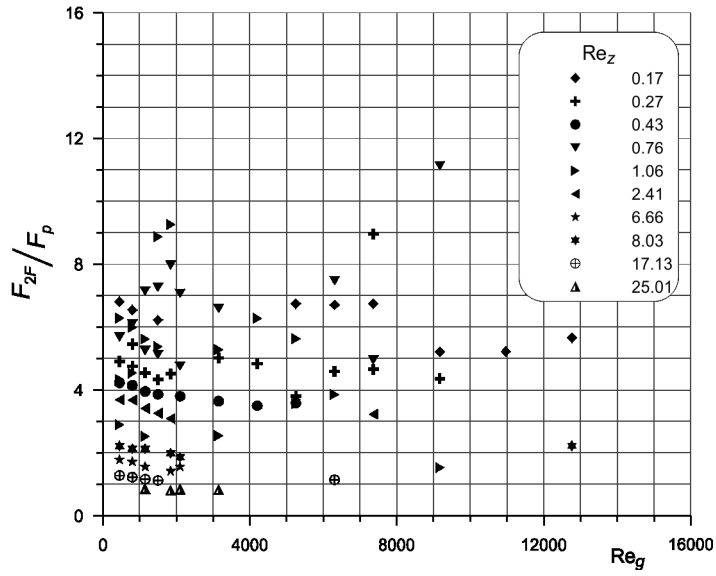$$\frac{F_{2F}}{F_p} = 46.73 \left(\frac{\varepsilon}{1-\varepsilon} \right)^{0.635} \mathrm{Re}_g^{-0.679} \mathrm{Re}_z^{-0.108} \tag{16}$$

When the measured values of the interfacial surface area F_{2F} were compared to the values calculated in accordance with (16), more than 85% of data points were found to fall within the relative error of $\pm15\%$. This equation may thus be recommended to be used for calculations of the interfacial surface area in those cases where gas and very-high viscosity liquid flow co-currently downward inside vertical pipes.

3. Summary

The analysis of experimental findings revealed a number of distinctive features in the nature of the down-flowing liquid films, which come from changes in the liquid viscosity specifications. A clear impact was found from the parameter on the local and average thickness values of the liquid film.

An increased liquid viscosity always produces thicker liquid films, while an increased velocity of the gas phase is responsible for liquid film thinning. Those parameters significantly influence the waving performance of the liquid film surface, and thus they influence the interfacial surface area.

The conditions for the heat and mass transfer processes are favourable under hydraulically forced annular down-flows of gas and very-high viscosity liquid, since thin and stable liquid films are formed over the whole pipe length in the falling-film process equipment, which means stable process conditions.

As the calculation methods recommended for those conditions turned out to offer high accuracy, they may be fully utilised both in design engineering and in the evaluation of performance of the falling-film equipment with hydraulically formed liquid films.

4. Nomenclature

F – surface, m^2
Re – Reynolds number,
We – Weber number,
a – amplitude of wave, m
c – velocities of wave, m/s
d – diameter, m
f – frequency of wave, 1/s
g – mass flux, kg/(m^2·s)
$\dot{m}$ – mass flow, kg/s
s – liquid film thickness, m
w – velocity, m/s
Γ – liquid flow rate per unit periphery, kg/(m·s)
η – viscosity, Pa·s
λ – length of wave, m

ρ – density, kg/m^3
τ – time, s
ϑ_z – equivalent linear dimension, m

5. Subscripts and superscripts

0   – superficial values,
$2F$ – two-phase flow,
l – liquid,
g – gas,
p – pipe internal surface area,
z – equivalent values for liquids.

References

[1] Andritsos N., Hanratty T.J., *Interfacial instabilities for horizontal gas-liquid flows in pipelines*, International Journal of Multiphase Flow, Vol. 13(5), 1987, 583–603.

[2] Czernek K., *Hydrodynamiczne aspekty projektowania aparatów cienko-warstewkowych dla cieczy bardzo lepkich*, Studia i monografie, Vol. 347, Oficyna Wydawnicza Politechniki Opolskiej, Opole, 2013.

[3] Czernek K., *Układy optoelektroniczne narzędziem do identyfikacji przepływów dwufazowych gaz-ciecz*, Inżynieria i Aparatura Chemiczna, 1, 2010, 31–32.

[4] Czernek K., Filipczak G., Witczak S., *Dynamika pierścieniowego dwufazowego przepływu gazu i cieczy bardzo lepkiej*, Przemysł Chemiczny, 87/2, 2008, 105–110.

[5] Czernek K., Witczak S., *Flow patterns of highly viscous liquid and down flowing gas in vertical pipes*, Chemical Engineering and Apparatus, Vol. 5s, 2003, 49.

[6] Du X.Z., Wang B.X., Wu S.R., Jiang S.Y., *Energy analysis of evaporating thin falling film instability in vertical tube*, International Journal Heat and Mass Transfer, Vol. 45(9), 2002, 1889–1893.

[7] Patnaik V., Perez-Blanco H., *Roll waves in falling films: an approximate treatment of the velocity field*, International Journal Heat and Fluid Flow, Vol. 17(1), 1996, 63–70.

[8] Troniewski L., Witczak S., Czernek K., *Hydrodynamics and heat transfer during two-phase gas-high viscous liquid flow in film reactor*, Chemical and Process Engineering, 27, 2006, 1341–1359.

[9] Witczak S., Czernek K., *Hydrodynamics of high viscosity liquid and gas down flow in vertical pipes*, Chemical Engineering and Apparatus, Vol. 3s, 2004, 177.

Roman Milwicz (roman.milwicz@put.poznan.pl)
Jerzy Pasławski

Institute of Structural Engineering, Faculty of Civil and Environmental Engineering,
Poznan University of Technology

Multiphase construction in single family housing. Case study

Etapowe budownictwo jednorodzinne. Analiza przypadku

Abstract

The dynamic development in the construction industry allows and at the same time forces us to design buildings with the ability to adapt to changing needs. The article discusses the formal aspects and the method of financing a single family house constructed in stages, depending on changing needs. A comparison of costs for a building constructed in stages and traditional building in the Polish realities for different scenarios of changing needs. The paper also presents the literature investigating the issue of the possibility of adapting buildings to changing needs. The basic problem is the risk of a financial trap involving the construction of a large house once and the financial problems resulting from: limitation of user numbers, limitation of financial resources, rising energy prices, high probability of selling a large house at a loss.

Keywords: Flexible construction, multiphase construction, sustainable construction

Streszczenie

Dynamiczny rozwój w branży budowlanej pozwala i równocześnie zmusza do projektowania budynków z możliwością adaptacji do zmiennych potrzeb. Artykuł traktuje o możliwościach formalno-prawnych oraz sposobie finansowania domu jednorodzinnego wznoszonego etapowo w zależności od zmieniających się potrzeb. Dokonano porównania kosztów dla budynku wznoszonego etapowo oraz budynku tradycyjnego w polskich realiach dla różnych scenariuszy zmieniających się potrzeb. Przedstawiono również literaturę zajmującą się zagadnieniem możliwości adaptacji budynków do zmieniających się potrzeb. Problem podstawowy to ryzyko pułapki finansowej polegającej na budowie jednorazowo dużego domu i problemach finansowych wynikających z: ograniczenia liczby użytkowników, ograniczenia zasobów finansowych, wzrostu cen energii, duże prawdopodobieństwo sprzedaży dużego domu ze stratą.

Słowa kluczowe: elastyczność w budownictwie, budownictwo etapowe, zrównoważone budownictwo

1. Introduction

In suburban and non-urban areas single-family housing is the most common way to solve the housing problem. Dynamic technology development in the construction industry makes it more efficient but also more difficult to predict. To make it possible to implement new solutions in existing buildings, the need arises to design buildings to incorporate possible changes – the ability called flexibility. This paper aims to illustrate the comparative analysis of the traditional detached house with the house constructed in stages in the case of an increase of demand for additional useful space. Phasing the construction process of a single-family house is a common phenomenon in the Polish reality, but it is not a process planned at the design stage and thus is characterized by large inconvenience for users – mainly by redundancy of space. Examination of the possibility of legal aspects will be an introduction to comparative analysis.

2. Legal aspects

Before the beginning of construction, the designer analyses user needs and opportunities associated with the investment. In the case of a detached house choice, one should take into account the occurrence of a variety of life situations. In regular houses there is an additional space for future use (redundant space). These solutions result in an increase in planned investment, which creates higher investment costs (CAPEX). Such a solution creates a so-called „financial trap". In the case of flexible solutions, the house is planned in such a way that its expansion in the case of increasing needs for additional space is simple and waste of space is minimized. There is no need to build a big house, but smaller with the option for future expansion. If the object is to be located in the areas covered by the Local Land Development Plan the possibility of a future expansion in the context of the regulations on the width of the facade or building area should be checked. In other cases application for a development decision by presenting the final appearance of the object is needed. This solution will help to avoid problems at the stage of expansion.

3. A construction permit

The application process for a regular construction permit is well known and associated with the submission of the application with complete project documentation according to the building [1]. The government has 60 days to issue the construction permit or submit comments. For a house constructed in stages, the process has to be divided into steps. The first looks regular and contains the first plan of the building. The next steps involve the creation of new projects for refurbishment of the house and applying for permission to expand.

4. Financial aspect

Many houses are financed by banking institutions in the form of mortgage loans. On the basis of cost estimates of the planned house, the expert's opinion and investor's income, bank determines the credit terms. From 2017, on the basis of Recommendation S [2] the investor is required to have financial contribution of 20% of the planned investment costs. Multi-phasing residential investment reduces the cost of construction and thus the amount of financial contribution, as well as the reduction of the mortgage costs or shortening of the loan. The next phases of construction, depending on the financial situation, can be financed with cash or by means of a mortgage in the same or another bank.

5. Flexibility in buildings – literature review

Adaptability to changing needs has a diverse definition in the literature, e.g. the ability to adapt. The ability to change volume, function or performance [3], ease of response to the changed conditions [4], presence of less common but more dramatic changes [5]. On the other hand, another group of researchers claim that adaptability of buildings means to remain in readiness for change in order to change or reduce the mismatch [6]. Flexibility in buildings has already been examined [7]. In this case, however, the flexibility related to the possibility of adapting house of a defined area to different needs changes over time, e.g. a varying number of users, and the possibility of adaptation by means of changing technology. The analyses are based on existing buildings undergoing adaptations. Among them are British terraced houses, four-storey blocks in Sweden, and office buildings with open space designed for self-development. In another place the need is described to design facilities to enable adaptation: "If the building does not support (technologically and technically) change and reuse you have only the illusion of sustainable construction" [8]. The work includes an extensive analysis of the literature and tries to create a holistic definition of adaptability. Interesting in terms of flexibility is also developing, showing an overview of the literature and trying to answer the question of how to design once, but for a long time [9] considerations of the economic aspects of the adaptation of the buildings can be found in the doctoral dissertation of Manewa [10]. According to Schmidt et al. [11] the ability to adapt can be divided into several categories:
- ▸ (scalability) – possibility of the volume change,
- ▸ (flexibility) – the ability to modify the space for a variety of purposes,
- ▸ (refitability) – the ability to change or renew components,
- ▸ (movability) – to change the configuration of components or movement.

There are also companies involved in buildings that allow for great flexibility in the context of increasing the volume of the building as well as its mobility. They offer modular homes allowing them to be transported and the interior to be adapted to different needs [12, 13]. The technology is based on wooden frame or steel and the object itself is divided into modules the size of the containers allowing transport.

6. Case study

The analysis proposes a hypothetical situation for a childless couple willing to build a detached house. They have limited financial resources, and therefore the construction will be financed from the assets obtained from a bank by means of a mortgage, the minimum contribution is at least 20% of the investment. The couple do not have any definite plans as to the size of the family, therefore the estimated development of the family is based on the statistics from the Central Statistical Office [14] which is presented below in Fig. 1.
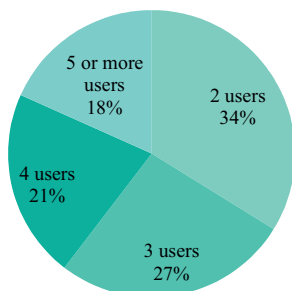

Fig. 1. The size of households with the probability of their occurrence [14]

On the basis of statistical analysis 4 scenarios are proposed: traditional (Scenario D) and flexible with 3 options and sub options (A, BI, BII, CI, CII) enabling adaptation to changing needs over time. For a given scenario, the number of instalments and credit costs have been obtained on the basis of consultation with an independent credit counsellor (interest rate of 3.4–3.6% depending on the length and size of the loan repayment). Only loans in the Polish currency were taken into account and the amount of net salary for a household of 5000 net (average net salary in the third quarter of 2016 amounts to 3024 PLN net [15], due to the young age of the couple and small experience factor 0.8 of the average wage was used).

Table 1. Estimation of input parameters for the analysed scenarios

		A	BI	BII	CI	CII	D
Initial Area [m²]		67	67	67	67	67	140
First expansion	Time from the initial construction	–	5 years	10 years	5 years	5 years	–
	size [m²]	–	30	30	30	30	–
Second expansion	Time from the first construction	–	–	–	10 years	15 years	–
	size [m²]	–	–	–	34	34	–
Initial capital [PLN]		49 000	49 000	49 000	49 000	49 000	90 000
Instalment [PLN]		2115	2115/ 1970	2115/ 1740	2115/ 2000	2115/ 1980	2050

Loan repayment period	9 years	14 years	14 years	19 years	19 years	20 years
m² cost [PLN/m²]	3 200					
Energy demand	120kWh/m² year					
Unit price of energy	0.25 PLN/kWh					

Based on the input data, a comparison of costs in the period of 20 years from the start of the investment was conducted. This period was adopted because of the payoff time of the investment and the loan repayment; additionally, the existing building is unlikely to need expansion. Option A is characterised by constant useful area at a level of 69 m². For the other options useful area changes with time option B – 97 m² while for option C and D – 140 m². It can be seen that with a conventional approach, rising total costs considerably in selected categories in comparison to a flexible solution that has the advantages of reduced initial user requirements, as illustrated in Fig. 2.
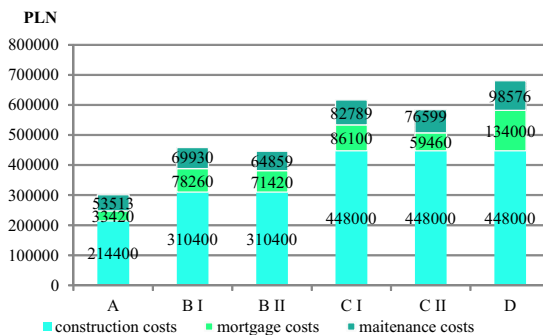
Fig. 2. Total cost (TOTEX) estimation for different options (20 year time horizon)

Differences arising from the implementation of the various options reach more than 300 000 PLN for option A and D. In the case of obtaining the same usable space after the longest 15 years difference between options B and D is mainly visible in the cost of credit. If we estimate a direct relationship between the demand for usable area with the number of family members Fig. 1 the result will be relationship presented in Tab. 2.

Table 2. Options and the ability to provide a rational surface

	Area	No. bedroom	No. users	Occurrence
I expansion	30	1–2	–	–
II expansion	34	1–2	–	–
A	67	1	2	Medium*
BI/BII	97	2–3	3–4	High*
CI/CII	141	4–5	5–6	Low*
D	140	4–5	5–6	Low*

* values were estimated on the basis of the data presented in Fig. 1.

Total costs associated with the mortgage and maintenance costs can also be analysed on the graph as a function of issued funds over time (Fig. 3). The visible difference can be seen at the very beginning of the investment (CAPEX) of a lower contribution from the investor and thus provide conditions for better housing affordability, which allows the investment at the lower limit of the budget. The options A and B also show significantly shorter time to repay the mortgage than in the case of C and D. With option C, we have to deal with double-increasing obligations to the bank.
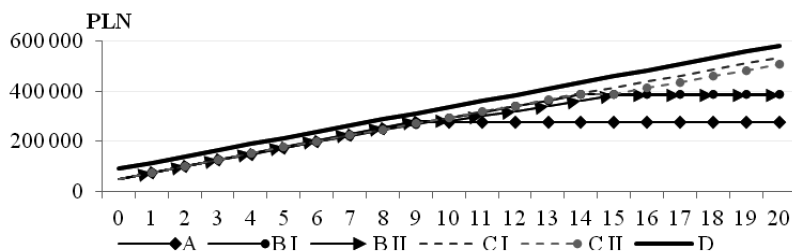

Fig. 3. The financial burden associated with the repayment of the mortgage

Flexibility application in the form of phasing construction should also bring financial benefits associated with the expenditure to cover the energy for heating purposes. The biggest differences are evident, of course, in the case of differences in the area of house after 20 years. However, even when reaching the same surface Options C and D investment flexibility proves to generate approximately 20 000 PLN savings compared to a traditional solution.
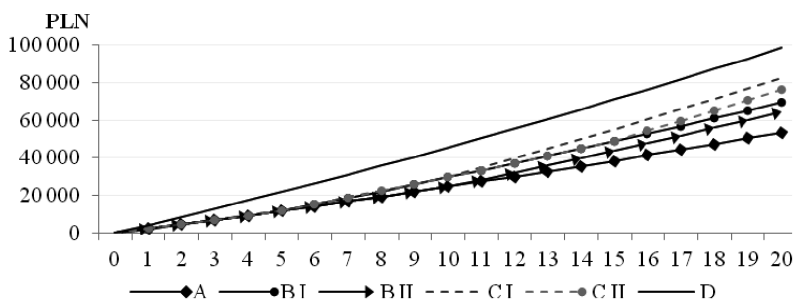
Fig. 4. Heating costs over 20 years for different options – annual price increase of 1.5%

7. Conclusions

After the literature review, it was found that the subject discussed is widely described in the scientific community. The main conclusions are:

1. Phasing of construction is one of the flexible responses to changing conditions at the time of need.
2. Based on the analysis of Construction Law the possibility of legal application flexibility is stated in the form of staging construction. But this should be based on an individual project customized to the needs of a particular investor.

3. Flexibility applied in this form can help to increase housing affordability (lower financial threshold of accession to the investment), by reducing their own contribution, and reduces the costs associated with mortgage, in addition to lowering energy demand;

4. Thanks to the phasing of investments, occurrence of the reduction in the risks associated with it and the lack of involvement of significant financial resources in the absence of an increase in demand for usable area and less financial obligation.

Only in a small number of cases of vague plans is there a need to invest in a house with an area of 140 m^2 (Tab. 2).

The authors analysed the legal aspects and plan a further in-depth study of flexibility in residential construction from the point of view of sustainable construction based on the analysis of the life cycle costs of a building.

References

[1] Croxton R., *Disassembly and Deconstruction*, Architectural Record, 2003.

[2] Prawo Budowlane art. 32 ustawy z 7 lipca 1994 r. – Prawo budowlane (Dz.U. z 2006 r. Nr 156, poz. 1118 z późn. zm.).

[3] Rekomendacja *s*, www.knf.gov.pl/Images/rekomendacja_s_tcm75-8566.pdf.

[4] Douglas J., *Building adaptation*, 2nd ed. Great Britain, Elsevier Ltd. 2006 (access: 2.12.2016).

[5] Kronenburg R., *Flexibile Architecture that responds to change*, Laurence King Publishers, London 2007.

[6] Leaman A., Bordass B., *Flexibility and Adaptability. In designing better buildings*, Macmillan S., Spon Press, 2004, 145–156.

[7] Friedman A., *The adaptable house: Designing homes for change*, McGraw-Hill, New York 2002.

[8] Schneider T., Till J., *Flexible housing*, Architectural Press, 2007.

[9] Croxton, *Disassembly and Deconstruction*, Architectural Record, 2003.

[10] Schneider T., Till J., *Flexible Housing: The Means to the End*, ARQ: Architectural Research Quarterly, 9(3/4), 2005, 287–296.

[11] Manewa R. *Economic Considerations for Adaptability in Buildings* PhD Thesis, https://dspace.lboro.ac.uk/2134/9457, Loughborough 2012 (access: 8.12.2016).

[12] Schmidt R., Eguchi T., Austin S., Gibb A., *What is the meaning of adaptability in the building industry*, http://adaptablefutures.com/wp-content/uploads/2011/11/Schmidt-et-al.-2010b.pdf (access: 20.12.2016).

[13] Danish housing company, www.addaroom.com (access: 20.12.2016).

[14] Flexible modular housing, www.flexihus.com (access: 20.12.2016).

[15] main statistics office, www.stat.gov.pl/download/gfx/portalinformacyjny/pl/defaul taktualnosci /5670/5/1/1/l_gospodarstwa_domowe_i_rodziny_nsp2011.pdf (access: 14.12.2016).

[16] Wages calculator, www.wynagrodzenia.pl/gus (access: 10.12.2016).

Aleksander Nicał (a.nical@il.pw.edu.pl)
Division of Production Engineering and Construction Management, Faculty of Civil Engineering, Warsaw University of Technology

Outlook for the implementation of selected ambient assisted living concepts for panel building

Perspektywy wdrożenia wybranych koncepcji ambient assisted living do budownictwa wielkopłytowego

Abstract

The paper presents an outline of the concept of Ambient Assisted Living that facilitates the daily functioning of elderly people living in panel buildings erected in the years 1970–1985. It describes the main assumptions of the concept and existing programs to support its implementation. The paper also contains characteristics and percentage share of the most popular building panel systems used in the construction process of residential buildings in Poland. Additionally, selected facilities for the elderly people in flats as well as the possibility of remodelling them for the installation of proposed bathroom environment, are presented.

Keywords: Ambient Assisted Living, panel building, elderly people

Streszczenie

W artykule przedstawiono zarys koncepcji „życia wspieranego przez otoczenie" ułatwiającej codzienne funkcjonowanie osobom starszym w obiektach wzniesionych w technologii budownictwa wielkopłytowego zrealizowanego w latach 1970–1985. Opisane zostały główne założenia koncepcji, dotychczasowe oraz programy wspierające jej wdrożenie. Artkuł zawiera także charakterystykę i procentowy udział w budownictwie najbardziej popularnych systemów wielkopłytowych, w jakich wznoszone były budynki mieszkalne w Polsce. Dodatkowo przedstawione zostały wybrane udogodnienia dla osób starszych w mieszkaniach, polegające na zastosowaniu innowacyjnego kompleksowego panelu łazienkowego i możliwości przebudowy mieszkania w tym celu.

Słowa kluczowe: Ambient Assisted Living, budownictwo wielkopłytowe, osoby starsze

1. Introduction

Construction, like many other sectors of the economy, is vulnerable to all kinds of social changes, including changes in the demographic structure of the country. Despite the continued growth of the world population, particularly intense in the last 40–50 years, in many developed and highly developed countries a decrease in the birth rate is observed. The consequence of these processes is inevitable change in the age structure of the population, resulting in a percentage increase in the population pyramid of the elderly people, generally equal to and exceeding 60 years. At the same time, a decrease in the share of children and young people is noticeable. In Poland, the period of political transformation that began in 1989 has also brought a number of significant changes in the demographic behaviour of the population. This same as in the developed countries of Western Europe, the mortality rate of society has been significantly improved. However, international migration, as well as a lower number of births and marriages and their durability has resulted in a decrease in Poland's population [1]. Such a situation in the long term will lead to the emergence and consolidation of the model of society in which older people are convicted only on their own capabilities. With this in mind, the implementation of technologies for elderly people to function independently seems reasonable to be implemented in Poland. Elderly people, in the large majority, spend a significant part of their time in homes by doing Basic Activities of Daily Living [4] including personal hygiene, dressing, moving around the apartment, the use of bathrooms and toilets. For this purpose, a wide range of solutions for residential buildings, contributing to easier use for the elderly, should be developed under the concept of Ambient Assisted Living. In the history of housing in Poland and the structure of the housing stock, it should be noted that for 30–40 years of building a very large proportion are panel buildings, accounting for up to 78.3% share of other technologies in the 1980s [3]. With high probability it can be assumed that the migration of people living in these buildings, considering the fact that generally these buildings are placed in very favourable locations, mostly in the city centres and districts with well-developed public transport, will not take place. Moreover, the panel buildings are currently being repaired and upgraded, which results in an increase in their usability and aesthetic.

It can be stated without a doubt that the problem of independent living for elderly people will in the near future affect a very large part of the inhabitants of panel buildings. Taking into account the technical parameters of these objects, which are unsuited to current standards, in particular regarding room and corridor width, living space, number and size of lifts, it is necessary to find ways to improve the current situation immediately.

2. Concept of Ambient Assisted Living

In order to meet the needs of an aging society, in 2008, the European Parliament and the European Council, on the basis of Article 185 of the Treaty on the Functioning of the European Union, adopted the Common Program of AAL (Ambient Assisted Living) 2008–2013, whose main objective was to stimulate the development of innovative products,

services and systems based on ICT technologies. Among other objectives to be achieved, it planned to:

- ▸ extend the time during which elderly people could live in conditions increasing their independence and mobility;
- ▸ support in maintenance of health and independent living for the elderly;
- ▸ promote a better and healthier life for people at risk,
- ▸ help and support carers, families and caring organizations;
- ▸ boost efficiency and productivity of resources in aging societies [14].

The AAL Joint Programme 2008–2013 is continued by the Active and Assisted Living Programme 2014–2020. Specific classifications of end-users are as follows:

- ▸ **the primary end-user** is the person who is actually using an AAL solution. He/she is considered as a single individual: "the Well-Being Person";
- ▸ **secondary end-users** are persons or organizations directly in contact with one or more primary end-user(s), such as relatives, friends, neighbours (informal carers), care organizations and their representatives (formal carers);
- ▸ **tertiary end-users** are private or public organizations that are not directly in contact with AAL solutions, but somehow contribute by organizing, enabling or paying for them [10].

3. Characteristics of selected panel building systems

The most intensive development of panel building systems in Poland was observed in the period between 1970–1985 (Fig. 1). Due to the favourable technical and economic indicators of the panel building, including lower labour costs and weight of the elements, as well as lower demand for cement, steel and wood in relation to large-block and traditional technology, the panel building systems dominated from the beginning of the 70s in residential buildings.
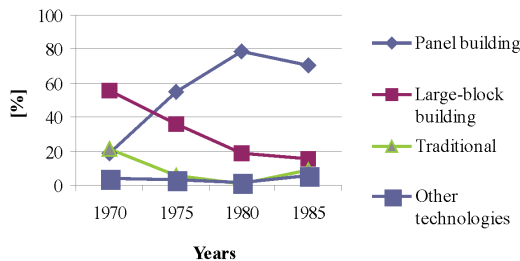
Fig. 1. Chart showing the share of each technology in residential buildings in Poland in the period between 1970–1985 [3]

Panel building technology in Poland was standardized in the following systems:

- ▸ central open standardization based on the unified large-scale element catalogues, forming ranges of prefabricates with a multiple module of 60 cm as a basis. This system allowed the creation of different room layouts in buildings, sections and flats, e.g. W-70, Wk-70;

- central closed standardization based on a number of typical elements and flat catalogues, enabling creation of a certain number of segments and their configuration in buildings, e.g. OWT-67, OWT-67/N, OWT-75, WUF-T, WUF-75, Szczeciński S-Sz,
- regional closed standardization based on a number of typical prefabricates and segment catalogues, enabling development of residential complexes in different regions. It consisted of: a) central regional systems, e.g. W-70/SG, W-70/PRAS-BET, Wk-70/SG, WK-70/Z, OWT-67NS, OWT-75NS, WUF-T/K (WUT-80GT), SZCZECIŃSKI S-Sz/SG, b) regional systems, e.g. WWP, RzWP, CzWP, FT/MG, ŁSM, RBM-75 (OWT-67 version for agriculture) [3].

In terms of usable area, regional standardization systems represent about 20% of the existing panel building systems (Fig. 2).

[%]

- W-70
- Wk-70
- OWT (all types)
- WUF-T
- S-Sz
- Regional

16,8%, 19,5%, 27,9%, 2,9%, 13,8%, 19,2%
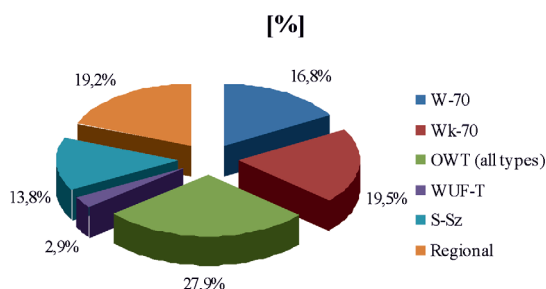
Fig. 2. Chart showing the percentage share of each system in the usable area of panel buildings in Poland in the period between 1970–1985 [3]

Due to the very large number of varieties of regional systems and its relatively small share compared to other panel building systems, the following systems are analysed: W-70, Wk-70, OWT, WUF-T and S-Sz (Tab. 1).

Table 1. Selected panel building systems [3]

System	Basic system parameters [cm]			
	Modular grid	Spacing of structural walls	Bay depth	Storey height
OWT	n × 270 × 480 n × 270 × 540	270 and 540	480 and 540	270
WUF-T	n × 150 × 480	300, 450, 600 and 750	480	270
W-70	60 × 60 (modular) and 60 × 120 (planned)	240, 360, 480 and 600	540 and 600	280
Wk-70	60 × 60 (modular) and 60 × 120 (planned)	240, 300, 360, 480 and 600	480 and 540	280
S-Sz	11 × 240 × 480	240 and 480	480 and 540	280

4. Selected concepts for residential facilities

Elderly people usually depend on others and are very often not able to move freely in their apartments, especially if the rooms are not spacious. Unfortunately, panel building systems in the years 1970–1985 were designed on the basis of norms NTP-59 and NTP-74, with limited living area per inhabitant [3].
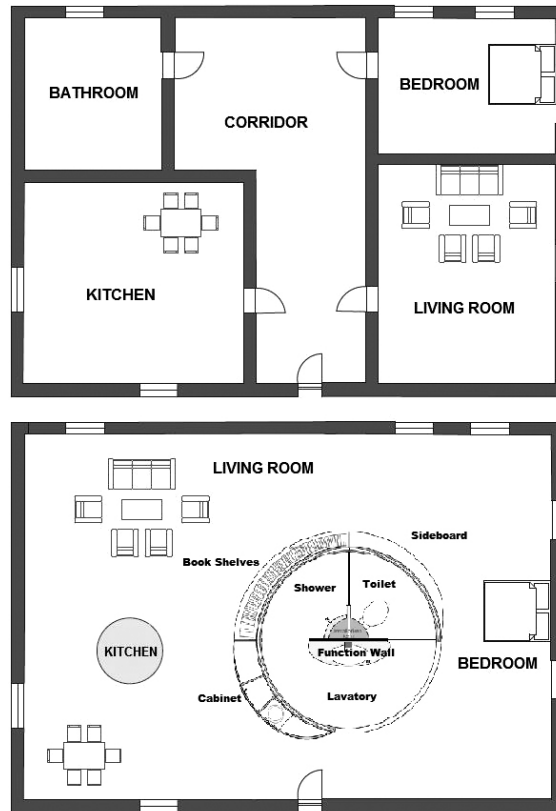
Fig. 3. Barrier-free arrangement of the apartment [2]

Due to narrow corridors, cramped rooms, small kitchens and bathrooms, the apartments, in terms of functional utility, are not suitable for elderly people. The solution in this area shows the concept of the barrier-free apartment arrangement. The idea of this concept is a complete elimination of the partition walls in the apartment. In addition, the concept also combines the bathroom and the kitchen in an integrated bathroom environment (Fig. 3). This bathroom environment panel is divided into 3 sections: a shower room, a toilet and a functional wall with washbasin. The shower room comprises a "bathing machine" that has water nozzles attached to the sides, which spray water as well as shower gel. Integrated blowers dry the user with hot air after showering. The washbasin is height-adjustable like the storage cabinets and

shelves attached to the outer wall [2]. This bathroom environment panel is adapted also for an electric wheelchair and has an adjustable handle to attach it. The wheelchair is resistant to water and can be easily connected to each of the 3 sections. Installation of the panel in the middle of the apartment facilitates its availability; however, attention must be paid to the proper integration of it with all installations. In particular, it is necessary to adjust sanitary water and gas supply, as well as sewer water disposal and ventilation.

Another concept assisting the elderly in assisted living facilities are PAMM Systems (Personal Aids for Mobility and Monitoring), which have been developed in the Field and Space Robotics Laboratory at MIT [11]. The PAMM can be either a cane or walker with a six-axis force-torque sensor mounted under the user's handle to serve as the main user interface. An admittance-based controller integrates the user input signals with the instruction of the schedule based planner, facility map information, and signals from an obstacle avoidance sensor in order to control the system [11]. The device is equipped with an on-board sensor that monitor the user's basic vital signs. The system is connected to a central computer via wireless link so that current information about the health and location of the user can be provided. Thanks to the signposts located on the celling of the apartment and the camera, the location of the PAMM is accurately determined (Fig. 4).
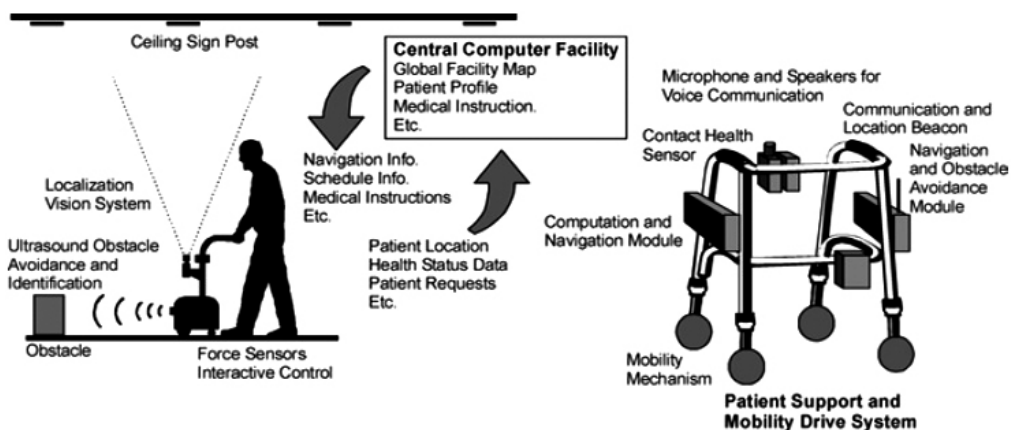
Fig. 4. PAMM system concept [11]

One important issue in constructing robotic walkers and mobile robot base platforms, equipped with two force-sensing handle bars, is shared control. The robot must be capable of providing navigation and guidance while maintaining a natural and predictable motion response [12]. It is essential to bind the control of two systems (an elderly human and a robotic walker) engaged in the task of navigation. Due to the fact that the goals of human and robot may often misalign, the shared control system must determine whether the human or the machine cedes control. The two components enabling shared control are a haptic interface for capturing user intent and control software that binds the two systems [12].

The haptic interface registers the user's intention through physical interaction. The interface transforms the force applied by the user into the robot's motion [12]. The haptic interface is equipped with force sensors, embedded into the handlebar structure of the walker robot. Handlebars are required to support and stabilize the ambulatory devices and should be planned so that the user's hands can grip them firmly. The placement of the force sensors inside the handlebars results in maintaining a steady hold by the user and manipulates the robotic walker in a manner more consistent with contemporary roller-based walkers [12]. An example of the haptic interface is shown in Fig. 5.
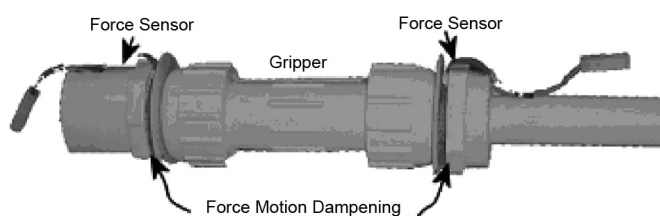
Fig. 5. The haptic interface handlebars [12]

5. Conclusions

The problem of an aging society in Poland will become more noticeable in the next few years. The crucial issue will concern ensuring decent living conditions for elderly people that should be understood as free, comfortable and safe performance of all daily activities in the apartment. Further research is needed in this area, in particular the behaviour of the elderly inside their apartments should be analysed, as for example: the time they spend on performing basic activities of daily living, such as washing, dressing, eating, distance covered in the apartment, location of everyday devices,. Additionally, a study concerning the feasibility of adapting the panel buildings to the concept of Ambient Assisted Living must be carried out. Great emphasis should be placed on housing redevelopment issues, especially to the potential removal of structural load-bearing walls and partition walls. Not without significance are issues in the adaptation of sanitary and electrical installations to the assembly of the bathroom environment panel.

References

[1]   Population projection 2014–2020, Central Statistical Office, Statistical Analysis and Studies, Warsaw 2014.
[2]   Bock T., Georgoulas C., Linner T., *Towards Robotic Assisted Hygienic Services: Concept for Assisting and Automating Daily Activities in the Bathroom,* Gerontechnology, 2012, 11(2), 362.

[3]   Dzierżewicz Z., Starosolski W., *Systemy budownictwa wielkopłytowego w Polsce w latach 1970–1985*, Oficyna a Wolters Kluwer business, Warszawa 2010.

[4]   McDowell I., Newell, C., Measuring Health: *A Guide to Rating Scales and Questionnaires*, 2nd edition, Oxford University Press, New York 1996.

[5]   Kotowska I.E., Jóźwiak J., *Nowa demografia Europy*, Roczniki Kolegium Analiz Ekonomicznych, Zeszyt 28/2012.

[6]   Adamczewski G., Nicał A., *Wielkowymiarowe prefabrykowane elementy z betonu*, Inżynier budownictwa 3/2012, 46–53.

[7]   Nicał A., *Selected technical solutions in construction for elderly people in Poland*, Archives of Civil Engineering 2016, 87–96.

[8]   Lenkiewicz W., Orczykowski A., Węglarz M., Nezwal J., Hron A., Janc L., Klemm H., Kumm H., *Uprzemysłowione budownictwo mieszkaniowe w Polsce, Czechosłowacji i Niemieckiej Republice Demokratycznej*, Arkady, Warszawa 1965.

[9]   Książek M., Nicał A., Nowak P., Rosłon J., *Europejskie podstawy nauczania menedżerów budowlanych*, Materiały Budowlane, 6/2016, 176–177.

[10]   Linner T., Georgoulas C., Bock T., *A Multi-Robotic Assistant System (MRAS): A development approach with application to the ageing society*, Gerontechnology 2012, 11(2), 381.

[11]   Yu H., Spenko M., Dubowsky S., *An Adaptive Shared Control System for an Intelligent Mobility Aid for the Elderly*, Autonomous Robots, Vol. 15, 2003, 53–66.

[12]   Morris A., Donamukkala R., Kapuria A., Steinfeld A., Matthews J.T., Dunar-Jacob J., Thrun S., *A Robotic Walker that Provides Guidance*, IEEE International Conference on Robotics and Automation, Vol. 1, p. 25–30, Taipei, Taiwan, 14–19 September 2003.

[13]   Griffiths P., Gillespie R. Brent, *Shared control between human and machine: haptic display of automation during manual control of vehicle heading*, Haptic Interfaces for Virtual Environment and Teleoperator Systems, 2004. HAPTICS '04. Proceedings. 12th International Symposium on 27–28 March 2004, 358–366.

[14]   www.aal-europe.eu (access: 24.01.2017).

[15]   https://ec.europa.eu/digital-single-market/en/active-and-assisted-living-joint programme-aal-jp (access: 24.01.2017).

Paweł Szeptyński (pszeptynski@pk.edu.pl)

Institute of Structural Mechanics, Faculty of Civil Engineering, Cracow University of Technology

Influence of non-uniformity of cracking on calculation of deflection of reinforced-concrete elements, according to eurocode 2

Wpływ nierównomierności zarysowania na obliczanie ugięć elementów żelbetowych według eurokodu 2

Abstract

Formulae for the deflection of two examples of isostatic systems (simply supported beam, cantilever) were derived, accounting for influence of distribution of bending moments on cracking and beam stiffness distribution, according to EC2. Numerical analysis of the problem for the same two examples as well as for two further hyperstatic systems was performed using an iterative FEM algorithm. The influence of non-uniformity of cracking on deflection and distribution of bending moments was shown to be negligible in typical practical design problems, therefore also an estimation of deflection on the basis of the distribution of bending moments and the value of the factor α_k obtained from linear solution (before redistribution) is shown to be justified.

Keywords: reinforced-concrete, cracking, deflection, Eurocode

Streszczenie

Wyprowadzono zamknięte wzory na ugięcia dla dwóch przykładów układów statycznie wyznaczalnych (belka swobodnie podparta, wspornik), uwzględniając wpływ rozkładu momentów zginających na zarysowanie i rozkład sztywności belki, zgodnie z EC2. Wykorzystując iteracyjny algorytm MES, przeprowadzono numeryczną analizę zagadnienia dla tych samych schematów statycznych oraz dwóch przypadków układów statycznie niewyznaczalnych. Wykazano minimalny wpływ nierównomierności zarysowania na wielkość ugięcia i rozkład momentów zginających w typowych praktycznych zagadnieniach projektowych, a tym samym stwierdzono zasadność szacowania ugięć na podstawie rozkładu momentów i wartości współczynnika α_k dla rozwiązania liniowego (sprzed redystrybucji).

Słowa kluczowe: żelbet, zarysowanie, ugięcie, Eurokod

1. Motivation

Design practice indicates that in the case of large-span reinforced-concrete (RC) buildings, e.g. large commercial or shopping centres, it is the Serviceability Limit State (SLS) not the Ultimate Limit State (ULS) that determines the final amount of reinforcement and thus the total cost of construction. As it becomes more common to limit floor deflection up to 1/500 of span length in order to prevent possible cracking of in-fill masonry walls due to forced deformation, the problem of precise determination of deflection becomes even more important because of economic reasons both for designers and investors. This problem is influenced by many factors, among which cracking, creep, settlement and global deformation of the structure should be mentioned. It is cracking which will be discussed in this paper.k

The algorithm for the calculation of deflections which is presented in the EC2 [1] standard is based on the model by Rostasy, Koch and Leonhardt [5]. The code states that having determined the curvature of a beam in every section in view of cracking total deflection should be obtained via numerical integration of obtained curvatures. The problem is non-linear as any change in the structure'srigidity stiffness due to cracking results in redistribution of the bending moments in hyperstatic systems. Such problems are usually solved in an iterative manner.

Before EC2 came into force in some countries, a different approach was a common design practice, namely: calculation of deflections with the use of a single value for the reducedrigidity stiffness of the cracked beam for all of its sections. The decrease in beamrigidity stiffness due to cracking for the whole beam was calculated for a single design value of the bending moment – the same one then used to calculate deflection according to formula [3]:

$$u = \alpha_k \frac{5}{48} \frac{M_{Sd} L_{eff}^2}{B} \tag{1.1}$$

or any equivalent, in which α_k is determined using the classical methods of structural mechanics. The clue aspect of this formula, which is discussed here, is whether M_{sd} and α_k are determined before or after the redistribution of moments. The commentary given in [2] is useless as it refers to an isostatic system in which such a redistribution does not occur. However, both old [3] and modern [4] handbooks on the design of RC structures suggest using α_k resulting from the linear solution even for hyperstatic systems. The origin of M_{sd} is discussed in both standards in a general way, stating that it should be determined with the use of analysis methods proper for the case under consideration: a linear–elastic analysis accounting for cracking or a non-linear analysis.

A simplified approach, widespread among designers, was to use the design values of M_{sd} obtained from the linear solution (before redistribution). It was due to considerable difficulties in determining the actual distribution of bending moments when the FEM software was not available in the past, or when it did not enable non-linear analysis. It must be admitted, however, that even nowadays performing non-linear analysis is expensive (this concerns the cost of software licenses as some commonly used commercial FEM software used in design offices still lacks the option for such calculations) and time-consuming.

It is obvious that such a simplified approach as the one described above cannot be strictly valid at least for two reasons:

▸ Integration of the curvatures determined for non-uniform stiffness distribution must result in a different total displacement than in the case of uniform rigidity stiffness decrease;

▸ In the case of hyperstatic systems, the distribution of moments depends on the relative distribution of rigidity stiffness – if, in turn, distribution of rigidity stiffness depends on the current distribution of moments, then the whole problem becomes non-linearly coupled.

It must also be stated clearly that the guidelines in the EC2 standard do not allow such an approach to be used. Despite this, it is still in use sometimes due to the simplicity of implementation in the calculation algorithms and due to its efficiency. The question that arises in this situation is whether the error occurring when using simplified approach mentioned above is acceptably small or not. It is often assumed that such an approach provides a "safe" solution, overestimating true deflection – as the problem is non-linear, such an assumption may at best be a plausible conjecture rather than a definite statement. However, as mentioned before, such an overestimation may emerge to be needless, unnecessarily expensive and – in some cases – even unacceptably dangerous: too large an amount of reinforcement may cause a situation in which the reinforcement steel is strained below yield strain and the concrete is compressed with a limit value. Such a situation is not allowed for bent elements as it may result in brittle destruction and sudden collapse. This might happen only in the case when the true load exceeds the design value, which should not take place at all; nevertheless, any over-reinforcement is improper at least for economic reasons.

2. Theoretical analysis

2.1. Assumptions

General relations governing the problem of determination of deflection of a bent beam (or slab in a one-direction bending state) are:

Equilibrium relation:

$$\frac{d^2}{dx^2}M(x) = -q(x) \tag{2.1}$$

Constitutive relation:

$$\frac{d^2}{dx^2}w(x) = -\frac{M(x)}{B(x)} \tag{2.2}$$

where:

q – external load,
M – bending moment,
w – deflection,
B – bending stiffness.

We assume also that the bending stiffness is reduced due to cracking according to the EC2 formula, approved by the European Committee for Concrete (CEB) and based on the propositions by Rostasy, Koch and Leonhardt [5].

$$B(x) = \begin{cases} E_c J_I & \Leftrightarrow M < M_{cr} \\ \dfrac{E_c J_{II}}{1 - \beta_1 \beta_2 \left(\dfrac{M_{cr}}{M(x)}\right)^2 \left(1 - \dfrac{J_{II}}{J_I}\right)} & \Leftrightarrow M \geq M_{cr} \end{cases} \tag{2.3}$$

where:

  E_c – the Young modulus of the concrete (mean or effective value, depending on the specific case),

  M_{cr} – cracking moment,

  J_I, J_{II} – cross-section's second moment of area in uncracked and cracked state respectively,

  β_1, β_2 – are factors accounting for rebar contact stress and influence of long-term loading respectively.

This provides a non-linear system of ordinary differential equations with discontinuous coefficients. Attempts to find a general solution to such a problem should be doomed to fail in advance. The problem simplifies greatly if one assumes a quadratic moment distribution – an assumption, which is usually fulfilled in most typical design problems. This account for uniform load $q(x) = q$ = const. and any boundary nodal displacements and point loads. Integration of equilibrium equations yields:

$$M(x) = -\frac{q}{2}x^2 + C_1 x + C_2 \tag{2.4}$$

where:

  C_1, C_2 – are constants.

The whole problem reduces now only to double direct integration of (2.2) which may be carried out analytically. If cracking occurs, three cases must be considered:

▸ **CASE 1:** $2C_2 q + C_1^2 < 0$

$$w(x) = \frac{\beta}{q} \ln\left|-\frac{q}{2}x^2 + C_1 x + C_2\right| - \alpha\left(-\frac{qx^4}{24} + \frac{C_1 x^3}{6} + \frac{C_2 x^2}{2}\right)$$

$$-2\beta\left[\frac{C_1 - qx}{q\sqrt{-\left(2C_2 q + C_1^2\right)}} \operatorname{atan}\left(\frac{C_1 - qx}{\sqrt{-\left(2C_2 q + C_1^2\right)}}\right)\right] + C_3 x + C_4 \tag{2.5}$$

▸ **CASE 2**: $2C_2q + C_1^2 = 0$

$$w(x) = \frac{2\beta}{q} \ln|C_1 - qx| - \alpha\left(-\frac{qx^4}{24} + \frac{C_1 x^3}{6} + \frac{C_2 x^2}{2}\right) + C_3 x + C_4 \qquad (2.6)$$

▸ **CASE 3**: $2C_2q + C_1^2 > 0$

$$w(x) = \frac{\beta}{q} \ln\left|(C_1 - qx)^2 - (2C_2q + C_1^2)\right| - \alpha\left(-\frac{qx^4}{24} + \frac{C_1 x^3}{6} + \frac{C_2 x^2}{2}\right)$$
$$-\frac{\beta}{\sqrt{2C_2q + C_1^2}}\left(x - \frac{C_1}{q}\right) \ln\left|\frac{qx - C_1 - \sqrt{2C_2q + C_1^2}}{qx - C_1 + \sqrt{2C_2q + C_1^2}}\right| + C_3 x + C_4 \qquad (2.7)$$

where:

$$\alpha = \frac{1}{E_c J_I} \frac{J_I}{J_{II}} > 0 \qquad (2.8)$$

$$\beta = \frac{\beta_1 \beta_2 M_{cr}^2}{E_c J_I}\left(1 - \frac{J_{II}}{J_I}\right)\frac{J_I}{J_{II}} > 0 \qquad (2.9)$$

The sign of $\Delta = 2C_2q + C_1^2$ depends on the number of distinct real roots of (2.4). In the first case ($\Delta < 0$), there are no real roots – when the load is applied downwards (gravitational load) such a situation is not likely to occur and for simple beams (single-span, without overhangs) without nodal displacements it is impossible. The second case ($\Delta = 0$) occurs when the extremum of moment distribution is at the same time the root of (2.4) – this happens, for example, at the end of a cantilever. The third case ($\Delta > 0$) is the one which describes most typical situations.

Equations (2.5)–(2.7) describe the deformation of the beam axis in the cracked area. In the uncracked version, the deflection is described with a fourth order polynomial function. The range of the cracked zone is not known in advance. In the case of isostatic systems it may be easily determined as the interval in which $\{x : |M(x)| > M_{cr}\}$, since the distribution of moments is known. Solving the problem reduces now to just finding the integration constants as a solution of the linear algebraic system given by the boundary conditions and compatibility conditions for deflection and angle of rotation at the boundaries of cracked zone. In the case of hyperstatic systems, both range of cracked zone and reaction forces (i.e. constant C_2) are unknown – finding them requires a solution to a complex non-linear algebraic system. For this reason, only two cases of isostatic systems are considered below.

2.2. Simply supported beam of length L under uniform load q

In a coordinate system with its origin in the middle of the beam span, the distribution of bending moments is given by the constants $C_1 = 0, C_2 = \dfrac{qL^2}{8}$. The derivation of the solution is rather schematic, yet lengthy – let us present only the results. Let us denote $EJ = E_c J_1$. Maximum deflection is as follows:

$$
\begin{aligned}
w_{max} &= \frac{5}{384}\frac{qL^4}{EJ} - \frac{2\beta}{q}\ln\left|1 + \frac{L_{cr}}{L}\right| \\
&+ \frac{5qL^4(\alpha EJ - 1)}{384\,EJ}\left[\frac{3}{5}\left(\frac{L_{cr}}{L}\right)^4 - \frac{4}{5}\left(\frac{L_{cr}}{L}\right)^3 - \frac{6}{5}\left(\frac{L_{cr}}{L}\right)^2 + \frac{12}{5}\frac{L_{cr}}{L}\right]
\end{aligned}
\tag{2.10}
$$

where the range of the cracked zone (located symmetrically in the middle of span) equals:

$$
L_{cr} = L\sqrt{1 - \frac{8M_{cr}}{qL^2}}
\tag{2.11}
$$

2.3. Cantilever of length L under uniform load q

In a coordinate system with its origin at the distribution of bending moments is given by constants $C_1 = \dfrac{qL}{2}, C_2 = -\dfrac{qL^2}{2}$. Maximum deflection is equal to:

$$
w_{max} = \frac{1}{8}\frac{qL^4}{EJ} + \frac{2\beta}{q}\ln\left|1 - \frac{L_{cr}}{L}\right| + \frac{qL^4(1 - \alpha EJ)}{8EJ}\left[\left(\frac{L_{cr}}{L}\right)^4 - 4\left(\frac{L_{cr}}{L}\right)^3 + 6\left(\frac{L_{cr}}{L}\right)^2 - 4\frac{L_{cr}}{L}\right]
\tag{2.12}
$$

Cracked zone length (located by support) is equal to:

$$
L_{cr} = L\left[1 - \sqrt{\frac{2M_{cr}}{qL^2}}\right]
\tag{2.13}
$$

3. Numerical analysis

3.1. Range of variation of problem parameters

Let us write explicitly the formulae for the second moment of area of the uncracked and cracked rectangular cross-section:

$$J_I = \frac{bh^3}{12} + bh\left(x_I - \frac{h}{2}\right)^2 + \alpha_e bd\left[\rho_1\left(x_I - d\right)^2 + \rho_2\left(x_I - a_2\right)\right] \tag{2.14}$$

$$J_{II} = \frac{bx_{II}^3}{3} + \alpha_e bd\left[\rho_1\left(x_{II} - d\right)^2 + \rho_2\left(x_{II} - a_2\right)\right] \tag{2.15}$$

$$x_I = \frac{bh^2 + 2\alpha_e bd\left(\rho_1 d + \rho_2 a_2\right)}{2\left[bh + \alpha_e bd\left(\rho_1 + \rho_2\right)\right]} \tag{2.16}$$

$$x_{II} = d\left[\sqrt{\alpha_e^2\left(\rho_1 + \rho_2\right)^2 + 2\alpha_e\left(\rho_1 + \frac{a_2}{d}\rho_2\right)} - \alpha_e\left(\rho_1 + \rho_2\right)\right] \tag{2.17}$$

where:

h	–	beam height,
b	–	beam width,
d	–	effective height,
a_2	–	distance from compressed reinforcement centroid to the compressed edge,
ρ_1, ρ_2	–	index of stretched and compressed reinforcement respectively,
$\alpha_e = E_s/E_c$	–	ratio of Young moduli of steel and concrete.

We shall now consider what factors influence the result narrowing our considerations to single reinforced ($\rho_2 = 0$) rectangular cross-sections. We may express effective height as $d = 0.95h$ which is not precise but a fair and useful approximation. In this way, the ratio $\dfrac{J_{II}}{J_I}$ becomes independent of the h/b ratio. Introducing a generalized surface load $p = q/b$ we may eventually consider our solution as dependent on four dimensionless factors:

- $\chi_1 = \dfrac{L}{h}$ (geometry of system),

- $\chi_2 = \dfrac{f_{ct}}{p}$ (strength to load ratio),

- $\chi_3 = \rho_1$ (reinforcement index),

- $\chi_4 = \alpha_e$ (steel to concrete stiffness ratio).

This is not a complete set of independent variables influencing the solution. We must also notice that α_e is itself a function of the shape of the cross-section, concrete class etc. Anyway, these four factors may be used in order to estimate the quantitative influence of non-uniformity of cracking on deflection. We shall now determine the range of variation of values of those parameters.

Considering the length-to-height ratio we may fairly assume that:

$$\chi_1 \in \langle 4; 30 \rangle$$

The lower bound is determined by the limitation that shorter beams should be considered as membrane shells. The upper bound corresponds to typical values for plates. Considering

the strength-to-load ratio we may assume that typical RC structures are usually made nowadays of concrete of C20/25 up to C30/37 class. This corresponds with the scope of values of average tensile strength $f_{ct} \approx 2$–3 MPa. Surface load (characteristic value) in turn may vary from 1.5 kPa (apartments – live load only) up to ca. 15 kPa (e.g. car park or mall live load + dead load of flooring and 30 cm thick RC plate). This gives us:

$$\chi_2 \in \langle 130; 2000 \rangle$$

The range of variation of the reinforcement index is limited the by the code requirements on maximal and minimal reinforcement:

$$\chi_3 \in \langle 0,0013; 0,04 \rangle$$

Possible values of α_e factor range usually from ca. 7 (immediate elastic deflection) to ca. 30 (final creep deflection):

$$\chi_4 \in \langle 7; 30 \rangle$$

As the SLS most often concerns the final creep deflection, we will assume long-term load ($\beta_2 = 0.5$). We will also assume ribbed reinforcement ($\beta_1 = 1.0$) as the smooth one in practically almost out of use as a longitudinal reinforcement.

3.2. Analysed cases

In order to verify the obtained theoretical formulae an iterative FEM script was written solving a single-span beam under uniform load. Four static schemes were considered:
- ▸ beam fixed at both ends,
- ▸ simply supported beam,
- ▸ cantilever,
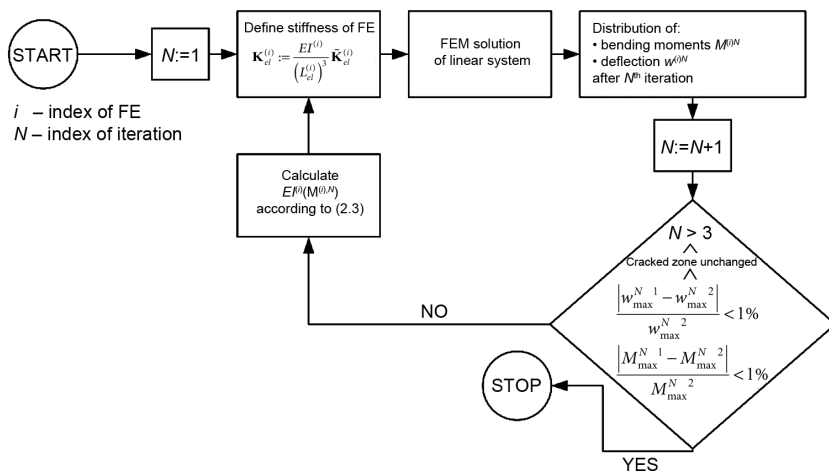- ▸ beam fixed at one end and pinned at the second one.

Fig. 1. Flowchart of iteration algorithm used for solution of non-linear problem

The loop end condition was a conjunction of three conditions: that last step increment in both deflection and extremal bending moment should be less than 1% of deflection or the extremal moment obtained in the previous step and that cracked zone in the last step should be the same as in the previous one. Additionally no fewer than 3 iterations must be performed. The beam was divided into 100 finite elements. After each iteration, each element's stiffness was recalculated according to formula (2.3), in which the value of bending moment for the element was taken as equal to an average value of its end nodes' bending moment values. A flowchart showing the general scheme of this algorithm is shown below.

16 basic cases were considered – each one corresponding with one combination of the extremal values of four factors introduced in previous sections. It is clear that such an "edge-value" analysis does not account for possible local extrema unless the joint influence of all of them provides a solution that depends on those factors in a monotonic way. The results, discussed below, indicate, however, that every solution (except for cantilever) corresponding with each combination of extremal values is almost identical with the simplified solution based on the moment and α_e factor determined for the uncracked system. For this reason, it may be supposed that no extremely distinct response of the system should be expected for any intermediate values. Such a supposition is of practical importance since any theoretically justified conclusions cannot be made in the case of such a complex, non-linear and self-coupled problem. These cases referred to extremal values of influence factors as follows:

Table 1. Edge-values of independent dimensionless parameters governing the problem for each analysed case

Case	χ_1	χ_2	χ_3	χ_4
1	30	2000	0.0013	30
2	30	130	0.0013	30
3	4	2000	0.0013	30
4	4	130	0.0013	30
5	30	2000	0.04	30
6	30	130	0.04	30
7	4	2000	0.04	30
8	4	130	0.04	30
9	30	2000	0.0013	7
10	30	130	0.0013	7
11	4	2000	0.0013	7
12	4	130	0.0013	7
13	30	2000	0.04	7
14	30	130	0.04	7
15	4	2000	0.04	7
16	4	130	0.04	7

Beam width – which has no major qualitative effect on the results obtained – was set at a constant numerical value $b = 1$ [m]. Each case was calculated four times for different sets of basic parameters, namely: span length (6 m or 9 m), tension strength and Young modulus of concrete (respective for C30/37 and C20/25 classes):

Table 2. Values of basic parameters governing the problem for each analysed sub-case

Case	L [m]	f_{ct} [MPa]	E_c [GPa]
A	6	2.9	32
B	6	2.2	30
C	9	2.9	32
D	9	2.2	30

A total number of 64 cases for each static scheme were analysed.

3.3. Results

The results obtained from the numerical solution were the same as those provided by the theoretical formulae. It emerged however that subcases A-D of any case 1–16 did not influence the result in any way. For most of the cases, there were only 3 iterations needed to fulfil the loop end conditions – maximum number of iterations needed in particular cases was 6. Cracking occurred only in cases 2, 6, 10 and 14 (long and low beam /thin plate/, small strength, strong load) and additionally for cantilever in cases 1, 5, 9, 13 (long and low beam / thin plate/, high strength, small load).

In all the cases considered, extremal values for the bending moment after redistribution did not change more than 5.369% (beam fixed at both ends, case 10) of the respective value obtained from the linear solution – it may be stated that in typical design problems the influence of cracking on the distribution of bending moments is of minor importance.

Also the α_k factor was calculated according to the formula:

$$\alpha_k = \frac{48}{5} \frac{w_{max} B}{M_{max} L^2}$$ (3.1)

Analytical values of α_k for chosen static schemes are:
- beam fixed at both ends, $\alpha_k = 0.6$
- simply supported beam, $\alpha_k = 1.0$
- cantilever, $\alpha_k = 2.4$
- beam fixed at one end and pinned at the second one.

$$\alpha_k = \frac{55\sqrt{33} + 39}{420} \approx 0.73948$$

In all cases except for cantilever, the obtained α_k values varied from those derived from the linear problem by less than 3.377% (beam fixed at both ends, case 10). For all schemes, the true maximum deflection was always smaller than the one obtained in the simplified approach.

An interesting conclusion emerges from the analysis of cases 1, 5, 9 and 13 for cantilever, which concern long and low beams (or thin plates) with high tensile strength under a small load. True maximal deflections were always smaller than those estimated with the simplified approach – in case 9, the reduction of deflection was as high as 54.174%. Such a situation occurs when the range of the cracked zone is very small, namely when the cantilever is only cracked at a short distance close to the support. The simplified approach assuming constant decrease of stiffness along whole beam must provide a considerable overestimation; however, it must be admitted that these cases correspond with very small absolute values of deflection (small load, high strength) – much smaller than the limit value.

In order to verify this result, a typical example of a balcony cantilever was analysed. We consider a 1.7 m long plate 20 cm thick, made of C20/25 class concrete. The load is 5 kPa of live load and 6.25 kPa of dead load (with flooring). Assuming reinforcement with A-IIIN class steel with $\alpha_1 = 3.5$ cm the ULS requires $\rho_1 = 0.001755$. The resultant final creep deflection $(\alpha_e = 3.5)$ corresponds with $(\alpha_k = 0.9437)$, which is more than 2.5 times as small as the 2.4 derived from the linear solution. In fact, the deflection obtained, equal to 2.81 mm, as well as the one estimated using the simplified approach, which equals 7.14 mm, are far smaller than the limit value $L/150 = 11.33$ mm. The cracked zone length is only 8.53 cm long, which is approximately 0.05 L.

Despite the fact that such a large overestimation concerns mostly those deflections which are very small, smaller than the limit permissible values (and thus may be fairly disregarded), it may be of interest to determine the conditions for which such overestimation occurs. This is the situation when the cracked zone length is very small. In the case of isostatic systems, the answer is obvious – it is when the bending moment exceeds the cracking value only slightly. A precise answer for hyperstatic systems is difficult to obtain due to the non-linearity of the problem. However, as the above analysis indicates, the distribution of bending moments corresponding with the linear solution is affected by cracking only to a small extent. For this reason, in the case of hyperstatic systems it may be stated that high overestimation of deflection, when using the simplified approach, occurs also when the bending moment (obtained for linear problem) exceeds the cracking value but is still very close to it. This may only be treated as a general guideline – any design process must verify the true deflection via numerical integration of the curvatures along the beam.

4. Conclusions

The analysis performed indicates that in most typical design conditions (material, load, static scheme, geometry) the influence of non-uniformity of cracking has minor influence on both the deflection and distribution of the bending moments. Differences between the

solution obtained by numerical integration of curvatures in non-uniformly cracked element and the solution assuming constant stiffness decrease along the element are not significant. In such situations, it is justified to use the simplified approach approximating deflection with formula (1.1) in which both the bending moment M_{Sd} and the α_k factor are the same as in the linear solution (disregarding the influence of cracking) while only bending stiffness B accounts for cracking according to the EC2 formula (2.3).

It must be noted that the above conclusions may be valid only in the case of typical designs – single span beams of average span length which are loaded uniformly with typical live load values and made of common materials. They were derived assuming that no qualitatively or quantitatively distinct response of the system occurs for intermediate values of parameters influencing the solution. As the problem is highly non-linear, such an assumption is – strictly speaking – not justified, yet it seems to be a probable supposition as the results obtained for combinations of "edge" (extreme) values do not differ one from another in a serious way. Any generalization of those statements for multiple-span beams or for two-way reinforced slabs is an extrapolation which requires numerical verification.

References

[1]   EN 1992-1-1:2004 *Eurocode 2: Design of concrete structures. Part 1-1: General rules and rules for buildings.*

[2]   PN-B-03264:2002 *Konstrukcje betonowe, żelbetowe i sprężone – Obliczenia statyczne i projektowanie.*

[3]   Kledzik W., Kledzik B., Kot A., *Wzory i tablice do projektowania konstrukcji żelbetowych*, Arkady, Warszawa 1982.

[4]   Łapko A., Bjarne C.J., *Podstawy projektowania i algorytmy obliczeń konstrukcji żelbetowych*, Arkady, Warszawa 2009.

[5]   Rostasy F.S., Koch R., Leonhardt F., *Zur Mindestbewehrung für Zwang von Außenwänden aus Stahlleichtbeton*, „Deutscher Ausschuss für Stahlbeton", Heft 267/1976.

Piotr Zabawa piotr.zabawa@pk.edu.pl
    Institute of Computer Science, Faculty of Physics, Mathematics and Computer Science
    of Cracow University of Technology

Simulation

of the CDMM-P paradigm-driven meta-modeling process

Symulacja procesu

metamodelowania sterowanego paradygmatem CDMM-P

Abstract

This article presents a simulation of the process of meta-model creation. The meta-model (modeling language) is created according to the Context-Driven Meta-Modeling Paradigm (CDMM-P) with the help of its implementation – Context-Driven Meta-Modeling Framework (CDMM-F). The simulation process may be applied to meta-model creation in an evolutionary approach to meta-modeling or may be used to check correctness of the meta-model, or to test the CDMM-F framework. This paper is focused on the verification and testing mentioned above.

Keywords: simulation, meta-modeling, open ontology, software engineering, software development process

Streszczenie

Artykuł prezentuje symulację procesu tworzenia meta-modelu. Metamodel ten (język modelowania) tworzony jest zgodnie z paradygmatem Context-Driven Meta-Modeling Paradigm (CDMM-P) z wykorzystaniem szkieletu (framework) stanowiącego jego implementację – Context-Driven Meta-Modeling Framework (CDMM-F). Proces symulacji może być zastosowany do tworzenia metamodeli zgodnie z podejściem ewolucyjnym do metamodelowania albo może być stosowany do weryfikowania poprawności metamodeli lub do testowania CDMM-F. Niniejszy artykuł koncentruje się na wspomnianym weryfikowaniu i testowaniu.

Słowa kluczowe: symulacja, metamodelowanie, ontologie otwarte, inżynieria oprogramowania, proces wytwórczy oprogramowania

1. Introduction

This paper presents a study focused on the software development process as the application domain of modeling and simulation. The modeling aspect is addressed here in order to create modeling languages, while the simulation is focused on research of the nature of this process.

The business goals of software development enterprises are constantly evolving. One of the goals is to increase reusability in order to shorten the time-to-market, minimizing business and product risks while also minimizing project and product costs. At the beginning, the reusability was addressed to subsystems and components. As a result, they were moved from one project to another in the binary form. It was a very good result as long as the customization of the system can be done by configuring it. This approach fails if the character of the configuration evolves from the linear via the tree-like to the graph-like ones, which is a frequent phenomenon. At the same time, enterprises were trying to create a universal, highly reusable source code – classes, packages, libraries. The pursuit of this goal could give good results as long as the responsibilities of software systems were taxonomised unambiguously. Unfortunately, they were not. The main reason was that owners, managers, architects of IT enterprises were starting from the premise that everything changes all the time. Nevertheless, each software system can be decomposed into the following elements: immutable elements, elements with immutable structure and mutable functionality, elements with immutable functionality and mutable structure, mutable elements.

In the late 90's, we witnessed the beginning of the standardization process of many model-driven technologies supporting software system development. It led to the standardization of modeling languages, leading to the creation of the Unified Modeling Language (UML), and at the beginning of XXI century – to the introduction of Model-Driven Architecture (MDA) standards. The application of these standards moved the subject of reusability slightly into the so-called reusable assets – models, knowledge base elements usually consisting of pieces of parameterized source codes or parameterized meta-codes. However, the same problems with correct decomposition of software systems as the ones mentioned above limited the application of new standards. Moreover, all of them, including Rational Unified Process (RUP), being the result of software development process standardization, as one of the possible instances of Unified Processes (UP), are very large. Their constantly growing size and complexity result from the assumption of incorporating each technology into the standards. That is, these standards are built as the supersets of everything available on the constantly growing IT market. In addition, this is a real barrier for people when they want to apply these standards in production process. Moreover, the process of acquisition of some technologies is unacceptably slow or it even fails.

The approach presented in this article is different – it offers a constructive approach to limit models and meta-models (modeling languages) to the notions that are necessary to support reusability and automation of software development process – the automation addressed at the creation of software development project artefacts from models. However, it is also based on some concepts mentioned above. One of the consequences resulting from the application of UML is the transformation of the evolutionary approach from the software development process (RUP) to the evolutionary approach to modeling

activities. In the approach presented in this paper, this evolutionary approach also affects meta-modeling. This is a natural consequence of limiting the modeling language at the beginning of the particular product creation and enriching this modeling language during this process. The process may encompass one product, many products, product-line, many product-lines. There are already some publications dedicated to the problem of meta-model evolution [14, 19, 15, 17, 21].

So, what is now the business goal of software development enterprises? It seems that the goal is to create a mechanism that supports reusability of meta-models being subject of evolution in software development processes. That is why the CDMM-P was invented and CDMM-F was implemented.

The name of CDMM underlines the significance of Context in this approach. This context plays the role of the configuration for the CDMM-F framework. It is a graph-like structure, so the disadvantages of the concept of configuration mentioned above are limited as a result. It is worth noticing here that there are two kinds of contexts: the static context, which helps to create static structures with well-defined responsibility (meta-models) [26, 23, 24, 25]; and the dynamic context, which helps to enrich functionalities of the static structure [3, 2, 4]. This article is focused on the static contexts only.

Thus, the natural application field for this approach is the creation of software system elements with immutable functionality and mutable structure, according to the classification presented above. However, this article is focused on the simulation of the process of creation meta-models, so it is not dedicated to any application domain.

2. CDMM-P Basics

The CDMM-P Paradigm was introduced in [26] and the special role of Context was illustrated in [23]. This paper presents the most important concepts of this approach.

The main idea of the CDMM-P is to assume that associative relationships (UML composition, aggregation, association) between classes (pure entity classes) are represented in the form of classes (entity relationship classes) and all these classes are not interrelated in any form in their source codes. The objects of entity relationship classes are injected into pure entity classes at run time on the basis of the graph-like configuration file. Thus, the mentioned file plays the role of the static context for the CDMM-F framework that supports the CDMM-P paradigm. This paradigm may be applied for the implementation data layer of target domain-specific software systems as well as just for the creation of graph modeling languages, like in the case of this article. In consequence, a meta-model architect can design a modeling language from scratch or can customize an existing modeling language (e.g. UML). In the last case, he/she can remove unnecessary elements from the UML and/or add extra elements to the UML meta-model. The meta-model created this way may be also the subject of evolutionary changes together with models created in the former versions of the modeling language.

The concept of the responsibility division introduced by the CDMM-P is illustrated in Figure 1 for the sample meta-model.
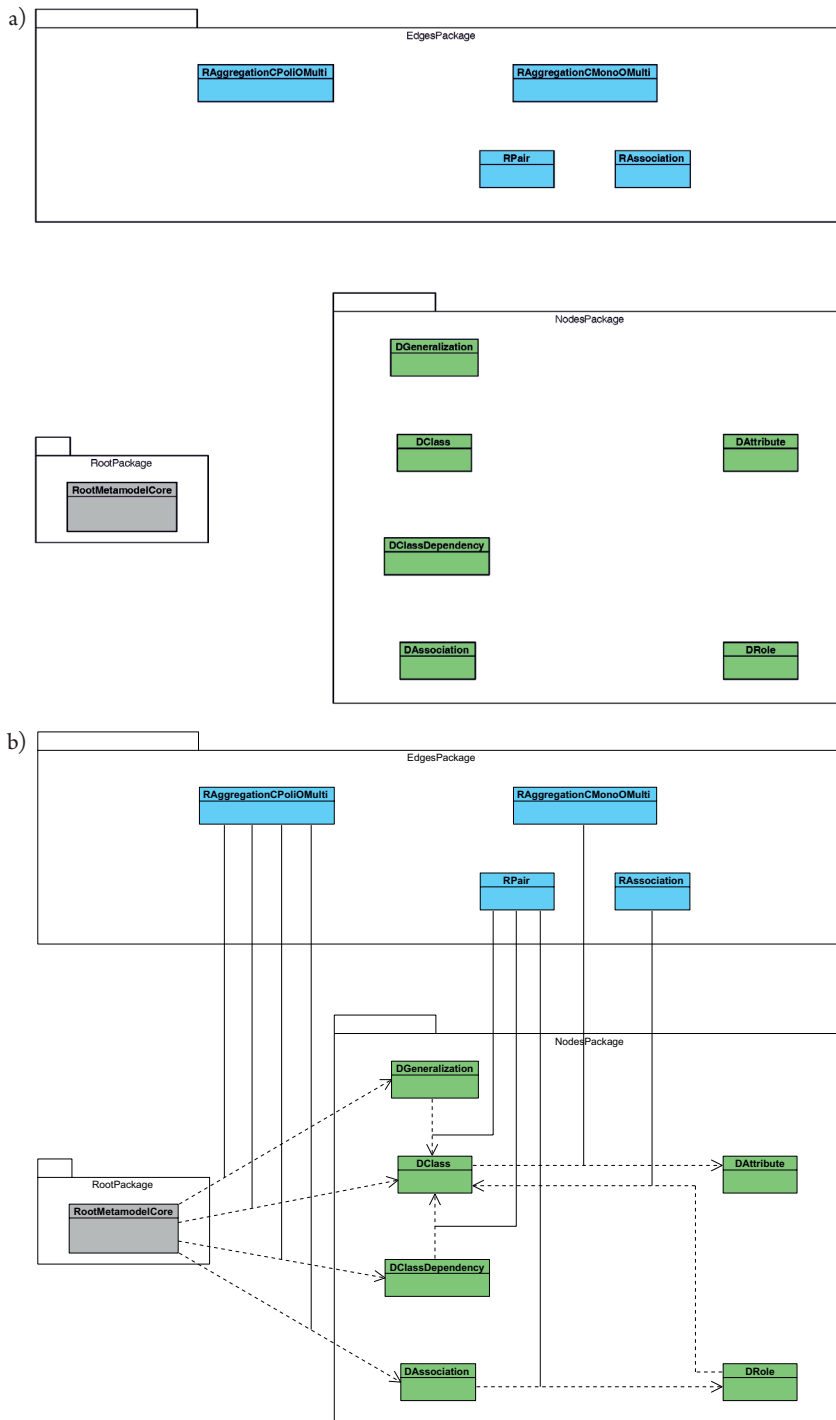
Fig. 1. Decomposition of responsibilities introduced by CDMM-P paradigm: a) unrelated meta-model classes, b) inter-related meta-model classes after relationship injections

The following color convention is applied in diagrams presented in Figure 1:
- ▶ Grey – framework elements that are immutable, as they belong to the framework,
- ▶ Green – user-defined meta-model elements representing meta-model nodes,
- ▶ Blue – user-defined meta-model elements representing meta-model edges.

It is worth noting that the concept of CDMM-P is based on open ontologies. This is new in comparison to the traditional closed ontology based modeling standards, like MOF, UML, MDA. As far as the author is aware, there are no similar solutions discussed in the literature, but some common ideas can be found in the context of ontologies. The open ontology concept not connected to software engineering is presented in [5, 10, 11]. There are some papers focused on the application of ontologies to domain model construction [8, 6, 22, 12] and its customization [20] dedicated to vertical OMG standards. Application of ontology for static class model inference [9] and for meta-language construction [18] are also known. The ontology can be used for application design, like in the case of JOINT system [16]. Ontologies can be designed from MOF-based MDA-compliant meta-model [7] or vice-versa [1].

3. Fundamentals of the CDMM-F Architecture

The CDMM-F framework was presented in [24]. Here, we present only the basics of its architecture that are relevant in the context of the simulation of the meta-modeling process.

The architecture of the CDMM-F framework was created in a form that fulfills the following criteria:
- ▶ should support CDMM-P paradigm,
- ▶ should be as convenient for the client of this framework as possible.

In order to satisfy the first criterion, the following technologies were chosen: Java, Spring and AspectJ. The graph configuration file is implemented in the form of a Spring application context file. The injection mechanism is based on injecting default interface implementations supported by both Spring and full version of AspectJ.

The second criterion is satisfied by an exchangeable API implementation and by introduction of proxy layer. The last element was introduced to eliminate conflicts between the names of methods injected from more than one interfaces.

4. Sample Meta-Model

In this section, a sample meta-model is shown in order to illustrate the concept of CDMM approach for defining modeling languages. It is then explained on the basis of the CDMM concept that relationship classes tend to be more complex than node classes of the meta-model. The classification of relationship classes is also introduced in this section. This classification is general, but it refers to the sample meta-model just to point the relationship classes under consideration.

The simple, but powerful, from the application perspective, sample modeling language is shown in Figure 1b. It consists of the three following packages, like in the case of each CDMM compliant modeling language:

- RootPackage – package containing CDMM-F framework elements (grey classes),
- NodesPackage – package containing user-defined meta-model node classes (green classes),
- EdgesPackage – package containing user-defined meta-model edge classes (blue classes)

All user-defined classes are implemented as completely independent of one another.

In order to define a new required modeling language, the CDMM-F user (meta-model architect) should:

- customize existing meta-modeling standard,
- customize his/her former meta-models,
- define new meta-model from scratch,
- reuse his/her former meta-models.

The last item is not interesting from the perspective of this article. In all remaining cases, the meta-model architect probably should introduce some nodes of a meta-model graph (meta-model classes) and/or introduce some new kinds of meta-model graph edges (meta-model relationships).

It seems from the analysis of available meta-models and from the IT market experience that new nodes are introduced more frequently than new edges. That is why the answer to the question if the edges should be injected into nodes or vice-versa is that nodes should be injected into the relationship. In consequence, the introduction of new node classes is simpler than the introduction of new edge classes. It increases the risks of the meta-modeling process connected to the implementation of relationship classes. That is why the simulation process is focused on this aspect of meta-modeling.

There are the following kinds of relationship classes when nodes are injected into edges:

- originated in separate parent class after injection (like RAggregationCMonoOMulti, RAssociation, RPair),
- originated in shared parent class after injection (like RAggregationCPoliOMulti),
- terminated in single object (like RAssociation, RPair),
- terminated in many objects (like RAggregationCMonoOMulti, RAggregationCPoliOMulti).

The main implementation risk is connected to correct handling of the dual nature (class sharing, number of objects) of each relationship class. That is why these classes should drive both testing and simulation processes.

5. Simulation of Meta-Modeling Process

The problem of testing model-driven tools is very complex and typically is performed in a way common for other kinds of software. However, the approach for testing CDMM-F is special and could also be applied for other software systems based on models.
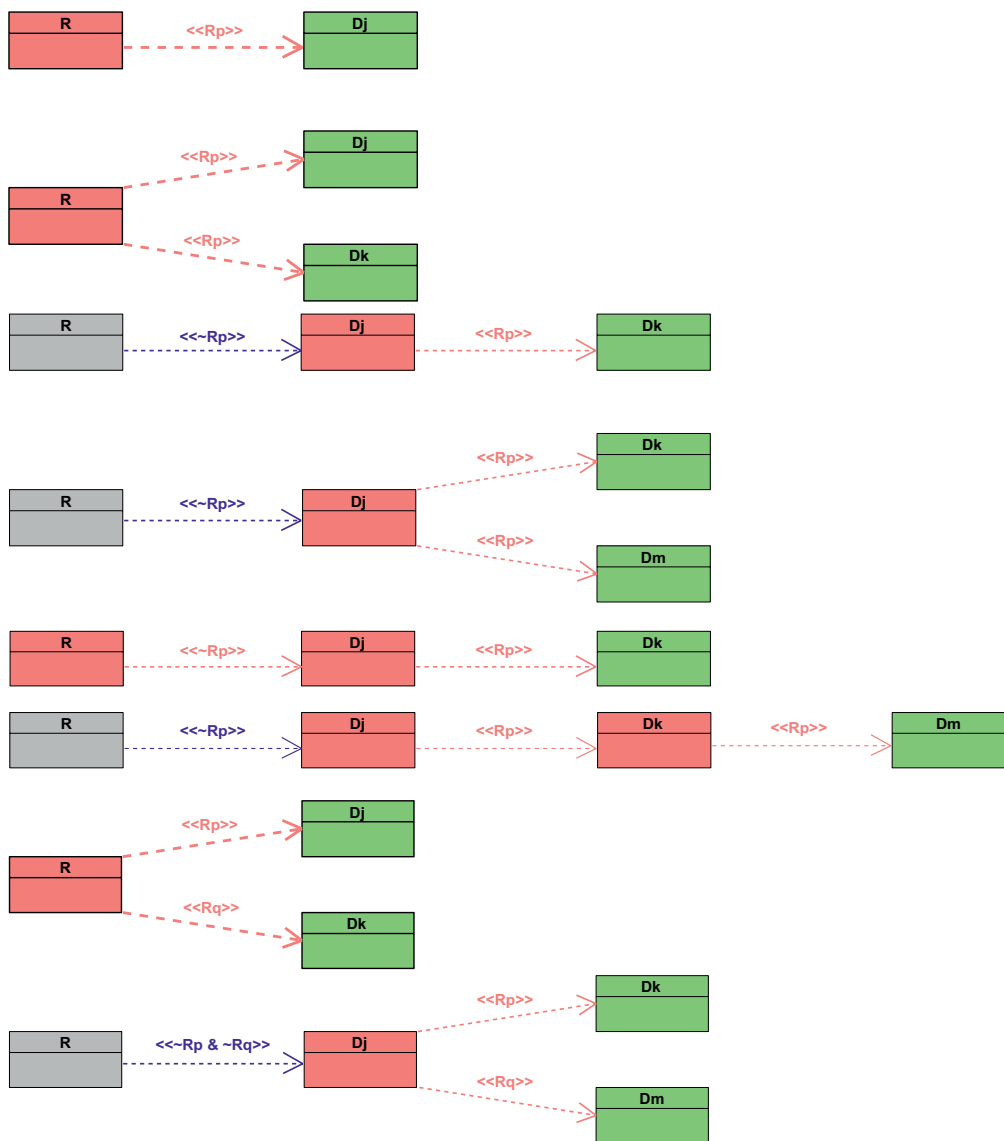
Fig. 2. Set of meta-model graphs identified as test kernels

Two testing stages were applied for the CDMM-F quality verification purposes:

▸ manual creation of specially designed meta-models,
▸ automated simulation of the usage of the CDMM-F framework in production.

The first stage was described in detail in [23]. Theoretical analysis of risks was performed first to create meta-models, which are useful for testing. Then, meta-models were created to address these risks. The meta-models taken into account are presented in Figure 2.

The following color convention is applied in diagram presented in Figure 2:
- ► Grey – framework elements that are immutable, as they belong to the framework,
- ► Green – user-defined meta-model elements representing meta-model nodes,
- ► Blue – user-defined meta-model elements representing meta-model edges,
- ► Red – meta-model elements that are subject of test.

From the perspective of the title of this paper, the second stage that is focused on simulation is more interesting. The simulation was designed according to the risk-driven rule, which is good for simulation purposes. The goal of simulation was verification of the quality of the CDMM-F correctness for many application context files. The risks are focused on manually created models, which were called test kernels. The simulation process idea was to surround each test kernel by generated pseudorandom graphs. They were called test contexts. Therefore, the simulation addressed the risk of a wrong cooperation of test kernels with the rest of almost any meta-model. This approach limited simulation effort costs and maximized the chance to identify potential problems connected to the implementation and usage of the CDMM-F framework.

The simulation process was performed in several stages:
- ► the set of meta-model graph nodes and the set of meta-model edges (two sets of classes) was prepared,
- ► all possible graphs built of these classes were generated automatically (the size of graph was limited),
- ► pattern matching algorithm was executed to recognize graphs that contained test kernels,
- ► manual creation of client code scanning meta-model via API for each recognized graph took place.

In order to further minimize the costs, the deterministic algorithm for generating graphs was not implemented. However, in place of it the non-determinism contained in Java hash tables implementation and included in Jung (Java Universal Network/Graph Framework) framework was used. It helped to surround risk kernels presented in Figure 2 by risk contexts – graphs generated by non-deterministic algorithm.

6. Simulation-Based Testing

The typical approach to the verification of the quality of model-driven systems, such as the CDMM-F one, is via testing. In the case of the subject, system tests were also implemented in iterative software development process. However, they were limited to unit tests. In fact, the CDMM-F framework should also be verified via integration tests. These tests are typically performed in a form that is not enough in this case – testers tend to manually define and implement only some non-trivial data structures that drive integration testing. This observation led to the significant improvement of the traditional approach, as the typical approach was exchanged by an automatic generation of a large set of data structures and thus integration testing became a simulation process.

Simulation technique and testing have similar goals – they are applied in order to maximize the probability of error identification by IT company customers. That is why software development company staff are interested in finding as many errors as possible – typically via testing. Nevertheless, both approaches do not guarantee that the software system will be finally free of errors as well as the verification process may not detect errors. Therefore, the IT companies go further – they try to maximize the probability that the product quality verification process (an investment) will find some errors. The best technique is to perform product and process risk analysis and to elaborate the testing strategy (also known from RUP as test plan) that maximizes the chance for finding errors.

The same is true both for the testing and the simulation technique. During implementation of CDMM-F, the simulation did not detect any errors, in contrast to unit-testing. This fact resulted from the asymmetry that was intentionally introduced to the development process. The main stress was put on careful design, iterative software development process and intensive iterative testing. The simulation was performed at the end of the process – thus not iteratively. This approach resulted from the very high risk level of new technology implementation. In contrast to typical production process, the success of the system creation was not guaranteed. In addition, the feasibility study approach cannot be performed, as the system itself is its feasibility study. That is why the investment into simulation was postponed in this special case. Thanks to the fact of simulation delay, the cost of the development was low and the risk of overinvestment was controlled. However, the duration of implementation was extended and the project risk was moved to the end of the simulation process. In the IT industry, there is usually no time for such careful design and testing due to time pressure. In addition, in this situation, the importance of the presented simulation technique grows significantly. The simulation allows to move the responsibility from design just to the simulation while keeping development cost low, allows to reduce the development process time and to address risk early if the simulation process is performed iteratively.

Manually created unit tests for CDMM-F were focused just on test kernels. The simulation process was executed for these test kernels surrounded by test contexts. As it was already mentioned above, the simulation process did not identified any defects. Some assumptions were made regarding the meta-model graphs generated during the simulation process. The graphs were simple directed and connected graphs and they did not contain transitive relationships or N-ary relationships. The number of nodes generated by the simulation was limited to the doubled number of the nodes in the largest test kernel, that is to 8 nodes. The test kernels were identified among the graphs generated by non-deterministic algorithm in loops limited to 20,000 iterations. It was observed during the experiments that exceeding the number of loops above this limit does not produce a noticeable number of new graphs, thus it is ineffective. The number of all different graphs generated this way was equal to 3100, while the theoretical number of such graphs is 882033440. The test kernels were found in 2800 graphs. Thus, the effectiveness of generating graphs, interesting from the testing perspective, was 90%. The number of graphs generated in this approach does not seem to be large enough in comparison to the theoretical one, but it is very attractive from the testing point of view, especially when compared to manual graph/test defining process.

7. Conclusions

The CDMM-F framework usage was the subject of the simulation process. The goal of this process was to check how the system might behave in a real production environment. A new approach used for the model-driven software system confirmed that this approach is useful for such a system. Moreover, the verification results obtained from the simulation process confirmed that this is a good approach to such verification, as the costs are naturally limited by this approach. At the same time, the risk-driven approach to simulation helps to maximize the probability of the success of this process, that is – to identify problems. The subject is interesting from the quantitative point of view and there are plans to investigate it in the future.

References

[1] Aßmann U., Zschaler S., Wagner G., *Ontologies, meta-models, and the modeldriven paradigm*, Calero C., Ruiz F. & Piattini M., eds, Ontologies for Software Engineering and Software Technology, Springer, 2006, 249–273.

[2] Bettini L., Bono V., *Type safe dynamic object delegation in class-based languages*, Proc. of PPPJ, ACM Press, 2008, 171–180.

[3] Bettini L., Capecchi S., Damiani F., *A mechanism for flexible dynamic trait replacement*, FTfJP '09, Genova 2009.

[4] Bono V., Damiani F., Giachino E., *On traits and types in a java-like setting*, TCS 2008 (Track B), Vol. 273, Springer, 2008, 367–382.

[5] Calero C., Ruiz F., Piattini M., *Ontologies for Software Engineering and Software Technology*, Springer, 2006.

[6] Djurić D., Devedžić V., *Magic Potion: Incorporating new development paradigms through meta-programming*, IEEE Softw. 27(5), 2010, 38–44.

[7] Djurić D., Gašević D., Devedžić V., *Ontology modeling and MDA*, Journal on Object Technology 4(1), 2005, 109–128.

[8] Djurić D., Jovanović J., Devedžić V., Šendelj R., *Modeling ontologies as executable domain specific languages*. presented at the 3rd Indian Software Eng. Conf., 2010

[9] Falbo R., Guizzardi G., Duarte K., *An ontological approach to domain engineering*, Procs. 14th Int. Conf. on Software Eng. and Knowledge Eng., 2002.

[10] Gašević D., Djurić D., Devedžić V., *Model Driven Engineering and Ontology Development*, Springer-Verlag, 2009.

[11] Gašević D., Kaviani K., Milanović M., *Ontologies, software engineering*, Handbook on Ontologies, Springer-Verlag, 2009.

[12] Guizzardi G., *Ontological foundations for structural conceptual models*, Telematica Instituut Fundamental Research Series 15, 2005.

[13] Guizzardi G., *On ontology, ontologies, conceptualizations, modeling languages, and (meta) models*, Frontiers in Artificial Intelligence and Applications, Vol. 155, Conference on

Databases and Information Systems IV, IOS Press, Amsterdam, 18–39; Selected Papers from the Seventh International Baltic Conference DB and IS 2006, 2007.

[14] Herrmannsdörfer M., *Evolutionary Metamodeling*, PhD thesis, Technical University in Munich, 2011.

[15] Herrmannsdörfer M., Ratiu D., *Limitations of automating model migration in response to metamodel adaptation*, Proc. of the Joint ModSE-MCCM Workshop on Models and Evolution, 2009.

[16] Holanda O., Isotani S., Bittencourt I., Elias E., Tenório T., *Joint: Java ontology integrated toolkit*, Expert Systems with Applications 40, 2013, 6469–6477.

[17] Iovino L., Pierantonio A., Malavolta I., *On the Impact Significance of Metamodel Evolution in MDE*. Journal of Object Technology 11(3), 2012, 1–33.

[18] Laarman A., Kurtev I., *Ontological meta-modelling with explicit instantiation*, [in:] Brand M. van den, Gašević D., Gray J. (eds.), SLE 2009, number 5969 in LNCS, Springer-Verlag, Berlin, 2010, 174–183.

[19] Langer P., Wimmer M., Brosch P., Herrmannsdörfer M., Seidl M., Wieland K., Kappel G., *A posteriori operation detection in evolving software models*, The Journal of Systems and Software 86, 2013, 551–566.

[20] Peng X., Zhao W., Xue Y., Wu Y., *Ontology-based feature modeling and application-oriented tailoring*, Reuse of Off-the-Shelf Components, Springer-Verlag, New York 2006, 87–100.

[21] Ruscio D. di, Iovino L., Pierantonio A., *Coupled Evolution in Model-Driven Engineering*. IEEE Software 29(6), 2012, 78–84.

[22] Tairas R., Mernik M., Gray J., *Using ontologies in the domain analysis of domain-specific languages*, Models in Software Engineering, Springer-Verlag, New York 2009, 332–342.

[23] Zabawa P., *Contex-Driven Meta-Modeling Framework (CDMM-F) – Context Role*. Technical Transactions, 1-NP, 2015, p. 105–114, DOI: 10.4467/2353737XCT.15.1 19.4156.

[24] Zabawa P., *Contex-Driven Meta-Modeling Framework (CDMM-F) – Internal Structure*. submitted for publication, 2015.

[25] Zabawa P., Nowak K., *Context-Driven Meta-Modeling – Simple Horizontal Case-Study*, submitted for publication, 2015.

[26] Zabawa P., Stanuszek M, *Characteristics of the Context-Driven Meta-Modeling Paradigm (CDMM-P)*, Technical Transactions, Vol. 3-NP/2014, 123–134.

Bartłomiej Macherzyński (bartlomiej.macherzynski@wp.pl)
Institute of Business Management, Faculty of Management, Częstochowa University of Technology

Maria Włodarczyk-Makuła (mwm@is.pcz.czest.pl)
Department of Chemistry, Water and Wastewater Technology, Faculty of Infrastructure and Environment, Częstochowa University of Technology

Ewa Ładyga
Institute of Mathematics, Faculty of Mechanical Engineering and Computer Science, Częstochowa University of Technology

Władysław Pękała
Department of Management Engineering, Faculty of Management, Częstochowa University of Technology

Comparison of parameters co-fermentation process of municipal sewage sludge with excess sewage sludge from treated coking wastewater

Porównanie parametrów procesu kofermentacji mieszaniny osadów komunalnych z nadmiernymi osadami z oczyszczania ścieków koksowniczych

Abstract

The study presents results concerning changes of physicochemical properties and biogas production during the co-digestion process. The sample constituted a mixture of raw and excess sludge that was inoculated and fermented. The sample is the abovementioned mixture with an addition of excess sewage. In the assumed test, the conditions of technological parameters of sewage sludge fermentation and its mixtures with sewage sludge coke did not differ from each other by more than 25% Therefore, excess sewage sludge from treated coking wastewater can be neutralized in the process of fermentation along with municipal sewage sludge provided a constant quality-quantitative control of sewage sludge and procedural parameters.

Keywords: biogas, co-fermentation, sewage sludge, sewage sludge from treated coking wastewater

Streszczenie

W pracy przedstawiono wyniki badań dotyczące zmian właściwości fizyczno-chemicznych oraz produkcji biogazu podczas procesu kofermentacji. Próbkę kontrolną stanowiły osady komunalne zaszczepione przefermentowanymi. Próbka badana to mieszanina komunalnych z dodatkiem nadmiernych osadów koksowniczych. W przyjętych warunkach badań wartości parametrów technologicznych fermentacji osadów komunalnych oraz ich mieszaniny z osadami koksowniczymi nie różniły się od siebie więcej niż o 25%. Zatem osady koksownicze mogą być unieszkodliwiane w procesie fermentacji wraz z osadami komunalnymi pod warunkiem stałej kontroli jakościowo-ilościowej osadów i parametrów technologicznych.

Słowa kluczowe: biogaz, kofermentacja, osady ściekowe, osady ze ścieków koksowniczych

1. Introduction

The anaerobic biological stabilization is currently the most common process of neutralizing sewage sludge in large wastewater treatment plants. Mineralization of biodegradable organic substrates is followed by an improvement of the drainage efficiency and a decrease of pathogenic organisms. The composition of fermented substrate depends on the quantity of the produced biogas and its composition. The content of methane in biogas varies from 50 up to 80% and depends on the content of proteins, carbohydrates and fats in sewage sludge subjected to the fermentation. In addition to the type of substrate, the fermentation process also depends on temperature, pH, process duration, presence of toxic substances, substratum load chambers, concentration of easily digestible components for micro-organisms and appropriate conditions of their development [1, 2]. Combustion of biogas allows for energy recovery. Therefore, produced biogas is used above all for the needs of covering demand for thermal energy and electricity. It is used for the needs of sewage treatment plants, such as heating digesters or powering devices for mixing and aerating [3, 4]. Taking into account the need to develop effective treatment methods of excess sewage sludge from treated coking wastewater, studies on the co-fermentation of this sewage sludge with municipal sewage sludge were conducted. An aim of these studies was to assess the effect of excess sewage sludge from treated coking wastewater on the technological parameters of fermentation, mineralization degree of organic compounds and biogas production.

2. Experimental procedure

2.1. Fermentation process

Sewage sludge coming from municipal sewage treatment plant and sewage sludge from coking sewer plant were used in the study. Primary sewage sludge and excess sewage sludge as well as the fermented sewage sludge were collected. Primary sewage sludge and excess sewage sludge from a primary and a secondary settle tank were collected, respectively. Fermented sewage sludge was collected from the fermentation chamber. The samples were collected as temporary. In the coking wastewater treatment plant, the sewage treatment is performed by the processes of denitrification and nitrification. The sewage flows through a gravel filter, tar separator, and desorption column before it is fed to the biological part of the treatment plant and is directed to the averaging tank. The excess sewage sludge with treatment wastewater coking was sampled as temporary (from recycled tank of sewage sludge). The anaerobic digestion (fermentation) tests were conducted in bioreactors fitted with nozzles intended for measuring biogas pressure. The following mixtures were prepared for the fermentation studies:
- ▸ municipal sewage sludge (mixture of primary sewage sludge and excess sewage sludge with the addition of fermented sewage sludge (1:1.5 v/v) as an inoculum) – control sample (K);
- ▸ municipal sewage sludge amended with excess sewage sludge from treated coking wastewater (10:1 v/v) – sample (B).

The sewage sludge mixtures were incubated for 16 days with no access to light in a thermostat at a constant temperature of 37 ± 2°C. The fermentation process was carried out in glass reactors with a volume of 1 L with a single power supply. The volume of sewage sludge was 0.7 L. The process was carried out in 6 reactors with the same mixture of sewage sludge. After 4, 8, 12 and 16 days, one reactor was eliminated and a necessary analysis was conducted. The process was completed in 16 days because the amount of secreted biogas was difficult to measure with a manometer.

2.2. Analytical methodology

In order to determine the follow of the digestion process, the selected physical-chemical properties of the sewage sludge were determined. The total suspended solids (TSS) and fixed suspended solids (FSS) of the sewage sludge before and after 4, 8, 12 and 16 days of incubation were analyzed. In the supernatants, the pH, alkalinity, chemical oxygen demand (DCOD) and volatile fatty acids (VFA) were determined. The above mentioned analyze were carried out before of the digestion process and after 4, 8, 12 and 16 days of samples incubation. The determinations were made in accordance with the methodology specified by Hermanowicz [5].

During the process, the atmospheric pressure and biogas pressure using the manometer in 24-hour intervals were monitored. The daily biogas volume using the Boyle-Mariott was calculated. The methane and carbon dioxide contents in biogas were determined four times. The analysis of biogas composition was performed using a gas chromatograph with a thermal-conduction detector (GC-TCD) (model Agillent GC 6890).

3. Results and discussion

3.1. Changes in the physico-chemical properties of sewage sludge during the fermentation process

The results of the physical-chemical analysis of sewage sludge during 16 days of stabilization are shown in Table 1.

In test sludge (K), there was a decrease in the contents of the total suspended solids by 21%. The share of organic matter in sludge after 16 days of incubation constituted 54% of the dry mass. Decomposition degree of organic matter was 29%. The contents of organic compounds determined as DCOD in supernatants from municipal sewage sludge (K) decreased by 88%.

In a mixture of municipal sewage sludge with industrial, the contents of dry matter before co-digestion process was 18.4 g/L. After the co-digestion process, there was a decrease in dry matter content by 18% (Table 2). Percentage of organic matter in fermented sludge was 54%. Decomposition degree of organic matter was 23%. The loss of organic compounds expressed with DCOD in supernatants was at a level of 81%.

Table 1. Changes in the physico-chemical properties of sewage sludge during the fermentation process – control sample

Ratio	Unit	Process time, day				
		0	4	8	12	16
pH	–	7	7.6	7.6	7.7	7.8
DCOD	mg O_2/L	970	660	320	241	110
Total suspended solids (TSS)	g/L	18.9	17.6	16.9	16.2	15.0
Fixed suspended solids (FSS)	g/L	7.5	7.2	7.1	7.1	6.9
	%	40	41	42	44	46
Volatile suspended solids (VSS)	g/L	11.4	10.4	9.7	9.1	8.1
	%	60	59	58	56	54

Table 2. Changes in the physico-chemical properties of sewage sludge during the co-fermentation process

Ratio	Unit	Process time, day				
		0	4	8	12	16
pH	–	7.3	7.6	7.7	7.8	7.6
DCOD	mg O_2/L	1300	940	400	390	240
Total suspended solids (TSS)	g/L	18.4	16.4	16.2	16.0	15.1
Fixed suspended solids (FSS)	g/L	7.9	7.5	7.4	7.2	7.0
	%	43	46	46	45	46
Volatile suspended solids (VSS)	g/L	10.5	8.9	8.8	8.8	8.1
	%	57	54	54	55	54

The VFA ratio to alkalinity was shown in Figure 1. The alkalinity after fermentation, determined in supernatants, was 3.55 and 3.50 g $CaCO_3$/L appropriately in the K and the B sample. The ratio of volatile fatty acids to alkalinity, decreased during the process, and after the process in test sludge, it was 0.11. In a mixture of municipal sewage sludge with excess sewage sludge from treated coking wastewater, the value of the VFA quotient to alkalinity did not exceed 0.90.
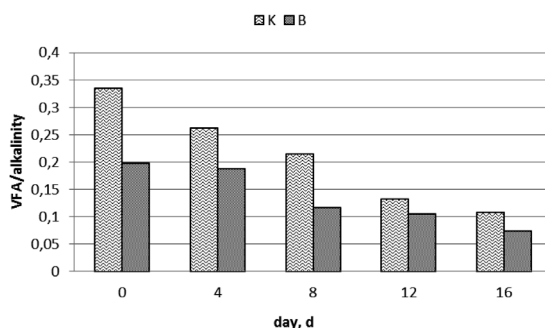

Fig. 1. The ratio of VFA to alkalinity

3.2. Biogas and methane production during the fermentation and co-fermentation processes

The amount of biogas produced during each day of fermentation was presented in Table 3. In municipal sewage sludge (K), the highest biogas production was achieved on the 3rd day (1.4 L), whereas in the mixture of municipal sewage sludge with excess sewage sludge from treated coking wastewater, it was achieved on the 4th day and it was 1.2 L. This might show that there is a temporary interruption of the co-digestion process (elongated lag-phase) in the presence of industrial sewage sludge. Total biogas production ranged from 0.94 L/g VSS (1.0 L) up to 1.03 L/g VSS (11.7 L) and the average methane content in biogas was between 61–69%. The amount of methane in relation to the contents of test sludge (K) was at the level of 8.1 L. About 28% less (5.9 L) compared with test sludge was received during co-digestion of mixtures of municipal sewage sludge with excess sewage sludge from treated coking wastewater.

Table 3. Daily as well as total biogas and methane production during the fermentation and co-fermentation processes

Sewage sludge/ Unit	Process time, day							
K	1	2	3	4	5	6	7	8
Σ L a)	1.3	2.7	4.1	5.4	6.4	7.3	8.2	8.9
Σ L b)	1.0	2.0	3.0	4.0	4.7	5.3	5.9	6.4
K	Process time, day							
	9	10	11	12	13	14	15	16
Σ L a)	9.5	10.0	10.6	10.9	11.1	11.4	11.6	11.7
Σ L b)	6.8	7.1	7.4	7.6	7.8	7.9	8.0	8.1
B	Process time, day							
	1	2	3	4	5	6	7	8
Σ L a)	1.0	2.1	3.2	4.4	5.3	6.1	6.8	7.3
Σ L b)	0.6	1.2	1.9	2.6	3.1	3.5	3.9	4.3
B	Process time, day							
	9	10	11	12	13	14	15	16
Σ L a)	7.8	8.3	8.8	9.1	9.3	9.6	9.8	10.0
Σ L b)	4.6	4.9	5.2	5.4	5.5	5.6	5.8	5.9

a) total production of biogas

b) total production of methane

Basic co-digestion parameters of municipal sewage sludge with excess sewage sludge from treated coking wastewater were presented in Table 4. The load of digesters was in a range of 0.40–0.55 g VSS/L d. The difference between maximum methane production (V_{max}) and the actual obtained value after 16 days was determined during fermentation. Its value corresponded numerically to the value of methane potential, residual in sewage sludge and changed in a range from 1.0 up to 1.5 L. Favorable results were obtained during co-digestion of municipal sewage sludge, where untapped methane potential constituted 10%. In studies conducted by Montusiewicz, the untapped biogas potential in sewage sludge ranged from 11.6 up to 14.1% [6].

During the fermentation process of municipal sewage sludge, as well as with excess sewage sludge from treated coking wastewater, the constant rate of generated methane ranged from 0.111 up to 0.147 d^{-1}. In studies conducted by Myszograj, constant rates for excess sludge ranged from 0.179 up to 0.203 d^{-1}, and for bio-fraction of municipal waste, they ranged from 0.077 up to 0.137 d^{-1} [7]. Both during co-digestion of municipal sewage sludge with excess sewage sludge from treated coking wastewater or with bio-fraction of municipal sewage sludge, the constant rates were on the same level.

Table 4. Parameters and the energy balance of the co-fermentation process

Parameters	Unit	K	B
Load of organic compounds in the fermentation chambers	g VSS/L d	0.55	0.40
Percentage of the organic substance decomposition	%	29	23
Production of biogas during digestion process	L	11.7	10.0
	L/g TSS	0.62	0.54
	L/g VSS	1.03	0.94
Content of methane in biogas on average	%	61	63
Production of methane during digestion process	L	8.1	5.9
	L/g TSS	0.43	0.39
	L/g VSS	0.71	0.68
The maximal (theoretical) methane production (Vmax)	L	9.1	7.4
	L/g TSS	0.48	0.40
	L/g VSS	0.80	0.70
The potential of methane remaining in sewage sludge	%	10	20
Constant rate of the methane production, k	d^{-1}	0.147	0.111
Nonlinear estimation error	L	0.14	0.16
Coefficient of determination, R^2	–	0.995	0.975

In the assumed test conditions of technological parameters of sewage sludge fermentation and its mixtures with sewage sludge, cokes did not differ from each other by more than 25% (total biogas productions, decomposition degree of organic matter, changes in the content of organic compounds expressed with DCOD, loss of dry matter and methane content in biogas).

Literature data show that, during mesophilic fermentation, the VFA concentration should be in the range from 50 to 500 mg CH_3COOH/L; alkalinity should be from 3.00 to 5.00 g $CaCO_3/L$, while the reduction in COD should be within the limits of 65–85%, and pH value should be within the limits of 7.2–8.2 [8, 9].

Studies conducted by Fukas-Płonka et al. showed that the loss of dry matter of sewage sludge in the fermentation process was 18%, and the decomposition degree of organic matter was at the level of 22%. Total biogas production was 2.5 L, while the amount of produced biogas from 1 g VSS entered into the reactor was at the level 0.18 L/g VSS. During fermentation of excess sludge, the total quantity of biogas was 1.2 L, which, expressed in the amount of dry organic matter, was 0.07 L/g VSS. The loss of organic compounds did not exceed 15% [10]. In other studies, in which preliminary sewage sludge was the research material, the concentration of volatile fatty acids in fermented sewage sludge fluctuated from 467 to 664 mg CH_3COOH/L, and the alkalinity from 3.24 to 3.51 g $CaCO_3/L$. The quotient of VFA/alkalinity was in a range from 0.14 up to 0.19. The loss of dry matter ranged from 20 to 28%, and organic matter from 28 to 35% [11].

In Borowski et al. studies, the loss of organic dry substance in excess sludge was recorded in the range from 23.7 to 43.0%, and the amount of biogas per organic dry matter unit was on average 0.3 L/g VSS. During the fermentation of preliminary sludge, the decomposition degree of organic matter was 38%, and the amount of biogas in relation to 1 g VSS was 0.27 L/g VSS [12, 13].

In earlier studies of authors published in the Annual Set The Environment Protection [14], a mixture of municipal sludge and excess sludge was subjected to co-digestion from coke waste treatment. Sewage sludge samples were collected in the winter season. DCOD value in supernatants decreased by 47% in fermentation of municipal sludge. Biogas production for sludge unit volume from test sludge was 4.6 L, and the amount of produced biogas per 1 g VSS was 0.47 L/g VSS. After the co-digestion process of a mixture of municipal sludge and coke, the decomposition degree of organic substances was 22%, and organic compounds expressed with DCOD rate amounted to 44%. The total amount of biogas from sludge unit volume for mixtures of municipal sludge with coke was 4.0 L, while the amount of biogas produced from 1 g VSS entered into the reactor was at the level of 0.31 L/g VSS [14].

The described studies were conducted in similar conditions, but excess coke sewage sludge was collected in the summer season in the process of modernization of the coking battery. In this case, decomposition of organic compounds, both for municipal sludge and that involving coke, expressed with the DCOD rate, was 2-fold higher than in the winter season. In addition, the amount of biogas was higher during the digestion of sewage sludge collected in the summer season. Therefore, it is possible to state that the concentration of easily biodegradable compounds was higher in sewage sludge collected in the summer season
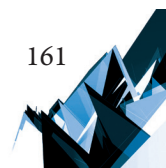
than the concentration of these compounds in sewage sludge collected in winter, readily biodegradable, resulting in greater amount of biogas compared to sewage sludge in the winter period. During the modernization of the coking battery, the production of coke was smaller, and simultaneously the concentration of toxic compounds was smaller, including polycyclic aromatic hydrocarbons (PAHs) in coke sewage sludge. This explains the production of a larger amount of biogas in the co-digestion process.

In studies on the fermentation of excess sludge conducted by Bohdziewicz et al., the removal degree of organic matter was 44.5%, and quotient of VFA/alkalinity – 0.1 [15]. Biogas production during fermentation of excess sludge was 0.30 L/g VSS, and the percentage of methane in biogas ranged from 51.3 to 72.0%. After the stabilization process, the biodegradation degree, determined on the basis of COD in excess sludge, was 41% [7].

Due to the loss of organic compounds, biogas production, and organic matter in fermented sludge, it is possible to state that municipal sewage sludge and mixture excess sewage sludge from treated coking wastewater were fermented well, since the values of studied sewage sludge parameters after the process were in a range given by other authors.

4. Conclusions

Based on the conducted studies, it is possible to present the following conclusions:
- ▶ Co-digestion of sewage sludge with excess sewage sludge from treated coking wastewater cannot exceed the mixing ratio of 10:1. While maintaining the above proportions, the technological parameters of sewage sludge fermentation and its mixtures with sewage sludge coke did not differ from each other by more than 25% (total biogas productions, decomposition degree of organic matter, changes in the content of organic compounds expressed with DCOD, loss of dry matter and methane content in biogas).
- ▶ Excess sewage sludge from treated coking wastewater can be neutralized in the fermentation process along with municipal sewage sludge provided that there is a constant quality-quantitative control of the sewage sludge and technological parameters. However, in order to confirm the above, it is necessary to conduct the study in a flow system.

References

[1] Sadecka Z., *Toksyczność w procesie beztlenowej stabilizacji komunalnych osadów ściekowych*, Monografie nr 105, Polska Akademia Nauk, Komitet Inżynierii Środowiska, Zielona Góra 2013.

[2] Podedworna J., Umiejewska K., *Technologia osadów ściekowych*, Oficyna Wydawnicza Politechniki Warszawskiej, Warszawa 2008.

[3] Bień J., Wystalska K., *Osady Ściekowe. Teoria i praktyka*, Wydawnictwo Politechniki Częstochowskiej, Częstochowa 2011.

[4] Sidełko R., Chmielińska-Bernacka A., *Zastosowanie reaktora kompaktowego do fermentacji metanowej odpadów komunalnych*, Annual Set The Environment Protection 15, 2013, 683–693.

[5] Hermanowicz W., Dojlido J., Dożańska W., Koziorowski B., Zerbe J., *Fizyczno-chemiczne badanie wody i ścieków*, Arkady, Warszawa 1999.

[6] Montusiewicz A., *Współfermentacja osadów ściekowych i wybranych kosubstratów jako metoda efektywnej biometanizacji*, Polska Akademia Nauk, Komitet Inżynierii Środowiska 98, Lublin 2012.

[7] Myszograj S., *Biochemical Methane Potential as Indicator of Biodegradability of Organic Matter in Anaerobic Digestion Process*, Annual Set The Environment Protection 13, 2011, 1245–1260.

[8] Kardos L., Juhasz A., Palko GY., Olah J., Barkacs K., Zaray GY., *Comparing of mesophilic and thermophilic anaerobic fermented sewage sludge based on chemical and biochemical tests*, Applied Ecology and Environmental Research, 9, 2011, 293–302.

[9] Álvarez A.A., Otero L., Lema J.M., *A methodology for optimising feed composition for anaerobic co-digestion of agro-industrial wastes*, Bioresource Technology 101, 2010, 1153–1158.

[10] Fukas-Płonka Ł., Janik M., *Fermentacja osadów nadmiernych*, EkoTechnika, 1, 2006, 52–56.

[11] Janosz-Rajczyk M., Dąbrowska L., Rosińska A., Płoszaj J., Zakrzewska E., *Zmiany ilościowo-jakościowe PCB, WWA i metali ciężkich w kondycjonowanych osadach ściekowych stabilizowanych biochemicznie*, Wydawnictwo Politechniki Częstochowskiej, Częstochowa 2006.

[12] Borowski S., Domański J., *Ocena procesu kofermentacji mieszaniny pomiotu kurzego, organicznej biomasy roślinnej i osadów ściekowych*, Ekologia i Technika, 4, 2009, 182-186.

[13] Borowski S., Domański J., *Kofermentacja pomiotu kurzego z osadami ściekowymi*, Ekologia i Technika, 3, 2012, 192–196.

[14] Macherzyński B., Włodarczyk-Makuła M., *Ocena możliwości unieszkodliwiania osadów koksowniczych w procesie kofermentacji*, Annual Set The Environment Protection, 17, 2015, 1142–1161.

[15] Bohdziewicz J., Kuglarz M., *Kofermentacja bioodpadów komunalnych i osadów ściekowych*, Ochrona Środowiska i Zasobów Naturalnych, 38, 2009, 36–43.
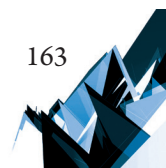
Roman Dyga (r.dyga@po.opole.pl)

Department of Chemical and Process Engineering, Faculty of Mechanical Engineering,
Opole University of Technology

Metal foams as structural packing in the construction of process equipment

Piany metalowe jako wypełnienia strukturalne w budowie aparatury przemysłowej

Abstract

The paper presents possibilities of the application of open-cell metal foams in the construction of process equipment. The article also describes results of own experimental studies on hydrodynamic and thermal phenomena occurring during fluid flow through channels packed with aluminium alloy foams. The collected experimental data enabled to determine, among others, pressure drops and the heat transfer coefficient, and to indicate main gas–liquid flow patterns.

Keywords: open-cell aluminium foam, gas–liquid flow, pressure drop, flow pattern, heat transfer

Streszczenie

W artykule przedstawiono możliwości wykorzystania otwartokomórkowych pian metalowych w budowie aparatury przemysłowej. Opisano wyniki własnych badań doświadczalnych dotyczących zjawisk hydrodynamicznych i cieplnych zachodzących podczas przepływu płynu przez kanały wypełnione pianami ze stopów aluminium. Zebrane dane eksperymentalne pozwoliły określić m.in. wartości oporów przepływu i współczynnika wnikania ciepła oraz wskazać podstawowe struktury przepływu gaz–ciecz.

Słowa kluczowe: otwartokomórkowa piana aluminiowa, przepływ gaz–ciecz, opory przepływu, struktury przepływu, wnikanie ciepła

1. Introduction

In the recent several years, there has been an increased interest in metal foams and their applications in the flow equipment. Open-cell metal foams are highly porous materials, in which metal has a form of a three-dimensional skeleton that forms relatively large and empty cells as adjacent polyhedral bodies. Such a structure gives the foams very high porosity, usually over 90%. High porosity and many "windows" joining individual cells allow fluid flow in the cellular space, which reduces energy costs of pumping the fluids through these materials. Moreover, open-cell foams have a high specific surface area, which in combination with low pressure drops makes them perceived more and more often as an alternative for other types of structural packing used in the construction of heat exchangers and mass exchangers. A relatively high thermal conductivity and a continuous skeleton structure that causes no heat resistance, which occurs at the interfaces of structural packing, makes foam applicable as specific fins on the external heat exchanging surface in thermal engineering. Technology allows for the production of foams from a wide spectrum of metal alloys. Foams are available that are made of materials that allow for their application in difficult working conditions, such as a high temperature or a chemically aggressive environment.

1.1. Metal foams in construction of process equipment

The literature presents information on the application of open-cell metal foam in the construction of compact heat-exchangers [3, 11], thermal storage [18, 20] and heat regenerators [2, 21], as well as chemical reactors [10, 19] including catalytic reactors [7, 13]. Moreover, foams can be used in evaporators of cooling equipment [6, 8] and solar collectors [22], as well as in column equipment [12, 15].

Studies on heat transfer in equipment filled with metal foams usually show significant (2 to 4 times) increase in the heat transfer coefficient in comparison with classic pipe and plate equipment not containing components increasing the heat transfer. According to Boomsm et al. [1] and Wang et al. [22], there may even be a 10-fold increase in the heat transfer coefficient. The authors of the paper [1] believe that an increased head transfer rate compensates increase in the demand of fluid pumping energy. As a result, heat exchangers with metal foams have greater heat transfer efficiency by up to 50% compared to plate heat exchangers. Metal foam heat exchangers also have a very good ratio of heat transfer rate to mass and volume of the exchanger. As reported by Ozmat et al. [11], it is possible to gain heat flux of up to 5000 kW/m².

As assessed by Youchison et al. [24], the structure of a foam skeleton provides relatively low pressure drops and a high heat transfer rate in comparison with sintered packed bed. Whereas Wang et al. [21] report better calorific effect of a foam exchanger in comparison with analogical equipment with copper mesh packing.

Quite different conclusions were drawn by the authors of the papers [14, 16]. Their studies involved a comparison of the heat transfer in tubular heat exchangers with heat transfer surface developed using metal foam and traditional fins. According to Sertkay et al. [16], the heat

transfer rate in the exchanger with intertubular spaces filled with metal foam is approx. 2 times lower than for lamellar fins. Similarly, Ribeiro and Barbosa [14] believe that exchangers with finned radiators have better thermohydraulic parameters.

Research works pay a lot of attention to foam applications in the flow boiling processes [6, 17]. Presence of foam temperature of the heating surface and shifts departure from nucleate boiling towards much higher heat flux [17, 23]. Hu et al. [6] report that heat transfer coefficient recorded during the flow of boiling coolant through a flat channel filled with metal foam is 1.5–2.6 higher than for boiling on flat surface (channel without packing). Even a higher difference (2–4 higher for the foam) occurs for boiling in pipes. At the same time, the authors of the paper [6] highlight the fact that presence of metal foam causes a significant increase in agent pressure drops, which contributes to a decrease in the cooling system efficiency.

An increase in heat transfer rate may be achieved using foam as packing of tubes of solar collectors. As stated by Wang et al. [22], the greater the heat transfer rate is as a result of flow disturbances in a boundary layer, the more intense the fluid mixing in the entire tube volume and an increased effective thermal conductivity due to foam in the pipe.

Available literature data indicate that despite an increasing number of research works, there are still difficulties in the determination of process effects obtained by the application of foams in the process equipment. There are numerous doubts or even contradictions regarding basic issues of heat transfers and flow hydrodynamic through cellular space of the foams. This is especially true for processes involving two-phase gas–liquid mixtures. So far, there has not been sufficient identification of the effect of flow conditions and foam geometrical parameters on pressure drops and changes in phase void fractions. There is no information on the flow pattern occurring during two-phase flow through metal foams and conditions of their formation.

Due to numerous gaps in knowledge, it was decided to conduct own experimental research on the effect of flow conditions, fluid properties and foam skeleton geometric parameters on the hydrodynamic and thermal phenomena in single- and two-phase gas–liquid flow through open-cell metal foams.

2. Scope and execution of experiments

The studies were conducted using three foams from aluminium alloys (Fig. 1) – two of AlSi7Mg alloy and one of Al 6101. The foams had similar porosity φ and a skeleton shape, but different geometric dimensions of the cells. Similarity of some foam parameters was necessary in order to clearly determine the effect of cell size on the thermal and flow processes occurring in the cellular space. Pore density was treated as a distinguishing factor of individual foams, which according to the foam manufacturers, was 20 and 30 PPI for AlSi7Mg foams and 40 PPI for Al 6101 foam. For metal foams, a term pore is used to indicate the "window" connecting adjacent cells (Fig. 1d). Pore and cell sizes were determined graphically based on microscopic image analysis of the foam skeleton. The images were taken at a 15x zoom with a scanning microscope. Per suggestions of the authors of the paper [9], equivalent diameter

was taken a cell size d_c of value equal to diameter of the circle of circumference equal cell circumference. An equivalent diameter of the pore was defined analogically d_p. Equivalent values were determined as averages from measurements of over one hundred cells and pores. The selected foam parameters are summarised in Table 1.
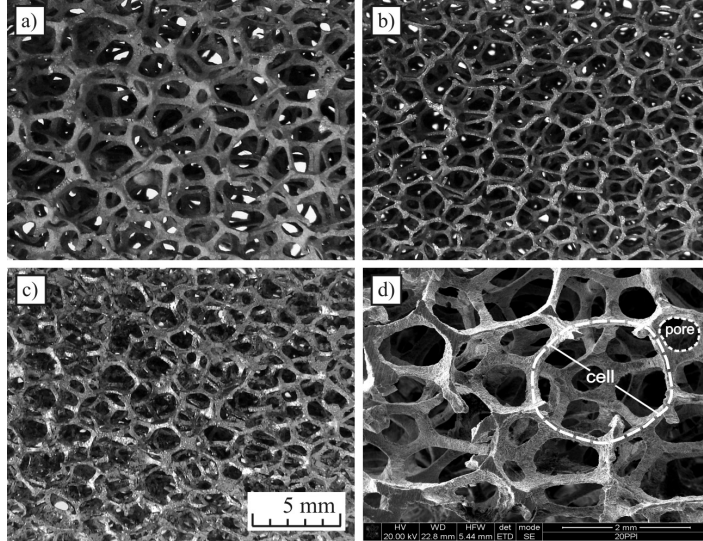

Fig. 1. Foams used in experiments: a) foam 20 PPI, b) foam 30 PPI, c) foam 40 PPI, d) microscopic image

An immediate purpose of the experimental studies was to measure pressure drops and changes in the temperatures of the fluid pumped through a channel filled with foams. For two-phase flows, void fractions of phases were measured and flow patterns were identified. Air, water and machine oil Velol-9Q were used as working liquids. The most important in terms of research subject, oil properties at 20°C were: viscosity $\eta_{ol} = 0.0086$ Pa·s, density $\rho_{ol} = 859.8$ kg/m³, specific heat $c_{ol} = 1848.8$ J/(kg·K), thermal conductivity $k_{ol} = 0.128$ W/(m·K).

Table 1. Specification of tested foams

Foam (alloy)	φ [−]	k_s [W/(m·K)]	$d_c \cdot 10^{-3}$ [m]	$d_p \cdot 10^{-3}$ [m]
20 PPI (AlSi7Mg)	0.9336	150.4	3.452	1.094
30 PPI (AlSi7Mg)	0.9435	189.4	2.255	0.712
40 PPI (Al 6101)	0.9292	189.4	2.386	0.824

The measurements were conducted using an experimental stand, of which the main component was a horizontal channel with an internal diameter of 0.02 m, fully packed with aluminium foams (for each type of foam an independent channel was made). In the central

part of the channel, there was a measurement section of 1.27 m in length, where pressure drops and changes in the temperatures of the fluids and the channel wall were measured. The measurement section was preceded by a flow stabilising section. Downstream of the measurement section, there was an outlet section made of plexiglass, which despite the presence of packing, allowed for the observations of two-phase flow patterns occurring in the channel. A measurement section of the channel was heated externally on the length of 1.18 m, using a resistance heater coiled around the channel. In the heated part of the channel, the metal foam was glued to the external surface of the channel using a thermally conductive epoxy-aluminium adhesive. The measurement section was insulated with mineral wool. A diagram of the test stand with the location of the measurement instruments is presented in Figure 2, while the real view of the measurement section is presented in Figure 3.

The test stand was supplied with air from a pneumatic unit. Water (demineralised) was pumped using a multi-stage impeller pump, while oil – gear pump. Fluid streams were measured using various types of flow-meters of a high accuracy class. For air stream, due to high pressure drops and related changes in the air density, mass flow metres were used.

The pressure drop was measured as the difference of pressures between channel points 1 m apart from each other. The measurements were conducted using a set of five piezoresistive differential pressure sensors with a total measurement range of 0–150.000 Pa. For the determination of the air density, excess pressure in the channel was also measured. Phase void fractions were measured using the so-called trapping method. At the same time, using pneumatically controlled diaphragm valves, the inlet and outlet of the measurement section were closed. The trapped in the channel liquid volume in relation to volume of channel measurement section corresponded to the liquid fraction in the gas–liquid mixture.
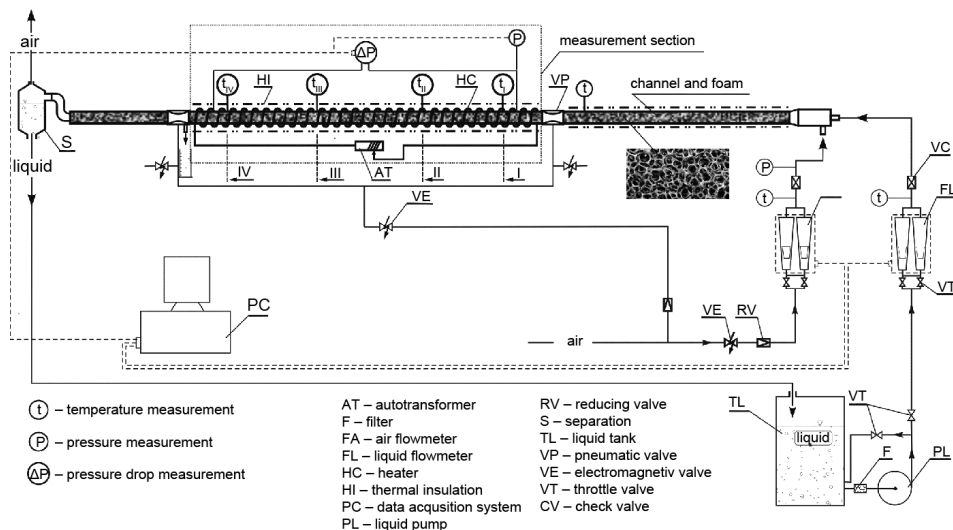

Fig. 2. Diagram of test stand

169

Temperatures of fluids and channel walls were measured using K-type thermocouples of 1 mm in diameter. Temperatures of the fluid and the wall were measured at four points along the channel (cross-section I, II, III and IV in Fig. 2). In each of the four cross-sections, 8 thermocouples were places. Measuring tips of five of them were inside the channel at different distances from its axis (in the vertical plane). Tips of three thermocouples were placed in the channel wall at distance of 0.5 mm from the internal channel surface.

The measurements were conducted for a relatively wide range of changes in the fluid velocities in order to obtain both laminar and turbulent flow. Fluids superficial velocity w_f was taken as a value characterising flow conditions. This velocity shall be understood as the average velocity of fluid through empty measurement channel neglecting the presence of the foam and a second fluid for a gas–liquid flow.

The measurements were conducted for adiabatic and nonadiabatic flow. In the latter case, the power of channel heating heaters was set at a level ensuring fluid temperature increase by at least 10 K.
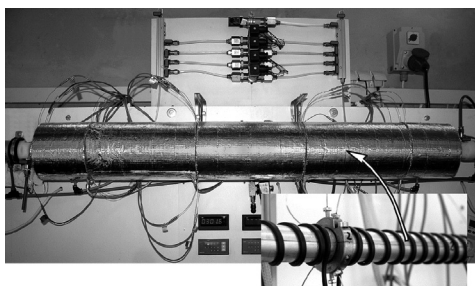

Fig. 3. Measurement section of test stand

Table 2. Experimental conditions

phase, f	w_f^* [m/s]	ζ_f [−]	t_f [°C]
air, a	0.028–9.88 (0.028–2.39)	0.313–0.998	21–95
water, w	0.003–0.270 (0.006–0.061)	0.002–0.988	24–88
oil, ol	0.003–0.167 (0.006–0.061)	0.002–0.988	19–93

* velocity range in brackets is for two-phase flow

3. Results of flow hydrodynamics and heat transfer

The measured single-phase flow pressure drops increase exponentially with the increase of fluid velocity. Figure 2 presents an example of such behaviour for pressure drops for water. For all three fluids, the lowest pressure drops were recorded for flow through foam 20 PPI, while

the greatest were observed for flow through foam 40 PPI. Foam 20 PPI has the largest cells, which makes it less resistant to flow than foams with smaller cells. Despite the fact that cell size of foam 40 PPI is slightly greater than for foam 30 PPI, pressure drops on foam 40 PPI are significantly higher than for flow through foam 30 PPI. This is due to the lower porosity and numerous local deformation of foam 40 PPI skeleton.

Pressure drop on tested foams can be described using Forchheimer equation,

$$\frac{\Delta P}{\Delta L} = \frac{\eta_f}{K} \cdot w_f + \rho_f \cdot \beta w_f^2,$$ (1)

where:

K – foam permeability, m²,

β – foam inertial coefficient.

This equation is commonly used to describe flow through granular porous media, for which K and β are material specific constants. As shown in the paper [5], metal foams have various permeability and inertial coefficients, depending on the properties of fluids pumped through them. Due to this fact, applicability of the Forchheimer equation for fluid flow through metal foams is limited.
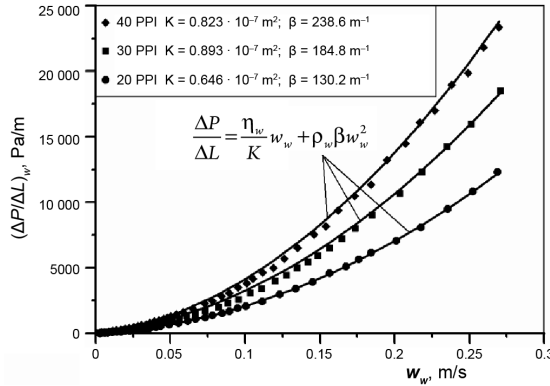

Fig. 4. Water pressure drop

A characteristic value for the single-phase through metal foams may be friction factor λ. It was concluded that this factor may be used as a generalised value that correctly describes the pressure drop on various foams, if its value is determined, allowing for geometric parameters of the foams. The value of the friction factor was determined based on the measured pressure drops and Darcy-Weisbach equation with hydraulic diameter d_h, adopted to be of equivalent value, determined based on two mutually independent parameters characterising foam geometry – porosity ϕ and pore diameter d_p,

$$d_h = \frac{\phi \cdot d_p}{1 - \varphi}$$ (2)

Analysis of change in the friction factor as a function of Reynolds number are given by the equation,

$$\mathrm{Re}_f = \frac{w_f \cdot d_h \cdot \rho_f}{\varphi \cdot \eta_f} \tag{3}$$

enables determination of nature of the flow through individual foams. Form low Reynolds number range, the friction factor decreases linearly (Fig. 5), which indicates that flow is laminar. For flow of both liquids, as well as for air, the flow is laminar when Re_f does not exceed a value of approx. 150. A clear departure of the curve of friction factor from linearity, when $\mathrm{Re} > 150$, prove loss of flow stability and intensification of flow disturbances with increase in Re_f. It shall be noted that for Reynolds number below approx. 1300, a slope of the curve of changes in the friction factor is clearly greater than for $\mathrm{Re} > 1300$. It may be assumed that for $\mathrm{Re} \approx 150–1300$ the flow has a transient Forchheimer nature. As indicated by the current state of knowledge, in the Forccheimer flow range, departures from the laminar flow are small. As the fluid velocity increases, the flow becomes more and more unstable and to a great extent exhibits features of the turbulent flow ($\mathrm{Re}_f > 1300$).
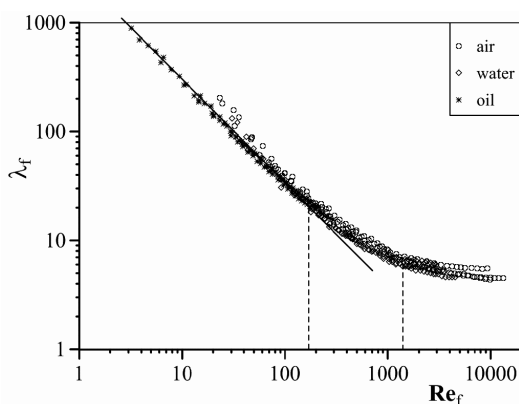

Fig. 5. Changes in friction factor as a function of Reynolds for flow of air, water and oil

The nature of changes in the two-phase flow pressure drop $(\Delta P/\Delta L)_{2f}$ is presented in Figure 6 as shown by the example of air-water flow through foam 40 PPI. Two-phase flow pressure drops are determined by phase velocity and they increase monotonically with increasing velocity, both for air w_a and water w_w.

The only departure is a sudden decrease in the value of pressure drops observed for a series of points for water flow with a velocity of 0.061 m/s. Apparently, the ungrounded decrease in the flow pressure drops despite the fact that the increase in air velocity is related to a change in the flow pattern – from plug flow to stratified flow.
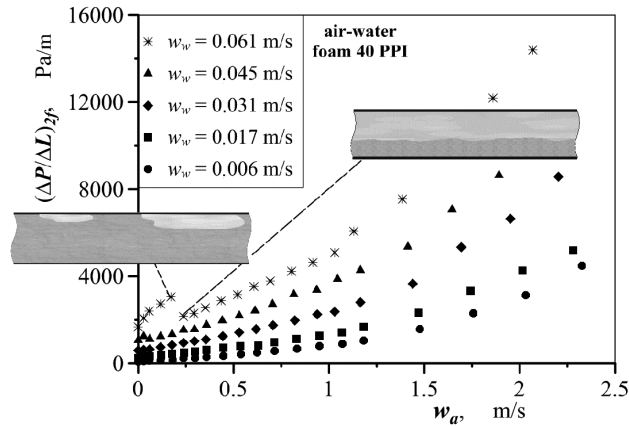
Fig. 6. Character of changes of pressure drops in air-water flow, with pressure drop reduction effect

Air-water flow occurred mainly as a stratified flow. For small streams of air introduced into the channel, a plug flow was also observed. For air-oil flow, apart from stratified and plug flow, semislug and slug flow patterns were also observed. The greater variety of air-oil flow patterns results in more irregular curve of changes in a pressure drop for this flow, especially for flows with relatively high oil velocity, when semislug and slug flow were observed in the channel.
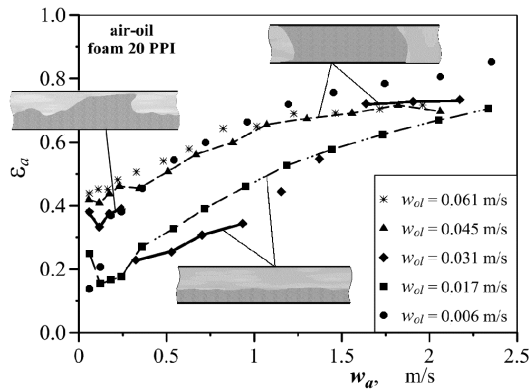
Fig. 7. Effect of phase velocity and flow pattern on value of air void fraction, in flow with oil

Flow patterns also strongly affect values of void fractions of the phases. As shown in Fig. 7, when the type of the flow changes, there is a step change in the air void fraction.

The types of flow patterns formed in the channel packed with open-cell metal foam are determined by mutual relations of fluid velocity and their properties. There was no effect of foam geometric parameters on gas–liquid flow patterns found. In the analogical flow conditions, i.e. at the same phase velocity and fractions, identical flow patterns were observed for all of the foams (for a specific mixture of gas and liquid). It is also worth noting that foam

does not cause greater phase dispersion than flow through an empty channel. Flow patterns in the channels packed with foam correspond to flow patterns occurring for a two-phase mixture flow through empty channels.

The heat transfer analysis was based on changes measured in the temperatures of the fluid and channel walls at the flow route, and heat balance in the heated part of the measurement section of the channel.

In the single-phase flow, in order to increase the fluid temperature from a value at the beginning of the heated channel section (cross-section I in Fig. 2) to a temperature at the section outlet (cross-section IV), a heat transfer rate Q_f is required,

$$Q_f = G_f \cdot \left(i_{f,\text{IV}} - i_{f,\text{I}} \right) \tag{4}$$

where:

G_f – fluid mass flow,

$i_{f,\text{I}}, i_{f,\text{IV}}$ – fluid enthalpy at the beginning and end of the measurement section.

In the two phase flow, heat transferred between the heated channel and air-liquid mixture has a value equal to the total of heat transfer rates to both fluids,

$$Q_{2F} = Q_a + Q_L , L \equiv w, ol \tag{5}$$

Value of fluid enthalpies was determined for average temperatures in the considered channel cross-sections (I and IV). For air enthalpy, a steam contained in the air was taken into account. Air humidity was measured upstream of the measurement channel. For the two-phase air-water flow, due to the need of accounting for latent heat of water vaporisation, air enthalpy was calculated for the assumed saturated state.

The calculated heat transfer rate and Newton equation allow for the determination of heat transfer coefficient from the channel wall to the fluid α_f (α_{2f} in two-phase flow),

$$\alpha_{f(2f)} = \frac{Q_{f(2f)}}{F_b \cdot \left(\overline{t_b} - \overline{t_f} \right)_m} \tag{6}$$

where:

F_b – internal surface area of wall of the heated channel section.

Due to the changing temperatures of the fluid and the wall at the flow path, value of expression $\left(\overline{t_b} - \overline{t_f} \right)_m$ was determined by approximate integration of differences of these temperatures,

$$\left(\overline{t_b} - \overline{t_f} \right)_m = \frac{1}{L_{\text{VI}} - L_{\text{I}}} \int_{L_{\text{I}}}^{L_{\text{IV}}} \left(\overline{t_b} - \overline{t_f} \right) dL \tag{7}$$

Temperatures of the wall $\overline{t_b}$ and the fluid $\overline{t_f}$ were assumed as average values from all the thermocouples located in the wall (12 pcs) and inside the channel (20 pcs) located at four equidistant channel lengths (Figure 2 – cross-sections I, II, III and IV).

For all three fluids, the heat transfer coefficient in the single-phase flow shows a similar dependency on the flow conditions and parameters of the foam in the channel. Figure 8 presents an example of such behaviour of α recorded for the heating of water. The heat transfer coefficient increases with the increase of the fluid velocity. Moreover, for the same water velocity, α_w has different values for channels packed with different foams. This is probably due to differences in the foam structures and their thermal conductivity. The lowest values of the heat transfer coefficient were reported for flow through foam 30 PPI. Taking into account foam specific surface area, which next to channel internal surface area, is a "component" of heat transfer surface, coefficient α_w in flow through foam 30 PPI shall value greater than for flow through foam 20 PPI, which having larger cells, have a lower specific surface area. The behaviour observed in the studies is opposite. It shows that in the channels packed with foam, heat transfer occurs to a large extent between the channel wall and the fluid.
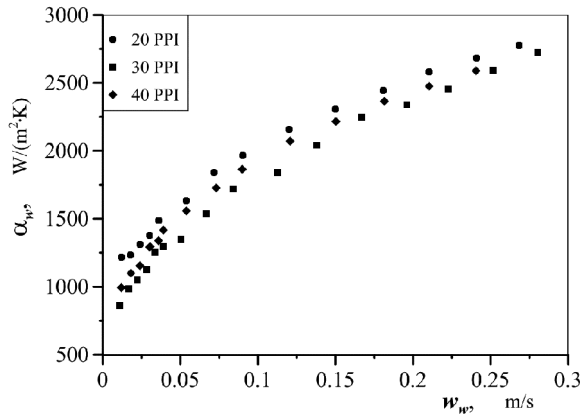

Fig. 8. Heat transfer coefficient for water flow through channels packed with various aluminium foams

The transfer coefficient for flow through foam 40 PPI has intermediate values – between values corresponding to flow through foams 20 and 30 PPI. The foam 40 PPI is geometrically similar to foam 30 PPI (similar cell and pore sizes), but it has significantly higher thermal conductivity of the skeleton k_s equal 189 W/(m·K), while k_s = 150.4 W/(m·K) for foams 20 PPI and 30 PPI. Taking into consideration the fact that part of the heat is transferred from wall to foam and then through it to the fluid, various values of thermal conductivity of the foam skeleton undoubtedly have an effect on obtaining higher values of the heat transfer coefficient for flow through foam 40 PPI, in comparison to foam 30 PPI. Results of heat conduction in the foam-fluid system are described in the paper [4].

The value of the heat transfer coefficient for the two-phase flow is greater than for the single-phase flow. For all the cases of the flow, i.e. both for air-water flow and air-oil flow through all three foams, the heat transfer rate increases with an increase in the velocity of each phase. However, liquid has greater effect on the value of α_{2f} as shown in Figure 9. Ten-fold increase in water velocity (from 0.006 to 0.061 m/s) causes approx. two-fold increase

of heat transfer coefficient. While multiple increases in the air velocity causes only a small (several percent) increase in the value of α_{2f}. Analogical behaviour in changes of heat transfer coefficient was observed for the air-oil flow.
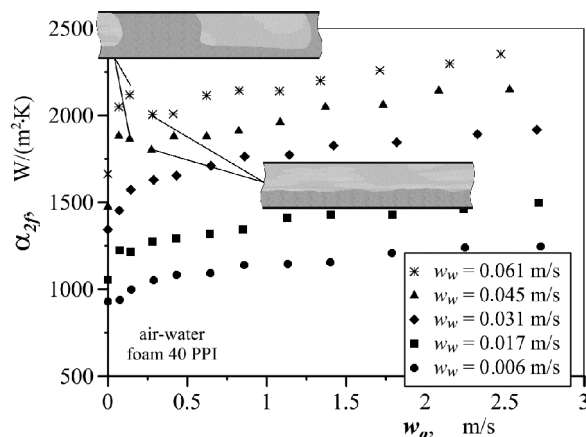

Fig. 9. Heat transfer coefficient for air-water flow for various fluid velocities

Under the conditions of changing flow patterns, some departures from the tendency of an increase in the heat transfer coefficient with an increase in the fluid velocities can be observed. However, the impact of patterns on the heat transfer rate is not as pronounced as for pressure drops and phase fractions and it points out only for air-water flow, when flow pattern changes from plug to stratified one. Under the same conditions, the greater pressure drop reduction effects were observed for the two-phase flow and step changes of void fraction of phases.

Just as for the single-phase flow, the highest values of heat transfer coefficient α_{2f} were reported for flow through foam 20 PPI and the lowest for flow through foam 30 PPI.

4. Summary

Open-cell metal foam may be used in the construction of various process equipment. There are high expectations regarding the application of foams in heat and mass exchangers, where they can be used as structural packing. In such application, it is necessary to identify factors determining pressure drops and the heat transfer in the space packed with metal foams. Results of own experimental results in that scope indicate that fluid pressure drops through channels packed with aluminium alloy foams depend on fluid velocity and fluid properties, foam porosity, cell size and shape of the cellular skeleton.

Foam geometric parameters to a smaller extent affect the heat transfer rate. Nevertheless, the heat transfer coefficient for heating the fluids in channels packed with foams under the same flow conditions has different values depending on the foam the fluid is pumped through.

These differences are as high as 20% (under conditions of the executed tests). Moreover, an effect of the foam skeleton thermal conductivity on the heat transfer between the fluid and the wall channel can be also observed.

Two-phase flow pressure drops depend mainly on flow hydrodynamic conditions, including flow patterns. In the channels filled with aluminium foams, flow patterns typical for empty channels occur. The following four basic flow patterns may be distinguished among the patterns observed in the studies: plug, semislug, slug and stratified flow patterns. The type of the formed flow patterns is determined solely by flow conditions (velocities, properties and void fractions of phases). There was no effect of foam geometric parameters on the flow patterns found.

Changes in the flow patterns are often accompanied by sudden, reaching dozens of percents, changes of values of $(\Delta P/\Delta P)_{2f}$ and ε_f. The effect of the flow patterns on value of the heat transfer coefficient in the two-phase gas–liquid flow is less pronounced.

References

[1] Boomsma K., Poulikakos D., Zwick F., *Metal foams as compact high performance heat exchangers*, Mechanics of Materials, 35, 2003, 1161–1176.

[2] Cha J.S., Ghiaasiaan S.M., Kirkconnell C.S., *Longitudinal hydraulic resistance Parameters of cryocooler and stirling Regenerators in periodic flow*, Advances in Cryogenic Engineering: Transactions of the Cryogenic Engineering Conference – CEC, 53, 2008, 259–266.

[3] Cookson E.J., Floyd D.E., Shih A.J., *Design, manufacture, and analysis of metal foam electrical resistance heather*, Int. J. Mechanical Sciences, 48, 2006, 1314–1322.

[4] Dyga R., Płaczek M., *Heat transfer through metal foam–fluid system*, Experimental Thermal and Fluid Science, Vol. 65, 2015, 1–12.

[5] Dyga R., Płaczek M., *Przepuszczalność i współczynnik inercji pian aluminiowych o komórkach otwartych*, Inżynieria i Aparatura Chemiczna, 4, 2013, 300–301.

[6] Hu H., Zhu Y., Ding G, Sun S., *Effect of oil on two-phase pressure drop of refrigerant flow boiling inside circular tubes filled with metal foam*, International Journal of Refrigeration, 36, 2013, 516–526.

[7] Incera Garrido G., Patcas F.C., Lang S., Kraushaar-Czarnetzki B., *Mass transfer and pressure drop in ceramic foams: Adescription for differentporesizesand porosities*, Chemical Engineering Science, Vol. 63, 2008, 5202–5217.

[8] Ji W.-T., Qu Z.-G., Li Z.-Y., Guo J.-F., Zhang D.-C., Tao W.-Q., P*ool boiling heat transfer of R134a on single horizontal tube surfaces sintered with open-celled copper foam*, International Journal of Thermal Sciences, 50, 2011, 2248–2255.

[9] Kamath P.M., Balaji C., Venkateshan S.P., *Experimental investigation of flow assisted mixed convection in high porosity foams in vertical channels*, International Journal of Heat and Mass Transfer, 54, 2011, 5231–5241.

[10] Lévêque J., Rouzineau D., Prévost M., Meyer M., *Hydrodynamic and mass transfer efficiency of ceramic foam packing applied to distillation*, Chemical Engineering Science, 64, 2009, 2607–2616.

[11] Ozmat B., Leyda B., Benson B., *Thermal applications of open cell metal foams*, Character and Manufacturing Processes, Vol. 19(5), 2004, 839–862.

[12] Pangarkar K.,Schildhauer T.J., van Ommen J.R., Nijenhuis J., Moulijn J.A., Kapteijn F., *Heat transport in structured packings with co-current downflow of gas and liquid,* Chemical Engineering Science, 65, 2010, 420–426.

[13] Paserin V., Marcuson S., Shu J., Wilkinson D.S., *The chemical vapor deposition technique for Inco nickel foam production–manufacturing benefits and potential applications*, Cellular Metalls and Foaming Technology, 2003, ftp://207.102.129.71/Richard/stuff/Ni-MH/ metfoam_03_paper.pdf (access: 17.11.2013).

[14] Ribeiro G.B., Barbosa Jr.J.R., *Comparison of metal foam and louvered fins as air-side heat transfer enhancement media for miniaturized condensers*, Applied Thermal Engineering, 51, 2013, 334–337.

[15] Stemmet C.P., Meeuwse M., van der Schaaf J., Kuster B.F.M., Schouten J.C., *Gas–liquid mass transfer and axial dispersion in solid foam packings*, Chemical Engineering Science, 62, 2007, 5444–5450.

[16] Sertkaya A.A., Altınısık K., Dincer K., *Experimental investigation of thermal performance of aluminum finned heat exchangers and open-cell aluminum foam heat exchangers*, Experimental Thermal and Fluid Science, 36, 2012, 86–92.

[17] Tadrist L., Miscevic M., Rahli O., Topin F., *About the use of fibrous materials in compact heat exchangers*, Experimental Thermal and Fluid Science, 28, 2004, 193–199.

[18] Tian Y., Zhao C.Y., *Thermal and exergetic analysis of Metal Foam-enhanced Cascaded Thermal Energy Storage (MF-CTES)*, International Journal of Heat and Mass Transfer, 58, 2013, 86–96.

[19] Tschentscher R., Schubert M., Bieberle A., Nijhuis T.A., van der Schaaf J., Hampel U., Schouten J.C., *Tomography measurements of gas holdup in rotating foam reactors with Newtonian, non-Newtonian and foaming liquids*, Chemical Engineering Science, 66, 2011, 3317–3327.

[20] Vadwala P.H., *Thermal Energy Storage in Copper Foams filled with Paraffin Wax*, Master of Applied Science, Mechanical & Industrial Engineering University of Toronto, 2011.

[21] Wang K., Ju Y.L., Lu X.S., Gu A.Z., *On the performance of copper foaming metal in the heat exchangers of pulse tube refrigerator*, Cryogenics, 47, 2007, 19–24.

[22] Wang P., Liu D.Y., Xu C., *Numerical study of heat transfer enhancement in the receiver tube of direct steam generation with parabolic trough by inserting metal foams*, Applied Energy, 102, 2013, 449–460.

[23] Xu Z.G., Qu Z.G., Zhao C.Y., Tao W.Q., *Pool boiling heat transfer on open-celled metallic foam sintered surface under saturation condition*, International Journal of Heat and Mass Transfer, 54, 2011, 3856–3867.

Vladimir Frolov
Valerian Blinichev (blinich@isuct.ru)
Anatoly Bogorodsky
Alexander Vetyugov

Department of Machines and Apparatuses of Chemical Productions, Faculty of Chemical Engineering and Cybernetics, Ivanovo State University of Chemistry and Technology

Research of the influence of abrasive wear of grinding bodies in the rotational vibration mill

Badania zużycia ściernego korpusów w rotacyjnych młynkach wibracyjnych

Abstract

This paper presents the design of a new rotational vibration mill. Experimental research of abrasive wear of grinding bodies in the processing of quartz sand was conducted. The influence dependences of varied process parameters on the specific wear of grinding bodies are demonstrated. Besides, the influence dependence of particle size on the specific wear value is shown.

Keywords: grinding, mill, abrasive wear

Streszczenie

W pracy przedstawiono projekt nowego młynka wibracyjnego. Przeprowadzono badania eksperymentalne zużycia ściernego korpusów szlifierskich podczas stosowania piasku kwarcowego. Przedstawiono wpływ różnych parametrów procesowych na specyficzne zużycie ściernic. Dodatkowo przedstawiony został wpływ wielkości cząstek stałych (ziaren piasku) na zużycie korpusów ściernic.

Słowa kluczowe: szlifowanie, mielenie, zużycie ścierne

1. Introduction

The main objective of the development and improvement of devices for dispersing materials is the intensification of the milling process, reducing energy costs, increasing performance and durability.

Therefore, a rotational vibration mill was designed. Its feature is the use of two methods of influence on the material: abrasion and impact. The design parameters of the mill are presented in Table 1.

The vibration rotational mill [1] operates as follows. The starting material and the grinding bodies in the mill enter the drum 1 via the loading and unloading opening 2. The drum cover 3 is made of transparent material that allows observing the movement of grinding bodies and grinding material in the drum mill. As a result of the rotation of the drum 1, the starting material and the grinding bodies arrive in the upper part of the drum to the angle of repose and fall down, grinding the material by impact and abrasion. The ability to independently or jointly use three modes of milling (ball, vibration and vibration rotational mode) is achieved by the use of the tubular shaft 5, inside of which the drum 4 is installed, the shaft bearings 6 and the rotation axes of the shafts are displaced relative to each other by an eccentricity e equal to 1.5 mm (Fig. 1). After completing the grinding process of the loading-unloading opening 2 is mounted in the lower position. The finished material is removed only by vibrations through a loading-unloading aperture 2, wherein a separating sieve is arranged. The frequency of oscillation of the drum is regulated by converter E3-9100-003N vector and the angular speed of rotation of the drum is regulated by a set of pulleys of different diameters.
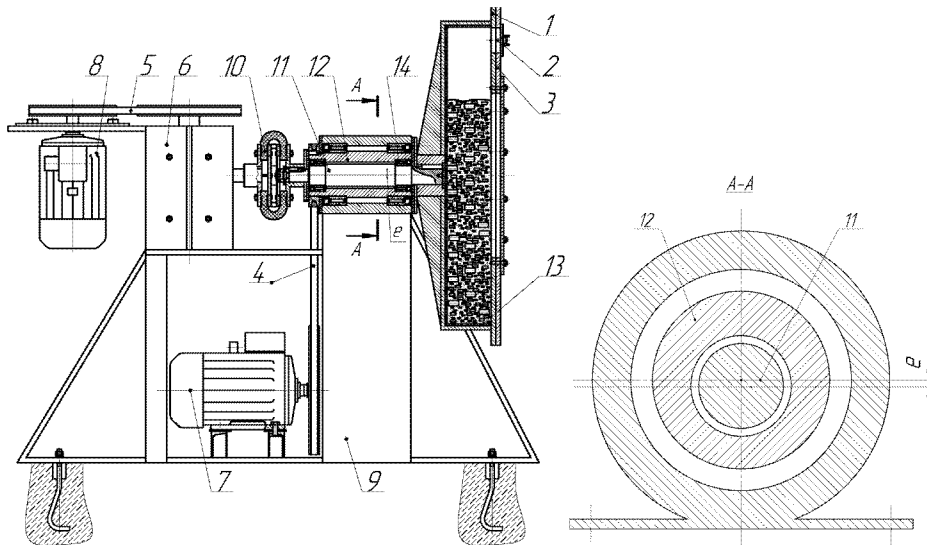

Fig. 1. 1. Scheme of rotational vibration mill: 1 – drum; 2 – loading and unloading opening; 3 – drum cover; 4, 5 – belt transmission; 6 – reducer; 7, 8 – motor; 9 – frame; 10 – flexible coupling; 11 – drum shaft, 12 – tubular shaft; 13 – grinding bodies and material; 14 – bearings, e – eccentricity

Table 1. Specifications of the rotational vibration mill

Parameters	Parameter values
Volume of the drum $[m^3]$	0.025
Drum diameter $[m]$	0.6
Drum width $[m]$	0.09
Diameter of loading and unloading opening $[m]$	0.01
Range of angular speed of rotation of the drum $[rpm]$	1–60
Range of frequencies of vibration of the drum $[Hz]$	1–50
Total engine power $[kW]$	1.7

2. Material grinding bodies and linings

Wear of the working bodies of mills by grinding the materials is important in the production of various powder materials because when there is wear, the contamination of the finished product occurs. Abrasive particles contacting with the surface of grinding bodies destroy the surface layer of the working bodies [2].

Therefore, for the industrial application of the rotational vibration mill, it was necessary to research the process of grinding bodies wear by abrasive particles, in order to determine the life of the working elements.

In order to protect the working surface of the drum rotational vibration mill from abrasion and to study the wear rate lining and cylindrical grinding bodies made of thick wear-resistant ceramic VC-100-2 are set (Fig. 2).

Fig. 2. Grinding bodies – cylinders of material VC-100-2

This material has the properties required for use in milling abrasives – high strength, hardness about 9 Mohs, wear resistance and chemical resistance, and a number of other parameters given in Table 2 [3]. Application of corundum is caused by increased demands on the purity of the final product.

Table 2. Material properties VC-100-2

Parameter	VC-100-2
Content of Al_2O_3 [%], not less	99,7
Water absorption [%]	0,02
Density [g/cm³], not less	3,88
Bending strength [MPa], not less	320
Temperature coefficient of linear expansion in the temperature range 20–900°C, $10^{-6}\,K^{-1}$	8,0
The dielectric constant, 1 GHz, 25°C	10,1
Dielectric loss 1 GHz, 20°C	10^{-4}
Volume resistivity of 100°C, OM × cm	10×14

The choice of grinding bodies is explained by the fact that the cylindrical grinding bodies have a large area of contact with the material being ground and give a higher productivity per unit of bulk density as compared with balls. The effect of grinding bodies of spherical shape on the material has a point-like nature, and in the case of a cylindrical shape, the contact area is several times higher given the same diameter. Therefore, it was necessary to compare the extent of wear, and we used 15 mm diameter steel balls and 20 mm diameter, and 20 mm high ceramic cylinders. Steel balls are made of steel 1.3505 and have a hardness of 179–207 HB.

No less important factor for more efficient operation of the mill is the choice of an optimum amount of grinding bodies. Therefore, it is very important to fill a certain number of grinding elements in the mill so that, while working, each row moves only along its trajectory, contacting with the other grinding bodies as little as possible. If you exceed the desired filling, it leads to the overconsumption of electricity and to accelerated wear of milling bodies and liner. Insufficient filling violates the right movement of the grinding bodies.

For ball mills, the optimal coefficient of fill is considered to be about 30–42%. Because the investigated mill is similar to the ball one, we choose the optimum utilisation of the grinding elements of $\approx 40\%$ [4].

Investigations of the wear rate of grinding bodies are made by means of analytical scales with an accuracy of 300 MWP 0.01 grams.

To protect the drum from wear, the inner surface of the drum is covered with ceramic tiles glued on a special silk-acetate material. The material of the lining is specially selected to minimise contamination of the crushed material and has high hardness.

3. Material for experimental research

The main materials used in the experiments were chosen as: quartz sand and alumina brand of GN.

The use of quartz sand as a raw material is primarily due to the fact that this material has a very wide use in research projects and allows you to compare the results of research. Secondly, the problem of inaccessibility of starting materials is excluded. Thirdly, silica sand has a high hardness of about 7 on the Mohs scale. Fourthly, the use of quartz sand is justified by its mechanical and chemical inertness. Prior to the experiments, all of the material has been thoroughly washed, dried, and dispersed to the required initial fractions.

The quartz sand used in experiments consists of the following components: SiO_2 – 75.0–94.0%, $FeO_2 + Al_2O_3$ – 2.6–4.2%, CaO – 0.5–2.0%, MgO – 0.0–0.4%, SO_2 – 0,1–0,8% [5].

Besides quartz, sand alumina is used in the experiments because it is more abrasive as compared to quartz sand. This is done to provide a comparison of different intensity grinding abrasive material properties, as well as the intensity of wear of the working bodies of these materials.

4. Investigation of the effect of grinding process parameters on the wear of grinding bodies

For cylindrical grinding bodies used in the study, it was found out that primarily surfaces wear, which leads to a circular cylinder shape, as shown in Fig. 3. Steel balls wear more evenly over the entire surface, without visible changes of balls in geometry.

In ceramic cylinders, there were significant differences in the strength of some individual elements, whereby the percentage of the surface wear of each differs considerably.
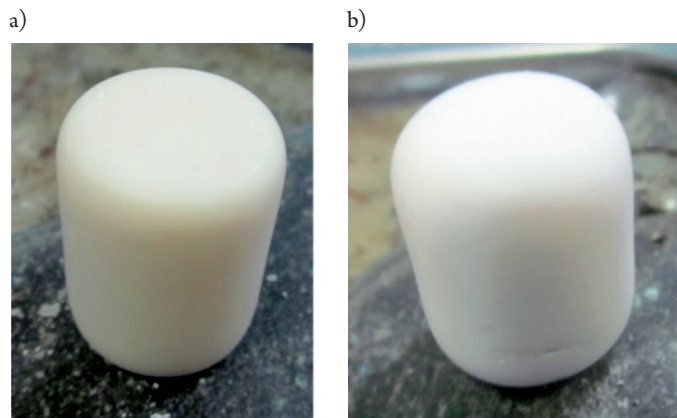
a)   b)

Fig. 3. Wear ceramic grinding bodies: a) before grinding, b) after grinding

Furthermore, dependence of the investigated wear grinding bodies from the drum rotation speed, the oscillation frequency and the percentage of fill material and the grinding bodies mill were studied. The worn surface of the working bodies was investigated in order to determine the wear mechanism.

Each experiment was carried out for 120 minutes, the wear rate was determined from the change in mass of one of the selected items and the total weight of grinding bodies.

The results of experimental studies have shown that the wear resistance of steel grinding bodies is several times smaller than that of the ceramic cylinder.

To determine the dependence of the wear grinding bodies, a series of experiments to grind alumina from the initial specific surface area of 300 m²/kg, as well as to grind quartz sand under the same process parameters, were conducted. In the experiments, the following parameters varied: the drum speed (45, 50, 55, and 60 rpm), the frequency of the drum vibrations (20, 30, 40 and 50 Hz), a drum filled with grinding bodies (15, 25, 30 and 40%) and a drum filled with grinding material (8, 12, 16 and 20%).
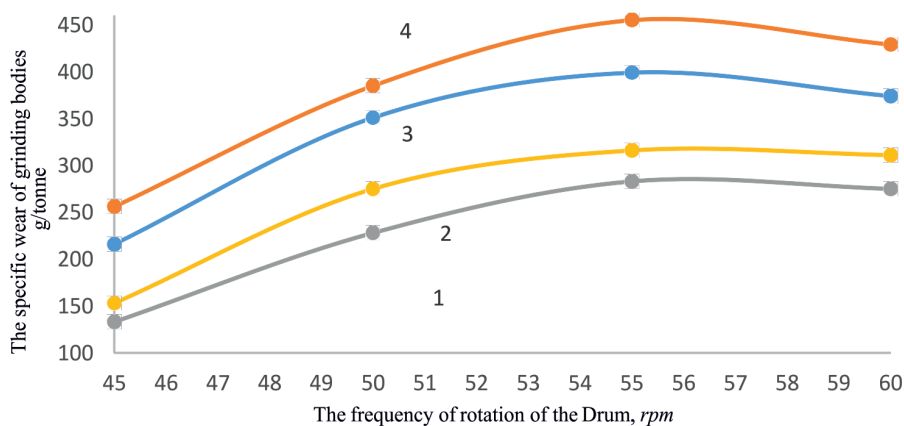
Fig. 4. Dependence of specific wear grinding bodies from the drum rotation speed: the grinding of quartz sand; 1 – ceramic cylinders; 2 – steel balls; the grinding of alumina 3 – ceramic cylinders; 4 – steel balls
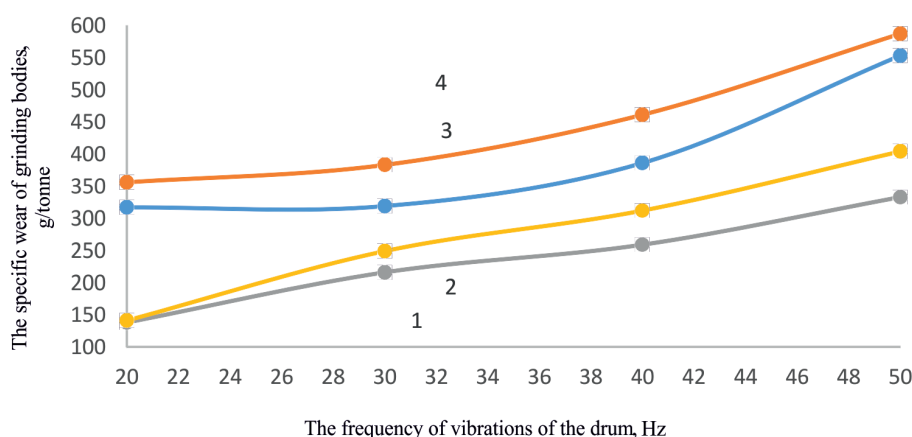

Fig. 5. Dependence of specific wear grinding bodies on the frequency of vibration of the drum: the grinding of quartz sand; 1 – ceramic cylinders; 2 – steel balls; the grinding of alumina 3 – ceramic cylinders; 4 – steel balls
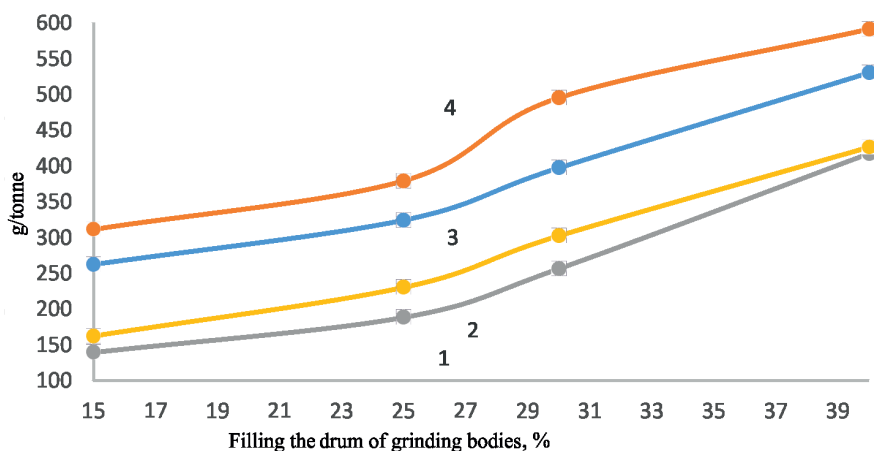
Fig. 6. Dependence of specific wear grinding bodies from the grinding bodies filling drum: the grinding of quartz sand; 1 – ceramic cylinders; 2 – steel balls; the grinding of alumina 3 – ceramic cylinders; 4 – steel balls
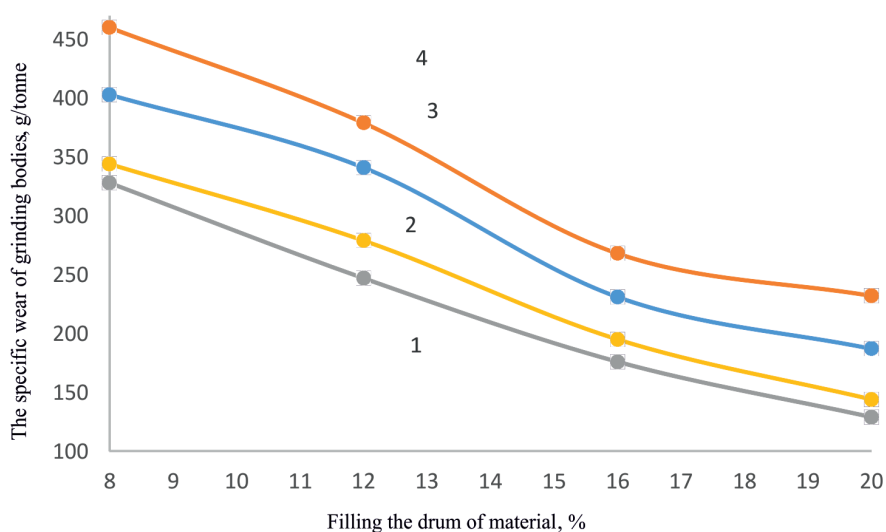

Fig. 7. Dependence of specific wear grinding bodies from filling the drum material: the grinding of quartz sand 1 – ceramic cylinders; 2 – steel balls; the grinding of alumina 3 – ceramic cylinders; 4 – steel balls

As is evident from Fig. 4, the increase in speed has led to an increase in the amortisation of the surface of grinding bodies. This can be explained by the greater force of impact between the working elements and the particulate material. No less significant factor in the deterioration of working bodies was the frequency of vibration of the drum (Fig. 5). With the increase in its intensity, the abrasion in the feed mill increased. The next experiment was similar to the previous one, but this time the investigated factors were the drum filling with

grinding bodies and the material being ground (Fig. 6, Fig. 7). The increase in the amount of grinding bodies resulted in higher intensity of abrasive wear, due to the increasing number of collisions between them per unit of time. However, the opposite situation was observed with the increase in the number of particles in the feed, since it does not allow more material to collide with each other, which minimises shots on the mill lining.

The graphs show that the grinding of the same material as the wear of steel and ceramic grinding bodies varies considerably. Note that the specific wear of steel balls was higher by at least 12%, and in some cases about 2 times greater than the ceramic cylinders. This is primarily due to the different hardness of material, steel balls have a larger mass, and hence greater collision strength.

In order to establish the dependence of the wear grinding bodies from abrasion and hardness of the material being processed, grinding of alumina as described above, and also less abrasive quartz sand was conducted. It was important to examine the effect of particle size on the wear amount. Previously, quartz sand was separated into desired fractions 1–2 mm, 0.5–1 mm, 0.25–0.5 mm, 0.125–0.25 mm and less than 0.125. Alumina was not used in this experiment, due to the lack of a large particles fraction. The research results are presented in Fig. 8.
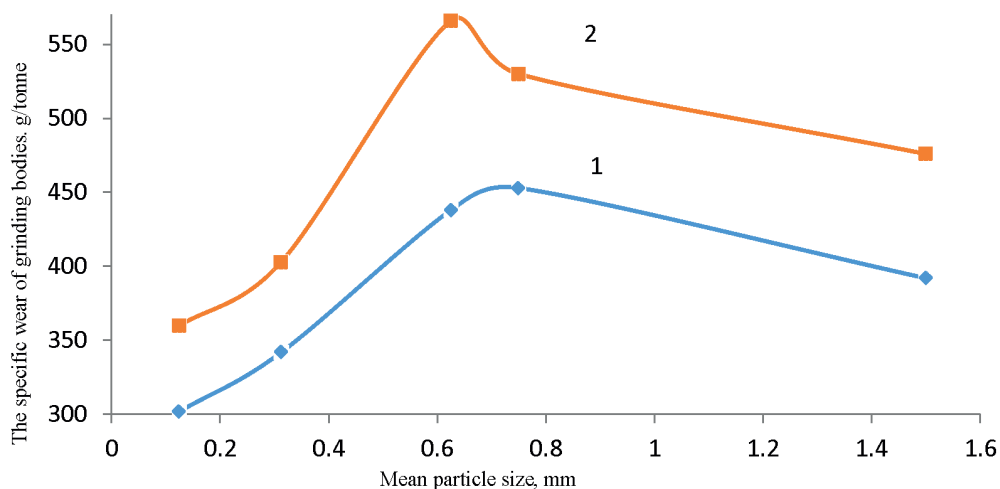

Fig. 8. Dependence of specific wear grinding bodies on the size of the crushed material particles;
1 – ceramic cylinders; 2 – steel balls

The above experiment has confirmed that particles, which roughly equal to 1 mm, have a large impact on the value of specific wear working mill surfaces. Based on the above experimental results, it can be concluded that it is necessary to use cylindrical grinding bodies constructed of VC-100-2 as the grinding bodies for grinding abrasives rotational vibration mill due to their increased wear resistance, and also the minimised contamination of the finished product (alumina).

References

[1] Frolov V., Blinichev V., Bogorodsky A., Vetyugov A., *Rotational vibration mill*, R.F. Patent №141029, May 27, 2014.

[2] Frolov V.S., Bogorodskiy A.V., Vetyugov A.V., Blinichev V.N., *Refractories & Technical Ceramics*, Vol. 3, 2014, 41–43 (in Russian).

[3] http://files.stroyinf.ru (access: 28.03.2017).

[4] http://nupo.narod.ru/teormil.htm (access: 28.03.2017).

[5] http://arxipedia.ru/cilikatnyj-kirpich/materialy-dlya-proizvodstva-silikatnogo-kirpicha.html (access: 28.03.2017).

Aleksandr G. Lipin (piaxt@isuct.ru)

Andrey A. Lipin

Faculty of Chemical Engineering and Cybernetics, Ivanovo State University of Chemistry and Technology

Ryszard Wójtowicz

Institute of Thermal and Process Engineering, Faculty of Mechanical Engineering, Cracow University of Technology

Mathematical modeling of heat and mass transfer of particles encapsulation in a fluidised bed

Modelowanie matematyczne wymiany ciepła i masy w procesie pokrywania cząstek w złożu fluidalnym

Abstract

The mathematical model, which allows to predict changes of the coverage degree, the moisture content and temperature of particles in process time, was developed. Taking into account changes of the evaporation surface due to an increasing particles coverage degree in the encapsulation process allows to describe the evolution of particles parameters more adequately and to select of process rational parameters.

Keywords: modelling, encapsulation, heat and mass transfer, the degree of coverage, fluidised bed

Streszczenie

Zaproponowano rozbudowany model matematyczny, który umożliwia wyznaczenie zmiany stopnia pokrycia, zawartości wilgoci i temperatury cząstek podczas ich pokrywania w złożu fluidalnym. Na podstawie zmian powierzchni parowania spowodowanych zwiększeniem stopnia pokrycia cząstek model ułatwia bardziej precyzyjny opis zmian ich parametrów oraz odpowiedni dobór parametrów procesowych.

Słowa kluczowe: modelowanie, pokrywanie cząstek, wymiana ciepła i masy, stopień pokrycia, złoże fluidalne

1. Introduction

Encapsulation of various particulate materials by shells protects them from the environment, provides a controlled release of the active substance and extends the shelf life of perishable and unstable substances [1].

There are several possible encapsulation methods, e.g. encapsulation by polycondensation and polymerisation on the particles surface, spray drying, spraying, pressing, extrusion, etc. [1].

In this paper, encapsulation of granulated fertilisers into polymeric shells in a fluidised-bed apparatus was carried out. Encapsulation was performed by spraying styrene acrylic polymer dispersion on particles of a fluidised bed. The amount of dispersion was 10–30% by weight of the granules. Drops of dispersion having faced with granules, spread over their surfaces and form a liquid film. Removal of the solvent by drying leads to solidification of film.

The process was carried out in the spouted bed. It provides intensive particle circulation. This way, conditions are created for a multiple passage of each particle through the nozzles irrigation area. It facilitates uniform distribution of the film-forming material over the surface of the treated granules.

The scheme of the laboratory installation for producing of encapsulated granules of mineral fertilisers is presented in Fig. 1. The fluidised bed apparatus has a cylindrical and tapered shape, with 70 mm in lattice diameter. Height of tapered part of the apparatus is 400 mm. Diameter of the top cylindrical part is 210 mm.
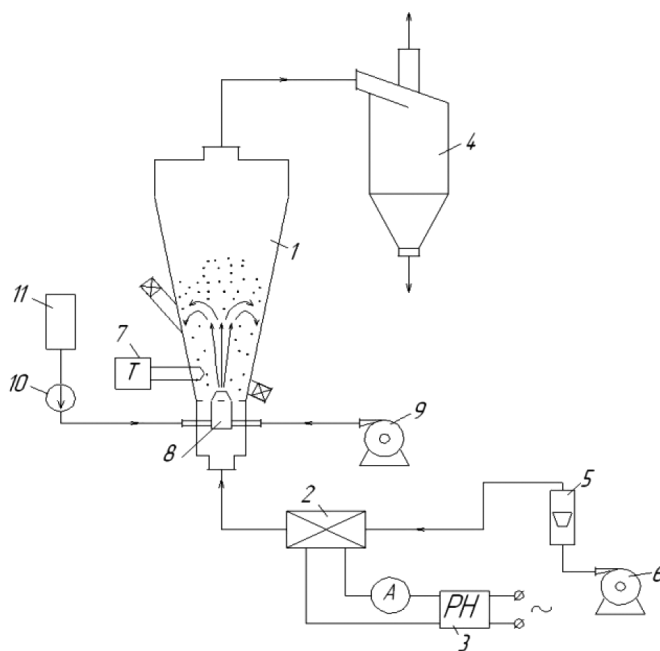

Fig. 1. Scheme of laboratory installation: 1 – fluidised bed apparatus, 2 – electric heater,
3 – voltage controller, 4 – cyclone, 5 – rotameter, 6 – blower, 7 – temperature measurer, 8 – nozzle,
9 – diaphragm compressor, 10 – dosing pump, 11 – tank for dispersion of shell former

This size ratio facilitates the organisations of the so-called air-fountain fluidisation mode. When the gas stream rises through a gas distributor plate in a bed of particles, a gas stream gushes along the vertical axis of the apparatus, taking upwards the part of granules. As granules move up, the gas velocity decreases and the granules movement slow down. When the particles reach a certain height, they fall in the peripheral zone, and roll down along apparatus walls to the gas distributor plate. Near the distributor plate, they are taken upwards again by the rising gas stream.

Fluidising agent (air) is heated by an electric heater 2. The temperature control is performed by changing the amperage through the electric heater coil with a voltage controller 3. Atmospheric air is pumped to electric heater by blower 6. Rotameter 5 serves to control the air flow. Intensive motion of particles in the apparatus 1 in a spouted bed mode may cause attrition. Cyclone 4 serves to clean the air flowing out of the apparatus from dust fraction of the treated product.

A fine polymer dispersion spraying is provided by pneumatic nozzle 8. The polymer emulsion is dosed into the nozzle by peristaltic pump 11 from the tank 10. Compressed air is supplied to the nozzle by a membrane compressor 9. The temperature measurer 7 allows to control the temperature of the granules bed in the apparatus. A thermocouple is used as a temperature sensor.

2. Mathematical model

Traditionally, in the simulation of drying particulate materials, the evaporating surface is assumed to be the surface area of the particles. The surface area of evaporation F_{evap} changes constantly in time during the encapsulation of particles (batch process).

$$F_{evap} = \pi \cdot d_{av}^{\,2} \cdot N \cdot x_{av} \tag{1}$$

where:

d_{av} – average diameter of particles,

N – the number of particles in the bed.

The degree of particle coating is defined as the part of the total surface of the particles coated with a protective shell in batch mode. It can be calculated by the formula [2]:

$$x_{av} = \frac{k_4 \cdot \left[z_2 - z_1 - z_2 \cdot \exp(z_1 \cdot \tau) + z_1 \cdot \exp(z_2 \cdot \tau) \right]}{z_1 \cdot z_2 \cdot (z_2 - z_1)} \tag{2}$$

where:

$k_1 = -k_b$; $k_2 = k_\lambda + k_t$; $k_3 = k_b \cdot k_t$; $k_4 = k_\lambda \cdot k_b$; z_1, z_2 – the roots of the characteristic equation:

$$z_{1,2} = 0.5 \cdot \left[k_1 - k_2 \pm \sqrt{(k_2 - k_1)^2 + 4 \cdot (k_1 \cdot k_2 + k_3)} \right] \tag{3}$$

where:

k_b – the relative flows of particles through the "bed" zone;

k_t – the relative flows of particles through the "torch" zone;

k_λ – a constant growth rate of the degree of coverage:

$$k_\lambda = \frac{n_d \cdot K_s \cdot g_d^2}{4 \cdot N_t \cdot d_{av}^2} \tag{4}$$

where:

d_d – drops diameter,

n_d – number of drops, produced by nozzle per unit time,

N_t – number of granules in the torch nozzle area,

K_s – spreading coefficient.

$$n_d = \frac{6 \cdot G_{disp}}{\pi \cdot \rho_{disp} \cdot d_d} \tag{5}$$

where:

G_{disp} – mass flow of dispersion,

ρ_{dsip} – dispersion density.

$$k_b = \frac{n_t}{N_b} = \frac{1}{\tau_c}, \quad k_t = \frac{n_t}{N_t} \tag{6}$$

where:

n_t – amount of particles, circulating through the irrigation zone per unit time;

N_b, N_t – amount of particles in zones "bed" and "torch", respectively;

τ_c – particles circulation period.

$$N_t = \frac{3 \cdot M_t}{\pi \cdot \rho_p \cdot d_{av}^3} \tag{7}$$

where:

M_t – the mass of particles in the nozzle area,

ρ_p – particle density.

Period of circulation is calculated as follows [3]:

$$\tau_c = \frac{6.58 \cdot H \cdot (1-\varepsilon)}{c_1 \cdot V_s \cdot (1-\varepsilon_t)} \cdot \sqrt{\frac{\rho_p \cdot d_p}{k_f \cdot \rho_{gas} \cdot \left(H + \frac{1.1 \cdot V_0 \cdot r_0}{c_1 \cdot V_s} \right)}} \tag{8}$$

The mass flow of the particles through the torch G_t of nozzle and the mass of particles in the torch area M_t are determined by [3]:

$$G_t = \frac{0.1 \cdot \pi \cdot V_0^2 \cdot r_0^2 \cdot (1-\varepsilon_t)}{V_s} \cdot \sqrt{\frac{k_f \cdot \rho_{gas} \rho_p}{d_p} \cdot \left(H + \frac{1.1 \cdot V_0 \cdot r_0}{c_1 \cdot V_s} \right)} \tag{9}$$

192

$$M_t = \frac{0.33 \cdot \pi \cdot r_p \cdot V_0^{\,2} \cdot r_0^{\,2} \cdot (1 - \varepsilon_t)}{c_1 \cdot V_a^{\,3}} \cdot \left[\frac{1}{2} - \frac{2 \cdot g \cdot d_p \cdot (\rho_p - \rho_{gas})}{45 \cdot k_f \cdot \rho_{gas} \cdot V_a^{\,2}} \cdot \frac{L_t}{H} \right] \tag{10}$$

$$L_t = \frac{V_0 \cdot r_0}{0.366 \cdot V_a \cdot c_1} \tag{11}$$

$$c_1 = 0.46 \cdot \left(\frac{g \cdot d_p^{\,3}}{\nu_{gas}^{\,2}} \right)^{0.1} \cdot W^{0.32} \tag{12}$$

where:

ρ_{gas}, ρ_p – densities of gas and solid particles, respectively;
ν_{gas} – kinematic coefficient of viscosity of gas;
d_p – particles diameter;
H – operating height of fluidised bed;
ε – bed porosity;
W – fluidisation velocity;
V_s – lift velocity;
k_f – coefficient of aerodynamic resistance;
V_o; r_o – initial velocity and radius of gas jet;
ε_t – porosity of "gas-solids" area of nozzle torch;
g – acceleration of gravity;
c_1 – empirical coefficient.

The mass of particles increases when dispersion droplets contact with the particles' surface. At the same time, due to evaporation of the solvent (water), the mass decreases. Since water evaporates from a thin film, we accept the assumption that the process of mass transfer is limited by external diffusion. The ratio of total moisture weight to the total weight of dry material was taken for quantitative characterisation of the particles' moisture content U:

$$U = \frac{m_p \cdot U_p + m_{polym} \cdot U_f}{m_p + m_{polym}} \tag{13}$$

where:

m_p – mass of original granule;
U_p – granule moisture content;
m_{polym} – weight of the polymer in the polymer film on the granule;
U_f – film moisture content.

The initial moisture content of the film $U_{f,0}$ is calculated by:

$$U_{f,0} = \frac{1 - B_{polym}}{B_{polym}} \tag{14}$$

where:

B_{polym} – the mass fraction of the polymer in the emulsion.

The denominator of the right side of formula (13) is a mass of dry material in the bed of encapsulated particles at the moment of time τ:

$$m_{dry} = m_p + G_{disp} \cdot B_{polym} \cdot \tau \qquad (15)$$

Change of the moisture content per unit of time:

$$\frac{d\left(U \cdot m_{dry}\right)}{d\tau} = \frac{d}{d\tau}\left(U \cdot \left(m_p + G_{disp} \cdot B_{polym} \cdot \tau\right)\right) \qquad (16)$$

where:

G_{disp} – dispersion mass flow,
τ – time.

Differentiation of equation (16) gives (17):

$$\frac{d\left(U \cdot m_{dry}\right)}{d\tau} = \left(m_p + G_{disp} \cdot B_{polym} \cdot \tau\right)\frac{dU}{d\tau} + U \cdot G_{disp} \cdot B_{polym} \qquad (17)$$

The flow of the evaporated moisture can be calculated by the equation of mass transfer. At the same time, the amount of moisture increases due to inflow of the emulsion.

$$\frac{d\left(U \cdot m_{dry}\right)}{d\tau} = -\beta_p \cdot \left(P_{surf} - P_{gas}\right) \cdot F_{evap} + G_{disp} \cdot \left(1 - B_{polym}\right) \qquad (18)$$

From equations (17) and (18), we can find the rate of moisture content change:

$$\frac{dU}{d\tau} = \frac{-\beta_p \cdot \left(P_{surf} - P_{gas}\right) \cdot F_{evap} + G_{disp} \cdot \left(1 - B_{polym}\right) - U \cdot G_{disp} \cdot B_{polym}}{m_p + G_{disp} \cdot B_{polym} \cdot \tau} \qquad (19)$$

where:

β_p – mass transfer coefficient,
P_{surf} – partial pressure of water vapour over film surface,
P_{gas} – partial pressure of water vapour in the drying agent,
$F_{evap.}$ – evaporation surface.

The pressure of water vapour over the film surface depends on the material temperature; therefore, an equation of the thermal balance in differential form is included in the mathematical model.

$$\frac{d}{d\tau}\left(\left(m_p + G_{disp} \cdot B_{polym} \cdot \tau\right) \cdot c_{av} \cdot t\right) = \alpha\left(t_{gas} - t\right) \cdot F_{h.tr.} - \beta_p\left(P_{surf} - P_{gas}\right) \cdot F_{evap} \cdot r^* \qquad (20)$$

where:

c_{av} – average heat capacity of the particles,

$F_{h.tr}$ – heat transfer surface,

t – particles temperature,

t_{gas} – gas temperature,

r^* – water vaporisation heat,

α – heat transfer coefficient.

The rate of temperature change is defined as follows:

$$\frac{dt}{d\tau} = \frac{\alpha\left(t_{gas} - t\right) \cdot F_{h.tr.} - \beta_p\left(P_{surf} - P_{gas}\right) \cdot F_{evap} \cdot r^* - G_{disp} \cdot B_{polym} \cdot t \cdot c_{av}}{\left(m_p + G_{disp} \cdot B_{polym} \cdot \tau\right) \cdot c_{av}} \tag{21}$$

The system of equations (19) and (21), allows to predict the change of moisture content and temperature of the particles in time of encapsulation process. The evaporation surface of particles depends on the degree of coverage (1) equations (19) and (21) and it must be solved together with the equation (2).

3. Results and discussion

The system of equations (1–21) was solved numerically by means of the Mathcad software. Figures 2a, b show the dependence of the degree of particle coating, the moisture content of film formed, temperature, and the overall moisture content per process time.
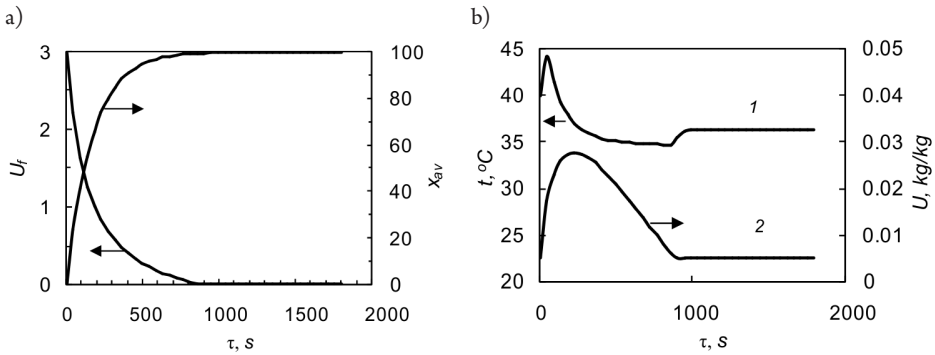

Fig. 2. Particles parameters per process time: a – degree of particle coating x_{av} and moisture content of film U_f per process time τ; b – temperature t, and the overall moisture content U per process time τ

The results of calculations show that at the initial stage of the coating formation, an increasing of temperature and moisture content of particles is observed. It is due to a lack of evaporation surface area. Furthermore, when the degree of coverage of the particles reaches 100%, the moisture content decreases to the initial humidity of the material.

The mathematical model shows the most important features of the process and it can be used for calculation of the fluidised bed apparatus.

References

[1] Ovchinnikov L.N., Lipin A.G., *Encapsulation of fertilizer in fluidized bed: a monograph*, ISUCT, Ivanovo 2011 (in Russian).
[2] Lipin A.G., Ovchinnikov L.N., Fedosov S.V., *Methods of evaluating the quality of granular materials encapsulation in a fluidized bed*, Izv. Vyssh. Uchebn. Zaved. Khim. Khim. Tekhnol., Vol. 43(1), 2000, 73–75 (in Russian).
[3] Buevich Yu. A., Minaev G.A., *Jet fluidization*, Khimiya, Moscow 1984 (in Russian).

Damian Semba

Anna Trusek-Hołownia (anna.trusek-holownia@pwr.edu.pl)
Department of Bioprocess and Biomedical Engineering, Faculty of Chemistry, Wroclaw
University of Science and Technology

Generation of homo- and heterogeneous microcapsules and their application

Wytwarzanie homo- i heterogenicznych mikrokapsułek oraz ich zastosowanie

Abstract

Microencapsulation is defined as a process during which the whole envelopment with (bio)catalysts, substrates etc. is included into hydrogel and/or surrounded by a porous polymeric membrane. However, the production of homogeneous, narrow size, distributed capsules is quite troublesome. The main problem is the way of obtaining a large number of capsules with a precisely predefined size. It is possible due to a device called an encapsulator. This equipment allows to produce homogeneous beads and core-shell systems with a predefined size in the range from 400 μm to 1600 μm, which is possible because of special nozzles with different diameters. There are a lot of microcapsule applications. In this paper, we would like to present the construction, principles of operation and selected applications of microencapsulation devices using the example of the BÜCHI–B390 encapsulator.

Keywords: microencapsulation; homogeneous beads; core-shell systems; encapsulator BÜCHI–B390

Streszczenie

Mikrokapsułkowanie definiowane jest jako proces, w którym całe środowisko zawierające m.in. (bio)katalizatory, substraty itp. zamykane jest w sieci hydrożelu i/lub otaczane porowatą polimerową membraną. Wytwarzanie jednorodnych kapsułek o wąskim rozkładzie wielkości jest dość kłopotliwe. Głównym problemem do rozwiązania jest sposób uzyskania dużej liczby kapsułek o dokładnie zdefiniowanej wielkości. Jest to możliwe przy użyciu urządzenia zwanego enkapsulatorem. Pozwala ono na wytwarzanie homogenicznych kapsułek i układów rdzeń–powłoka o zdefiniowanej wielkości w zakresie od 400 μm do 1600 μm, co jest możliwe za pomocą zestawu dysz o różnych średnicach. Istnieje wiele aplikacji mikrokapsułek. W artykule przedstawiona zostanie budowa, zasada działania i wybrane zastosowania urządzenia do mikroenkapsulacji na przykładzie enkapsulatora BUCHI-B390.

Słowa kluczowe: mikroenkapsulacja; homogeniczne mikrokapsułki; układy rdzeń-powłoka; enkapsulator BÜCHI–B390

1. Microencapsulation

Microencapsulation is often defined as a process in which some substances are entrapped in a coating, made of polymers, in order to obtain small capsules. These capsules have many useful properties. Mostly, this technique plays a large role in the food industry – incorporation of food ingredients, enzymes; however, nowadays, it is possible to distinguish more applications – in the pharmaceutical industry, it is used to enclose solids, liquids, or gases inside very thin wall, made of hard or soft soluble layer, in order to reduce the dosing frequency and prevent the degradation of active substance [1].

Microencapsulation techniques have to meet specific criteria in order to be introduced into the industry. These criteria could be subdivided into 2 groups [2]. The first one focuses on such issues like technical aspects of producing capsules, for example, simplicity of the method, high efficiency, ability to use viscous solutions, obtaining a range of different sized capsules and short time of production. The second group concerns capsule characteristics and narrow size distribution.

Microcapsules have been produced with various techniques, which differ from each other. Table 1 contains some examples. A lot of them is the modification of three basic techniques: phase separation (coacervation), solvent extraction/evaporation and spray-drying [3].

Table 1. Examples of microencapsulation methods [7]

Chemical processes	Mechanical processes
Solvent evaporation and extraction	Spray drying
Cryogenic solvent extraction	Spray chilling
Phase separation (coacervation)	Spray desolvation
Non-solvent addition	Supercritical fluid precipitation
Temperature change	Spinning disk and centrifugal coextrusion
Incompatible polymer or salt addition	Extrusion
Polymer-polymer or salt addition	Jet excitation
Polyelectrolyte complexation	
Interfacial polymerization	

Coacervation is a fast and simple method, but there are some solvent residues, which have to be ridden off, and often coacervating agents are present in microcapsules [4]. Another relatively easy method is spray-drying, but it cannot be used for thermolabile compounds. Moreover, control of the particle size during this method is difficult and yields are not so high [5].

The method used by an encapsulator device is called jet vibration (excitation). Studied by Rayleigh in late 19th century [6], it is based on the principle that using vibration frequency with a selected amplitude for a laminar jet will break it, which results in the formation of a droplet chain (equal size). It has been reported that this technique allows to obtain monodispersed homogeneous, spherical beads, with a narrow-size distribution. Simplicity of operation and setup are very important advantages. The production of droplets is not time-consuming and the efficiency is very high. Additionally, the jet-break up technique allows to operate under sterile conditions, which are compulsory for cell or microorganism encapsulation [8]. However, producing small sized particles (<100 pm) is quite troublesome and it demands the application of a different method.

In the mentioned technique, an operator obtains a single droplet chain, which means that one droplet is produced at a given time and the flow rate is closely related to the nozzle diameter [9]. Even if the nozzle diameter was larger, the production volume will still be at the same level. Scaling of the process is carried out by increasing the number of nozzles. The inability to extrude high viscosity polymers is another disadvantage of jet break-up systems. The high viscosity effect is minimized by increasing the temperature of the vibrating chamber during extrusion, but it works only to a certain extent. Because of that, low concentration solutions of polymers are applied, resulting in limited mechanical resistance of microcapsules [9]. Heating systems were developed by EnCapBioSystems and are currently supplied by BÜCHI [10].

2. Vibration jet system

The theoretical basis of a vibrational system are the Newtonian fluid dynamics, although there are reports indicating that it could be also applied for non-Newtonian liquids, such as carrageenans or alginates, in order to obtain microspheres by ionotropic gelation [11]. Some equations were applied to approximate the frequency and flow rates in order to obtain a break up of the laminar jet of a polymer into a droplet chain [12]. Serp et al., implied that, in order to determine values for the nozzle diameter using the empirical approach, all calculated values should be treated like a reference point [11]. Another important factor is that the size of the obtained capsule does not equal the diameter of the applied nozzle [13]. During formation of the droplet chain, there is also a necessity to disperse newly created spheres in order to prevent agglomeration (without dispersion, coalescence between droplets will lead to beads of double or triple volume). In the above system, this effect is accomplished by electrostatic repulsion forces system. It was first introduced by Brandenberger et al. [14]. Electrostatic field right after break-up charges the droplets and because of this fact – agglomeration effect is eliminated. Thanks to dispersion, microcapsules are distributed over a large surface of hardening bath, which results in monodispersed beads [12]. According to Brandenberger et al., the electrode potential is supposed to be in the range of 400–2500 V, which is strictly connected with the droplet diameter and jet velocity [14].

2.1. Encapsulator BÜCHI B-390

The device consists of several main parts. These are: bead producing unit, pressure bottles, and control unit (Fig. 1). The possibility of sterilizing (by autoclaving) all parts, which have contact with polymeric mixture, is another great advantage.

The agent intended for encapsulation (enzymes, cells, chemicals) is mixed with a polymer. The mixture is placed in a pressure bottle (**1**) and forced into the bead-producing unit (**2**) by adjustable air pressure (**P**). When the liquid is passing through the nozzle, thanks to vibrating unit (**3**), the laminar jet is broken up into equally sized droplets. The obtained droplets are then directed towards the electrical field between the nozzle (**4**) and the electrode (**5**) resulting in a surface charge. Because of that, beads are dispersing and they will not agglomerate before they fall down to the hardening bath (**9**). Additionally, the bath is electrically grounded to avoid the negative effect of "jumping" beads out of the beaker. During the process, it is possible to set the temperature of the apparatus – it can help with high viscosity liquids. The only difference between a single nozzle system and a concentric nozzle system is in the mounted pulsation chamber and the type of nozzle (both setups are presented in materials and method chapter).
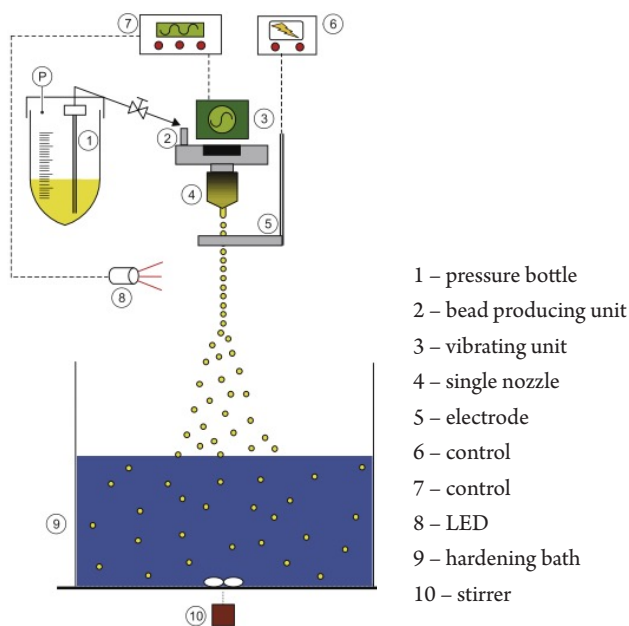

1 – pressure bottle
2 – bead producing unit
3 – vibrating unit
4 – single nozzle
5 – electrode
6 – control
7 – control
8 – LED
9 – hardening bath
10 – stirrer

Fig. 1. Schematic representation of the Encapsulator B-390

2.2. Nozzle configuration

The Encapsulator B-390 has four different nozzle configurations. The selected system depends on the type of beads/capsules, their assumed sizes and the material, which will be encapsulated. The first type is a single nozzle system, which allows to produce beads with

a predefined size from 150 μm to 4 mm. The second type is a concentric nozzle system, which enables to obtain core-shell capsules in single step process. The encapsulator may also be equipped with a flow vibration nozzle. It is used to produce smaller beads (size around 80 μm) from viscous solutions. Another configuration provided by the manufacturer is an air dripping nozzle system, which allows for encapsulation islets and cell clusters in beads. The evaluated configurations consist of the first two presented systems (Fig. 2) – single and concentric nozzle, the capabilities of which have been tested.
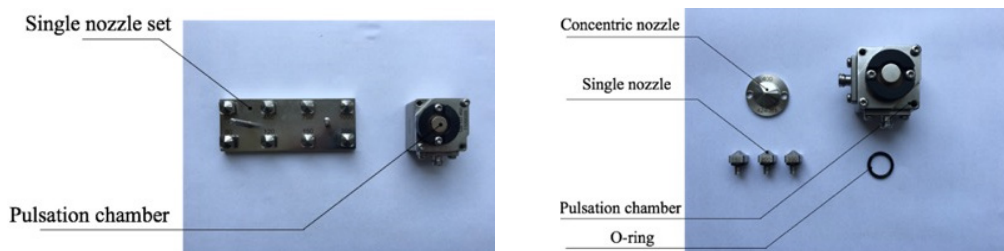
Fig. 2. Single nozzle configuration (left) and concentric nozzle setup (right)

2.3. Large scale production

The encapsulator provided by BUCHI is designed for research and development work and for producing small amounts of beads and capsules for commercial purposes. Mostly, it is used for the encapsulation of small quantities of specialized drugs and animal cells. After the development of encapsulation conditions, it could be used for larger scale production. Increasing the diameter of nozzle allows to obtain high production rates. According to the company, it is possible to establish the production rate at 40 ml/min [10]. Industrial production is much bigger – reaching several tonnes per day. In this case, it is achieved by increasing the number of nozzles. An encapsulator with a significant number of nozzles is able to extrude a polymer solution faster. Using values similar to the values developed in lab-scale, it enables the production of beads or capsules with much higher efficiency.

3. Biopolymers used in microencapsulation

There are a lot of biopolymers that are suitable for application in microencapsulation, particularly to obtain homogeneous structures. One of them is sodium alginate – linear anionic polysaccharide, distributed widely in the cell walls of brown algae, such as in *Laminiaria digitata* and *L. Hyperboria* [15]. Its structure can be divided into twoblocks: G-block (α-1,4-L-glucuronic acid) and M-block (β-1,4-D-mannuronic acid). Its popularity is a result of the ability to create gels by exchanging sodium ions by divalent calcium ions. The most popular model, which explains the chain-to-chain association, is the "egg-box model" [16]. The obtained gels are relatively stable at an acidic pH, but at an alkaline pH, they could

swell. Gels are biocompatible and easy to obtain. Therefore, alginate gel is widely used in drug delivery systems [17, 18, 19] and cell tissue engineering [20]. It plays a great role in the microencapsulation of vitamins [21], fragrances and flavors [22 and 23]. Fig. 3 presents the capsules obtained by us based on sodium alginate.
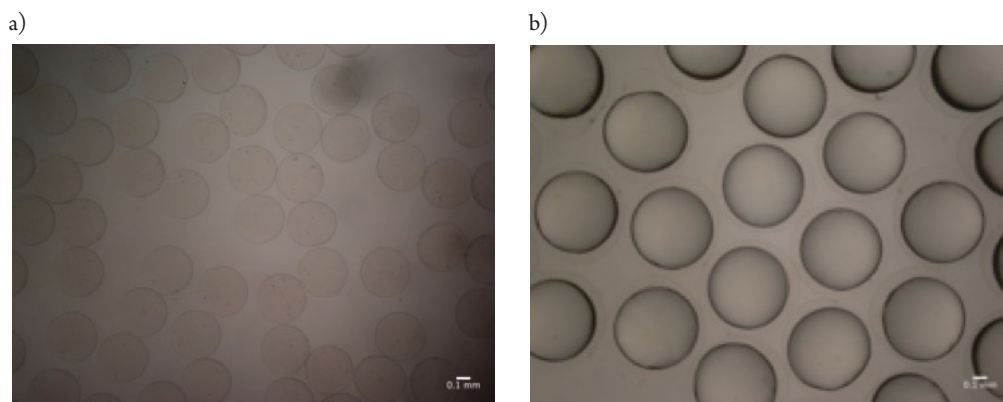
a)

b)

Fig. 3. Microscopic photographs of selected obtained microcapsules using the Encapsulator B-390 (Buchi): a) homogeneous from sodium alginate, nozzle size 150 mm, frequency 900 Hz, voltage 600 V, pressure 394 mbar; 50°C; b) heterogeneous with linseed oil in core and shelled by sodium alginate, concentric nozzle size 300 mm, core nozzle size 150 mm, frequency 790 Hz, voltage 2500 V, pressure 456 mbar; 50°C

Another great biopolymer, very useful in microencapsulation, is κ-carrageenan. It is a member of a large linear group of sulphated polysaccharides that are obtained from red algae (major sources are *Chondrus*, *Eucheuma*, *Gigartina*) [24]. All carrageenans have a common backbone of alternating β-1,3-D-galactose and α-1,4-D-galactose. For microencapsulating purposes, κ-carrageenan is used (Fig. 4). The differences that have a great influence on the properties of the above group include the number and position of the ester sulphate groups on repeating galactose units [25]. The higher the ester sulphate group content, the lower the solubility temperature of carrageenan. That phenomena occur in the production of lower strength gels or even inhibit gel formation (λ-carrageenan). Gel is formed in the presence of potassium or sodium ions [26]. κ-carrageenan is used for encapsulating essential oils [27], probiotics [28] and microorganisms [29].

Another great polymer of natural origin is chitosan. It is a cationic linear polysaccharide composed of a deacetylated unit (β-(1-4)-linked glucosamine) and a acetylated unit
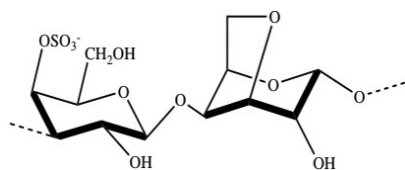

(N-acetyl-D-glucosamine) in a random order. Chitosan does not occur in nature too often – because of that, it is obtained by deacetylation of chitin (component of the cell walls of fungi and the exoskeletons of arthropods) [30]. The mentioned polysaccharide is nontoxic, biodegradable and biocompatible; all these features make it useful

Fig. 4. κ-carrageenan

in medicine and pharmacy [31]. What is more, hipocholesterolemic, hipolipidemic [32], antimicrobial [33] and antitumor activity [34] of chitosan have been reported. It is very often used for encapsulating enzymes [35], in dentistry [36], but also to manufacture matrices for drug delivery [37].

4. Applications of microencapsulation

Simplicity, result reproducibility and high efficiency are the greatest advantages of microencapsulation by the vibration jet technique. Because of that, a lot of applications have been developed.

Immobilization of cell systems is one of the most widespread uses of microencapsulation. In the brewing industry, that aspect was investigated for the last 20 years. Microencapsulated systems were successfully used for the secondary fermentation of beer [38] and for the production of alcohol-free or low-alcohol beer [39]. Despite the success in the introduction of immobilized microorganisms to some stages of beer production, such systems have not been applied for primary beer fermentation. This is caused by flavor variation produced by immobilized cells in final beers [40]. The blame for this lies in the insufficient consumption of free amino nitrogen, mass transport difficulties and restricted cell growth [41]. The metabolism of amino acids in yeast is closely related to the synthesis of the flavor compound, such as higher alcohols, esters, sulphur compound or vicinal diketones. Increasing the amino acid consumption could be carried out by minimizing external and internal mass transfer resistances. To deal with that size, texture and porosity of the immobilized polymer, the particles have to be adjusted. A smaller diameter of particles significantly decreases internal mass transfer restrictions [42]. In order to entrap yeast cells, low-density alginate and carrageenan gel microcapsules were used [43]. The optimal diameter was estimated by a short cultivation study and it is 0.5-0.6 mm for alginate microbeads loaded with brewing yeast. That size induces rapid cell proliferation and minimizes restriction in the mass transfer [43].

Capsules consisting of hydrophobic core and cross-linked polymeric shells are another example of microencapsulation applications. The core-shell system could be used in capsular perstraction of inhibitory products from bioprocesses [44]. Such systems are promoting rapid mass transfer thanks to a high surface area. Preventing the formation of stabilized emulsions and problems with toxic effect of organic phases for microorganisms are omitted by the separation of organic phase (core) by the capsule membrane from an aqueous environment [45]. The predominance of the core-shell system over beads is a much larger surface area. The mentioned system was applied to 2-phenylethanol extraction from a yeast bioconversion process. It helps to overcome respiratory inhibition by both phenylethanol and dibutyl sebacate. As an organic phase core, dibutyl sebacate was used and it was entrapped in calcium alginate hydrogel to form autoclavable liquid-core capsules [45].

Microencapsulation is also a method used in order to protect bacteria against gastric conditions. The increased interest in the role of probiotics bacteria in human health led to the entrapment of lactic acid bacteria in food, resulting in a new generation of "improved" food.

International Dairy Federation suggests that bacteria consumed within food should be active, abundant and to be at least 107 CFU/g [46]. The microencapsulation technique was used to investigate the survival of *Lactobacillus acidophilus* CSCC 2400 in simulated gastric conditions. The mentioned strain was encapsulated in calcium alginate with different concentrations and different sizes. As a result, it occurred that viability of the cells increased with an increase in the alginate capsule size and gel concentration. Research proved that the vibrating jet technique could be effectively used to produce microcapsules within an entrapped microorganism in order to protect it against harsh conditions in the human digestive system [47].

Enzyme encapsulation is also an example of the application of the vibrating jet technique in the dairy industry. During the cheese production process, in order to develop the flavor, texture and aroma, a long ripening time is required. Maturation of cheese in the traditional way demands a series of complex biochemical and microbiological processes and it takes a lot of time [48]. The simplest and easiest way to accelerate the process is to add exogenous enzymes, but because of enzyme loss in whey and a poor biocatalyst distribution, such a solution is uneconomical. However, encapsulated enzymes eliminate the enzyme irrecoverable problem and prevent immediate and extensive proteolysis as well as contamination of whey. At the end of the process, it is possible to separate immobilized enzyme from substrate in the milk and the curd mixture [49]. In Anjani et al. study, flavourzyme was encapsulated in alginate, chitosan and κ-carrageenan polymers. After encapsulation, the stability of the enzyme was investigated. Immobilization of flavourzyme in alginate matrix alone exhibited a poor immobilization efficiency, which was elevated by the addition of chitosan to the polymeric solution. Controlling the amount of released enzyme could modify the proteolysis, which is the main requirement for an optimal flavor development in cheese ripening [50].

Microencapsulation is also applied for improving the storage stability of various oils [51 and 52]. Oils and fats are products that are vulnerable to oxidation. Especially those, which are characterized by a high content of sensitive to oxidative deterioration components. This self-catalyzing process involves reactions like primary oxidation, secondary oxidation and hydrolytic rancidity [53]. Nowadays, instead of using some chemical additives to prevent oils form oxidizing, encapsulation techniques are applied. This provides a physical barrier (mostly made of biopolymers), which minimizes the influence of the external environment [54]. Sun-Waterhouse et al, proved that encapsulation of avocado oil significantly improves oil resistance to oxidation. During research, alginate and alginate-HMPC (hydroxypropyl methylcellulose) systems were compared. The combination of alginate and HPMC was a worse encapsulant than alginate alone [52].

5. Conclusions

For some time, microencapsulating techniques played a big role and found application in many industries, such as food, medical, biotechnology, agriculture, cosmetics. There are a lot of rules, which are obligatory to follow, if microcapsules are supposed to be introduced

to the market. Medical applications demand monodisperse, homogeneous, and spherical beads/capsules, with a small size and a narrow size distribution. To meet the mentioned requirements, jet-break up techniques are used. These techniques are quite easy to operate and have other useful features like high efficiency and short production time. A device called the encapsulator allows to produce beads/capsules, which meet most of the criteria. With the help of this device, even heterogeneous core-shell system, with predefined sizes of core and capsule, could be obtained. Moreover, it enables large-scale production due to the increased nozzle number.

Encapsulator BÜCHI B-390 is a device, which allows to obtain homogeneous beads of variable sizes with great efficiency and reproducibility. The device also enables to obtain heterogeneous capsules with predefined sizes of both the capsule as well as the core. The influence of some parameters on beads size was noticed. Increasing the nozzle size required a lower vibration frequency and an increased flow rate. Increasing the nozzle size and flow rate have a major influence on productivity.

References

[1] López A.F., Deladino L., Alba S.N., Miriam N.M., *Encapsulación de compuestos bioactivos con alginatos para la industria de alimentos,* limentech, Ciencia y Tecnología Alimentaria, 10(1), 2011.

[2] Whelehan M., Marison I.W., *Microencapsulation using vibrating technology,* Journal of microencapsulation, 28(8), 2011, 669–688.

[3] Aftabrouchad C., Doelker E.S.T.P., *Méthodes de préparation des microparticules biodégradables chargées en principes actifs hydrosolubles,* STP pharma sciences, 2(5), 1992, 365–380.

[4] Thomasin C., Johansen P., Alder R., Bemsel R., Hottinger G., Altorfer H., Wright A.D., *A Contribution to Overcoming the Problem of Residual Solvents in Biodegradable Microspheres,* Prepared by. Eur. J. Pharm. Biopharm, 42, 1996, 1.

[5] Johansen P., Merkle H. P., Gander B. *Technological considerations related to the up-scaling of protein microencapsulation by spray-drying,* European Journal of Pharmaceutics and Biopharmaceutics, 50(3), 2000, 413–417.

[6] Rayleigh L., *Philosophical Magazine,* Series 5, 1882, 184–186.

[7] Yeo Y., Baek N., & Park K., *Microencapsulation methods for delivery of protein drugs,* Biotechnology and Bioprocess Engineering, 6(4), 2001, 213–230.

[8] Vemmer M., Patel A.V., *Review of encapsulation methods suitable for microbial biological control agents,* Biological Control, 67(3), 2013, 380–389.

[9] Whelehan M., Marison I.W., *Microencapsulation using vibrating technology,* Journal of microencapsulation, 28(8), 2011, 669–688.

[10] BUCHI Labortechnik AG. Encapsulators B-390/B-395 Pro, Technical data sheet, http://www.buchi.com/en/content/spray-drying-encapsulation-solutions (access: July 2016).

[11] Serp D., Cantana E., Heinzen C., Von Stockar U., Marison I.W., *Characterization of an encapsulation device for the production of monodisperse alginate beads for cell immobilization*, Biotechnology and bioengineering, 70(1), 2000, 41-53.

[12] Heinzen C., Berger A., Marison I., *Use of vibration technology for jet break-up for encapsulation of cells and liquids in monodisperse microcapsules*, In Fundamentals of cell immobilisation biotechnology Springer Netherland 2004, 257–275.

[13] Marison I., Peters A., Heinzen C., *Liquid Core Caspules for Applications in Biotechnology.* In Fundamentals of cell immobilisation biotechnology 2004, Springer Netherlands 2004, 185–204.

[14] Brandenberger H., Nüssli D., Piech V., Widmer F., *Monodisperse particle production: A method to prevent drop coalescence using electrostatic forces*, Journal of electrostatics, 45(3), 1999, 227–238.

[15] Kikuchi A., Kawabuchi M., Sugihara M., Sakurai Y., Okano T., *Pulsed dextran release from calcium-alginate gel beads*, Journal of Controlled Release, 47(1), 1997, 21–29.

[16] Morris E.R., Rees D.A., Thom D., Boyd J., *Chiroptical and stoichiometric evidence of a specific, primary dimerisation process in alginate gelation*, Carbohydrate research, 66(1), 1978, 145–154.

[17] Lee B.J., Min G.H., *Oral controlled release of melatonin using polymer-reinforced and coated alginate beads*, International journal of pharmaceutics, 144(1), 1996, 37–46.

[18] Kamath K.R., Park K., *Biodegradable hydrogels in drug delivery*, Advanced Drug Delivery Reviews, 11(1), 1993, 59–84.

[19] González-Rodrıguez M.L., Holgado M.A., Sanchez-Lafuente C., Rabasco A.M., Fini A., *Alginate/chitosan particulate systems for sodium diclofenac release.* International Journal of Pharmaceutics, 232(1), 2002, 225–234.

[20] Wang L., Shelton R.M., Cooper P.R., Lawson M., Triffitt J.T., Barralet J.E., *Evaluation of sodium alginate for bone marrow cell tissue engineering*, Biomaterials, 24(20), 2003, 3475–3481.

[21] Yoo S.H., Song Y.B., Chang P.S., Lee H.G., *Microencapsulation of α-tocopherol using sodium alginate and its controlled release properties*, International journal of biological macromolecules, 38(1), 2006, 25–30.

[22] Lertsutthiwong P., Noomun K., Jongaroonngamsang N., Rojsitthisak P., Nimmannit U., *Preparation of alginate nanocapsules containing turmeric oil*, Carbohydrate Polymers, 74(2), 2008, 209–214.

[23] Zhu G.Y., Xiao Z.B., Zhou R.J., Yi F.P., *Fragrance and flavor microencapsulation technology*, In Advanced Materials Research, Vol. 535, 2012, 440–445. Trans Tech Publications.

[24] Craigie J.S., *Cell walls. In biology of the red algae*, K.M. Cole and R.G., Cambrige University Press, 1990, 221–257.

[25] Murano E., *Use of natural polysaccharides in the microencapsulation techniques*, Journal of Applied Ichthyology, 14(3–4), 1998, 245–249.

[26] Rochas C., Rinaudo M., *Mechanism of gel formation in κ-carrageenan*, Biopolymers, 23(4), 1984, 735–745.

[27] Dima C., Cotârlet M., Alexe P., Dima S., *Microencapsulation of essential oil of pimento [Pimenta dioica (L) Merr.] by chitosan/k-carrageenan complex coacervation method*, Innovative Food Science & Emerging Technologies, 22, 2014, 203–211.

[28] Anal A.K., Singh H., *Recent advances in microencapsulation of probiotics for industrial applications and targeted delivery*, Trends in Food Science & Technology, 18(5), 2007, 240–251.

[29] Shi L.E., Li Z.H., Zhang Z.L., Zhang T.T., Yu W.M., Zhou M.L., Tang Z.X., *Encapsulation of Lactobacillus bulgaricus in carrageenan-locust bean gum coated milk microspheres with double layer structure*, LWT-Food Science and Technology, 54.1, 2013, 147–151.

[30] Peniche C., Argüelles-Monal W., Peniche H., Acosta N., *Chitosan: an attractive biocompatible polymer for microencapsulation*, Macromolecular Bioscience, 3(10), 2003, 511–520.

[31] Muzzarelli R.A.A., Muzzarelli C., *Chitosan chemistry: relevance to the biomedical sciences*, In Polysaccharides I, 2005, 151–209, Springer Berlin Heidelberg.

[32] Sugano M., Fujikawa T., Hiratsuji Y., Hasegawa Y., *Hypocholesterolemic effects of chitosan in cholesterol-fed rats*, Nutr. Rep. Int, 18, 1978, 531–537.

[33] Tokura S., Ueno K., Miyazaki S., Nishi N., *Molecular weight dependent antimicrobial activity by chitosan*, In New Macromolecular Architecture and Functions, 1996, 199–207, Springer Berlin Heidelberg.

[34] Hirano S., Tokura S., *Proceedings of the Second International Conference on Chitin/Chitosan.* Japanese Soc. Chitin, Tottori Japan 1982.

[35] Peniche H., Osorio A., Acosta N., De La Campa A., Peniche C., *Preparation and characterization of superparamagnetic chitosan microspheres: Application as a support for the immobilization of tyrosinase*, Journal of applied polymer science, 98(2), 2005, 651–657.

[36] Shibasaki K., Matsukubo T., Shugihara N., Tashiro E., Tanabe Y., Takaesu Y., *Kokku Eisei Gakai Zasshi*, 1988, 38.

[37] Şenel S., Kremer M.J., Kaş S., Wertz P.W., Hıncal A.A., Squier C.A., *Enhancing effect of chitosan on peptide drug delivery across buccal mucosa*, Biomaterials, 21(20), 2000, 2067–2071.

[38] Pajunen E., Grönqvist A., Ranta B., *Immobilized yeast reactor application in continuous secondary fermentation in industrial scale operation*, In Proceedings of the European Brewing Convention Congress, Lisbon 1991, 361–368.

[39] Lommi H., *Immobilized yeast for maturation and alcohol-free beer*, Brew. Dist. Int, 5, 1990, 22–23.

[40] Pilkington P.H., Margaritis A., Mensour N.A., Russell I., *Fundamentals of immobilised yeast cells for continuous beer fermentation: a review*, Journal of the Institute of Brewing, 104(1), 1998, 19–31.

[41] Hayes S.A., Power J., Ryder D.S., *Physiology of immobilised cells and the application to brewing*, Brew. Dig. 66 (11), 1991, 28–33.

[42] Nedovic V.A., Obradovic B., Leskosek-Cukalovic I., Vunjak-Novakovic G., *Immobilized yeast bioreactor systems for brewing—recent achievements*, In Engineering and manufacturing for biotechnology, 2001, 277–292, Springer Netherlands.

[43] Nedović V.A., Obradović B., Leskošek-Čukalović I., Trifunović O., Pešić R., Bugarski B., *Electrostatic generation of alginate microbeads loaded with brewing yeast*, Process Biochemistry, 37(1), 2001, 17–22.

[44] Wyss A., Von Stockar U., Marison I.W., *Production and characterization of liquid-core capsules made from cross-linked acrylamide copolymers for biotechnological applications*, Biotechnology and bioengineering, 86(5), 2004, 563–572.

[45] Stark D., Münch T., Sonnleitner B., Marison I.W., Stockar U.V., *Extractive Bioconversion of 2-Phenylethanol from l-Phenylalanine by Saccharomycescerevisiae.* Biotechnology Progress, 18(3), 2002, 514–523.

[46] Ouwehand A.C., Salminen S.J., *The health effects of cultured milk products with viable and non-viable bacteria*, International Dairy Journal, 8(9), 1998, 749–758.

[47] Chandramouli V., Kailasapathy K., Peiris P., Jones M., *An improved method of microencapsulation and its evaluation to protect Lactobacillus spp. in simulated gastric conditions*, Journal of microbiological methods, 56(1), 2004, 27–35.

[48] McSweeney P.L., *Biochemistry of cheese ripening.* International Journal of Dairy Technology, 57(2-3), 2004, 127–144.

[49] Kailasapathy K., Lam S.H., *Application of encapsulated enzymes to accelerate cheese ripening.* International Dairy Journal, 15(6), 2005, 929–939.

[50] Anjani K., Kailasapathy K., Phillips M., *Microencapsulation of enzymes for potential application in acceleration of cheese ripening*, International Dairy Journal, 17(1), 2007, 79–86.

[51] Wang W., Waterhouse G.I., Sun-Waterhouse D., *Co-extrusion encapsulation of canola oil with alginate: effect of quercetin addition to oil core and pectin addition to alginate shell on oil stability*, Food research international, 54(1), 2013, 837–851.

[52] Sun-Waterhouse D., Penin-Peyta L., Wadhwa S.S., Waterhouse G.I., *Storage stability of phenolic-fortified avocado oil encapsulated using different polymer formulations and co-extrusion technology*, Food and Bioprocess Technology, 5(8), 2012, 3090–3102.

[53] Choe E., *Effects and mechanisms of minor compounds in oil on lipid oxidation*, Food lipids: chemistry, nutrition, and biotechnology, 2008, 449–474.

[54] Neethirajan S., Jayas D.S., *Nanotechnology for the food and bioprocessing industries.* Food and bioprocess technology, 4(1), 2011, 39–47.

Marian Sikora (marian.sikora@bwigroup.com)

BWI Poland Technologies sp. z o. o., Kraków

The pressure and the vibration measurement in automotive shock absorbers

Pomiary drgań i ciśnienia w amortyzatorze hydraulicznym w zawieszeniu samochodowym

Abstract

The purpose of this article was to develop a measurement system for analyzing the dynamic behavior of automotive hydraulic dampers as well as to examine the internal pressures in each hydraulic chamber of the damper. Dampers are one of the components of the vibration/noise system that originates at the contact point/surface between the wheel and the road, and then ends at the body of the vehicle. Specifically, dampers are often a source of flow-induced or motion-induced noise due to the operation of the valves. In this paper, measurement results are presented in the form of time histories of the internal pressures and piston rod acceleration, respectively. Fast Fourier Transform (FFT) graphs are also presented in order to identify the major components of the phenomena under investigation in a frequency domain.

Keywords: automotive, double-tube shock absorber, vibration, noise, dynamics

Streszczenie

Celem poniższego artykułu jest stworzenie systemu pomiarowego umożliwiającego badanie dynamiki pracy amortyzatora hydraulicznego oraz pomiar zmian ciśnienia w jego komorach roboczych. Amortyzator hydrauliczny jest istotną częścią układu zawieszenia pośredniczącą między drogą i kołem a karoserią samochodu. Wraz z elementami mocującymi i sprężyną zawieszenia stanowi ścieżkę przekazywania siły na samochód od podłoża. Amortyzatory hydrauliczne są często źródłem hałasu spowodowanego przepływem cieczy lub pracą zaworów hydraulicznych. W celu lepszego zrozumienia zjawisk zachodzących w obiekcie w artykule zostały umieszczone przebiegi czasowe obserwowanych wielkości fizycznych. Analiza częstotliwościowa (FFT) pozwoliła na wskazanie charakterystycznych częstotliwości drgań w amortyzatorze.

Słowa kluczowe: przemysł samochodowy, amortyzator hydrauliczny dwururowy, drgania, hałas, dynamika

1. Introduction

In brief, the automotive vehicle suspension shock absorber or a damper has been a well-known and established technology in the industry [2]. Its success has been due to its simplicity and modular design. Lessons learned over the years allowed for the elimination of assembly problems and specialized production. At the same time, from the engineering standpoint, a typical passive vehicle damper is a compromise between handling properties of a car, passenger comfort and safety as well as NVH (Noise, Vibration, and Harshness). Despite its simplicity, a good damper design is always an engineering challenge. Recently, new automotive trends in vehicle chassis design have generated new research and engineering efforts. For example, the engine and powertrain noise reduction have caused all noise sources due to vehicle chassis operation to become recognizable and audible by both the driver as well as the passengers. It is, therefore, vital to propose means for eliminating and/or improving the passenger comfort through changes in the device that would result in noise reduction.

The force output of vehicle dampers is a sophisticated function of the hydraulic valve's characteristics, damper geometry, compliance of fluid chambers, cavitation, friction, gas pressure, fluid properties, etc. In general, the subject of damping force generation in the automotive damper has been under consideration for years. Lang [10] developed a dynamic model of a twin-tube damper. The author considered the contribution of oil compressibility along with cylinder wall expansion and vapor generation. The model of a preloaded spring type valve included the disc inertia as well as viscous damping forces, contact force, geometric preload and force due to change in momentum of the fluid. By far, the work of Lang has remained the most cited academic contribution to the topic of damping force generation in the devices. Further efforts to model the damping force output of this device are well known Duym [3, p. 109–127], Farjoud [6, p. 1437–1456], Ferdek [7, p. 627–638]). On the NVH side, Kruse [8, 9] highlighted three basic approaches towards noise reduction. Optimizing the damping force allows one to reduce force excitation. It could lead to damper performance deterioration. Optimizing the damper mount reduces the noise transmission. Often it is a sufficient method; however, it does not change the basic phenomena. According to Kruse, the optimum way to meet customer requirements was to modify the dynamic structural properties for the reduction of vibrational response. In his study, the author included the measurement of excitation displacement, damping forces, piston rod acceleration and pressures in fluid chambers of an exemplary damper. The modal analysis of piston rod dynamic behavior was also conducted. Finally, the displacement, damping force and acceleration measurements have formed an experimental base for the studies undertaken by Czop and Sławik [1, p. 1937–1955].

In the paper, the author reveals a measurement system for the acquisition of damper internal phenomena. The test approach includes the measurements of piston rod acceleration, displacement and internal pressures. The test configuration allows the investigation of phenomena occurring in the damper under various operating conditions. In the paper, the author presents several data sets performed at a number of excitation frequencies and the peak velocity of 0.25 m/s. In-depth analysis of the obtained results is also performed in detail.

2. Measurement system

In this section, the author highlights all key elements of the damper measurement system. Some approach examples can be find in papers [4, p. 39–47], [5, p. 24–29]. To conduct the measurement, the MTS hydraulic actuator was used as shown in Fig. 1. As shown, the damper's reservoir was rigidly attached to the MTS's fixture subjected to sinusoidal displacement inputs. The damper piston rod was then attached to the elastic (rubber-type) top mount (the top mount stiffness is maintained at the same level during all experiments). The top mount is connected to the upper head of the MTS hydraulic actuator. In this configuration, the damper can be operated in a manner similar to that in a real vehicle.
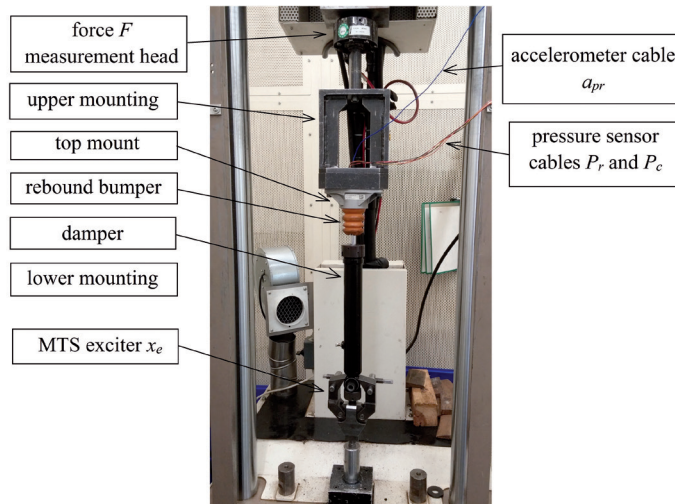
Fig. 1. Measurement test rig

The base parameters of the investigated damper configuration were: piston rod mass – 0,4 kg, gas pressure: 6 bar; maximum length in extension: 540 mm; maximum displacement (stroke): 150 mm; inner tube diameter: 32 mm; piston rod diameter: 14 mm; inlet cross-section area (rebound): 25 mm²; inlet cross-section (compression side): 22,7 mm².

The LMS AD/DA card SCADAS III is used in the measurement system for the purpose of data acquisition and PC communication. Acceleration and pressure signals are then directly registered by the LMS module. The displacement and force signals are collected by the MTS controller, and then transferred to the LMS card at the sampling rate of 12.8 kHz.

During the tests, the damper was subjected to oscillatory sinusoidal displacement inputs at the peak velocity of 0.25 m/s as follows:

▸ +/−30 mm 1.33 Hz;
▸ +/−8 mm 5 Hz;
▸ +/−4 mm 10 Hz;
▸ +/−2 mm 20 Hz.

The experimental damper prototype was instrumented in such a way to fit two pressure sensors PA-4LC for acquiring the pressure signals in rebound and compression fluid chambers, respectively. As shown in Fig. 3, the respective pressure signals were then collected using the sensors in the P&R (piston and rod) assembly, located above and below the piston. Technical specifications of the PA-4LC sensors are:

Table 1. Pressure sensor – parameters [11]

Type	Dimensions [mm]	Pressure Range	Storage Temperature	Operating Temperature	Output
4 LC	Ø11 × 4.2	0 … 100 bar abs.	−10 … +80°C	0 … 50°C	0.5 … 4.5 V

The goal of the bench test was not to reproduce exact on-the-vehicle test conditions, but to conduct comparison analysis. Although the top mount of a damper has a big influence on the acceleration level on the car, the measurement still gives useful data. It allow to test different configurations of the damper in a simple way on a component level.

Fig. 2. Measurement system layout. Measured signals: excitation displacement – x_e, piston rod acceleration – a_{pr}, pressure in compression chamber – P_c, pressure in rebound chamber – P_r and damping force – F

Fig. 3. Instrumented piston rod and top mount unit incl. 4 LC type pressure sensors [11]

3. Measurements results

The results of measurements are presented in the form of time histories of pressures, displacements and acceleration. The prescribed tube displacement input was measured during the experiment. The measured output was piston rod acceleration (not displacement). Moreover, pressure difference vs. excitation displacement and excitation velocity is presented, too. The results are illustrated in Figs. from 4 to 9.

Charakterystyki siły nie zostały podane w funkcji przemieszczeń i prędkości względnych ponieważ w układzie nie jest mierzone przemieszczenie tłoczyska. Natomiast przemieszczenie uzyskane drogą całkowania jest obarczone szeregiem błędów całkowania oraz nieznajomością warunków początkowych.

The high amplitude and low frequency excitation (see Fig. 4) show a low dynamic state. Both movements are separated. During the rebound (upward) movement, the pressure in the rebound chamber is around 2.4 MPa, the pressure in the compression chamber is low, slightly decreasing down to gas pressure. During the compression (downward) movement, the pressure in the rebound chamber is around 3.45 MPa and the pressure in the compression chamber is 4.15 MPa. At transition points, the pressures in both chambers are low and close to gas pressure.

As the frequency of the excitation increases, the situation changes. Figs 5a, 6a and 7a show that the maximum acceleration amplitude increases with the excitation frequency. The biggest change can be observed at the rebound-compression transition point. In the dynamic situation, the pressure in the rebound chamber is not fully released (see Fig. 5b, Fig. 6b and Fig. 7b). The pressure drop vs. displacement plots (see Fig. 5c, Fig. 6c and Fig. 7c) and pressure drop vs. velocity graphs (see Fig. 5d, Fig. 6d and Fig. 7d) show that the damping efficiency decreases with the excitation frequency (on the component level).

The low amplitude and high frequency (Fig. 7) show the dynamic situation in detail. During the rebound movement, the pressure level in the rebound chamber is approx. 2.3 MPa, the pressure in the compression chamber is low and slightly decreasing to the gas pressure level. While during the compression, the pressure in the rebound chamber is much lower at approx. 1.87 MPa, and the pressure in the compression chamber is 2.35 MPa. The pressure signal is shifted with respect to the displacement excitation input. During the transition (rebound-compression), the pressures in both chambers are still low and close to the gas pressure level. For comparison, during the compression-rebound transition, the damper operation is delayed. Effectively, the rebound pressure is not relieved and maintained at a relatively high amplitude of the internal pressure.

Fig. 8 shows the FFT of the rod acceleration signal calculated based on one cycle and normalized by the maximum input acceleration. Clearly, characteristic components appear around 360 Hz. The 20 Hz excitation results in frequency components augmented within the range of 260–500 Hz. Fig. 9 shows two configurations of the same damper assembly. The first one is basic, whereas the second one included modified valves (yet producing same steady-state force output). The modification allows to improve the dynamic characteristics; the dynamic force characteristics and controlled leaks were modified. The pressure in the compression chamber rises faster and achieves higher values. The pressure in the rebound chamber also shows bigger variance. At the compression-rebound transition, the second configuration shows a low-pressure fluctuation. As a result, a lower acceleration of the piston rod can be observed.
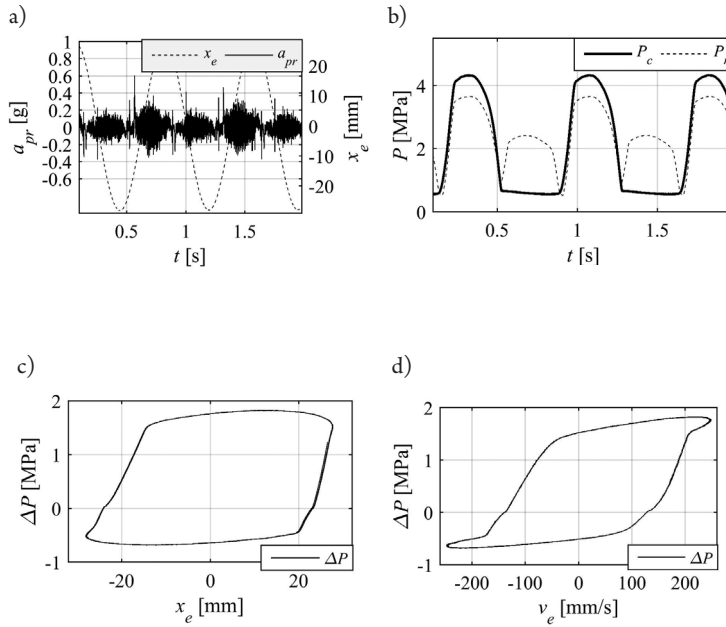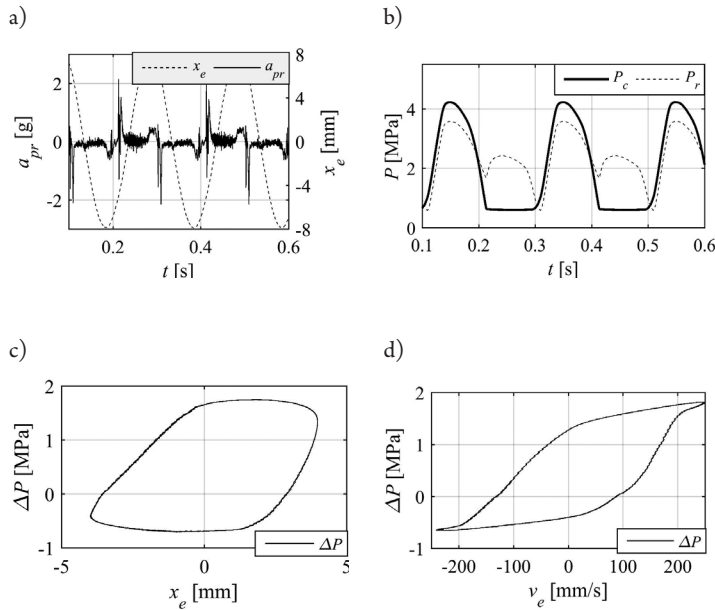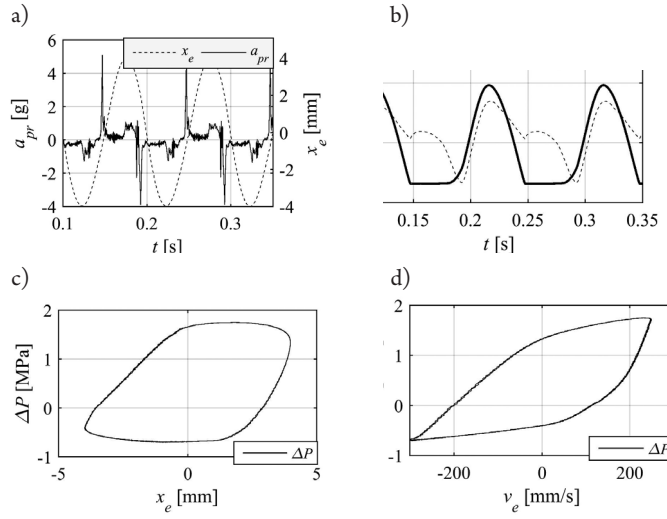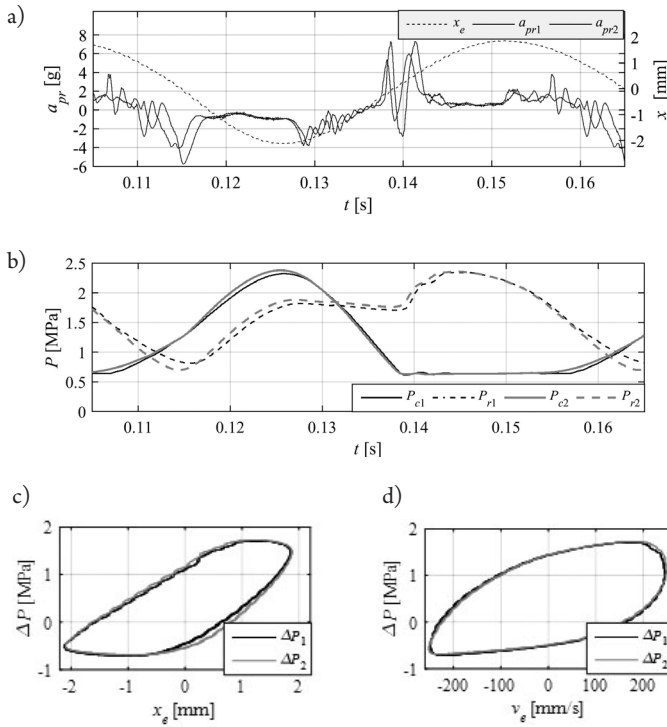
Fig. 4. Measurement results, excitation 1.33 Hz +/−30 m: a) piston rod acceleration a_{pr} and displacement x_e, b) pressure in compression P_c and rebound P_r chamber, c) pressure difference ΔP vs. displacement x_e, d) pressure difference ΔP vs. velocity v_e. ($\Delta P = P_r - P_c$)

Fig. 5. Measurement results, excitation 5 Hz +/−8 mm: a) piston rod acceleration a_{pr} and displacement x_e, b) pressure in compression P_c and rebound P_r chamber, c) pressure difference ΔP vs. displacement x_e, d) pressure difference ΔP vs. velocity v_e. ($\Delta P = P_r - P_c$)

Fig. 6. Measurement results, excitation 10 Hz +/−4 mm: a) piston rod acceleration a_{pr} and displacement x_e, b) pressure in compression P_c and rebound P_r chamber, c) pressure difference ΔP vs. displacement x_e, d) pressure difference ΔP vs. velocity v_e $(\Delta P = P_r - P_c)$

Fig. 7. Measurement results, excitation 20 Hz +/−2 mm: a) piston rod acceleration a_{pr1}, a_{pr2} and displacement x_e, b) pressure in compression P_{c1}, P_{c2} and rebound P_{r1}, P_{r2} chamber, c) pressure difference ΔP vs. displacement x_e, d) pressure difference ΔP $(\Delta P = P_r - P_c)$ vs. velocity v_e. The subscript 1 refers to the first configuration, 2 denotes the second damper configuration

215
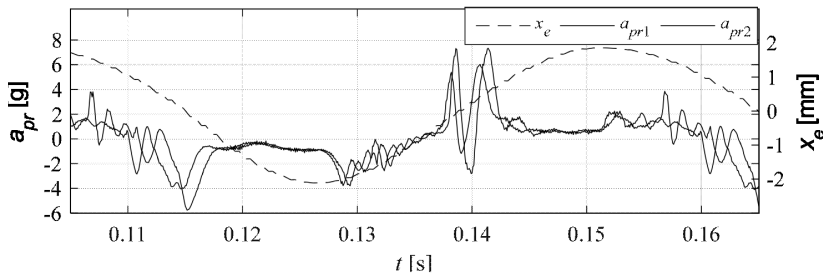
Fig. 8. The FFT of P&R acceleration, calculated based on one cycle and divided by maximum input acceleration (normalized to maximum input acceleration). Although input signal is a constant frequency sinewave (1.3 Hz; 10 Hz; 20 Hz), the output has a wide frequency band. The curves show the dynamic response of the system due to the internal phenomena
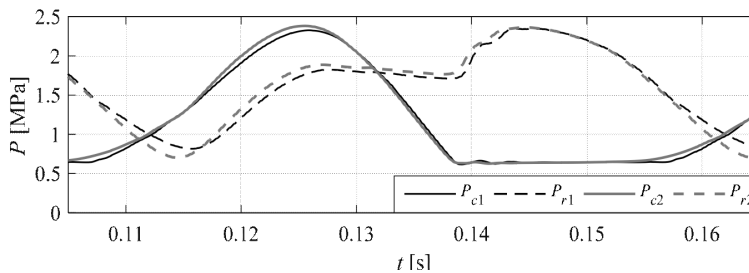
Fig. 9. The FFT of P&R acceleration, calculated based on one cycle and divided by maximum input acceleration (normalized to maximum input acceleration), dashed line present improved damper performance

4. Summary and conclusions

The proposed measurement test stand allows for the investigation of the dynamic characteristic of automotive double-tube shock absorbers. The developed instrumented prototype will be used for improving the dynamic behaviour of the valves in automotive dampers. In the paper, the author presents data acquired for the excitation frequencies up to 20 Hz, which is usually well above the natural frequency of unsprung mass in automotive vehicle suspensions. As the frequency of the excitation increased, the stroking amplitude decreased to maintain constant peak velocity. To conclude, the frequency has a direct impact on the operation of the examined valves. As the frequency increased, the rod acceleration was augmented, too. The acceleration peak amplitude was at the valve's transition points, i.e. at valve's opening/closing. The FFT analysis of the acceleration signal shows the natural frequency at approx. 360 Hz. It is, therefore, apparent that the flow-induced vibrations are transmitted through the top mount module to the body of the car. The phenomenon may be perceived as noise by passengers in the vehicle cabin.

Finally, further work will be focused on dynamic characterization of the damper under investigation, and a further improvement of the operation of the device.

References

[1] Czop P., Sawik D., *A high-frequency first-principle model of a shock absorber and servo-hydraulic tester*, Mechanical Systems and Signal Processing 25(6), August 2011, 1937–1955.

[2] Dixon J.C., *The shock absorber handbook*, Professional Engineering Publishing Ltd and John Wiley and Sons, 2007.

[3] Duym S., Steins R., Reybrouck K., *Evaluation of shock absorber models, Vehicle System Dynamics*: International Journal of Vehicle Mechanics and Mobility 27(2), 1997, 109–127.

[4] Dzierżek S., Knapczyk M., Malinowski M., *Extending passive dampers functionality for specific ride and handling requirements*, Czasopismo Techniczne, 6-M/2008, 39–47.

[5] Eickhoff M., Sonnenburg R., Stretz A., *Piston rod vibrations in damper modules – causes and remedies*, ATZ, Vol. 112, 2010, 24–29.

[6] Farjoud A., Ahmadian M., Craft M., Burke W., *Nonlinear modeling and experimental characterization of hydraulic dampers: effects of shim stack and orifice parameters on damper performance*, Nonlinear Dynamics, Vol. 67, Issue 2, January 2012, 1437–1456.

[7] Ferdek U., Łuczko J., *Modeling and analysis of a twin-tube hydraulic shock absorber*, Czasopismo Techniczne, 2-M/2012, 627–638.

[8] Kruse A., *Analysis of dynamic pressure build-up in twin-tube vehicle shock absorbers with respect to vehicle acoustics*, SAE International, Vehicle Dynamics Expo 2008, Stuttgart 2008.

[9] Kruse A., *Characterizing and reducing structural noises of vehicle shock absorber system*, SAE Technical Report 2002-01-1234, 2002.

[10] Lang H.H., *A study of the characteristics of automotive hydraulic dampers at high stroking frequencies*, The University of Michigan, 1977.

[11] Pressure sensor data sheet: http://www.keller-druck.com/picts/pdf/engl/4lc_9lc_e.pdf (access: 14.04.2015).

Wojciech Otowski (wotowski@fizyk.ifpk.pk.edu.pl)
Gabriela Lewińska

Institute of Physics, Faculty of Physics, Mathematics and Informatics, Cracow University
of Technology

Light sources and their influence on vision organ

Źródła światła i ich wpływ na narząd wzroku

Abstract

The aim of the study was to compare light sources. The paper presents the spectrum of light intensity for natural and artificial sources. Analysis of the spectra was carried out because of their importance for the health of the eye.

Keywords: light source, spectrum analysis, electromagnetic radiation, the eye

Streszczenie

Celem artykułu jest porównanie źródeł światła. W pracy zostały zaprezentowane widma natężenia światła dla źródeł naturalnych i sztucznych. Przeprowadzona została analiza widm ze względu na ich znaczenie dla zdrowia narządu wzroku.

Słowa kluczowe: źródła światła, analiza widm, promieniowanie elektromagnetyczne, oko

1. Introduction

All people are exposed to a certain dose of electromagnetic radiation (for instance sunlight). The influence of electromagnetic radiation on a person (the person's life and health) is significant. It can be both a positive and a destructive factor.

Ultraviolet light (ranging from 10 nm (extreme ultraviolet – EUV) to 400 nm (ultraviolet A – UVA)) activates changes in molecules, such as DNA, lipids and proteins. Near-infrared, infrared and far-infrared radiation (700 nm – 1 mm) causes thermal activation or inactivation, coagulation, and change of phase. Light in the range from 180 nm to 400 nm may result in erythema, keratitis, conjunctivitis, cataract, retinitis, accelerated aging of the skin and skin cancer. Exposure to visible light (especially blue) may cause inflammation of the retina. Far-infrared radiation can cause thermal injury; denaturation of proteins and tissue coagulation. Blue light damage to the retina has research support. Ham was first to show that an exposure to 441 nm light produces a photochemical lesion at power levels too low to raise the retinal temperature by an appreciable amount ($< 0.1°$) [1].

However, there is one more aspect connected with radiation still overlooked in studies. The light spectrum generated by artificial sources differs in shape from the solar spectrum. In many cases, for a very narrow wavelength range, we see peak(s); large increase of intensities. This means that, for a selected wavelength, the eye will accumulate excessive amounts of energy. This in turn leads to damage.

1.1. The eye

The human eye is an organ that reacts to visible light (400 to 700 [nm]). Due to photosensitive cells (namely rods and cones in the retina), incident light is converted into signals that are transformed by the brain into color images. Note that the cone sensitivity depends on the light intensity. In the process of seeing, the eyeball (bulbus oculi), which is responsible for the process of receiving the image, as well as elements of the nervous system, are responsible for transmitting the signal to the brain. The optic nerve needs a minimum energy of 10^{-17} [J] to induce a series of impulses in the brain. The photoreceptor cells contain photopigment molecules, which are transducers of light energy into biological response. Each photopigment molecule consists of two parts; a light sensitive chromophore (molecule derived from vitamin A (11-cis retinal)) and a protein backbone (helical stricture).

Each photoreceptor generates a baseline signal through the continuous transport of sodium ions (Na+) out of the inner segment of the cell and the import of potassium ions (K+) from the outside. At the same time, sodium ions can enter the outer segment via small pores. When the cell body is not exposed to light, the resulting ion imbalance produces a small, steady electric voltage of about 40 [mV] across the cell. Consequently, the so-called "dark current" (baseline signal) is produced. To create a nerve impulse, light "reduces" this baseline photoreceptor current [2].

When the chromophore is hit by a photon of the proper energy, it instantly changes shape (a photoisomerization effect). As a result, the opsin molecule also changes shape, which in

turn changes the baseline electrical current across the cell body. This "simplified" process by which the retina translates light energy (from photon absorption) into nerve impulses (nerve output) is completed within 50 microseconds. Care must be taken that "the proper energy" means energy of photopigment (wavelength) peak sensitivity.

Each photopigment (photosensor) reacts with the highest probability on the proper energy photon. Reaction on other energy photons is less likely and requires a large number of photons (greater light intensity).

Human color vision is enabled by three types of photoreceptors:

- the scotopic band is represented by rod photoreceptors – it is monochromatic vision in very low light (night-vision),
- the photopic band is represented (primarily) by cone wavelength-dependent photoreceptors – it is color vision under suitably bright (well-lit, luminance level 10 to 10^8 cd/m²) conditions,
- the "meltopic" band which is a non-imaging photoreceptor – it is a stimulator of the biological clock [3].

In the late 1990's, the "meltopic" photoreceptor was recognized, which has sensitivity in the blue spectral range. It is the wavelength-dependent suppressor of melatonin production [4].

Research has found that exposure to bright white or blue light at night is associated with insomnia and increased risk for a wide range of diseases.

Due to light adaptation (or sensitivity regulation), the human eye can detect illuminance in the range of 10^{14} – from 10^{-6} [lx] to 10^8 [lx] (note: midday sun is even 10^9 [lx] – see Fig. 1) [5]. Spectral sensitivity is the relative efficiency of detection, of light or other signal, as a function of the frequency or wavelength of the signal [6]. It has been established that the maximum spectral sensitivity of the human eye under daylight conditions is at a wavelength of 555 [nm] (green), while at night the peak shifts to 507 [nm] (blue-green) [7]. Spectral sensitivity may be expressed as a quantum efficiency. Spectral response functions of the three human photoreceptors are presented in Fig. 2.
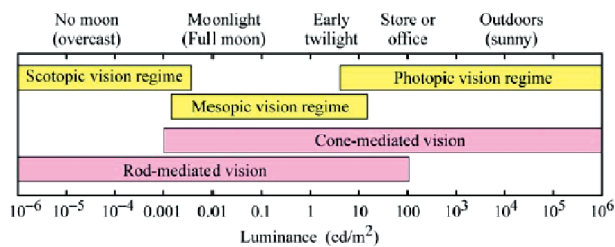

Fig. 1. Approximate luminance ranges of human vision and corresponding photoreceptors [5]

Much about it is the probability to catch light energy (a quantum of light) as a function of wavelength [7, 8]. It may be expressed with units, such as amperes per watt [9–11]. However, the light adaptation mechanisms are not clear yet.

The responses of the rod and cone cells have a nonlinear dependence [6]. On the other hand, the light effective excitation of photopigment is rather linear [2].
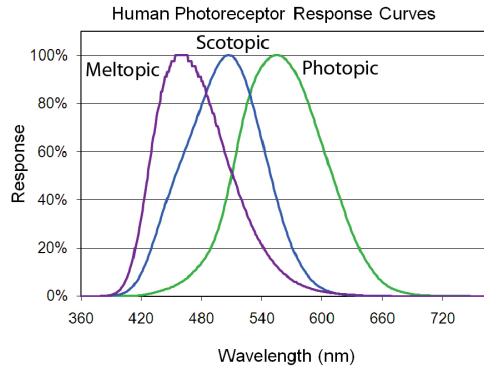
Fig. 2. Spectral response functions of the three human photoreceptor bands [6]

One should note that the signal of a photoreceptor representing light is transmitted through the nerve impulse as a change in the "dark current" [2]. The human eye reacts to the light incident on a physical surface (the illuminance) and/or emitted from a surface (the luminance). The comfort range for luminance is much smaller (from 10^{10} [lx] to 10^{40} [lx]) compared to the illuminance. However, this is coherent with the fact that our visual system does not adapt to the actual illuminance. The retina has a static contrast ratio of around 100:1. As soon as the eye moves, it re-adjusts its exposure both chemically and geometrically. Hence, the dynamic contrast ratio amounts to about 1 000 000:1. The rods are more sensitive and allow vision in low light conditions (so-called scotopic vision); they also have a great ability to perceive moving objects. Cones are responsible for color vision in bright light (also called photopic vision). The human system adapts to the average luminance (diffuse light). The light adaptation occurs relatively quickly.

There are two ways that light will damage your eye [12]:

1. Thermal damage when too much energy is concentrated on the retina. For visible and infrared light reaching the retina, melanin and haemoglobin are the primary absorbers. Power of 20 [mW] is enough to cause thermal damage. This takes place for instance when the person is exposed to a very bright light pulse, shorter than 20 μs. Usually, when the rise in temperature is at least 10°C above the physiological temperature, then thermal damage occurs, which leads to thermal denaturation of many proteins [13]. Wavelengths between 800 nm to 1400 nm (which are heat) are able to oxidize or decompose photopigment moleculesł

2. Photochemical damage when photons can destroy chemical bonds (in organic molecules; for instance, the cornea and the lens absorb part of the infrared radiation – mainly water bands at 980 nm, 1200 nm, and 1430 nm [13]). "Photochemical damage occurs when light is absorbed by a chromophore and leads to the formation of an electronically excited state of that molecule, which then undergoes either chemical transformation itself and/or interacts with other molecules, leading to chemical changes of both interacting molecules, or to a transfer of the excitation energy to the other molecules" [13]. It needs to be highlighted that photochemical damage does

not cause a substantial increase in the temperature of the tissue. Electromagnetic energy of the violet and blue (400–500 [nm]) wavelengths (near UV), is sufficient to destroy photopigment molecules.

The wavelengths' effect of photochemical damage to the retina is present in Table 1.

Table 1. The wavelengths' effect of photochemical damage to the retina

Wavelength [nm]			
463	500	520	630–720
Irreversible damage to S cones	Damage to rods	Reversible damage to M cones	Reversible damage to L cones

There is a photomechanical (or photoacoustic) damage when for instance a pulse laser produces a thermoelastic pressure wave. Light energy is absorbed faster than the relaxation of the mechanical wave.

Sunlight (the solar irradiance) may damage the human retina. In the midday, sun energy varies between 1.5 and 122 [W/cm^2]. So, even several minutes of exposure are sufficient to damage the retina (photochemical effect). Energetic UV sun radiation is absorbed by oxygen and generates the ozone.

Due to the effects of ultraviolet radiation on living organisms, the UV spectrum can be divided into three subgroups:

- ▸ UV-A – wavelength: 315–400 [nm], photon energy: 3.10–3.94 [eV],
- ▸ UV-B – wavelength: 280–315 [nm], photon energy: 3.94–4.43 [eV],
- ▸ UV-C – wavelength: 100–280 [nm], photon energy: 4.43–12.4 [eV].

The most harmful radiation to humans is radiation from the entire range of C and most of the B range. Happily, UV-C is completely absorbed, and UV-B is mostly absorbed by the ozone layer and atmosphere. UV-A is not absorbed by the ozone layer and as a result, about 97% of UV-A light reaches the Earth's surface [14].

2. Light sources

The light sources can be divided according to the emitting light process on natural (objects found in nature that produce light) and artificial (Human made objects that produce light) objects. Natural sources of light include sunlight, the stars, volcanoes, meteorological lightning, light of fire and biochemical sources. Artificial light sources can be classified as an incandescent bulbs, a halogen lamp, gaseous discharge light (metal halide, fluorescent tube, compact fluorescent tube), LED (light-emitting diodes) light (red LED, green LED, blue LED, RGB LED, white LED). Despite the variety of natural sources of light, the most significant impact on humanity is had by the nearest star – the sun. Solar radiation is the main source of energy on earth. We may say that the earliest form of artificial light used to illuminate an area were campfires and torches. The next step was to use oil lamps. Later, candles were invented. With time, electric lamps improved lighting of the darkness. We want to present the different light sources and compare their spectra with the with that of the sun.

3. Experiment

We carry out the spectra absorption measurements using a spectrometer HR4000CG-UVNIR Ocean's Optics. This spectrometer has the ability to perform spectroscopic measurements, such as absorbance, reflectance, and emission in the range from 200 nm to 1100 nm. Light is transmitted into the spectrometer through an optical fiber. The spectrometer measures the amount of light and transforms the collected data into digital information.

All presented spectra are obtained by use. We divided them into two types: a dome-shaped spectrum (a continuous spectrum) and the multiple peaks spectrum (a discrete spectrum superimposed on a continuous spectrum).

Figure 3 shows the daylight spectrum. This spectrum has a dome shape. On the dome-shape base, we do not see any additional peaks. It can be concluded that this is the most optimal light source. Daylight spectrum has a shape similar to that of the solar spectrum. However, passing through the atmosphere, the light is absorbed and scattered, and it final form is ragged. In this article, we will consider this spectrum as reference.
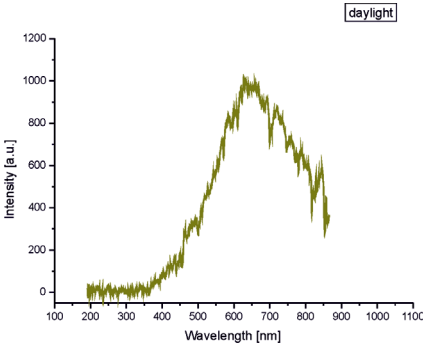
Fig. 3. Daylight spectrum

Candle spectrum

Candles emit light of a continuous range of wavelength (frequencies). The candle spectrum is smoothed with the single potassium (K) maximum at 780 nm (Fig. 4).
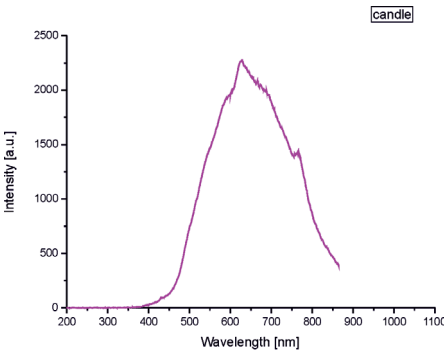
Fig. 4. Candle spectrum

Kerosene lamp spectrum

Kerosene lamp emits light of a continuous range of wavelength. The spectrum is also smoothed (Fig. 5), but we have to keep in mind that luminous efficacy of a kerosene flame is very low.
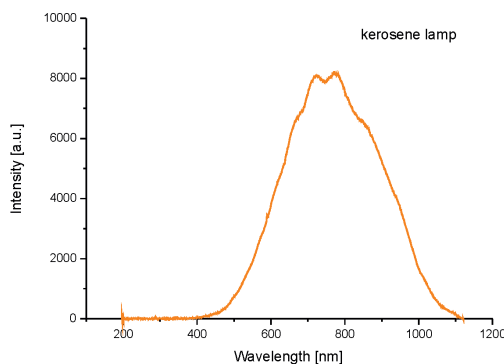
Fig. 5. Kerosene lamp

Incandescent bulb spectrum

Incandescent bulbs produce a continuous electromagnetic spectrum. The nature of this form of radiation may be explained by Planck's law. In Figure 6, we present the incandescent bulb spectra for three different total power lamps.
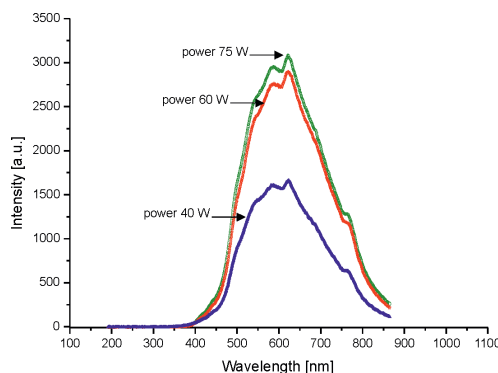

Fig. 6. Incandescent bulb spectra (three bulbs of different power consumption)

Looking at the incandescent bulb spectra, we may argue that the emitted light does not disrupt the natural sensitivity of the human eye in the whole range of wavelengths. However, we should keep in mind that incandescent bulbs are inefficient energetically; less than 5% of the electric energy is converted into visible light [14]. On the other hand, incandescent bulbs are irreplaceable in applications where accurate color reproduction is important. The spectrum emitted from an incandescent bulb reproduces colors almost perfectly. The colour temperature is 2100–3000 K. In Figure 7, one can compare the three normalized spectra of sunlight, incandescent bulb and candle.
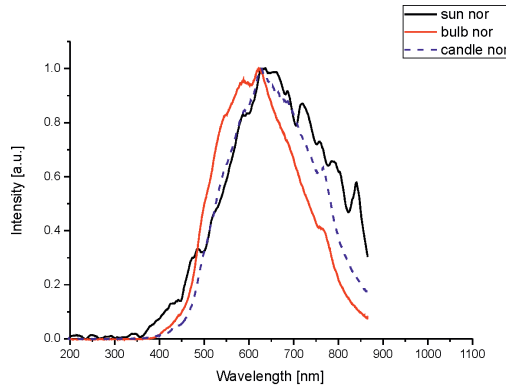
Fig. 7. Three normalized spectra of sunlight, incandescent bulb and candle

Mercury-vapor spectrum

A mercury-vapor lamp is a type of discharge lamp in which light is produced by an electrical discharge in mercury vapor. The spectrum consists of several very thin lines (Fig. 8). Mercury-vapor lamps are characterized by an arc discharge. In these lamps, there is a strobe effect. In mercury-vapor lamps, less than 10% of the energy is converted into visible light. The rest of the energy is converted to heat and UV.
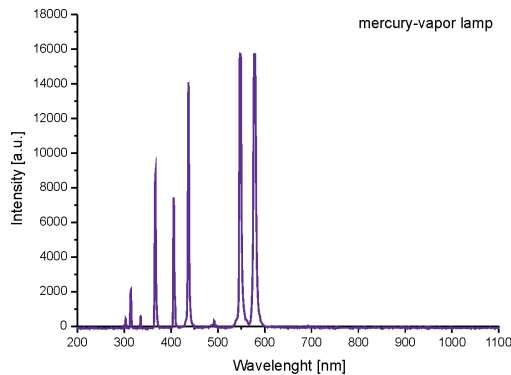
Fig. 8. The mercury-vapor lamp spectrum

Using the phosphor, the part of UV radiation is converted into white light, which in turn gives a better color reproduction. The colour temperature is about 4800 K with phosphor and 6600 K without phosphor. We would like to emphasize that the spectrum is not dome-shaped.

Halogen bulb spectrum

Halogen bulbs are also an incandescent emitter. They are filled with a small amount of a halogen (for example iodine, which is at a higher pressure: 7–8 atm), preventing the darkening of the bubble from the inside. They operate at a higher temperature. Halogen forms a chemical compound with

tungsten. This compound circulates together with the gas in the bulb. Then, it decomposes into tungsten and halogen because of the heat of the filament. As a result takes place transfer of tungsten particles from the bulb onto the filament. This is the so-called halogen regenerative cycle. Like an incandescent light emitter, the halogen lamp radiates a continuous spectrum of light; from ultraviolet to infrared (Fig. 9). What is worth noting is the fact that the spectrum of halogen lamp (2800–3400 [K]) is closer to sunlight than the standard tungsten (2000–3500 [K]). The spectrum is shifted toward blue. Seeing that the lamp can operate at a higher temperature, it emits some UV radiation. The doped-quartz glass of halogen bulbs blocks UV.
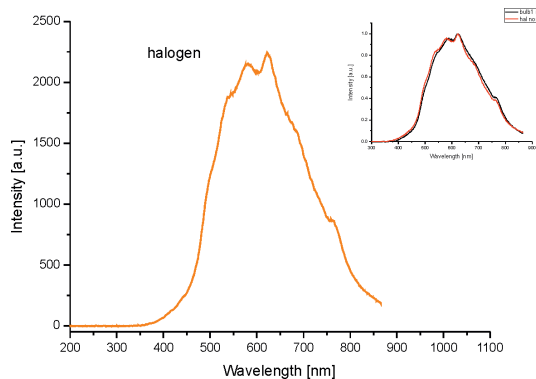
Fig. 9. Halogen bulb spectrum (Inset: normalized spectra of incandescent bulb and halogen lamp)

Fluorescent tube spectrum

Fluorescent tubes (fluorescent lamps) produce light differently than incandescent bulbs. An electric current flowing through an argon gas and a small amount of mercury vapor in tube generate invisible (short-wave) ultraviolet light. This light arouses luminophor on the inside of the tube to emit a visible light. Colour temperature is 2300–6800 K. The color reproducibility is more than 80%.
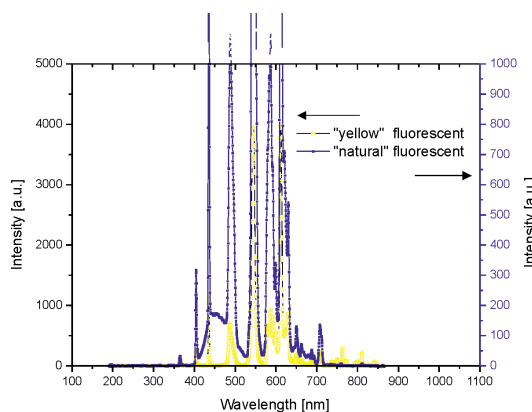

Fig. 10. Fluorescent tubes spectra – left scale "yellow" fluorescent tube, right scale "natural sunshine" fluorescent tube

The fluorescent spectra presented in Figure 10 are of the multiple peaks type. A discrete spectrum superimposed on a continuous base is visible for "natural sunshine" fluorescent tube (right scale). This shape results from the physical mechanism of radiation: the electrons acquiring energy and then losing it. According to the laws of quantum mechanics, when the electrons lose energy, they emit a specific electromagnetic wave. As one can see for the selected wavelength (selected color), the intensity increases several times. This means that the selected photoreceptor should reduce its sensitivity. However, the human eye sensitivity regulation mechanism affects the whole eye and not individual photoreceptors. In Figure 11, one can compare normalized spectra of sunlight, incandescent bulb and fluorescent tube.
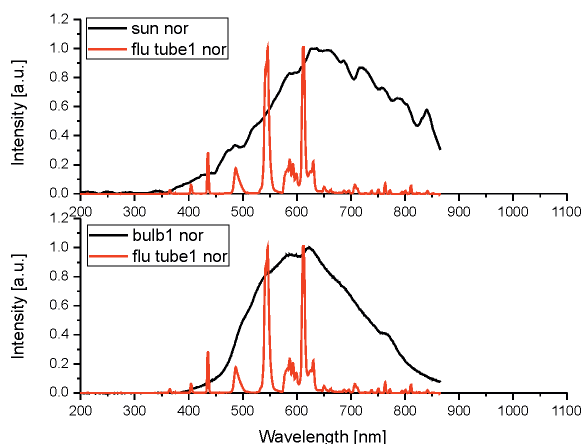

Fig. 11. Normalized spectra of sunlight, incandescent bulb and fluorescent tube

An extreme case of peak type radiation is laser (Light Amplification by Stimulated Emission of Radiation) (Fig. 12). Lasers are not considered as a source of light in everyday use – they are rather used as a tool in science, medicine and technology. On any device that uses laser, a warning is placed about the possibility of eye damage.
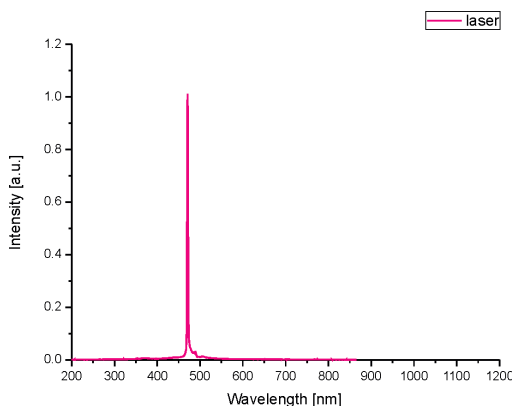

Fig. 12. Spectrum of laser

Xenon lamp spectrum

We need to mention that many of today's cars use xenon headlights. Xenon lamp spectrum is of multiple peaks type. It brings all the negatives of this kind of lamps. Besides, there are some very strong emission lines in the near infrared, roughly in the region of 800–1000 [nm] (Fig. 13).
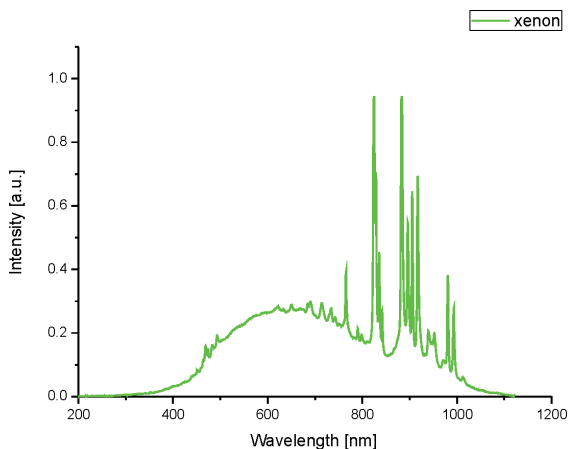

Fig. 13. Xenon lamp spectrum

LED bulb spectrum

Currently, the best solution seems to be new lighting technology, namely LED bulbs. In recent years, the popularity of LED (Light Emitting Diodes) bulbs increased. Their spectrum is explicitly marked by a broad maximum (Fig. 14). Light emitting diode is a semiconductor light source. Controlled by voltage, the p-n junction diode, releasing recombine electrons-electron holes energy in the form of light (photons); this is electroluminescence effect. The color of the light (the energy of the photon) is specified by the band gap energy of the semiconductor.

Nevertheless, LED bulbs can emit white light (WLED). There are two ways to reach it. Firstly, the WLED lamp may consist of red, green and blue LED sources – these sources combined emit white light base on Maxwell's color triangle. Secondly, a more popular method is to use a blue LED light sources and the phosphor coating, which change the light spectrum. By using several layers, the light spectrum can be compared to that emitted by the sun.

We should keep in mind that the principle of bulb-type LED operation is based on the Graetz bridge. So, one can expect pulsation. In Fig. 15, the pulsation of the light intensity of the WLED is presented.

However, there is still a lot of controversy. The European Commission report (Health Effects of Artificial Light) saying that LED blue light causes a photochemical risk to the eye; "Blue light is (...) recognized as being harmful and dangerous for the retina, as a result of cellular oxidative stress (...)" – citation [15, 16]. The other main risk is from glare. The report say that, for indoor lighting, it is generally agreed that luminance higher than 10,000 cd/m² causes visual

discomfort whatever the position of the lighting unit in the field of vision. Because the emission surfaces of LEDs are highly-concentrated point sources, the luminance of each individual source can be 1000 times higher than the discomfort level. The level of direct radiation from this type of source can therefore easily exceed the level of visual discomfort [17]. To produce white light, LED electronics must emit light at short wavelengths, which makes them potential sources for suppressing melatonin at night [18].
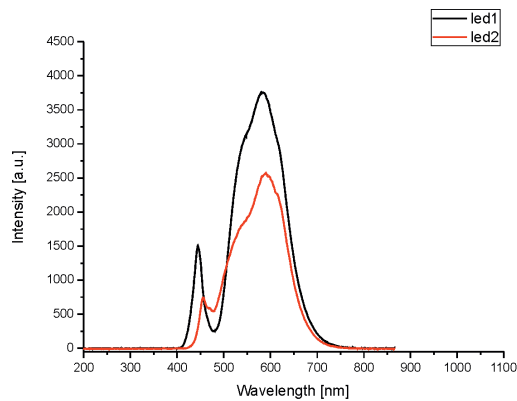

Fig. 14. Spectra of commercially available LEDs from different manufacturers

In the opinion of the authors, LEDs have many advantages over incandescent light sources like lower energy consumption, longer lifetime, faster switching and dome-shape spectrum.
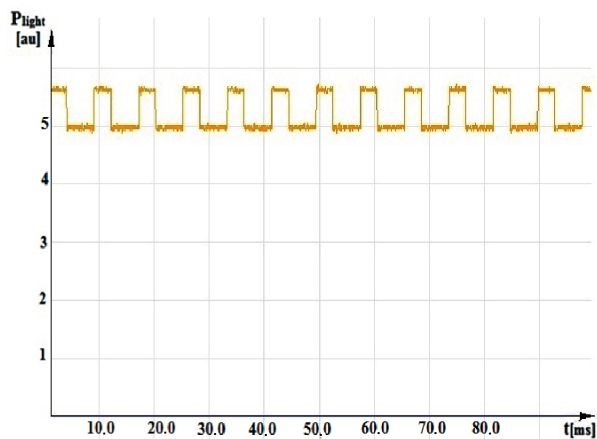

Fig. 15. Pulsation of the light intensity of the WLED (frequency ω = 100 Hz)

Nowadays, LEDs are often applied to highlight different kinds of displays, such as televisions, computer screens, lighted wallpaper or cell phones. Light Emitting Diodes are now used as car headlamps, traffic signals, street lights and architecture lighting. LEDs are used in commercial and home areas.

Considering the rapid development of the LED technology (organic light-emitting diodes (OLEDs), quantum dot LEDs), we may expect an elimination of the defects of LEDs.

4. Summary

In this paper, we wanted to point out that, in addition to the traditional assessment of the sources of light (which is largely quantitative assessment) based mostly on power consumption, one should consider, even qualitatively, the health effects of artificial light. This effect is partially encoded in (or related to) the shape of the spectrum. Estimation of this effect is difficult because it requires extensive research on a large set of people (on a large population) for a long time. The authors believe that the best shape of the spectrum for the human eye is the one that best approximates the spectrum of the sun (dome-shaped like). Each additional high-intensity narrow peak endangers the human eye. The human eye has no mechanism for a selective reduction of the amount of incident light.

However, avoidance of the negative effects of new technologies can bring in long-term, measurable and positive economic effects.

References

[1]   Ham W.T Jr., Mueller HA., Ruffolo J.J Jr., Clarke A.M., *Sensitivity of the retina to radiation damage as a function of wavelength*, Photochem Photobiol, Vol. 29, 1979, 735–743.

[2]   Grieve K., Roorda A., *Intrinsic Signals from Human Cone Photoreceptors Investigative*, Ophthalmology & Visual Science, 49, 2008, 713–719.

[3]   Brainard G.C., Hanifin J.P., Greeson J.M., Byrne B., Glickman G., Gerner G., Gerner E., Rollag M.D., *Action Spectrum for Melatonin Regulation in Humans: Evidence fora Novel Circadian Photoreceptor*, J. Neuro, 21, 2001, 6405–6412.

[4]   Provencio I., Jiang G., De Grip W.J., Hayes W.P., Rollag M.D., *Melanopsin: An opsin in melanophores, brain, and eye*, Proc. Nat. Acad. Sci., 95, 1998, 340–345.

[5]   He S., Dong W., Deng Q., Weng S., Sun W., *Seeing more clearly: recent advances in understanding retinal circuitry*, Science, 302, 2003, 408–411.

[6]   Fritzsche H., Poirier E., *A Systematic Neutron Reflectometry Study on Hydrogen Absorption in Thin Mg1-xAlx Alloy Films*, Canadian Journal of Physics, 88, 2010, 10–15.

[7]   Gross H., Blechinger F., Achtner B., *Handbook of Optical Systems*, Vol. 4, Wiley-VCH, 2008.

[8]   Wilkinson M.H.F., Schut F., *Digital Image Analysis of Microbes*, John Wiley and Sons, 1998.

[9]   Barten P.G.J., *Contrast Sensitivity of the Human Eye and Ist Effect on Image Quality*, SPIE Press, 1999.

[10] Young M., *Optics and lasers*, Springer, 1993.

[11] Dyer S.A., *Survey of Instrumentation and Measurement*, Wiley-IEEE, 2001.

[12] Northrop R.B., *Analysis and Application of Analog Electronic Circuits to Biomedical Instrumentation*, CRC Press, 2004.

[13] Good G.W., *Light and Eye Damage American Optometric Association*, http:// physics. stackexchange.com/posts/158274/revisions (access: 25.06.2016).

[14] Levine M.W., *Levine & Shefner's Fundamentals of sensation and perception*, Oxford 2006.

[15] Rüchard E., *Światło widzialne i niewidzialne*, PWN, Warszawa 1962 (in Polish).

[16] LEDs Magazine, *Light and human health: LED risks highlighted*, http://www. ledsmagazine.com/articles/2010/11/light-and-human-health-led-risks-highlighted. html (access: 18.05.2016).

[17] European Commission, *Health and Consumers, Health Effects of Artificial Light*, http:// ec.europa.eu/health/scientific_committees/opinions_layman/artificial-light/en/ index.htm (access: 18.05.2016).

[18] Good G.W., *Light and Eye Damage*, American Optometric Association, December 2014.

[19] Wood B., Rea M.S., Plitnick B., Figueiro M.G., *Light level and duration of exposure determine the impact of self-luminous tablets on melatonin suppression*, Applied Ergonomics, 44, 2013, 237–240.